A NANOPHYSIOMETER TO STUDY FORCE – EXCITATION COUPLING IN SINGLE CARDIAC MYOCYTES

By

Andreas Augustinus Werdich

Dissertation

Submitted to the Faculty of the

Graduate School of Vanderbilt University

in partial fulfillment of the requirements

for the degree of

DOCTOR OF PHILOSOPHY

in

Physics

May, 2006

Nashville, Tennessee

Approved by:

Professor Franz Baudenbacher

Professor Jonathan Gilligan

Professor Frederick R. Haselton

Professor M. Shane Hutson

Professor David W. Piston

Professor John P. Wikswo

ACKNOWLEDGMENTS

This work would have never been possible without the support of many great people who I want to thank here.

I am very grateful to have Dr. Franz Baudenbacher as my PhD adviser, chair of the committee and as a very good friend. He supported me during the past five years in many respects. His advice has been, and is continuing to be, essential for my success. He always took time for me, even when it meant to discuss a presentation or a manuscript on a Sunday evening. Franz gave me the freedom and the opportunity to pursue my own ideas and I enjoy very much working with him. I truly cherished my time in the Baudenbacher laboratory where I found out that I really love the combination of engineering and biology and that this is what I want to do in the future. My thanks to Franz will go beyond graduate school.

I am honored that I had the opportunity to work with Dr. John Wikswo. I want to thank him for being a member of my dissertation committee. His enormous knowledge and his expertise in science and engineering are impressive and inspiring to me. I admire John's passion for teaching and his skills to communicate with people. I learned from him that it is not only important to do a good experiment, but also to be able to present results well and to interest others in your own ideas. I feel that part of John's success is based on his extraordinary ability to connect with people, making them excited about new projects and proud of what they are doing. This is an important quality of leadership which I would like to acquire myself one day.

I want to thank the other members of my PhD committee, Dr. David Piston, Dr. Rick Haselton and Dr. Jonathan Gilligan for their time and efforts that they invested in my graduate study, and for the many interesting discussions that really helped me to focus on science. I would like to thank Dr. Shane Hutson for joining my committee and for his suggestions to improve the dissertation.

I would like to thank Dr. André Kleber at the University of Bern who I consider a great mentor and friend. I learned from him a lot about experimental techniques, cardiac physiology, science and human nature. I hope that I will be able to continue our collaboration and to learn from him in the future. I admire André as an accomplished scientist, cardiologist and an extraordinary engineer. He designed and constructed an optical fiber array, a photodiode amplifier and a precision translational microscope stage for our fluorescence setup, all of which I have learned to appreciate during my graduate work. I also want to thank him for his personal advice, helping me to make some very important personal and professional decisions.

I would like to thank Dr. Mark Anderson for his support and for his generous gift of the genetically engineered mice. Without his help and guidance, I would not have been able to do the single cardiac myocyte experiments that led to this dissertation. His weekly group meetings in which I was encouraged to participate and our numerous scientific discussions inspired me and helped me to achieve good quality results. There are many things that I can learn from Dr. Anderson and I hope that I can continue to work with him in the future. I also want to thank the members of the Anderson laboratory, in particular, Dr. Yuejin Wu and his wife Jinying Yang, and Dr. Jingdong Li for teaching me how to isolate cardiac myocytes.

I want to give special thanks to Dr. Vernat Exil for encouraging me to do optical recordings with his very-long-chain acyl-coenzyme a dehydrogenase deficient mice. He is a great person to work with. We obtained very exciting results that raised many interesting questions which are worth pursuing in future experiments.

I want to thank my friend Dr. Eduardo Lima for his help with the instrumentation and data analysis. Eduardo is the "Matlab and Labview Guru" who can do magic with data. Without his expertise, I would still be looking for some meaningful data in my noisy extracellular potential recordings. His contribution to the results was essential and I hope that we are going to work together on other projects in the future.

I want to thank my friend Ron Reiserer who was extremely helpful with technical support during my experiments. He is taking great care of the equipment inside and outside of the clean rooms which significantly increases the efficiency of my work. Ron also fabricated many of my electrodes on thin cover glass that I used with the Nanophysiometer (most of which I broke during the experiments, sorry!).

I would like to say thanks to Dr. Borislav Ivanov for helping me with the electrochemistry, for developing the platinum black deposition process and for his great humor.

I thank Dr. Igor Ges for fabricating electrodes and for using the Nanophysiometer in his pH experiments. It is great to know that the development of the Nanophysiometer will continue after my graduation

I would like to thank all the other members of the Baudenbacher laboratory for their support.

I want to thank all the members of the VIIBRE group, especially Cheryl Cosby, Allison Price, and Don Berry for their administrative support. I want to thank John Fellenstein and Bob Patchin in the machine shop for the quick and precise fabrication of many mechanical parts that made up the fluorescence detection setup and the Nanophysiometer.

I want to thank all my friends here in Nashville, and in other places, for their companionship and friendship.

I owe my parents and my sister Eva a great debt of gratitude for their unconditional love and support at all times. Living 5000 miles away from them has never been, nor will it ever be, easy. Without their consistent encouragement and faithfulness, I would not have come to America; I would never have accomplished my Ph.D. education at Vanderbilt University; nor would I have met my wife Xiang.

At last, but most importantly, I want to thank my wife Xiang for her never ending love, her passion and her patience. It is a miracle that we came half way around the world to meet here in Nashville. Because being married with her is the best thing that ever happened to me, coming to Vanderbilt University to study Physics was the best decision I ever made.

TABLE OF CONTENTS

Page

LIST OF TABLES

LIST OF FIGURES

LIST OF ABBREVIATIONS

BioMEMS	Biological micro electronic mechanical systems
CaMKII	Ca^{2+}/calmodulin dependent protein kinase II
CICR	Calcium induced calcium release
FDAR	Frequency-dependent acceleration of relaxation
FFT	Fast Fourier transform
GL	Glucose
I_{Ca}	Transmembrane Ca^{2+} current through L-Type Ca^{2+} channel
LTCC	L-type calcium channel
NCX	Na^{+}/Ca^{2+} exchanger
PA	Palmitic acid
PDMS	Poly-dimethylsiloxane
PKA	Protein kinase A
PLN	Phospholamban
PMT	Photomultiplier
ROI	Region of interest
RyR	Ryanodine receptor
SERCA	Sarcoplasmic reticulum calcium ATPase
SR	Sarcoplasmic reticulum
TnC	Troponin-C
TnI	Troponin-I
VLCAD	Very-long-chain acyl-coenzyme a dehydrogenase

CHAPTER I

INTRODUCTION

1.1 Significance

Force – excitation coupling in single cardiac myocytes

Since 1900, cardiovascular disease (CVD) has been the No.1 killer in the United States. Nearly 2500 Americans die of CVD each day, an average death in every 35 seconds. CVD claims more lives each year than the next 4 leading causes of death combined, which are cancer, chronic lower respiratory disease, accidents, and diabetes mellitus.

Heart failure is a chronic and progressive disorder of the heart characterized by progressive deterioration of cardiac pump function. It poses a 1 in 5 lifetime risk on both men and women [2, 3]. Heart failure is typically a secondary entity that occurs when the myocardial function is diminished by an underlying pathological condition such as cardiomyopathy (acquired from chronic ischemia, hypertension or diabetes), valve disease, congenital malformation, or arrhythmia. The long-term response of the heart to these initiating insults is electrical and mechanical remodeling leading to a progressive deterioration of contractile function [4-6]. While the causes of heart failure are distinctively different, the functional characteristics of the failing myocardium are surprisingly consistent. In the early stage of heart failure the first changes observed are slowing of the rates of contraction and relaxation and prolongation of the action potential. Later, in a more advanced stage of heart failure, reduced force production and shortening

are consistently observed [4-8]. The pathophysiological mechanism behind myocardial failure is not known but there is reason to believe that it originates from alterations in force – excitation coupling of the component cardiac myocytes [6]. It is well understood that in muscle cells calcium plays an important role in the process that couples an electrical depolarization to force generation. In the heart, depolarizing pace maker cells generate a depolarizing wave that spreads rapidly from one myocyte to another across gap junctions [9], causing an almost synchronous depolarization of the entire heart. Intracellular calcium concentration rises as a consequence of the electrical depolarization and directly activates the contractile machinery of the cell to produce force and contraction. In contrast to skeletal muscle in which force is graded by the recruitment of muscle fibers, in heart muscle, all cells participate in each beat [10]. As a result, cardiac contractile force can only be regulated by changing the force developed by the individual cardiomyocyte. Therefore, force-excitation coupling in the heart is generally studied in isolated cardiac myocytes.

Furthermore, the isolated cardiac myocyte is a more suitable model to study the dynamics of active and passive force generation than any multicellular preparation (e.g. trabeculae and papillary muscles). Mechanical studies in excised cardiac muscle have led to ambiguous results because of the poorly defined viscoelasticity of the extracellular matrix [11, 12], and because no clear representation of the relation between passive and active forces is evident [13]. Additional series elasticity in large muscle preparations may arise from the end compliance related to the attachment of recording devices. Finally, inhomogenities of strain and stress even in one-dimensional isolated muscle preparations have shown to produce a significant structural and functional nonuniformity in both

passive and active responses [14]. It is customarily assumed that the load (force) and strain are uniformly distributed throughout the cross section and along the length of the specimen. The implicit assumption of a uniform contractile state is evident in almost all the papillary muscle literature that presents data on muscle contraction dynamics.

The same argument is true when intracellular electrical activity is monitored in tissue preparations using fluorescent dyes. Because of the large volume of excised muscle preparations, the dye distribution may be highly nonuniform and may even change during the measurement.

In summary, the isolated intact isolated cardiac myocyte is the ideal model for studying force – excitation contraction coupling because it provides almost direct access to a relatively small number of contractile units (sarcomeres) in a single cohesive structure well defined by the sarcolemma membrane.

Phospholamban – a target protein for therapy of myocardial dysfunction

Disordered cellular calcium homeostasis is a hallmark of heart failure. This observation was first documented by Gwathmey and co-workers [15] and has been described multiple times in various models of heart failure. In fact, dysregulation of calcium handling is universal in structural heart disease, although, the details of this 'remodeling' process differ amongst different models, between animal species and between different time points during disease progression [7, 8, 16]. The reduction in contractile force development in failing human cardiac myocytes is accompanied by a markedly prolonged declining phase of the Ca^{2+} transients [15, 17-20]. Intracellular calcium release during the cardiac cycle is graded and depends largely on the amount of Ca^{2+} entering the cell

through sarcolemmal ion channels (in a process called calcium induced calcium release, CICR) and on the filling state of the sarcoplasmic reticulum (SR), the intracellular calcium store. The prolongation of the Ca^{2+} transient is the direct result of a decrease in the activity of the intracellular Ca^{2+} pump (SERCA2a), which is responsible for the transport of cytosolic Ca^{2+} back into the SR. The reduced rate of SR Ca^{2+} uptake decreases the amount of calcium available for release during the cardiac cycle. As a result, force generation, contraction amplitude and rate of relaxation are diminished in heart failure. Phospholamban (PLN) is an intracellular SR protein and a negative regulator of SERCA2a activity [21, 22]. The PLN – SERCA2a interaction controls the calcium content of the SR and ultimately cardiac contractility [23, 24]. It is well established that a decrease in PLN phosphorylation and in the SERCA2a/PLN expression ratio contributes to the contractile dysfunction in myocardial failure [25, 26]. In fact, overexpression of SERCA2a via gene transfer restored calcium handling, contractility and the frequency response in isolated failing human cardiomyocytes [19, 27]. The results of targeting PLN in failing human cardiac myocytes are promising: (1) Decreasing phospholamban expression restores contractility in failing ventricular myocytes; (2) ablation of phospholamban results in improvement in contractility similar to that of SERCA2a overexpression. Studies by Kranias et al. [23, 24, 28] have clearly shown that murine models of phospholamban knockout have enhanced contractility.

Frequency adaptation in phospholamban and CaMKII deficient cardiac myocytes

An important observation made in many *in vitro* studies is that non-failing and failing human myocytes have similar contractile characteristics at low workloads, i.e. slow

pacing rates, low extracellular [Ca^{2+}] or in the absence of catecholamine stimulation [15, 29, 30]. Specifically, peak force (or shortening) is not significantly different in non-failing vs. failing human LV muscles or myocytes at slow (< 30 bpm), and the rates of force development or shortening are only modestly lower than normal in failing cardiac muscle. Increasing the pacing rate within the physiological range causes the contractility to increase in non-failing myocytes (positive force – frequency relationship) but causes it to decrease in cardiac myocytes isolated from failing human hearts (negative force – frequency relationship) [15, 30]. These results support the hypothesis that changes in cellular Ca^{2+} handling are a final common pathway for progressive deterioration of cardiac pump function in myocardial failure at increasing pacing rates. In fact, abnormal SR Ca^{2+} loading has been suggested to produce significant changes in force – excitation coupling in failing human myocytes at physiological stimulation frequencies [31, 32]. The interpretation of these results is severely complicated by the fact that the mechanism of frequency adaptation in the heart is not well understood in both nonfailing and failing cardiac myocytes.

When the stimulation frequency is increased, the mammalian heart responds with an acceleration of relaxation (FDAR) allowing it to refill more rapidly between beats [33]. Schouten *et al.* [34] speculated that a faster relaxation at steady state (SS) *vs.* post-rest beats was due to the activity of the endogenous enzyme Ca^{2+}/Calmodulin dependent protein kinase II (CaMKII). Several reports showed that the higher average cytosolic [Ca^{2+}] occurring at a higher heart rate, could activate CaMKII in a frequency-dependent manner to phosphorylate PLN leading to an increase in SERCA2a activity, a decline in $[Ca^{2+}]_i$ and an acceleration of relaxation [35-37]. However, recent results from Valverde

et al. indicate that PLN phosphorylation by CaMKII may not be the mechanism of FDAR in the heart [33]. These results lead to a key hypothesis of this dissertation and are discussed in more detail in Chapter V.

1.2 Specific aims

The following specific aims describe the objectives of the dissertation:

Aim 1. Develop experimental techniques to measure absolute intracellular calcium concentration in isolated cardiac myocytes with high temporal resolution. A single cardiac myocyte high bandwidth fluorescence detection system was designed and constructed based on an inverted microscope and combined with an optical fiber array which was coupled to photomultipliers. The fluorescent Ca^{2+} indicators Fluo-3, X-rhod-1 and Indo-1 were used to quantify changes in intracellular Ca^{2+} concentrations occurring during the cardiac cycle. A high temporal resolution (< 0.5 ms) permitted the recording of the fast (~ 10 ms) upstroke of the Ca^{2+} release.

Aim 2. Develop and apply the Nanophysiometer, a microfluidic network combined with a thin film microelectrode array for long-term physiological multi parameter recordings from single cardiac myocytes. The Nanophysiometer has extensively been used to measure extracellular potentials, intracellular Ca^{2+} concentrations and sarcomere length from isolated cardiac myocytes. Most importantly, the Nanophysiometer automatically aligned and stabilized single cells during long-term contraction measurements. On-chip thin-film microelectrodes were used for electric field stimulation but were also applied for recording extracellular potentials and ion- and metabolite concentrations in the extracellular space (e.g. pH, K^+, O2, glucose, lactate, etc.).

Aim 3. Develop methods to quantify sarcomere force generation in single cardiac myocytes with high spatial resolution. A single cardiac myocyte contractility system was set up using a high speed CCD camera in combination with an inverted microscope. Sarcomere acceleration was measured in single cardiac myocytes and used to quantify changes in active force development under consideration of passive forces. A high spatial resolution (< 5 nm) was achieved by using a FFT algorithm and the Nanophysiometer. The microfluidic device stabilized single cardiac myocytes during long term sarcomere length measurements and permitted the recording of a large number of contractions (>100). Averaging of multiple contraction transients significantly increased the S/N ratio and improved the spatial resolution of the measurement compared to a culture dish experiment. Calcium and contraction measurements were combined by using the electric field stimulus as a reference time point.

Aim 4. Measure force – excitation coupling in single cardiac myocytes isolated from PLN deficient mice. Phospholamban ablation has been shown to increase the rates of contraction and relaxation in isolated cardiac myocytes. However, in the literature, the increased contractility (positive inotropic effect) observed in phospholamban deficient cardiac myocytes (PLN-/-) has been consistently attributed to an increased Ca^{2+} release. The optical imaging techniques described in aims 1-3 were applied to test the hypothesis that the positive inotropic effect of PLN ablation is amplified by an increase in the response of the myofilaments to changes in cytosolic Ca^{2+} concentration.

Aim 5. Measure the frequency response of the SR Ca^{2+} release and uptake in single cardiac myocytes isolated from PLN and CaMKII deficient cardiac myocytes.

PLN phosphorylation by CaMKII has previously been shown to occur *in vivo* in a frequency-dependent manner and was therefore suggested to play an important role in the frequency-dependent acceleration of relaxation (FDAR). The fluorescence techniques developed in aim 1 were used to quantify the frequency-dependent adaptation of the Ca^{2+} transient in PLN and CaMKII deficient cardiac myocytes.

Aim 6. Use the Nanophysiometer to measure extracellular potentials in single cardiac myocytes. Extracellular potentials resulting from spontaneously initiated calcium waves were measured in single nonattached cardiac myocytes using integrated thin film microelectrodes. The microelectrodes were also used to measure extracellular pH in a microfluidic device. When the techniques described in aims (1-3 and 6) are combined, the Nanophysiometer will allow for rapid extracellular volume exchange, selective perfusion of single cells, electrical recordings of extracellular potentials, ion- and metabolite concentrations in the extracellular space (e.g. pH, K^+,O_2, glucose, lactate, etc.), and simultaneous optical measurements of intracellular ion concentrations (e.g. $[Ca^{2+}]_i$ and pH_i) and sarcomere length in field stimulated cardiac myocytes at physiological pacing frequencies.

CHAPTER II

BACKGROUND

2.1 Force – excitation coupling in ventricular cardiac myocytes

Anatomy of the heart and the conducting system

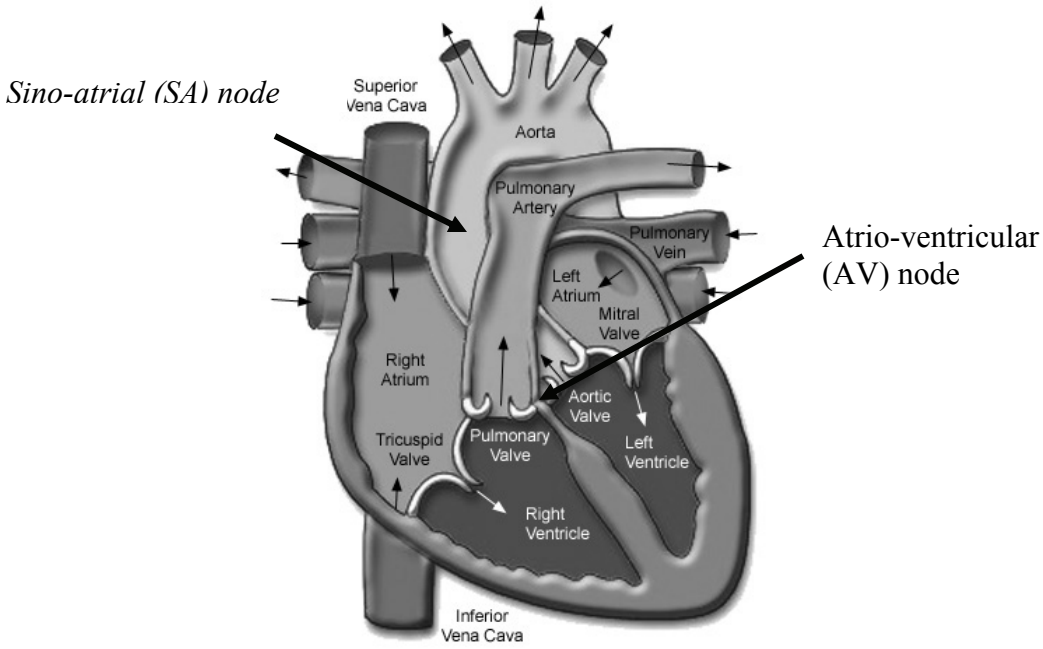

Figure 1. Cross section of a human heart.
Adapted from www.texasheartinstitute.org

It will be helpful for the following account to introduce some elementary anatomy and to define a few important terms in cardiac electrophysiology. The heart is composed of four chambers (Figure 1), two of which are large with thick walls. These are the ventricles, which pump blood into the two main arteries. The right ventricle pumps blood into the pulmonary artery that supplies the lung circulation, and the left ventricle pumps

blood into the aorta which supplies the systemic circulation. The other two chambers are small with thin walls and are called atria. The right atrium receives blood from the systemic circulation and passes it onto the right ventricle to enter pulmonary circulation. The left atrium receives blood from the pulmonary circulation and passes it onto the left ventricle to enter the systemic circulation. Electrical activity is initiated in the sino-atrial (SA) node which is a band of fine muscle fibers lying near the junction of the superior vena cava and the right atrium. Cells in this region (the SA node) are able to generate spontaneous action potentials by a mechanism known as the pacemaker mechanism. Although it is not the only region of the heart to possess pacemaker mechanism, its beating rate is higher than that of any of the other pacemaker regions so that it sets the pace of the heart as a whole. The action potential (AP) is the transmembrane potential waveform E_m that initiates cardiac excitation contraction coupling (see below). The AP is responsible for the propagation of excitation information from cell to cell and allows the heart to function as an electrical and mechanical syncytium. After initiated at the SA node, the AP spreads through the atrial muscle to produce atrial contraction. Atrial and ventricular muscles are not continuous. Electrical activity spreads to the ventricles through one point, the atrio-ventricular (AV) node, a small band of tissue connecting the two kinds of cardiac muscle. Cells in the AV node transmit the electrical impulse slowly to ensure a significant delay between atrial and ventricular contraction. The bundle of His are specialized fibers in and beyond the AV node that conduct the electrical excitation rapidly to the apex and to the surfaces of the two ventricles. Therefore, the large ventricles are excited almost simultaneously. A more comprehensive treatment of action potential generation and propagation in the heart can be found in some excellent reviews

by Yellen (1998) [38], Carmeliet (1999) and Kléber (1997, 2004) [9, 39]. All experiments described here are performed on cardiac myocytes isolated from the left and right mouse ventricles.

Calcium cycling in ventricular cardiac myocytes

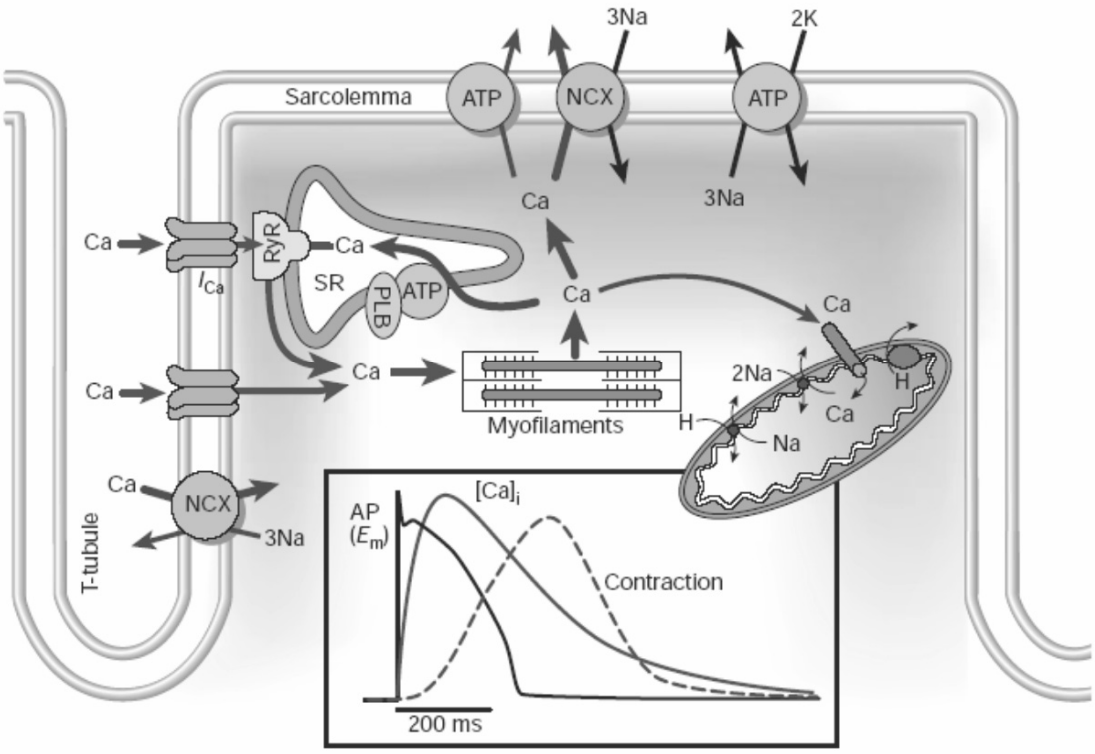

Figure 2 Scheme of the Ca^{2+} cycle in a cardiac ventricular myocyte. Ca^{2+} ions enter via the L-type calcium channel (LTCC, I_{Ca}) or Na^{+}/Ca^{2+} exchange (NCX). Calcium influx regulates intracellular SR Ca^{2+} release by the ryanodine receptor (RyR). Ca^{2+} is removed from the myofilaments and cytosol by the SR Ca^{2+} – ATPase pump which is modulated by phospholamban (PLB, PLN), transmembrane Ca^{2+} – ATPase pump, NCX and mitochondrial uniporter. Insert: action potential (E_m), calcium transient ($[Ca]_i$) and contraction in a rabbit cardiac myocyte. Figure adapted from [41].

The transmembrane potential controls ion channels and transporters, and a depolarization leads to the influx of calcium and the genesis of the calcium transient. Calcium is considered perhaps the most important ion involved in the intricate workings of the heart. It is crucial to the process of excitation contraction coupling (ECC) in cardiac myocytes. ECC is defined as the process from electrical excitation to the mechanical contraction of the heart, whose purpose is to propel blood out [40-42]. Calcium currents are main contributors to the electrical activity of the heart and a direct activator of the myofilaments causing contraction. Contractile dysfunction and arrhythmias in pathological conditions are very often the consequence of alterations in the Ca^{2+} handling of the cardiac myocyte [43-45].

Figure 2 shows a schematic of calcium signaling in a ventricular cardiac myocyte. Depolarization of the cell membrane during an AP (insert of Figure 2) opens voltage-dependent trans-sarcolemmal L-type calcium channels (LTCC, I_{Ca}). Calcium enters the cell during the action potential mainly through the LTCC and through the reverse-mode Na^{+}/Ca^{2+} exchanger (NCX). The inward transmembrane Ca^{2+} current triggers massive release of Ca^{2+} ions from the sarcoplasmic reticulum (SR) in a process called "calcium induced calcium release" (CICR). Together, sarcolemmal Ca^{2+} influx and SR Ca^{2+} release raise the intracellular free calcium concentration about five fold to ~1 μM, allowing Ca^{2+} to bind to the myofilament protein troponin C (TnC), which subsequently causes contraction of the myofilaments [6, 42]. Relaxation occurs when Ca^{2+} is removed from the cytosol. This is achieved through several routes, the importances of which are species dependent. In rabbit ventricular myocytes, 70 % of the activator Ca^{2+} is removed by the ATP-dependent SR Ca^{2+} pump (SERCA2a), 28 % by NCX, and only 1 % by the "slow"

systems – sarcolemmal Ca^{2+} ATPase and mitochondrial Ca^{2+} transport. The balance of Ca^{2+} fluxes is similar in rabbit, ferret, dog, cat, guinea pig and human. In mouse and rat myocardium, Ca^{2+} removal is directed more towards the SR due to a higher density of pump molecules [46], resulting in a balance of 92 % for SERCA2a, 7 % for NCX and 1 % for the slow systems. Therefore, in the intact mouse cardiac myocyte, Ca^{2+} removal from the cytosol is mainly governed by Ca^{2+} uptake into the SR.

Human hearts have a larger cardiac reserve than mice because they are able to elevate the amount of Ca^{2+} stored the SR by increasing SERCA2a activity (e.g. during beta-adrenergic stress), leading to an increase in fractional Ca^{2+} release and in the rate of contraction. For the cardiac myocyte to be at steady state, the amount of Ca^{2+} extruded or compartmentalized from the intracellular space during twitch relaxation must be the same as the amount of Ca^{2+} that enters the cytoplasm or is released from intracellular compartments during each beat, otherwise the cell would gain or loose Ca^{2+}. Therefore, in steady state, the same amount of Ca^{2+} that is released from the SR is taken back up into the SR via the SR Ca^{2+} pump. Similarly, the same amount of Ca^{2+} that enters the cell through the LTCC is removed from the cytosol via NCX.

Regulation of contractility by phospholamban

The trigger for relaxation of the ventricular cardiac myocyte is the lowering of the cytosolic Ca^{2+} concentration mainly by the activity of SERCA2a. Phospholamban (PLN) is a 52-amino acid protein of 6.1 kDa that forms a homopentamer with an apparent mass of 22-kDa which colocalizes with SERCA2a in the cardiac SR membrane as indicated in Figure 2 (see reviews by Simmerman and Jones [21] and MacLennan and Kranias [22]).

Kinetic analysis showed that in its unphosphorylated state, PLN diminishes the apparent affinity of SERCA2a for Ca^{2+} with little or no effect on the maximum Ca^{2+} transport rate (V_{max}). Unphosphorylated PLN limits the rate of Ca^{2+} uptake into the intracellular store. In contrast, phosphorylation of PLN by cAMP and cGMP dependent protein kinase A and C (PKA and PKC), respectively, at Ser-16 [47], and by Ca^{2+}/Calmodulin dependent protein kinase II (CaMKII) at the distinct site Thr-17 [35, 48] relieve this inhibition thereby increasing the rate of SR Ca^{2+} uptake. As a result, the relief of the inhibitory function of PLN on SERCA2a is considered the principal contributor to the positive inotropic and lusitropic effects of β-agonists [49-51]. The PLN gene was targeted in numerous studies to gain insight into the role of this protein in the regulation of cardiac contractility. Heterozygous and homozygous gene deletion was used as a tool to study cardiac contractility mice in which PLN levels were reduced by 60 % and 100 %, respectively [24, 28]. The reduced level of PLN expression was associated with a linear increase in the affinity of SERCA2a for Ca^{2+} and with a linear increase in rates of myocyte relaxation [28, 52]. Interestingly, the rates of contraction were significantly increased in whole hearts [53] and in isolated cardiac myocytes [54]. It was reported that "[..] Changes in cardiac myocyte contractility reflect increases in the amplitude and rates of the rising and falling phases of the Ca^{2+} transient, which, in turn, reflect the fact, that the size of the Ca^{2+} store is increased in PLN null animals.[..]" [22]. Indeed, an increased SR Ca^{2+} load was consistently reported in PLN deficient cardiac myocytes [52, 55] which may have caused the higher Ca^{2+} release [54, 55]. However, changes in contractile protein expression and phosphorylation observed in PLN deficient mice [56, 57] that are known to affect the activation of contraction in PLN deficient hearts suggest that an

increased systolic Ca^{2+} concentration may not be the only cause of the positive inotropic effect of chronic PLN gene deletion. The data presented in Chapter IV show that the post-translational changes in the contractile machinery have increased the response of the myofilaments to changes in $[Ca^{2+}]_i$ in PLN deficient cardiac myocytes. This question is addressed in great detail in Chapter IV.

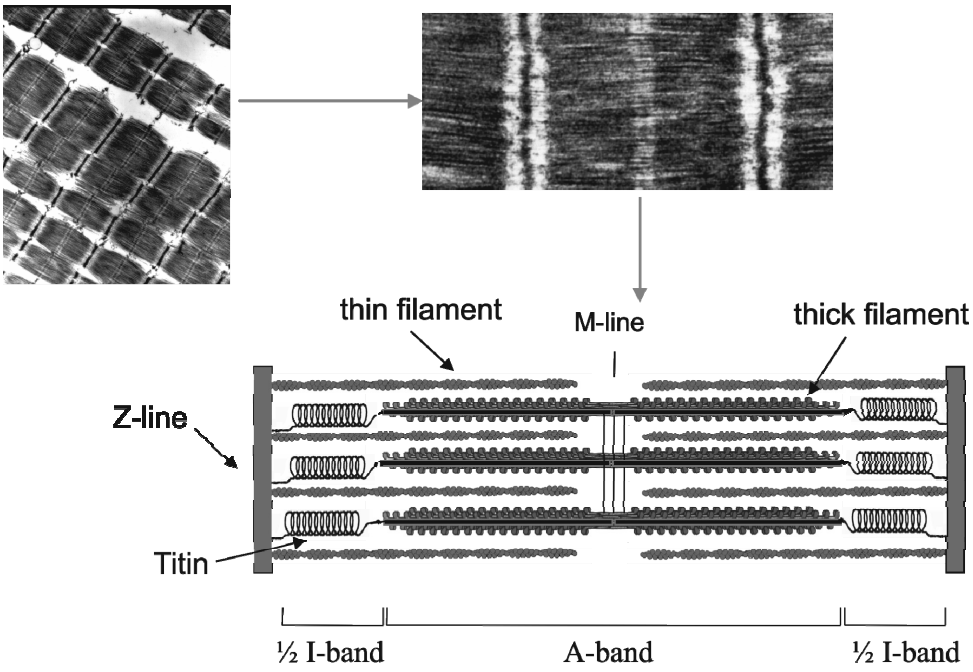

Figure 3. Electron-microscope images from cardiac muscle showing the sarcomere appearance. (Bottom) Schematic of the ultra structure of the myofilaments in one sarcomere which underlies the striated appearance of the sarcomere.
Figure adapted from: Ion Wizard SarcLen Data Acquisition User's Guide, Ionoptix 2000.

Activation of contraction by cytosolic [Ca^{2+}]

The contractile apparatus is built of repeating sarcomeres which occupy 45 - 60 % of the cell volume in the mammalian ventricle. Myofilaments are composed of mainly four different proteins: myosin (thick filaments), actin, tropomyosin and troponin (thin filaments) [52, 58]. The myofilaments are the contractile machinery of the cell and indeed they represent the end effector responsible for converting chemical energy into mechanical energy. Figure 3 shows two electron-microscope images and a schematic of the sarcomere structure. The thin filaments are anchored at the Z-line, which defines both ends of the sarcomere with the thick filaments in between. The sarcomere is only 1.5 to 4 µm long, depending on muscle type and degree of stretch. The optical properties of the

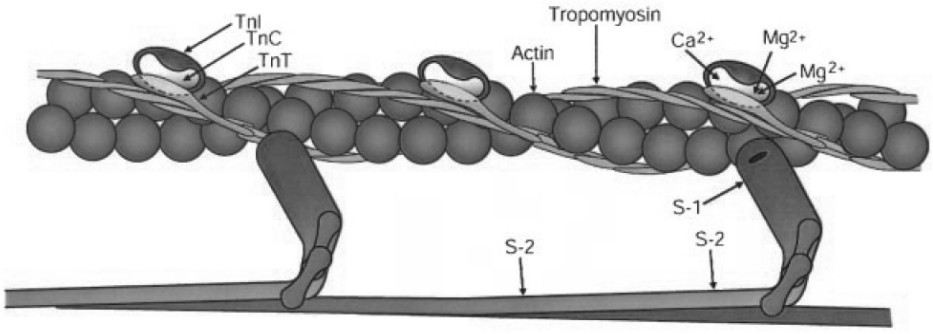

Figure 4. Schematic diagram of the thick filaments (red, bottom) composed of myosin heavy chains and the thin filaments (blue, top) composed of actin, tropomyosin and troponin (I, C and T domain). Figure adapted from [58].

thick and the thin filaments are strikingly different. The region characterized by a higher density of thin filaments is almost transparent and has therefore been labeled the isotropic, or I-band. The regions of high densities of thick filaments have a dark appearance and are therefore labeled the anisotropic, or A-band (Figure 3). Between the thin filaments there are thick filaments which are composed of myosin. The rise in cytosolic Ca^{2+} concentration is the event which activates the myofilaments, and a fairly clear picture (though not complete) of the molecular basis for this regulation has been developed [59].

Figure 4 shows a more detailed schematic of the thick and thin myofilaments. Each thick filament is composed of ~300 myosin molecules. Each myosin heavy chain has a long (~ 130 nm) α-helical tail (S-2 domain) and a globular head (S-1 domain). The S-2 regions of the myosin heavy chain form the main axis of the thick filament. The S-2 heads form the crossbridges to actin on the thin filaments, contain the site of ATP hydrolysis, and have two light chains associated with each head. The backbone of the thin filament is composed of two chains of the globular protein G-actin, which form a helical double stranded F-actin polymer. Tropomyosin is a long flexible protein which lies in the groove between the actin strands and spans about 7 acin monomers. The troponin complex is made of three subunits: troponin C (TnC, Ca^{2+} binding subunit), troponin I (TnI, inhibitory subunit, which also binds to actin). TnT has a globular carboxy region and an elonagated shape that lies along tropomyosin over about 3 actin monomers.

In the resting cardiac myocyte, tropomyosin covers the binding sites for myosin on actin. When $[Ca^{2+}]_i$ rises, Calcium binds to the Ca^{2+} specific site of TnC causing tropomyosin to move away from its blocking position on the thin filament and allowing myosin to

bind to actin and form crossbridges (myosin S-1 head portions protruding from the myosin filament). Upon activation, the crossbridges can interact with the thin filament and produce either force or relative filament movement by a rotation of the myosin S-1 head under ATP hydrolysis. Isometric force would be analogous to storing the potential energy of the myosin head rotation temporarily in an elastic component of the myosin molecule. Alternatively, the rotational movement can produce relative motion of the thick and the thin filaments (i.e. sarcomere shortening) if the muscle force exceeds load. A single crossbridge may develop a force of 0.2-1 pN and the physical filament translation from a single crossbridge cycle is 5-10 nm or 0.25-25 % of sarcomere or muscle length. The chemical steps involved in the crossbridge cycle have been extensively characterized [42]. In the non-attached cardiac myocytes crossbridge cycling can be monitored by measuring sarcomere shortening (Section 3.2). At resting lengths, the amount of Ca^{2+} released from the intracellular stores during a twitch is typically insufficient to saturate all thin filament sites. Thus, maximum force or power under physiological conditions is not fully utilized. Increases in twitch force and power can be achieved by increasing the likelihood of crossbridge formation between myosin and actin, e.g. by increasing the delivery of Ca^{2+} to the myofilaments, accelerating crossbridge formation kinetics, or increasing the responsiveness of TnC to Ca^{2+} [41, 58, 60, 61].

The relationship between force and $[Ca^{2+}]_i$ is highly nonlinear as a result of the strong myofilament cooperativity with respect to $[Ca^{2+}]_i$ [10, 58, 62, 63]. A decrease in myofilament Ca^{2+} sensitivity is observed during acidosis, when phosphate and Mg^{2+} concentrations are elevated, as well as during beta-adrenergic stimulation [64]. An increase in myofilament Ca^{2+} sensitivity occurs dynamically during diastole, when the

heart fills with blood, resulting in a stronger contraction with increasing volume (Frank-Starling mechanism) [65]. The sensitivity of the myofilaments to cytosolic Ca^{2+} is further enhanced by caffeine and certain inotropic drugs. Half-maximal activation of contraction requires about 70 μmol of Ca^{2+} per liter of cytosol to raise $[Ca^{2+}]_i$ to about 600 nM. This indicates strong cytosolic Ca^{2+} buffering (~ 100:1).

2.2 Force measurements in single cardiac myocytes

Limitations of existing techniques

The isolated heart cell is free of collagen and contains relatively few myofilaments in a single cohesive structure. It allows almost direct access to the measurement of activator $[Ca^{2+}]_i$, sarcomere length, cross-bridge contractile responses and is therefore ideally suited for mechanical studies. In contrast to the structural simplification is the inherent challenge of noninjurious cell attachment to a force-transducing device. The major limitation in attachment of intact cells to a force transducer is the extreme sensitivity of the sarcolemma to applied stress. Isolated cardiac myocytes were attached to a force transducer using single-barreled suction micropipettes [66, 67]. However, the success rate was extremely low because of the high stress on the sarcolemma at the tips of the micropipettes. Other technique have been developed using compliant fibers or glass beams attached to each end of the cell [68-70], but the procedures described are time consuming and require a unique experimental setup. Commercial force transducers are available that can be used to resolve the ~ μN forces generated by a single cardiac myocyte. However, in cases where the force detection system is not submersible, some part of the force sensing system must pass through a

liquid-air interface. The surface tension of the meniscus around the connecting element though this interface can be of ~10μN, and thus way above the level of the forces generated by the single cardiac myocyte. [71] Therefore, extreme interface stability and reproducibility are required to measure myocyte forces with these transducers.

Sarcomere acceleration as an index of contractility

Cell shortening and sarcomere length in intact nonattached cardiac myocytes are readily measured using noninvasive optical techniques. However, several assumptions are necessary to interpret the sarcomere shortening in terms of contractility. The active contraction of an unattached myocyte reveals the maximum degree of shortening of the

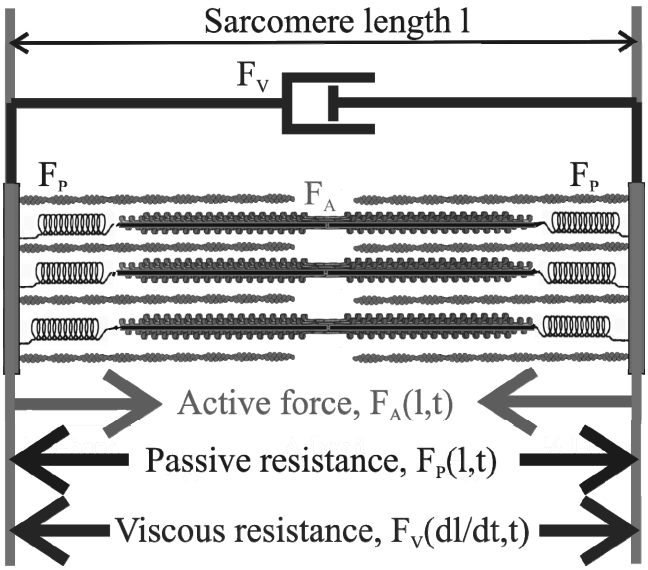

Figure 5 Mechanical model of the sarcomere with directions of active force and passive and viscous resistance during shortening
Figure adapted from: Ion Wizard SarcLen Data Acquisition User's Guide, Ionoptix 2000.

minimally loaded cell. In the absence of external force, cardiac myocytes attain an equilibrium sarcomere length of ~1.9 μm. Figure 5 shows a mechanical model of the sarcomere. Sarcomere compression or stretch is opposed by passive elastic and viscous forces F_P and F_V. The passive force F_P is largely dominated by the extensible region of the large protein titin that runs from near the Z-line to the edge of the A band and is indicated symbolically by the springs in Figure 5. When the sarcomere shortens to a degree below the slack length, the thick filament moves into titin's near Z-line region. As a result, titin's extensible region is compressed, generating the so-called restoring or passive force F_P that pushes the Z-lines back toward their slack length position (Figure 5). Additionally, a viscous resistance, F_V, provides a damping force during contraction and re-extension which is proportional to the shortening velocity *dl/dt*. The mechanical model of the sarcomere shown in Figure 5 is comparable with and overdamped pendulum returning to its equilibrium position from a mechanical excursion (viscoelastic vibration model).

The second time derivative of the sarcomere length *l* during the contraction process is a measure of the total force F_T which is the sum of all forces, which are time *t* and length dependent:

$$F_T(l,t) = F_A(l,t) - F_P(l.t) - F_V(dl/dt,t) = m \cdot \frac{d^2 l(t)}{dt^2} \qquad (2.6)$$

Equation 2.6 shows that measuring of sarcomere shortening alone is not sufficient to infer changes in the active component of the contractility because an increase in sarcomere acceleration may be a result of a softer sarcomere rather than a result of an increase in the active force. Therefore, passive elastic and viscous forces need to be considered when sarcomere length us used as a measure of contractility in single cardiac myocytes. In the

following discussion, the components of the overall resistance are presented in more detail. Molecular force spectroscopy and atomic force microscopy (AFM) have been used to measure the passive force directly in isolated polymer solutions.

Kellermayer *et al.* found that the elastic properties of titin could be described by a wormlike chain (WLC) model [72]. The exact solution of this model yields its potential energy as a function of the relative length change, $s = l/L$, where l is the time-dependent length and L the maximum, time independent length of the unfolded molecule (i.e. $l<L$). An algorithm to calculate the exact solution of the WLC model by numerical iteration was presented by Bouchiat *et al.* [73]. A good analytical approximation of the WLC model suitable for fitting of experimental force-length relationships of titin was given by Bustamante *et al.*:

$$F_P(s) = \frac{k_B T}{L_P}\left[\frac{1}{4(1-s)^2} - \frac{1}{4} + s\right] \tag{2.7}$$

where k_B is the Boltzmann constant and T the absolute temperature. L_P is the persistence length which is defined as the length along the polymer chain over which the tangent vectors of the chain become decorrelated. The persistence length of a polypeptide chain measures the elastic stiffness of the chain and decreases with increasing stiffness. For the rigid native folded titin molecule, L_P is on the order of 15 nm [72]. The WLC force-extension curve is a highly nonlinear function: at low extension ($s<<1$), force grows linearly with s with a slope of $k_BT/L_P \sim 0.3$ pN per molecule. At high extension, the force diverges as $(k_BT/L_P)[4(1-s)^2]^{-1}$.

Information about possible changes in passive forces caused by an intervention may be obtained by comparing contraction and relaxation. Figure 5 and equation 2.7 indicate that a change in the passive loading of the sarcomere would affect contraction and relaxation

differently. In fact, compression of crossbridges or stress on the cytoskeleton as may occur in the anoxic heart [74, 75] decreases the persistence length L_P thereby increasing the passive loading F_P of the sarcomere at any given fractional shortening *s*. As a result, during ischemia, the rate of shortening is slowed, while the rate of relengthening is accelerated. On the other hand, isoproterenol, a beta-adrenergic agonist, increases the active force of shortening, F_A, with no influence on the passive loading as evidenced by an increase in both the rates of shortening and relaxation [76]. A change in the passive loading of the sarcomere may also be identified by comparing the sarcomere length at the times when the maximum acceleration is reached during contraction and relaxation. A softer sarcomere would be characterized by a decreased passive resistance F_P (equation 2.7) at all extension levels and would thus be shorter during contraction and longer during relaxation at the time when the maximum acceleration is reached (Chapter IV). The contribution of the viscous force F_V to the overall mechanical resistance was measured by Niggli and Lederer [77]. They found that viscous damping was proportional to the velocity of sarcomere contraction:

$$F_V = B\frac{ds}{dt}, \tag{2.8}$$

where B is the viscous damping constant (in units of $Ns\ m^{-1}$). Under the assumption that an intervention does not change the viscosity constant, ratios of viscous force equal ratios of contraction rates.

In summary, when assessing the mechanism of an intervention, passive restoring force and viscous damping must be considered when relative sarcomere shortening is used as

an index of contractility. Important information about the passive forces may be obtained by comparing rates of contraction and relaxation or by measuring the sarcomere length reached at the time of maximum acceleration during contraction and relaxation, as discussed in more detail in Chapter IV.

CHAPTER III

THE NANOPHYSIOMETER

3.1 Device concept, design and fabrication

The integration of Bio-Micro-Electro-Mechanical Systems (BioMEMS) with biology and the development of self-contained lab-on-chip devices will provide powerful tools to study novel aspects of cell physiology. Large scale *in vivo* like biological experiments on a chip are possible through the introduction of microfluidics technology and mass fabrication techniques, which permit the fabrication of microfluidic channels, reservoirs, valves and pumps using bio-compatible materials [78, 79]. Miniaturized on-chip cell cultures have been developed as part of cell-based toxin detectors [80-84] and micro- or nanoscale devices for novel experiments in cell biology [85]. Microfluidics technology offers tremendous potential for rapid biological analysis in quantitative systems biology, complementing or replacing traditional single cell measurement techniques such as patch-clamp [86-90] or fluorescence microscopy [84, 91, 92]. However, the development of microfluidics technology for scientific research is still in its early stage, as indicated by the small number of commercially available systems. Furthermore, the use of microfluidics for single cell manipulation and measurement is most often presented as "proof of concept" rather than being widely utilized as a research tool in mainstream life sciences. Microfluidic cell retention structures have been used to position and stabilize single cells during physiological recordings. Results obtained from cells confined in a restricted extracellular space provided by the microfluidic

environment seemed to be consistent with those obtained from cells in larger volumes as long as continuous solution exchange was provided. Klauke *et al.* demonstrated electrical field stimulation of single adult cardiac myocytes in an open architecture microchannel array [93]. Prolonged pacing of single cardiomyocytes in a 100 pl volume bath did not affect calcium transients although it reduced the sarcomere contraction amplitude after 40 minutes. The reduction in contractility in the small volumes could be partially rescued by replacing the bath solution and did not occur in a larger, 5 nl volume. This observation shows that metabolite accumulation occurs in a restricted extracellular space thereby affecting the amplitudes of contraction. Other studies showed that prolonged electrical stimulation of isolated adult cardiac myocytes in micro-chambers did not impair excitation-contraction coupling as verified by optical recordings of action potentials, Ca^{2+} transients and cell shortening [94-96].

The Nanophysiometer is a microfluidic-based device and a tool for physiological measurements on single isolated cardiac myocytes. The advantage of the microfluidic approach is that cells can be automatically positioned and confined under the microscope without damaging the sensitive cell membrane. Furthermore, the design of the microfluidic network permits the continuous perfusion of the entire cell, rapid extracellular volume exchange or selective perfusion of a membrane patch and the creation of well defined concentration gradients along a single cardiac myocyte.

Device fabrication using soft lithography

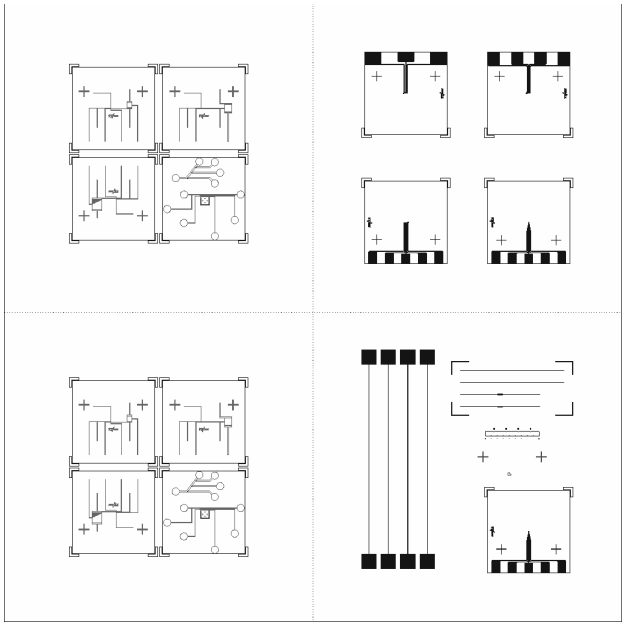

Figure 6. Layout of a chrome mask with microfluidic structures (left) and microelectrodes (right).

The Nanophysiometer is a microfluidic device based on microscopic channels and made of Poly(dimethylsiloxane) (PDMS), a biocompatible polymer.

PDMS is flexible, optically transparent (and therefore compatible with fluorescence microscopy) and inexpensive. It is also impermeable to water and highly permeable to gases [97]. It can be formed with ease by a molding process and bonded to other materials, which is an important advantage over glass and silicon, especially when rapid prototyping is required.

The technique used to manufacture the Nanophysiometer is called “soft lithography” and was pioneered by George M. Whitesides [78, 98-101].

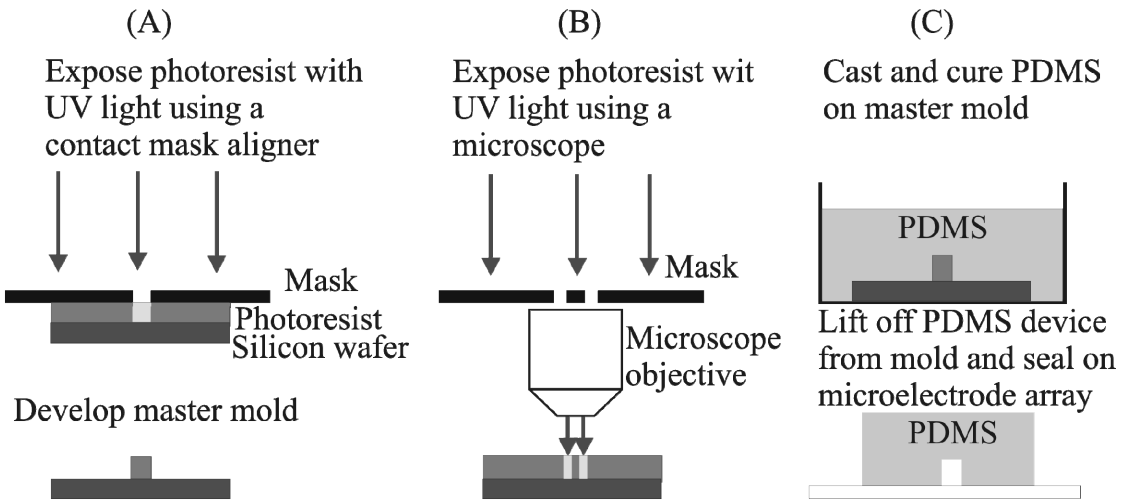

Figure 7. Photolithographic and molding process to fabricate microfluidic devices.

It was later adapted by Stephen R. Quake who demonstrated the fabrication of complex microfluidic channel structures, including on-chip active valves and peristaltic pumps using a multilayer PDMS fabrication process [79, 102-105].

The design of the microfluidic structure is drawn using a standard computer-aided design (CAD) program. Once the desired design is available in form of a digital drawing, commercial services transfer the patterns onto film transparencies (for > 25 µm size structures) or chrome masks (for > 2 µm size structures).

The layout of a typical chrome mask is shown in Figure 6 with patterns for the fabrication of microfluidics (left) and microelectrodes (right). The mask is then used in an UV photolithography process to generate a master mold as shown in Figure 7. A thick layer of photoresist (e.g. the photo curable epoxy SU-8) is spin-coated onto the surface of a silicon wafer. Using different types of SU-8 with various viscosities in combination with different spin-coating velocities, thicknesses of 1-300 µm can be reliably achieved. The

photoresist is then exposed to UV light through the chrome or film mask. A film mask has a lower spatial resolution with a typical smallest feature size of 25 μm. In order to achieve a higher resolution, additional size reduction can be achieved by placing a microscope objective in the light path between the photo mask and the silicon wafer (Figure 7B). It is important to note that objectives and optical elements used for size reduction in the exposure process reduce the effective area available for the microfluidic structure. Unexposed areas are removed in a chemical development process leaving only the channel relief structure on the surface of the wafer, which serves as a replica master mold. A PDMS/curing agent mixture (typically 10/1) is then cast onto the master and cured for 60 min at 70 ºC. The elastomer is then peeled off the master, producing the final replica bearing the designed microstructures. Small access holes are punched into the elastomer before it is sealed onto a glass substrate containing a thin-film microelectrode array. Further details about the design and application of the Nanophysiometer are presented in Chapter III. A more detailed description of the soft lithographic microfabrication process can also be found in the literature [78, 79, 98, 103].

Chemical control of the extracellular environment

Cells and reagents are moved through the microfluidic channels of the Nanophysiometer by manually applied pressure gradients.

The directions of the pressure gradients used to confine and perfuse single cardiac myocytes inside the Nanophysiometer are indicated by the arrows in Figure 8A. Chemical control of the extracellular space around a cardiac myocyte is achieved by

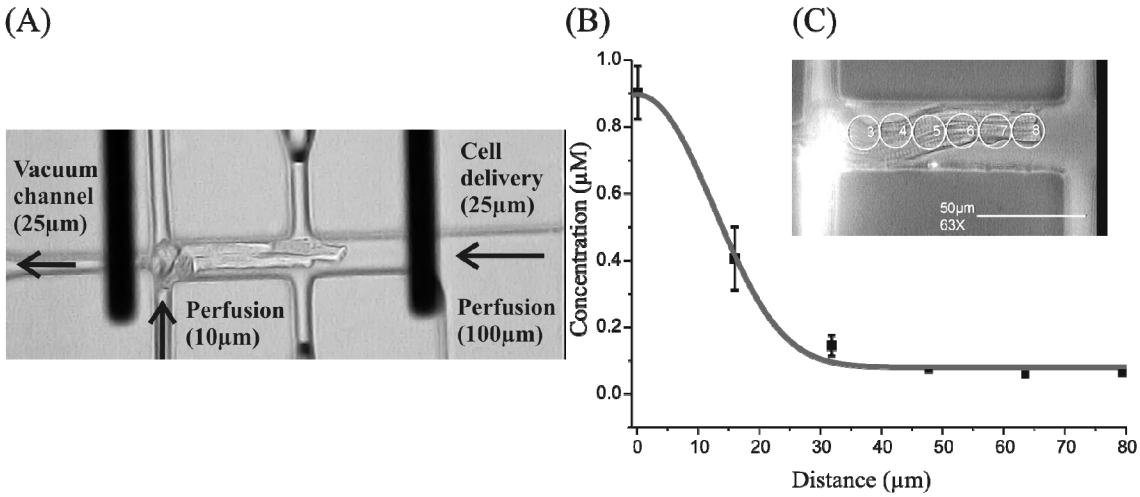

Figure 8. (A) Bright field microscope image of a cardiac myocyte confined inside the Nanophysiometer. The black lines are thin film microelectrodes used for field stimulation. Arrows indicate the directions of pressure gradients for continuous perfusion. (B) Concentration gradient measured by 6 PMTs along a single cardiac myocyte. (C) Bright field microscope image of the cardiac myocyte used in the experiment.

rapid solution exchange through microchannels leading into the measurement volume as shown in Figure 8A.

The pressure gradients along the smaller perfusion channels in the Nanophysiometer allow continuous perfusion of the entire cell or parts of the membrane. In Figure 8B, the selective perfusion of a membrane patch is demonstrated. In this experiment, one end of the cell was perfused for 10 s through a microfluidic channel by a 1 µM fluorescent solution (Sulforhodamine 101), while the fluorescence was measured at six different positions along the myocyte. The position of the fluorescence detectors are indicated by the white circles in Figure 8C. The resulting fluorescence intensities were well described by the solution of the one-dimensional diffusion equation indicating laminar flow through the perfusion channels and diffusion-limited mixing along the cell [106].

Stimulation of cardiac myocytes in the Nanophysiometer

Thin-film microelectrodes are suitable for field stimulation of cardiac myocytes in the Nanophysiometer. In order to avoid changes in pH due to electrolysis during prolonged stimulation, electrode potentials must be kept below the reduction potential of water, i.e. 0.83 V. This requirement can be achieved by using microelectrodes with small inter-electrode distances. These microelectrodes require small electrode potentials to yield high electric fields. An approximate electric field strength on the order of 100 V/cm may be established by applying just 1 V across two parallel microelectrodes which are located 100μm apart (Chapter IV). Cell membranes have a relatively small conductance compared with the extracellular medium. Therefore, the imposed electric field produces a flow of current primarily around the cell, resulting in a highly inhomogeneous electric field gradient along the cell surface. Given that the interior of the cell is essentially isopotential, the surface potential gradient results in a spatially varying transmembrane potential which can activate transmembrane currents through voltage-gated ion channels. Theoretical and experimental descriptions of electric field stimulation of single cardiac cells can be found in the published work of Leslie Tung *et al.* [107] and Vinod Sharma *et al.* [108, 109].

3.2 Optical measurements of cytosolic calcium concentration and sarcomere length in the Nanophysiometer

Fiber – optical system for high-resolution multi-parameter recordings

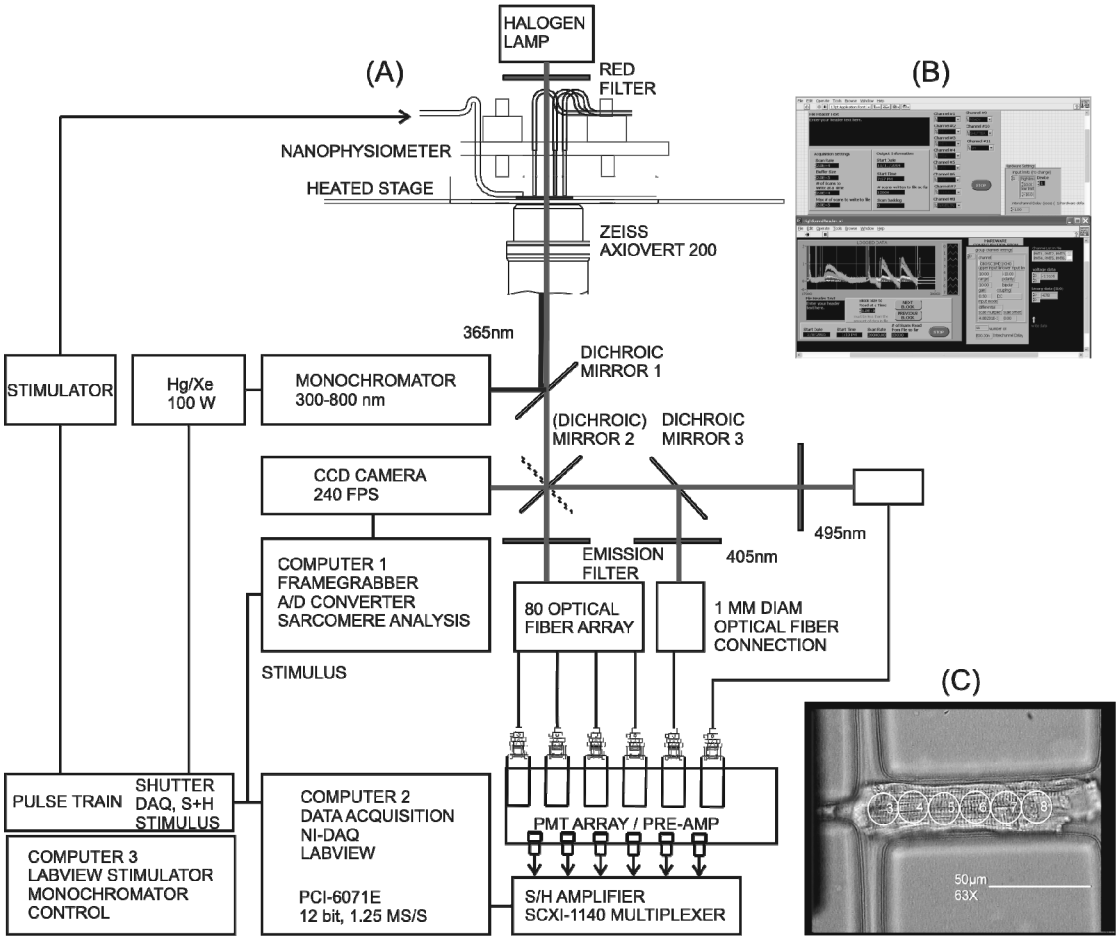

Figure 9. (A) Schematic representation of the optical setup for intracellular calcium and sarcomere length measurements on single cardiac myocytes in the microfluidic device. (B) Screenshot of the Labview data acquisition software. (C) Optical mapping of 6 fibers positioned along a single cardiac myocyte in the Nanophysiometer.

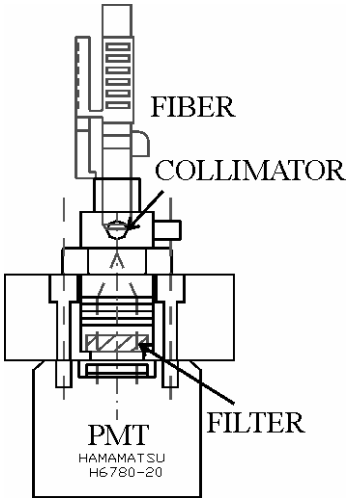

Figure 10 Fiber - PMT connection.

Figure 9 shows the optical setup which was designed for the measurement of intracellular calcium concentration and sarcomere length from isolated single cardiac myocytes trapped in the Nanophysiometer. It was built around an inverted microscope (Axiovert 200, Carl Zeiss, Germany) equipped with an epi-fluorescence light train. A monochromator (Optoscan, Cairn Research Ltd., Kent, UK) was used to select the wavelength for dye excitation. It permitted wavelength selection from the 100 W Hg/Xe lamp emission in the range of 300-800 nm with a variable bandwidth of 1-30 nm which was controlled via galvano-driven input and output slits. The monochromator was also capable of fast wavelength-switching allowing ratiometric excitation (e.g. using fura-2) with switching times dependent of the wavelength range of less than 2 ms. Red light which did not excite the Ca^{2+} sensitive dyes was generated by a halogen lamp above the Nanophysiometer and used for whole-cell-high-speed sarcomere imaging via a 240

frames-per-second CCD camera (Myocam, Ionoptix Corp., Milton, MA). The halogen light was transmitted by the dichroic mirror 1 and reflected by the mirror 2 onto the sarcomere camera which was connected to a frame grabber card installed in the computer 1 for the measurement of sarcomere length. Alternatively, turning the mirror 2 by 90 º allowed indo-1 fluorescence detection via wavelength separation of the free dye (maximum emission at 405 nm) and the Ca^{2+}-bound dye (maximum emission at 495 nm). The principle of ratiometric $[Ca^{2+}]_i$ detection is described in more detail below. Replacing mirror 2 by a dichroic mirror permitted the simultaneous measurement of $[Ca^{2+}]_i$ and sarcomere length. The fluorescence light was collected alternatively by six 1 mm diameter optical fibers selected from a 80-fiber array at the base port of the microscope or by two optical fibers at a side port of the microscope which were optically aligned to collect the fluorescence light from the same spot on the cell at two different emission wavelengths (for calibrated indo-1 measurements, Figure 9C). Each fiber was connected to a photomultiplier (PMT, H6780-20, Hamamatsu) via a custom designed connection as shown in Figure 10. The PMTs were mounted inside a shielded aluminum box and powered by batteries to reduce noise.

The optical fiber connections were designed to accommodate 8 mm diameter filters to allow multiple-wavelength fluorescence detection.

Optical mapping of the six fiber positions was accomplished by means of a scan converter which allowed mixing of the video feed with a computer drawing of the fiber geometry. Figure 9C shows the outlines of the 6 optical fibers on a single cardiac myocyte in the Nanophysiometer. Measurements of $[Ca^{2+}]_i$ and sarcomere length were accomplished by using two separate data acquisition systems, i.e. computer 1 and

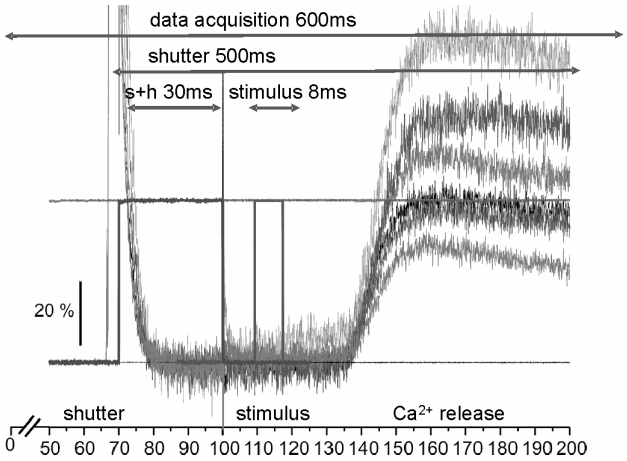

Figure 11 Control signals for fluorescence detection.

computer 2, equipped with A/D converter boards, with scan rates of 20 KHz and 1 KHz, respectively. Calcium and sarcomere length measurements were synchronized by the stimulus. To limit the exposure of stained cells to the phototoxic excitation light, shutter opening and stimulus were precisely controlled by a third computer.

Computer 3 (Figure 9A) was used to generate a pulse train that opened the shutter 40 ms before the stimulus as shown in Figure 11. Additionally, when the pre-amplifier was operated in AC-coupled mode, a 30 ms sample and hold pulse (s+h) was initiated 5 ms after the opening of the shutter to temporarily reduce the output feedback resistor of the amplifier from 10 MΩ to 1 KΩ which shortened the time constant of the high-pass filter from 10 s to 1 ms, thereby avoiding saturation of the amplifier at high background fluorescence intensities. For calibrated indo-1 calcium measurements, however, the

amplifier was operated in DC mode to allow recording of diastolic $[Ca^{2+}]_i$ and background fluorescence.

Measurement of cytosolic Ca^{2+} concentration

The most popular method for measuring cytosolic $[Ca^{2+}]_i$ in mammalian cells is to monitor the fluorescence of a calcium-sensitive indicator. Fluorescent probes for calcium are moderate to high-affinity calcium-binding molecules [110, 111]. They emit light upon excitation at a given wavelength. The intensity of the emitted light is a function of the amount of calcium bound to the dye molecules. Under the assumption that the dye concentration is small enough so that the fluorescence contribution induced by a given molecular species is proportional to the concentration of that species, the measured fluorescence intensity of a mixture of free and Ca^{2+} - bound indicator is given by:

$$F = S_f \cdot c_f + S_b \cdot c_b , \tag{2.1}$$

where c_f and c_b are the concentrations of the free and Ca^{2+} bound indicator, respectively. The two states of the dye are described by two proportionality coefficients, symbolized by S_f and S_b for the free and the Ca^{2+} bound dye. The S factor depends on the excitation intensity, extinction coefficient, path length, quantum efficiency and the instrumental efficiency of collecting emitted photons. Assuming 1:1 complexation, c_f and c_b are related by $c_b = c_f [Ca^{2+}]_i / K_d$, where K_d is the effective dissociation constant of the dye. Defining $F_{min} := S_f (c_f + c_b)$ and $F_{max} := S_b (c_f + c_b)$ and solving equation 2.1 for $[Ca^{2+}]_i$ yields the calibration equation for a single wavelength dye:

$$[Ca^{2+}]_i = K_d \frac{F - F_{\min}}{F_{\max} - F} . \tag{2.2}$$

Equation 2.2 clearly shows that $[Ca^{2+}]_i$ is not directly proportional to the fluorescence intensity, but depends on F_{min} and F_{max} which are the minimum fluorescence in a Ca^{2+}-free environment and the maximum fluorescence at saturated $[Ca^{2+}]$, respectively. Under these conditions any given fluorescence reading from the intracellular dye may be compared with a calibration in which the dye is forced into known states of high and low Ca^{2+} saturation. However, F_{min} and F_{max} each depend on dye distribution and detector sensitivity. Hence, any intervening loss of dye or change in instrument sensitivity jeopardizes the calibration and may be mistaken for a change in $[Ca^{2+}]_i$. Therefore, calibration of single wavelength dyes is not reliable, although several approaches have been reported [112, 113]. The uncalibrated fluorescence intensity may be used to qualitatively identify transient changes in $[Ca^{2+}]_i$. To avoid these complications, ratiometric fluorescent indicators have been developed that are characterized by a shift in excitation or emission wavelength upon binding to Ca^{2+} ions. The ratio of the fluorescence intensities F_1 and F_2 at two excitation (or emission-) wavelengths λ_1 and λ_2 is in principle sufficient to calculate absolute $[Ca^{2+}]_i$ independent of total effective dye concentration or instrument sensitivity:

$$\begin{aligned} F_1 &= S_{f1}c_f + S_{b2}c_b \\ F_2 &= S_{f2}c_f + S_{b2}c_b \end{aligned} \tag{2.3}$$

With $R:=F_1/F_2$, the fluorescence ratio at the two wavelengths is given by:

$$R = \frac{S_{f1} + s_{b1}[Ca^{2+}]_i / K_d}{S_{f2} + S_{b2}[Ca^{2+}]_i / K_d} \quad . \tag{2.4}$$

Solving equation 2.4 for $[Ca^{2+}]_i$ and substituting $R_{min}:=S_{f1}/S_{f2}$ and $R_{max}:=S_{b1}/S_{b2}$, one obtains

$$[Ca^{2+}]_i = K_d \frac{R - R_{\min}}{R_{\max} - R} \cdot \frac{S_{f2}}{S_{b2}} . \qquad (2.5)$$

Equation 2.5 is analogous to the calibration equation 2.2 for a single wavelength dye, but independent of total dye concentration and instrument sensitivity. In order to quantify absolute $[Ca^{2+}]_i$ concentration, we have established a protocol for *in vivo* calibration of the Calcium indicator dye indo-1, which is presented in Chapter IV.

Measurement of sarcomere length

Due to the periodic repetition of sarcomeres in the muscle, the dark A-band and light I-band alterations result in a striated appearance. One sarcomere length would be defined as the distance from the middle of one I-band to the middle of the next when viewed under the light microscope. This distance may not be measured accurately. Therefore, alternative methods have been developed to get a good estimation of sarcomere length.

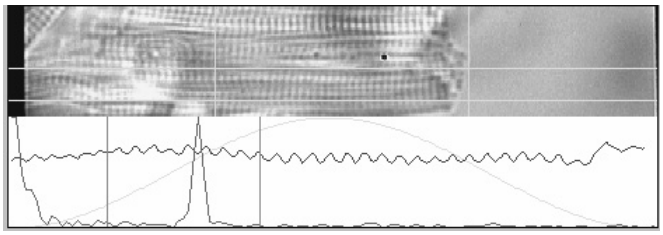

Figure 12. (Top) microscope image of a single cardiac myocyte with the ROI defined by the yellow rectangle. (Bottom) average density trace (black) derived from the ROI and powerspectrum (red).
(Adapted from Ionoptix Corporation, Ion Wizard SarcLen Data Acquisition User's Guide, 2000)

The approach used by the Ion Wizard SarcLen data acquisition software is to estimate the frequency of the striation pattern, i.e. how many sarcomeres can be found per length. The sarcomere length is measured from a user-defined region-of-interest (ROI) which is a box enclosed by four yellow lines as shown in Figure 12. All calculations are performed on a density trace derived from the ROI. Each pixel is assigned a value of brightness and because of the periodic repetition of the sarcomere the density trace has a sinusoidal appearance with the wavelength representing the sarcomere length. The density trace is transformed via a fast Fourier transform (FFT) algorithm from the spatial domain into the frequency domain. The output of the FFT is presented in form of the power spectrum in the lower part of Figure 12. The power spectrum is a representation of the relative contribution of each spatial frequency in the density trace. The most dominant pattern in the density trace, the dark-light transitions of the sarcomeres, appears as a sharp peak in the power spectrum. The average sarcomere length can then be derived from the peak of the power spectrum. Finally, the reciprocal value of the peak in the power spectrum (in units of pixels/sarcomere) is multiplied with a calibration factor (in length/pixel) to yield an average value of the sarcomere length in the ROI. The great advantage of this method is that it provides sub-pixel spatial resolution.

Analysis of Ca^{2+} and sarcomere length recordings

The time dependent changes of intracellular calcium concentration and sarcomere length were fit to empirical functions to calculate time constants and multiple time derivatives. All calculations were performed using Matlab (R14, The MathWorks, Inc.). During the action potential, calcium ions enter the cell through LTCC and trigger massive release of

Ca^{2+} through the intracellular Ca^{2+} release channels. The intracellular Ca^{2+} release channels are called ryanodine receptors (RyR) and are located in the membrane of the SR [114-116]. When a RyR opens, $[Ca^{2+}]_i$ in its vicinity rises immediately to levels above 10μM, resulting in the activation of neighboring RyRs. When the channel closes, the local Ca^{2+} transient dissipates rapidly (~ microseconds) due to the diffusion of Ca^{2+}. Models of RyR kinetics have been derived from experiments performed on isolated channels in lipid bilayers using flash photolysis of caged Ca^{2+} (such as DM-nitrophen) to simulate fast changes in $[Ca^{2+}]$ in the microenvironment of the reconstituted channel. The apparent calcium sensitivity of the open probability, P_o, in response to a Ca^{2+} spike was described by a Hill equation [117], based on binding of n_H Ca^{2+} ions to channel [118]:

$$P_o = \frac{[Ca^{2+}]^{n_H}}{K_{Ca}^{n_H} + [Ca^{2+}]^{n_H}}, \tag{2.8}$$

Where $K_{Ca}^{n_H}$ describes the calcium sensitivity of the RyR, i.e. the Ca^{2+} concentration required to activate 50 % of the channels, which was found to be on the order of 40 μM [118-120]. The time course of RyR activation was best fit by an exponential association function raised to the power of n_a [121]:

$$P_o = P_o^{\max}\left(1 - e^{-\frac{t}{\tau_a}}\right)^{n_a} \tag{2.9}$$

Interestingly, although equations 2.8 and 2.9 were originally derived to fit RyR activation in isolated channels, they were well suited to fit the rising phase of the Ca^{2+} transient in the intact cell as presented in Figure 13.

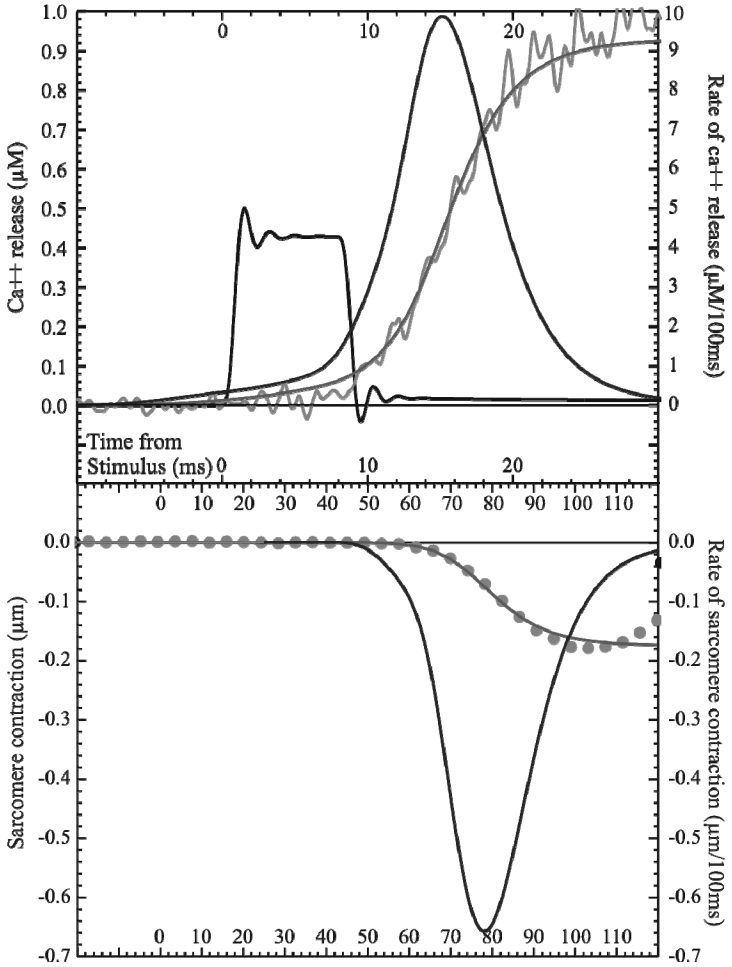

Figure 13. Top: Fit of Ca^{2+} release (red) to the rising phase of the Ca^{2+} transient (grey line) and first time-derivative (blue). Bottom: Fit of sarcomere contraction (red) to the data (grey circles) and first time-derivative (blue).

The Hill slope n_H was between 2 and 4 in isolated RyRs, strongly suggesting that binding of several Ca^{2+} ions must occur before the channel can open. In the intact cell, however, RyRs are organized in clusters of ~100 release units with strong interactions between them [40]. Therefore, the hill coefficient in equation 2.6 cannot be expected to represent single channel binding kinetics [122]. In fact, n_H was consistently smaller than 1 in the

intact cells. Nevertheless, the model provided a good fit to the data allowing the calculation and analysis of multiple time derivatives without amplifying noise contributions in the experimental data. The same equations used to model SR Ca^{2+} release provided a good fit to the sarcomere contraction data as shown in the bottom portion of Figure 13.

During relaxation in mouse myocardium, more than 90 % of activator Ca^{2+} is taken up by the ATP-dependent SR Ca^{2+} pump, SERCA2a [41].

Calcium uptake and sarcomere relaxation at the time t were best fit by a linear combination of two exponential

functions: $$\left[Ca^{2+}\right] = A \cdot \exp\left\{-\frac{t+t_0}{\tau_1}\right\} + B \cdot \exp\left\{-\frac{t+t_0}{\tau_2}\right\} \qquad (2.10)$$

Measurements of the time constants τ_1 and τ_2 in equation 2.10 have been used previously to characterize the falling phase of the Ca^{2+} transient [33, 52, 123-125] and therefore, unique solutions were desired. However, five free parameters in equation 2.10 did not to allow a unique fit, so that a reduction of free parameters was required. The number of free parameters could be reduced to three by normalizing the Ca^{2+} transients at the maximum cytosolic $[Ca^{2+}]_i$:

With $\frac{d\left[Ca^{2+}\right]}{dt} = 0$ and $[Ca^{2+}] = 0$ at the time $t = 0$, one obtains:

$$t_0 = \tau_1 \cdot \ln\left[A\left(1-\frac{\tau_2}{\tau_1}\right)\right], \text{ and } B = \exp\left\{\frac{t_0}{\tau_2}\right\}\left[A \cdot e^{-t_0/\tau_1} - 1\right] \qquad (2.11)$$

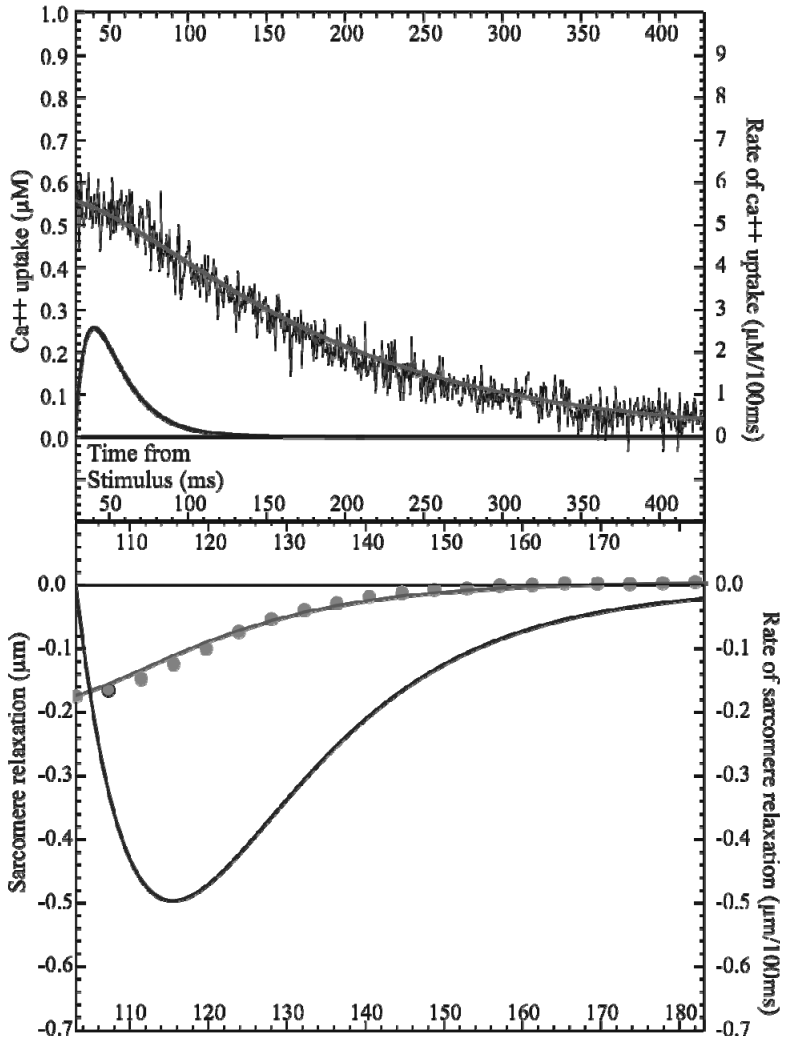

Figure 14. (Top) Fit of Ca^{2+} uptake (red) to the falling phase of the Ca^{2+} transient (grey line) and first time-derivative (blue).(Bottom) Fit of sarcomere relaxation (red) to the sarcomere length measurement during relaxation (grey circles) and first time-derivative (blue).

A representative fit of Ca^{2+} uptake and sarcomere relaxation using equations 2.11 and 2.12 is shown in Figure 14.

CHAPTER IV

SARCOMERE ACCELERATION IN PHOSPHOLAMBAN DEFICIENT CARDIAC MYOCYTES REVEALS AN ALTERED MYOFILAMENT RESPONSE TO CYTOSOLIC CALCIUM CONCENTRATION

4.1 Abstract

Abnormal calcium cycling in animal models of heart failure and in human failing hearts is characterized by impaired sarcoplasmic reticulum (SR) Ca^{2+} uptake and diminished SR Ca^{2+} stores. A reduced level of SR Ca^{2+} ATPase pump (SERCA2a) molecules and a reduced degree of phosphorylation of phospholamban (PLN) is believed to contribute to the depressed SR Ca^{2+} uptake in heart failure. Interventions that target the SERCA2a – PLN interaction hold therapeutic promise by restoring cytoplasmic Ca^{2+} transients and contraction. In mice, PLN ablation is associated with elevated SR Ca^{2+} load and with a linear increase in the extent and rate of myocyte shortening and relaxation. These positive inotropic and lusitropic effects of genetic PLN deletion have been attributed to the upregulation of Ca^{2+} transients. However, PLN knock out results in significant reordering of contractile proteins, leading us to hypothesize that an increase in the myofilament Ca^{2+} sensitivity contributes to the faster sarcomere contraction in cardiomyocytes lacking PLN. We used a microfluidic device to trap myocytes in a physiologically realistic space that facilitates sarcomere shortening and Ca^{2+} transient measurements.

We measured sarcomere acceleration from free contracting wild type (WT) and PLN knock out (PLN-/-) ventricular myocytes and used it as an index of cellular inotropy. The maximum sarcomere acceleration was 9.1 ± 2.1 fold increased ($P<0.001$) while Ca^{2+} release was moderately increased (1.65 ± 0.30 fold, $P<0.01$) in PLN-/- compared to WT

cardiomyocytes. Furthermore, at the time minimum sarcomere length, cytosolic Ca^{2+} concentration was almost 50% smaller in the PLN-/- cells. Our data add a physiological dimension to a previously published proteomic analysis showing that chronic PLN ablation changes myofilament composition. PLN-/- ventricular myocytes have significantly enhanced myofilament responses to systolic $Ca^{2+}{}_i$. Our results provide novel insight into myofilament contractile responses to chronic PLN gene deletion.

4.2 Introduction

Heart failure remains the leading cause of mortality and morbidity in developed countries. Diminished calcium transient amplitude, reduced sarcoplasmic reticulum (SR) Ca^{2+} content and impaired Ca^{2+} re-uptake are observed in cardiac myocytes from failing human hearts. Furthermore, altered protein expression profiles and phosphorylation states of key sarcoplasmic reticulum (SR) components were found in failing cardiac myocytes [6, 44, 126]. The reduced cardiac output observed in failing human hearts has been attributed to changes in the calcium transient [16, 50]. Correcting the calcium transient is therefore a rationale to recover cardiac contractility in heart failure patients. Phospholamban (PLN) is one critical regulator of calcium homeostasis in the heart and a key therapeutic target in the treatment of heart disease. The PLN monomer is a 6.08 kDa, 52 amino acid transmembrane protein that is located in the cardiac SR (see reviews by [21-23]). It binds to and inhibits the activity of the SR Ca^{2+} pump (SERCA2a), which actively transports Ca^{2+} into the SR to lower cytosolic calcium concentration allowing relaxation to occur. PLN inhibits SERCA2a by decreasing Ca^{2+} transport and ATPase activity at low intracellular calcium concentrations. Phosphorylation by cAMP-dependent

protein kinase (PKA) and Ca^{2+}/Calmodulin-dependent protein kinase II (CaMKII) at high cytosolic intracellular calcium concentration relieves this inhibition allowing greater Ca^{2+} transport across the SR [127-129]. Mice engineered for PLN deletion (PLN-/-) have an increased rate of ventricular relaxation in whole hearts [130], in papillary muscle preparations [36] and in single cells [54]. Most strikingly, PLN ablation prevented the functional, structural and histological abnormalities in a mouse model of dilated cardiomyopathy that shows characteristics of heart failure [131]. Several other studies have clearly shown the beneficial effects of chronic PLN suppression on cardiac function and remodeling in myocardial cells isolated from human failing hearts [132] and in animal model of heart failure [132-135]. However, other reports indicate that correcting the Ca^{2+} transient alone might not translate into improved cardiac function or into reversal of remodeling [136, 137]. Furthermore, the inheritance of two copies of the human PLN mutation, Leu39stop, which can be considered the equivalent to a PLN-null genotype, led to dilated cardiomyopathy and heart failure [138]. Discrepancies between the cardiac phenotypes in mice and in humans may originate from differences in the balance of myocyte Ca^{2+} fluxes because humans have a larger cardiac reserve, i.e. a potential for a gain in SR Ca^{2+} content [41].

There is evidence that genetic PLN ablation leads to systemic biochemical remodeling which might affect mice differently than humans. Proteomic analysis of hyper-dynamic PLN knockout mouse hearts revealed alterations in the expression level of more than 100 ventricular proteins, along with changes in the phosphorylation state of important regulatory proteins [56, 139]. Interestingly, the proteins affected by phospholamban ablation could be divided into two groups: metabolism and contractile apparatus.

Quantitative Western blotting confirmed changes in the two subunits of the myosin light chain (MLC-1 and MLC-2), which associate with the heavy chains to form a functional contractile unit. The atrial isoform of MLC-1 was down-regulated while its ventricular isoform was upregulated. In addition to the MLC-1 isoform switching, MLC-2a protein levels were higher in the PLN-/- than in the wild-type control hearts. Two dimensional ^{32}P autoradiography also showed that phosphorylation of MLC-2v was significantly increased in the PLN-/- ventricles. Phosphorylation of MLC-2v accompanies sarcomere organization and may facilitate the incorporation of additional actin/myosin crossbridges into the sarcomere allowing for higher organization of the sarcomeric architecture [140]. It has been shown in rat and human cardiac muscle to increase the calcium sensitivity of the myofilaments leading to an increased contraction at a given amount of cytosolic calcium concentration [141, 142]. Thus, these compensatory changes in contractile proteins may result in enhanced myocardial contractility, but they had never been considered as major contributors. In fact, the positive inotropic effect of PLN deletion was attributed to the increased SR Ca^{2+} load leading to increased amplitudes and rates of intraventricular pressure in isolated whole heart preparations [24, 53, 139] and increased twitch contraction amplitudes and velocities in single cells [52, 54, 55, 143].

We investigated the time course and the amplitude of the $Ca^{2+}{}_i$ transients in relation to the amplitude and velocity of the sarcomere shortening and relaxation in cardiac myocytes isolated from PLN-/- and wild type (WT) control hearts. The aim of the study was to test whether or not the Ca^{2+} sensitivity of contractile machinery is changed in phospholamban deficient cardiac myocytes. Furthermore, we present a novel microfluidic based

technique to confine single cardiac myocytes and thereby reducing motion artifacts during prolonged optical recordings.

4.3 Methods

Microfluidic device fabrication and cell manipulation

The microfluidic cell trap is based on a previously published device [144]. Briefly, an inverted relief microchannel structure was produced by photolithography in a 30 μm thick layer of photoresist (SU8-2050, Microchem) on a 3 ” diameter silicon wafer (master) by exposing it to UV light through a metal mask (Advance Reproductions) using a contact mask aligner. The photoresist was developed according to the manufacturer’s instructions. A 5 mm layer of PDMS, poly-dimethylsiloxane was cast onto the master in a plastic culture dish at the standard PDMS/curing agent mixing ratio of 10/1 [98]. After 3 h of curing in a 60 ºC convection oven, PDMS devices were cut out and separated from the master. Microchannel access holes were punched through the elastomer by means of 1mm diameter sharpened stainless steel capillaries. The PDMS structure was manually aligned and sealed by auto-adhesion on the microelectrodes which were deposited on #1 cover glass by ion beam evaporation [145]. Stainless steel capillaries were inserted into the PDMS access holes and connected to 1 ml syringes via 0.5 mm inner diameter microtubing (Cole Parmer). The cell trap consisted of a 25 μm wide and 220 μm long channel with a 5 μm wide restriction at the one end where the cell was held by suction as shown in Figure 15B. Occasional cell damage caused by the trapping procedure could be identified immediately by hyper contracture followed by cell death. However, more than 80 % of the cells showed no sings of cell damage with sharp edges and clear striation patterns. These cells remained viable and could be electrically stimulated in the

microchannel for at least one hour. The voltage required to pace the cells was less than 500 mV, which prevented gas formation due to electrolysis, a common problem in culture dish experiments with electrode separations on the order of millimeters.

Isolation of ventricular cardiac myocytes

Animal studies conformed to the guidelines of the Vanderbilt University Institutional Animal Care and Use Committee and to the Guide for the Care and Use of Laboratory Animals published by the US National Institutes of Health (NIH Publication No. 85-23, revised 1996). Male phospholamban knockout mice, 3-4 months of age, and their wild-type littermates were anesthetized by intraperitoneal injection of 3 mg/10ml Avertin solution (5 mg Avertin per 10 g body weight, T48402, Sigma-Aldrich) containing Heparin (H9399, Sigma-Aldrich). The heart was rapidly excised and placed into ice-cold Ca^{2+}-free Hepes-buffered normal Tyrode (NT) solution. The NT solution contained (in mM): Na^+ 140, K^+ 4.5, Mg^{2+} 0.5., Cl^- 150, $H_2PO_4^-$ 0.4, HCO_3^- 10, Hepes 10, glucose 10 and no Ca^{2+}. Calcium chloride was added where specified. The aorta was cannulated and the heart was perfused with NT solution at room temperature for 10 min to stop contractions. The perfusion was then switched to NT solution containing 10 μM Ca^{2+}, 178 U/ml collagenase (CLS2, Worthington Biochemical) and 0.64 U/ml protease (P5147, Sigma-Aldrich) for 8 to 10 min at 37 ºC. Ventricles and septum were cut away, coarsely minced, and placed into NT solution. Myocytes were dispersed by gentle agitation and the Ca^{2+} concentration was gradually increased to 0.5 mM. After 15 min, 10 mg/ml bovine serum albumin (A9647, Sigma-Aldrich) was added to the solution in which cells were stored until used, usually within 3 hours after isolation.

Measurement of indo-1 calcium transients

Cells were loaded with the cell-permeant acetoxymethyl ester form of the calcium sensitive dye indo-1 (I1203, Molecular Probes-Invitrogen). Stock solutions were prepared by dissolving 1 mg of the dye in 200 µl anhydrous DMSO (276855, Sigma-Aldrich) yielding a stock concentration of 5 mM. The stock solution was stored in 20 µl aliquots desiccated and frozen at -20 ºC until used. For each experiment, one aliquot (20 µl) of the stock solution of the dye was added to 5 ml of cell suspension to yield a final concentration of 20 µM. Cells were kept in the staining solution for 5 min at room temperature and then centrifuged at 27 g for 10 min. The supernatant was removed and the cells were re-suspended in Tyrode solution containing the final calcium concentration of 1.0 mM. Cells were incubated in Tyrode solution for another 30-40 min to allow complete intracellular indo-1 de-esterification. To reduce phototoxic effects, only 200 µl of stained cells were pipetted into the bath solution for each fluorescent measurement after which the bath solution was completely replaced. The bath solution contained Tyrode solution at 1.0 mM $CaCl_2$.

Microscope configuration

The microfluidic device was mounted on the stage of an inverted microscope (Axiovert 200, Carl Zeiss, Germany) and the trap was magnified by a 63X, 1.4 NA oil immersion lens (Plan Apochromat, Carl Zeiss, Germany). The Indo-1 dye was excited by a monochromator (Optoscan, Cairn Research Ltd, UK) at a wavelength of 365 ± 15 nm. The excitation light was reflected by a 390 nm dichroic mirror (390DRLP, Omega

Optical Inc.) onto the cell. A second dichroic mirror (450 DCLP, Omega Optical) in the emission path was used to split the fluorescence light into a transmitted (F495) and a reflected beam (F405). Each beam was passed through a bandpass emission filter with a center wavelength of 495 ± 10 nm (495DF20, Omega Optical) and 405 ± 20 nm (405DF43, Omega Optical). The light from the two beams was finally collected by two 1 mm diameter optical fibers (P1000-2-UV-VIS, Ocean Optics) representing a ~16 μm diameter spot on the cell and converted into an electric current by two photomultiplier modules (H6780, Hamamatsu). The photo currents were converted into voltages and amplified by custom-built DC coupled amplifiers and digitized at a sampling rate of 20 KHz by an A/D converter board (PCI-6071E, National Instruments) in a standard PC.

Calibration of Indo-1 calcium fluorescence

Calibration of the indo-1 fluorescence signals was carried out at the end of the experiment according to a previously published method [146]. Background and autofluorescence were subtracted from the signal before the fluorescence ratios (R=F405/F485) were converted to free $[Ca^{2+}]_i$ according to the equation [110]: $[Ca^{2+}]_i=K_d \cdot \beta \cdot [R-R_{min}]/[R_{max}-R]$. The dissociation constant for indo-1 was taken as previously published *in vivo* as $K_d = 844$ nM [146]. The ratio of the free/bound indo-1 fluorescence at 485 nm was $\beta = 2.37 \pm 0.27$. For in vivo measurements of R_{min} and R_{max}, indo-1 loaded cells were washed for 10min in calcium-free Tyrode solution containing 5mM EGTA and 10 mM caffeine to empty the intracellular Ca^{2+} stores. Cells were then washed for 15 min in NT solution containing 5mM EGTA. To achieve metabolic inhibition and to avoid hyper contracture during the increase of the extracellular calcium

concentration, 3 μM carbonyl cyanide p-(tri-fluoromethoxy)-phenylhydrazone (C2920, Sigma-Aldrich) was added. To obtain R_{min}, 10 μM of the nonfluorescent Ca^{2+} ionophore A23187 (B7272, Sigma-Aldrich) was added to the solution and measurements were taken after the fluorescence at both wavelengths reached stable values. For R_{max} determination, the bath solution was EGTA-free and contained 15 mM Ca^{2+} to saturate the intracellular dye. The Ca^{2+}-ionophore was present during all calibration measurements.

Sarcomere contraction measurements

Sarcomere contraction was measured from cells trapped inside the microfluidic device using a commercial contractility system (Ionoptix Corp.) consisting of a 240 frames-per-second CCD camera (Myocam), a frame grabber PC card (FRGRAB), an analog/digital converter (DSI200) to record the stimulus, and the data acquisition software (Ion Wizard). The camera was connected to a side port of the microscope. Cells were field stimulated (square waves, 8 ms stimulus duration, 25 % above threshold) at 1 Hz until steady state was achieved and only those cells exhibiting stable steady-state conditions were included in the study. Indo-1 fluorescence and sarcomere contraction were determined in separate experiments, although simultaneous measurements are possible. However, we decided for separate measurements to avoid Ca^{2+} buffering and phototoxicity during sarcomere contraction measurements [147]. The timing of the stimulus was recorded for each calcium and contraction transient and used as a reference to synchronize both measurements.

Data analysis and statistics

Data were analyzed in Matlab (R14, The MathWorks). The data were fit to empirical functions for the purpose of calculating multiple time derivatives. Intracellular calcium release $[Ca^{2+}]_i$ was best fit by a modified model of isolated RyR activation as previously described [121]: $[Ca^{2+}]_i=[Ca^{2+}]_{max}\cdot (P/1-P)^n$, where P is the time-dependence of the Ca^{2+} release, defined by a single exponential function raised to the power of m: $P = 0.5\cdot(1-e^{-t/\tau})^m$. The parameters n, m, and τ were used as fit parameters. Calcium uptake was best fit by a sum of two exponential functions: $[Ca^{2+}]_i = A\cdot e^{-t/\tau 1} + B\cdot e^{-t/\tau 2}$. The parameters A, B, $\tau 1$ and $\tau 2$ were used as fit parameters. $[Ca^{2+}]_i$ was replaced by the sarcomere length in the above equations to fit the contraction measurements.

Maximum rates of Ca^{2+} release and sarcomere contraction were defined as the maxima of first time-derivatives of the Ca^{2+} and the contraction transients, respectively. Sarcomere acceleration was defined as the second time-derivative of the sarcomere contraction. The duration of the Ca^{2+} release and the duration of sarcomere contraction were defined as the times from 10 % to 95 % of the maxima of the Ca^{2+} and the contraction transients, respectively.

Data are expressed as means ± S.E.M. Statistical significance was determined by Student's t test for unpaired observations between wild type (PLN+/+) and phospholamban deficient (PLN-/-) cells. A p value < 0.05 was considered statistically significant. All data presented was taken from four animals in each group. The number of cells used in the statistical analysis is indicated in Figure 3.

4.4 Results

Microfluidics facilitates cell alignment and reduces motion artifacts

To get reliable, high resolution sarcomere length measurements, the striation pattern of the cell had to be aligned in the field of view and the position of the cell maintained during the whole time course of the experiment. The microfluidic device shown in Figure 15 automatically aligned and stabilized single cardiac myocytes during optical recordings.

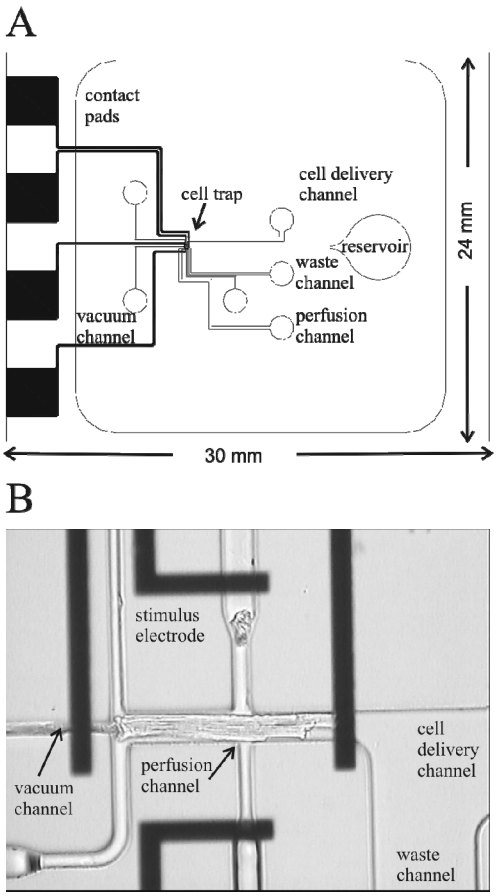

Figure 15. PDMS microfluidic cell trap. (A) Schematic overview of the microfluidic device sealed on a microelectrode array with cell delivery and perfusion channels that can be used to expose the cell to drugs. The cell trap near the center of the device can hold and perfuse a single cell during measurements. (B) Microscope image of the cell trap occupied by a single cardiac myocyte with microelectrodes for field stimulation parallel and perpendicular to the cell.

Single cardiac myocytes were pulled into the microfabricated cell trap by a negative pressure applied to the vacuum channel as shown in Figure 15B. Figure 16A and B show multiple sarcomere contraction recordings from a single cell in a culture dish and in the microfluidic cell trap, respectively. The recordings in the culture dish (Figure 16A) could only be analyzed during the first seven contractions. A slight rotation induced by the contraction led to measurement artifacts indicated by positive contraction amplitudes. In contrast, Figure 16B shows stable and highly reproducible recordings of sarcomere length from a confined myocyte inside the microfluidic cell trap with an improved signal to noise ratio.

Reproducible recordings over long periods of time allowed us to average 40 to 50 transients, thereby significantly increasing the S/N ratio and preserving the bandwidth of the measurement.

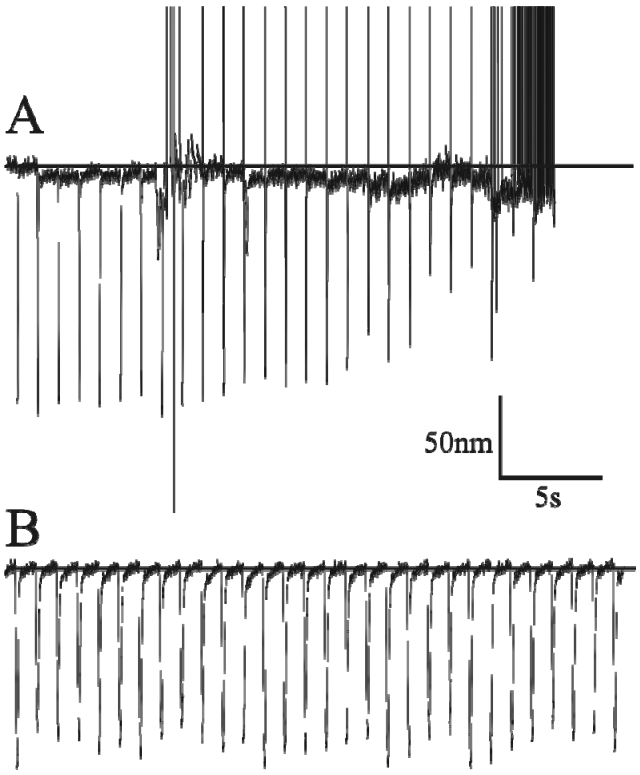

Figure 16. Sarcomere contraction measurements in the microfluidic device. (A) Sarcomere length measurement from an unattached cardiac myocyte contracting in a perfusion chamber. (B) Sarcomere length measurement from a contracting cardiac myocyte inside the microfluidic channel, where the movement of the cell is restricted.

Phospholamban ablation increases calcium release and sarcomere contraction amplitude

Phospholamban gene ablation has previously been shown to increase the SR Ca^{2+} content resulting in an increased Ca^{2+} release, leading to an increase in the amplitude of

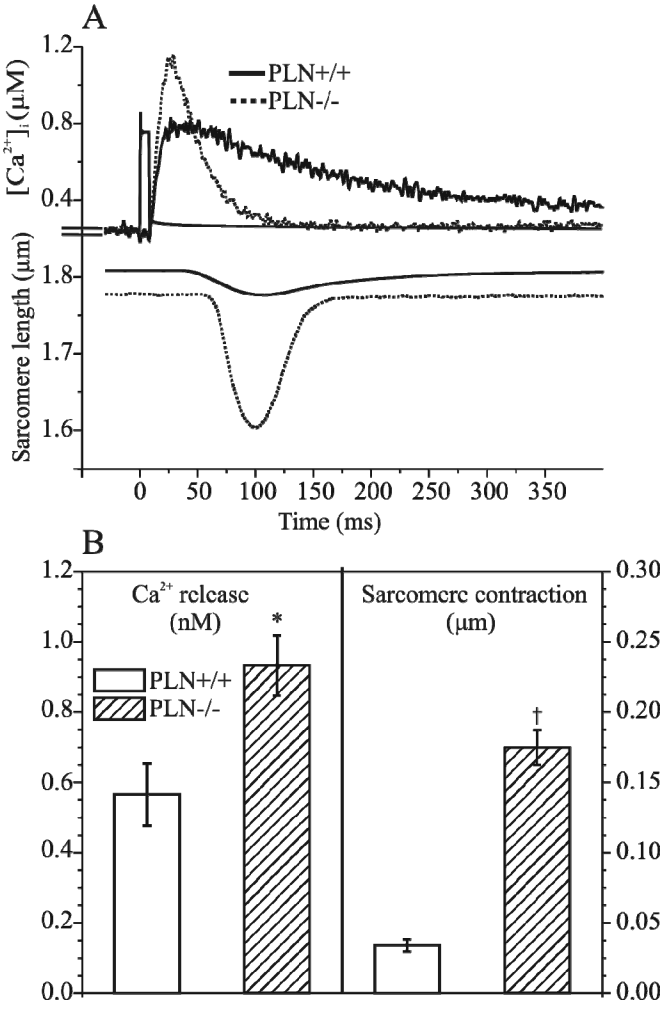

Figure 17 Cytosolic Ca^{2+} concentration and sarcomere length in PLN+/+ and PLN-/- cells. (A) Average steady state intracellular indo-1 Ca^{2+} transient from PLN+/+ cells (n=13) and PLN-/- cells (n=17). Every cell was represented by an average of 5-6 consecutive indo-1 transients. (B) Average steady state sarcomere length transients from PLN+/+ cells (n=12) and PLN-/- cells (n=10). Every cell was represented by an average of 40-50 consecutive contraction transients. (B) Maximum Ca^{2+} release in PLN+/+ and PLN-/- cells (left) and peak sarcomere contraction amplitude in PLN+/+ and PLN-/- cells (right). *,†: $p<0.05$

sarcomere contraction. However, the dynamics of the Ca^{2+} release in combination with the contraction have not been characterized in PLN -/- mice. Figure 17A shows Ca^{2+} transients and dynamic changes in sarcomere length relative to a stimulation pulse during a single contraction. Indo-1 Ca^{2+} transients from PLN-/- cells were larger in amplitude and shorter in duration. Maximum Ca^{2+} release was increased 1.65 ± 0.30 fold in the PLN-/- cells. Peak Ca^{2+} release was 932 ± 85 nM in PLN-/- cells and 566 ± 88 nM in the PLN+/+ cells, as shown in Figure 17B.

The increased peak Ca^{2+} release in the PLN-/- cells was accompanied by a 5.12 ± 0.73 fold increased peak sarcomere contraction amplitude with magnitudes of 174 ± 12 nm in the PLN-/- cells and 34.1 ± 4.2 nm in the PLN+/+ cells. The data are shown in Figure 17B. Diastolic sarcomere length was shorter in the PLN-/- cells with 1.78 ± 0.02 μm compared to 1.81 ± 0.02μm in the PLN+/+ cells, while there was no difference in the diastolic $[Ca^{2+}]_i$. The fractional sarcomere shortening during contraction was therefore 1.89 ± 0.24 % in the PLN+/+ and 9.85 ± 0.6 8 % in the PLN-/- cells, respectively.

Phospholamban ablation alters calcium release and the dynamics of sarcomere contraction

A large contributing factor in myofilament activation is the rate of rise of intracellular calcium concentration [61, 63].

Therefore, we compared the time courses of the Ca^{2+} release and the sarcomere contraction in more detail as shown in Figure 18.

Time to maximum Ca^{2+} release was not significantly changed, with 19.97 ± 0.83 ms in the PLN+/+ cells and 19.3 ± 1.0 ms in the PLN-/- cells (Figure 18A).

The maximum Ca^{2+} release rate was increased 1.85 ± 0.15 fold in the PLN-/- cells, with 6.15 ± 0.37 μM per 100ms in the PLN+/+ cells and 11.39 ± 0.68 μM per 100 ms in the PLN-/- cells (Figure 18B).

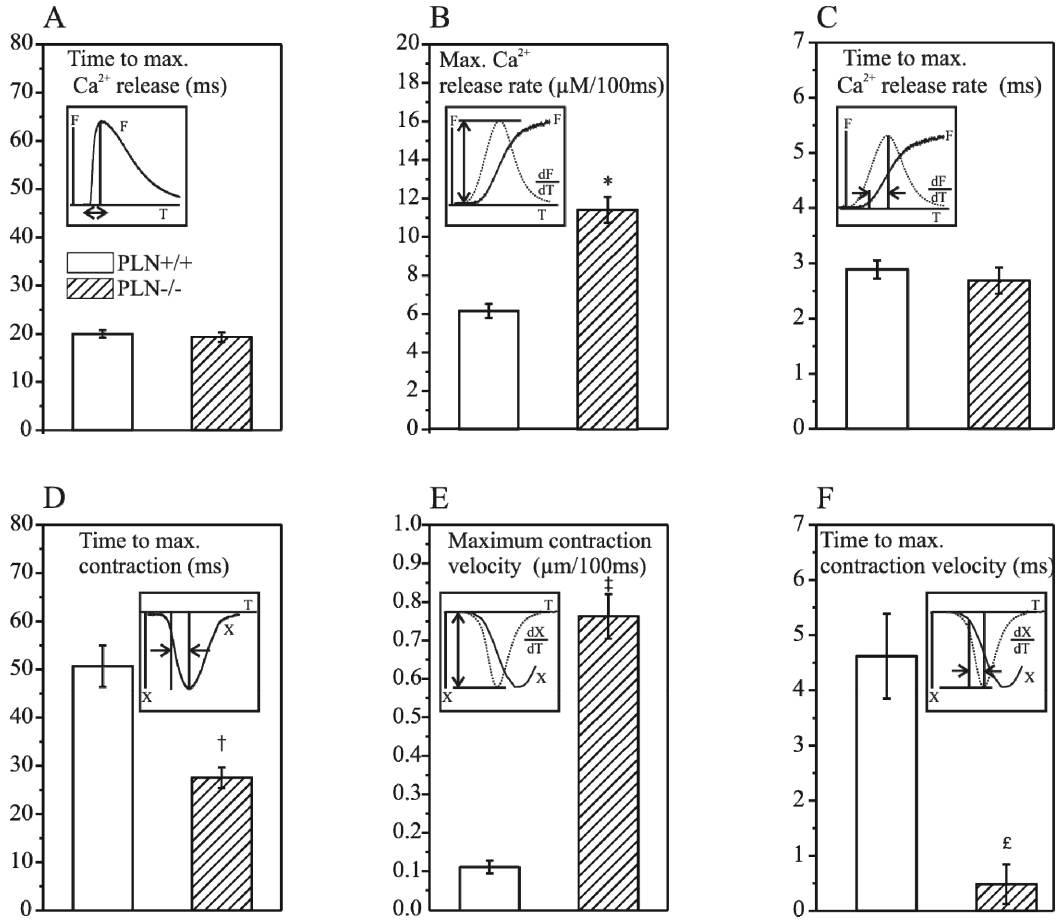

Figure 18. Time course analysis of Ca2+ release and sarcomere contraction in PLN+/+ and PLN-/- cells. (A) Time from 10 % to 90 % of the rising phase of the $[Ca^{2+}]_i$ transient. (B) Maximum rate of the intracellular Ca^{2+} release. (C) Time from 10 % of peak $[Ca^{2+}]_i$ to the maximum rate of Ca^{2+} release. (D) Time from 10 % to 90 % of the rising phase of the sarcomere length transient. (E) Maximum contraction velocity. (F) Time from 10 % of peak sarcomere contraction to maximum contraction velocity.

Furthermore, the times until the maximum Ca^{2+} release rate was reached were similar in both groups, with 2.89 ± 0.17 ms in the PLN+/+ cells and 2.69 ± 0.24 ms in the PLN-/- cells (Figure 18C). These times were measured relative to the time point when the Ca^{2+}

concentration reached 10 % of the maximum. Since the times to maximum Ca^{2+} release were the same for both genotypes, the increased maximum rate of Ca^{2+} release in the PLN-/- cells could be attributed to the increased Ca^{2+} release amplitude.

In contrast, the time it took for the sarcomeres to reach their maximum shortening was almost 50 % smaller in the PLN-/- cells compared to the WT control cells. We measured a time of 50.7 ± 4.3 ms in the PLN+/+ cells and 27.5 ± 2.2 ms in the PLN-/- cells, respectively. Furthermore, our data analysis showed a large increase in the maximum sarcomere contraction velocity of 6.8 ± 1.1 fold in the PLN-/- cells compared to control, corresponding to a maximum shortening velocity of 0.113 ± 0.017 μm per 100 ms in the PLN+/+ cells and 0.764 ± 0.058 μm per 100 ms in the PLN-/- cells.

The faster sarcomere shortening was also reflected by the time it took the sarcomeres to reach the maximum velocity of contraction. The PLN+/+ cells reached the maximum velocity of contraction in 4.62 ± 0.77 ms, while the PLN-/- cells only needed 0.48 ± 0.36 ms, as measured from the time of 10 % contraction (Figure 18D).

In summary, the sarcomere contraction velocity was increased 6.8 ± 1.1 fold and was reached 9.6 ± 1.6 times faster. Calcium release amplitude and rate were increased only 1.65 ± 0.30 and 1.85±0.15 fold, respectively in PLN -/- mice compared to WT control.

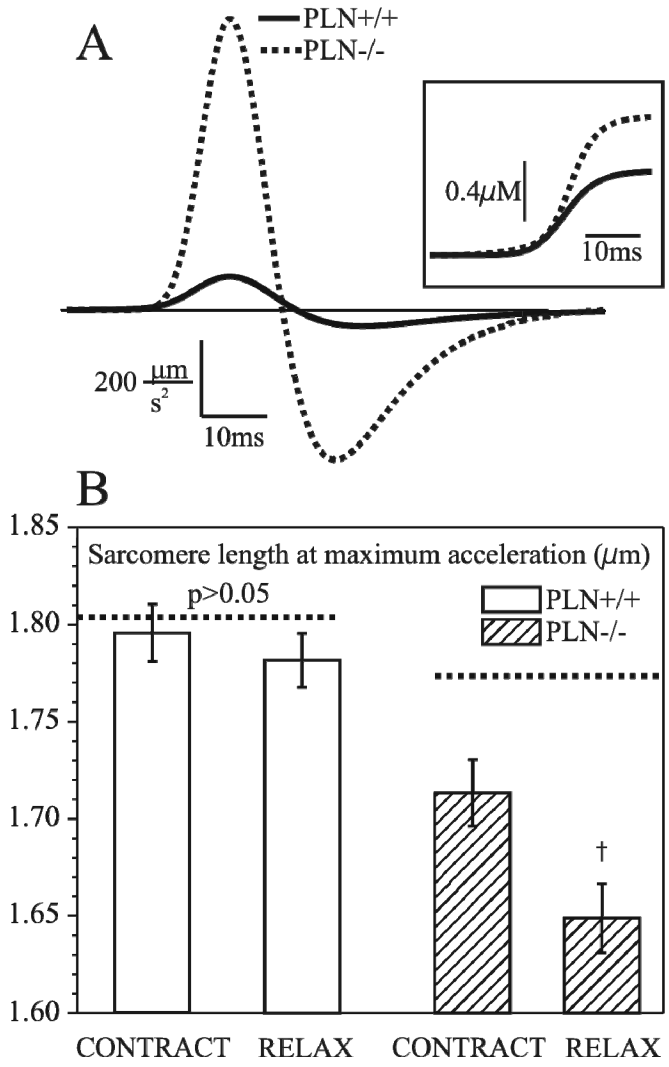

Figure 19. Sarcomere acceleration of PLN+/+ and PLN-/- cells (A) Time course of the sarcomere acceleration during contraction in PLN+/+ (solid line) and PLN-/- (dotted line) cells. The increased sarcomere acceleration was accompanied by a moderate increase in Ca^{2+} release (insert). (B) Sarcomere length at the time at which the maximum acceleration was reached during contraction (CONTRACT) and relaxation (RELAX). Dotted lines represent the diastolic sarcomere length.

In order to compare active and passive forces during contraction and to assess whether the increased inotropy in the phospholamban deficient cells could be the result of the increased Ca^{2+} release, we used the acceleration of sarcomere shortening as an index of contractility. Figure 19A shows the sarcomere acceleration as a function of time in the PLN+/+ and the PLN-/- cardiac myocytes. Sarcomere acceleration was consistently increased in the PLN-/- cells during the entire time course of contraction.

The peak sarcomere acceleration was increased 9.1 ± 2.1 fold in the PLN-/- cells with absolute values of 84 ± 18 $\mu m/s^2$ in the PLN+/+ cells and 766 ± 67 $\mu m/s^2$ in the PLN-/- cells (Figure 19A).

The maximum sarcomere acceleration during compression and relaxation is proportional to the maximum total force, which is the sum of the positive active force which compresses the sarcomeres and the negative passive force that resists shortening (see discussion). Peak force was developed at almost diastolic sarcomere length (dotted lines in Figure 19A) in the PLN+/+ cells, i.e. at 1.796 ± 0.015 μm during contraction and at 1.782 ± 0.014 μm during relaxation. In contrast, the sarcomeres of the PLN -/- cells were compressed to a much larger extent at the time of maximum force. Sarcomere length at peak force was 1.713 ± 0.023 μm during contraction and 1.649 ± 0.018 μm during relaxation in the PLN null myocytes.

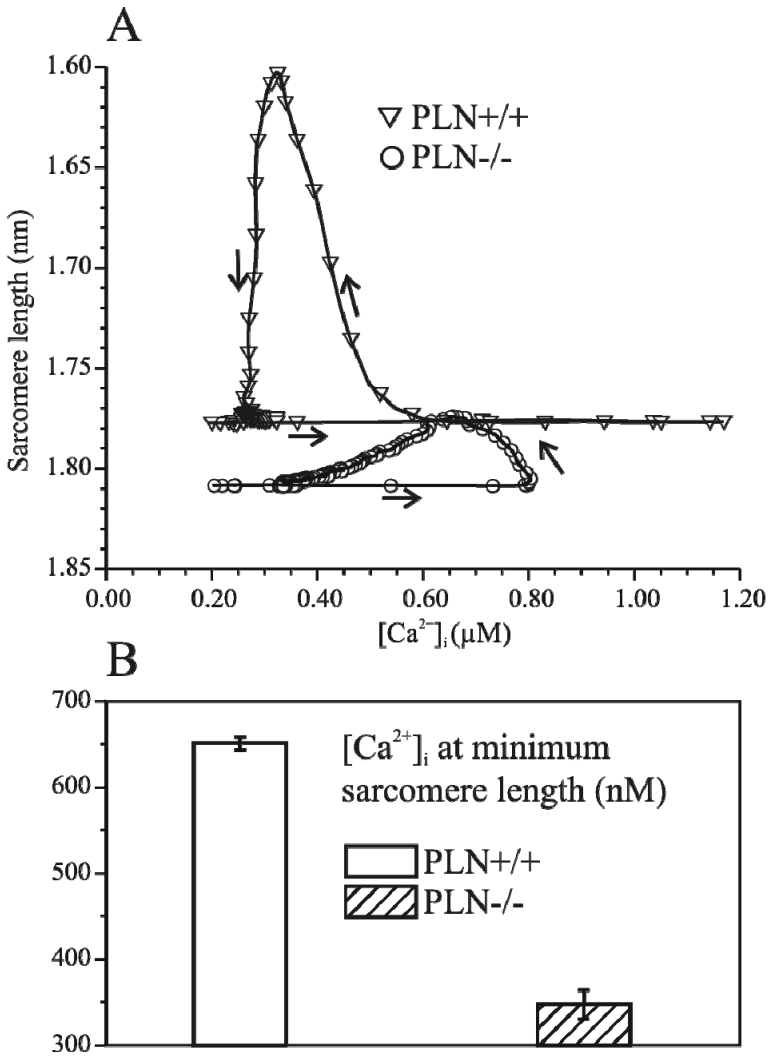

Figure 20. Phase plots of PLN+/+ and PLN-/- cells. (A) Average twitch sarcomere length as a function of $[Ca^{2+}]_i$ during the cardiac cycle in PLN+/+ and PLN-/- cells. Arrows indicate the time direction of contraction and relaxation. The circles and triangles represent 5ms time intervals in the PLN+/+ and PLN-/- transients, respectively. (B) Intracellular Ca^{2+} concentration at the maximum sarcomere length for PLN+/+ and PLN-/- cells.

Phospholamban ablation increases the response of the cardiac myofilaments to changes in intracellular calcium concentration

PLN-/- cells showed a large increase in sarcomere acceleration with only a moderate increase in the peak calcium release and no significant change in the time course of the Ca^{2+} release. We have used phase plots as a method to identify a change in the Ca^{2+} sensitivity of contraction. This method has been described to investigate shifts in the myofilament Ca^{2+} sensitivity in isolated cardiac myocytes [148]. Within each contraction the phase-plane diagram of sarcomere length and cytosolic $[Ca^{2+}]_i$ concentration forms a counter-clockwise loop as indicated by the arrows in Figure 20A. The symbols which are drawn on top of each phase trajectory represent 5 ms time intervals. The larger mean distances of the triangles during contraction and relaxation on top of the PLN-/- trace indicate the increased velocities of contraction and relaxation in these cells compared to the WT control cells. The PLN-/- phase plot in Figure 20A clearly shows a hysteresis as a result of the delay between the peak $[Ca^{2+}]_i$ and the onset of sarcomere shortening which can also be inferred from Figure 17A. The prominent shift of the PLN-/- phase trajectory to the left is consistent with an increase in the myofilament Ca^{2+} response in these cells, as cell shortening and the re-lengthening occurred at lower intracellular calcium concentrations compared to the PLN+/+ cells. The shortest sarcomeres were observed in the phospholamban deficient cells at a cytosolic Ca^{2+} concentration which was close to the diastolic level, i.e. 347 ± 17 nM, and much smaller than in the PLN+/+ control cells (651.1 ± 7.5 nM).

The phase plot clearly showed a characteristically different response of the cardiac myofilament to a given cytosolic calcium concentration which could explain the increased contractility of the PLN-/- sarcomeres.

4.5 Discussion

Time course of the Ca^{2+} release and the sarcomere contraction in the PLN-/- cells

Our quantitative analysis of the time courses of the calcium release and sarcomere contraction revealed, that the shorter time-to-maximum contraction amplitude and the shorter time-to-maximum contraction velocity were not reflected by corresponding changes in the Ca^{2+} transient (Figure 18). Furthermore, the maximum rate of calcium release was increased in the PLN-/- cells due to the higher peak $[Ca^{2+}]_i$ which was reached in both groups at the same time (Figure 18A). We observed that changes in the time course of SR Ca^{2+} release were not correlated with corresponding changes in the time course of sarcomere contraction. The force – $[Ca^{2+}]_i$ relationship during a dynamic twitch is characteristically different than in the steady state. The steady-state force – $[Ca^{2+}]_i$ relationships are measured in tetanized mouse and rat cardiac muscle preparations and are highly non-linear with hill coefficients between 5 and 10 [63, 149, 150] indicating a large increase of force with intracellular calcium concentration. Force – $[Ca^{2+}]_i$ relationships measured during a twitch are characterized by a much smaller rise in force for a given increase in cytosolic $[Ca^{2+}]$. In intact mouse ventricular muscle during a twitch, force increased approximately linearly with systolic Ca^{2+} concentration [149-151]. The difference to the steady state is an apparent loss of myofilament Ca^{2+} sensitivity and cooperativity as a result of the fast changing cytosolic Ca^{2+} concentration,

which may not allow the formation of a dynamic equilibrium at any time during the transient [62, 63]. This effect is even more pronounced in mice with PLN deletion leading to a further reduction in the force generation due to the extremely short Ca^{2+} transients. Therefore, the increase in the rate of sarcomere contraction in the PLN null myocytes may be the result of an increased amplitude (rather than a change in the time course) of the Ca^{2+} release or the result of a change in the Ca^{2+} sensitivity of the myofilaments.

Sarcomere acceleration as an index of myocyte contractility

We compared the relative changes in sarcomere acceleration in the PLN-/- cells with previously published data on the twitch peak force – peak $[Ca^{2+}]_i$ relationship in WT mouse cardiac muscle to decide if the increased maximum Ca^{2+} release was indeed responsible for the increased contractility in the PLN deficient cells.

In order to infer relative changes in contraction force from changes in sarcomere acceleration several assumptions about restoring forces need to be made. The active shortening response of an unattached cardiac myocyte reveals the maximum degree of shortening in a minimally loaded cell. The titin network provides the main contribution to the contraction opposing restoring force that limits shortening [72, 152, 153]. Therefore, the total force acting upon an unloaded sarcomere is the sum of the positive active force F_A and the negative passive elastic resistance, F_P. In addition to the elastic resistance, a viscous resistance F_V provides a damping force during contraction which is proportional to the rate of shortening, i.e. $F_V = B\ ds/dt$, where B is the damping constant and s the

sarcomere length [77]. Altogether, the total force F_{TOT} acting upon the sarcomere during contraction can be described as:

$F_{TOT}=F_A - F_P - F_V$, where F_A, F_P are the time and length-dependent active and passive elastic forces, respectively, and F_V is the time and velocity dependent viscous resistance. The total contraction force per sarcomere unit, F_{TOT}, is proportional to the sarcomere acceleration, i.e. $F_{TOT} = m \cdot a$, where m and a are the mass and acceleration of the sarcomere, respectively. Because sarcomere acceleration measures total force per sarcomere, both an increase in the active force and a decrease in the passive resistance would increase acceleration during contraction.

The comparison of contraction with relaxation suggests that PLN deletion did not decrease the passive forces opposing shortening during sarcomere contraction. Interventions that increase the effective elastic constant were shown to slow down the rate of shortening but accelerate the rate of re-lengthening [74, 75] in the anoxic heart (due to compression of crossbridges). Likewise, a softening of the elastic properties of the sarcomere would lead to increase the rate of contraction but decelerate relaxation. Therefore, a softer sarcomere would be shorter during contraction and longer during relaxation at the time of maximum force development.

The data in Figure 19 show that the sarcomere length at the time of maximum acceleration was shorter in the PLN null myocytes during contraction and relaxation compared to the WT control. Since we observed a shorter sarcomere length both during contraction and relaxation we cannot assume that the passive forces opposing sarcomere contraction are decreased in the PLN -/- at maximum acceleration. In fact, the

significantly smaller sarcomere length during relaxation compared to contraction in the PLN-/- cells is indicative of an increase in stiffness of the sarcomeres.

This was also reflected by the 12.14 ± 2.4 fold increased maximum relaxation velocity (data not shown) compared to the 6.8 ± 1.1 fold increase in maximum contraction velocity. Furthermore, the shorter diastolic sarcomere length in the PLN-/- cells contributed to an increase in the passive forces at all sarcomere lengths as predicted by the classical Frank-Starling effect [154].

Therefore, we found that the assumption was justified that the passive sarcomere restoring force in phospholamban deficient cells, F_P^{PLN}, at the time of maximum acceleration, t_{max}, was not smaller than in WT control, so that $F_P^{WT}(t_{max}) \leq F_P^{PLN}(t_{max})$. Under this assumption, the total force per sarcomere at the time t_{max} can be estimated as:

$$m^{PLN} \cdot a^{PLN} = F_{TOT}^{PLN} = F_A^{PLN} - F_P^{PLN} - F_V^{PLN} \leq F_A^{PLN} - F_P^{WT} - \frac{F_V^{PLN}}{F_V^{WT}} F_V^{WT} \qquad (4.1)$$

Assuming that genetic phospholamban deletion did not change the intracellular viscosity, the ratio of viscous forces may be replaced by the ratio of contraction velocities, i.e. $V = F_V^{PLN} / F_V^{WT} = v^{PLN} / v^{WT}$, where V denotes the ratio of the PLN-/- and WT contraction velocities at the time t_{max}. The sarcomere mass, m^{PLN}, is comparable in the PLN-/- and wild-type hearts, as no difference in the heart/body weight ratio was found [24]. Therefore, we assume that the sarcomere mass of the PLN-/- cells can be approximated by that of the WT cells:

$$m^{PLN}a^{PLN} \approx m^{WT}a^{PLN} \approx m^{WT}\frac{a^{PLN}}{a^{WT}}a^{WT} = R \cdot F_{TOT}^{WT} = R \cdot [F_A^{WT} - F_P^{WT} - F_V^{WT}] \quad (4.2)$$

We defined R as the ratio of PLN -/- and WT sarcomere accelerations.

Taking equations 4.1 and 4.2 together yields a relationship between the ratios of sarcomere acceleration and active force in the unloaded cardiac myocytes:

$$R \cdot F_A^{WT} + (1-R) \cdot \frac{F_P^{WT}}{F_A^{WT}} + (V-R) \cdot \frac{F_V^{WT}}{F_A^{WT}} \leq \frac{F_A^{PLN}}{F_A^{WT}} \quad (4.3)$$

The data presented in Figure 19B indicates that the passive force in the wild-type cells, $F_P{}^{WT}$, was small compared to the active force, $F_A{}^{WT}$, because the maximum acceleration was reached at a sarcomere length which was (within the standard error interval) equal to the diastolic value, while the contraction velocity reached nearly 20% of its maximum value at that time. This indicates a considerable active force development at almost diastolic sarcomere length. Therefore, the passive component of the total force at the time t_{max}, $F_P{}^{WT}$, may be neglected in first approximation compared to the active force, $F_A{}^{WT}$. In fact, Helmes *et al.* [153] directly measured the passive restoring forces in rat cardiac myocytes by selectively digesting titin. They found that the passive force decreased approximately linear during relaxation and that it was negligible at the diastolic value. Taken together, the ratio of the active forces developed in unloaded PLN-/- and WT cardiac myocytes can be estimated by:

$$R + (V-R) \cdot \frac{F_V^{WT}}{F_A^{WT}} \leq \frac{F_A^{PLN}}{F_A^{WT}} \quad (4.4)$$

If an intervention is known not to influence the elastic properties of the titin network, the inequality sign in equation 4.4 may be replaced by and equal sign, yielding a direct

relationship between ratios of active force and ratios of sarcomere shortening velocity and acceleration.

The PLN-/- sarcomeres showed an R = 9.1 ± 2.1 fold increase in the maximum acceleration and a V = 28.6 ± 2.0 increase in the shortening velocities at the time t_{max} when the maximum total force was reached. The ratio of viscous damping to active force, F_V^{WT}/F_A^{WT}, can only take values between 0 and 1. Niggli *et al.* found that this ratio may likely exceed 30 % in the range of experimentally observed twitch shortening velocities [77]. On the other hand, Peak Ca^{2+} release was only slightly increased (1.65 ± 0.30 fold). The relationship 4.4 allowed us to compare our data to twitch-force peak-$[Ca^{2+}]_i$ measurements in isolated intact mouse trabeculae and small papillary muscles [149, 150]. In these preparations, a two fold relative increase in the active force of shortening corresponded to an increase in $[Ca^{2+}]_i$ concentration in the rage from 0.5 to 1.0 μM. Therefore, based on our $[Ca^{2+}]_i$ measurements, the ratio of the active forces in PLN-/- and WT is expected to be smaller than 2. However, in the PLN-/- cardiac myocytes we measured an overwhelmingly a nine fold increase in the sarcomere acceleration along with a 28 fold increase in viscous loading which clearly indicates a change in the force-$[Ca^{2+}]_i$ relationship in the phospholamban deficient cardiac myocytes.

Myofilament response to intracellular $[Ca^{2+}]$

A further indication for a change in the myofilament response to intracellular Ca^{2+} in the PLN null myocytes can be visualized by plotting sarcomere length as a function of Ca^{2+} release, as presented in Figure 20. The shift in the PLN-/- phase plot to the left shows a much smaller cytosolic calcium concentration at the onset of contraction and relaxation

than in the WT cells (Figure 20B), which is characteristic for an increase in the Ca^{2+} myofilament sensitivity [148] in these cells.

Summary and Implications

In summary, our results showed a significant change in the force – Ca^{2+} relationship in cardiac myocytes isolated from phospholamban deficient mice. The smaller cytosolic calcium concentrations at the onset of contraction and relaxation are indicative of an increase in Ca^{2+} myofilament sensitivity. As a consequence, therapeutic interventions that target on the SERCA2a – PLN interaction may alter the myofilament response to cytosolic [Ca^{2+}].

Acknowledgments

This work was supported in part by DARPA, AFOSR, NIH, the Whitaker Foundation, and the Vanderbilt Institute for Integrative Biosystems Research and Education (VIIBRE).

Note

This Chapter has been submitted for publication in a modified form with the following list of authors: Andreas A. Werdich[1]; Eduardo A. Lima[1], Mark E. Anderson[2] and Franz J. Baudenbacher[1]

[1] Department of Biomedical Engineering, Vanderbilt University, Nashville, TN, USA

[2] Departments of Medicine and Physiology, Carver College of Medicine, University of Iowa, Iowa City, IA

CHAPTER V

DIFFERENTAIL EFFECTS OF PHOSPHOLAMBAN AND CAMKII ON CALCIUM UPTAKE AND RELEASE IN ISOLATED CARDIAC MYOCYTES AT PHYSIOLOGICAL PACING RATES

5.1 Abstract

Phospholamban (PLN) is a critical regulator of sarcoplasmic reticulum (SR) Ca^{2+} uptake and a known target of the multifunctional Ca^{2+} and calmodulin-dependent protein kinase II (CaMKII). CaMKII activity has been shown to hasten both SR Ca^{2+} uptake and release via phosphorylation of PLN and the SR Ca^{2+} release channel (RyR2) in a frequency-dependent manner. However, most studies in mice were performed at low frequencies and at room temperature using pharmacological CaMKII inhibitors.

We tested the role of PLN and CaMKII in the regulation of SR Ca^{2+} uptake and release in 500 isolated cardiac myocytes using transgenic mice expressing a CaMKII inhibitor in the presence and absence of PLN and at pacing frequencies ranging from 0.2 Hz to 10 Hz. In PLN deficient cardiac myocytes, Ca^{2+} uptake significantly shortened with pacing frequency but was not affected by chronic CaMKII inhibition. Ca^{2+} release increased with pacing frequency but was not affected by genetic CaMKII inhibition in the presence of PLN. However, PLN ablation alone and in combination with chronic CaMKII inhibition slowed Ca^{2+} release by 16+-7 % and 37+-10 %, respectively at 10 Hz. Our data provide novel insight into Ca^{2+} responses to chronic *in vivo* PLN gene deletion and CaMKII inhibition at physiological pacing rates.

5.2 Introduction

Calcium ions enter the cell via voltage-gated sarcolemmal Ca^{2+} channels during depolarization, triggering massive Ca^{2+} release from the sarcoplasmic reticulum (SR) into the intracellular space [41]. The increase in free intracellular calcium concentration ($[Ca^{2+}]_i$) initiates the contraction of the myofilaments. For relaxation to occur, most of the cytosolic calcium is transported back into the SR by the ATP driven calcium pump (SERCA2a). The rate at which SR Ca^{2+} uptake occurs is modulated by phospholamban (PLN), a 52-kDa SR protein which inhibits Ca^{2+} uptake into the intracellular stores in its unphosphorylated state. In vivo, phosphorylation of PLN by cAMP dependent protein kinase (PKA) and Ca^{2+}- calmodulin-dependent protein kinase (CaMKII) relieves this inhibition leading to a higher calcium pump activity [21, 22]. When the heart rate increases, an increase or decrease of the developed force (positive or negative force-frequency relationship) may occur paralleled by an acceleration of relaxation (frequency-dependent acceleration of relaxation, FDAR). While the force-frequency relationship can be either positive or negative, depending on many factors such as species, origin of the tissue, range of frequencies, temperatures or calcium concentration, the time course of contraction and relaxation is unanimously accelerated with increased pacing frequency and thus preserved across all preparations and species [124]. The frequency-dependent acceleration of relaxation (FDAR) is a purely SR related phenomenon, because it is abolished by inhibition of the SR Ca^{2+} uptake [32, 155, 156]. Phospholamban can be phosphorylated by CaMKII, which itself is active along the SR and *in vivo* known for affecting PLN [157], the L-type Ca^{2+} channel (LTCC) [158] and the cardiac Ca^{2+} release channel (RyR2) [159]. CaMKII phosphorylates PLN at Thr17, a site which is distinct

from the PKA phosphorylation site at Ser16. The frequency dependence of CaMKII activity was first discovered by De Konick and Schulman, who showed in an elegant *in vitro* experiment that CaMKII is capable of decoding the frequency of repetitive calcium spikes [160]. Others confirmed the hypothesis of a frequency-dependent activation of CaMKII activity in the heart showing that an increased pacing rate not only elevated the CaMKII activity in whole heart preparations [159], but specifically increased PLN Thr17 phosphorylation without altering the PKA-mediated Ser16 phosphorylation [33, 35, 37]. In contrast, pharmacological or genetic CaMKII inhibition reduced phospholamban Thr17 phosphorylation [48, 161, 162] and slowed SR Ca^{2+} uptake in isolated ferret [125] and rat [156] cardiac myocytes. FDAR was markedly reduced in mice expressing Thr17-Ala mutant PLN in a PLN null background [37]. The pharmacological CaMKII inhibitor KN-93 completely abolished FDAR in isolated mouse muscle and prevented the frequency-dependent shortening of the Ca^{2+} transient in isolated rat myocytes [123]. However, other reports clearly show that the role of CaMKII phosphorylation of PLN is still a controversy. In a recent study, Valverde *et al.* showed that FDAR occurred without a significant change in the phosphorylation state of PLN residues in the intact rat heart and in isolated cat papillary muscle preparations, and concluded that CaMKII phosphorylation pathways were not involved in FDAR [33]. Furthermore, the force-frequency relationship was flat and FDAR was absent in papillary muscles isolated from PLN null mice [36]. Other studies showed that the frequency-dependent acceleration of SR Ca^{2+} uptake was still present in PLN null myocytes, but could be prevented by adding KN-93 to the medium in these cells [52, 123]. As a consequence, a phospholamban independent mechanism of FDAR was suggested via direct SERCA2a phosphorylation

[163, 164], but this hypothesis was strongly challenged by other reports that refused this possibility [165, 166]. CaMKII may also play a role in the regulation of the cardiac SR Ca^{2+} release channel (RyR2). CaMKII phosphorylation of RyR2 at the CaMKII specific site (Ser2815) increased the open probability of the isolated channel [167, 168] and increased SR Ca^{2+} release in intact cardiac myocytes [125, 169, 170]. RyR2 phosphorylation was increased after pacing, suggesting a frequency-dependent regulation of SR Ca^{2+} release in the heart [159]. However, the effect of CaMKII on the RyR2 is controversial because other studies showed that CaMKII activity may decrease the open probability of the RyR2 [171, 172]. The interpretation of previously published studies on the frequency dependence of Ca^{2+} uptake and cardiac muscle relaxation may be complicated by the different experimental conditions and unspecific side effects of pharmacological CaMKII inhibitors. Most studies in mice were performed at room temperature and at maximum pacing rates ranging from 2 to 5 Hz, while the physiologic heart rate of mice is in the range of 10 to 12Hz. Because calcium transients are short in mouse myocytes, intracellular $[Ca^{2+}]_i$ levels and CaMKII activity are expected to rise significantly with increasing pacing frequency [160]. Furthermore, pharmacologic CaMKII inhibitors, such as KN-93, KN63 or W-7 are known to have unspecific side effects on cardiac ion channels [173, 174]. Clearly, the current literature shows that the role of CaMKII in the frequency-dependent regulation of calcium uptake and release is not resolved. The goal of this study was to determine whether CaMKII activity or the presence of phospholamban is required for the frequency-dependent acceleration of Ca^{2+} uptake at physiological pacing frequencies and temperatures. Furthermore, we investigated the effects of CaMKII activity on the time course of the intracellular Ca^{2+}

release in the presence and absence of PLN. We used a previously published model of chronic cardiac CaMKII inhibition by cardiomyocyte delimited expression of a specific CaMKII inhibitory peptide (AC3-I) that targets a conserved region of the CaMKII regulatory domain as well as a transgenic control mouse expressing an inactive scrambled version of the peptide (AC3-C) [162, 175]. Transgenic AC3-I and AC3-C mice were interbred with PLN-/- mice to eliminate PLN-dependent CaMKII contributions to the SR Ca^{2+} uptake and release.

5.3 Methods

Mice with genetic CaMKII inhibition

The AC3-I and AC3-C mice were generated by synthesis of a minigene based on the peptide sequence of AC3-I (KKALHRQEAVDCL) or AC3-C (KKALHAQERVDCL) [176] and was described earlier [162]. Both AC3-I and AC3-C were fused to enhanced green fluorescence protein (eGFP) for stabilization and to label the cellular tissue distribution for the transgenically expressed proteins.
PLN null mice [177] were interbred with AC3-I and AC3-C mice for > 4 generations and the genetic identity of PLN-/- pubs with transgenic expressing of AC3-I or AC3-C was confirmed using PCR [162]. There was no evidence of cellular hypertrophy in isolated ventricular myocytes, based upon equivalent cell membrane capacitance measurements. We isolated single cells from 3 to 5 months old male and female mice (about half of the cells originated from female mice). Wild-type (WT), AC3-C, AC3-C x PLN-/- and PLN-/- littermates served correspondingly as controls.

Isolation of ventricular cardiac myocytes

Animals were cared for according to PHS Guide for the Care and Use of Laboratory Animals. All animal protocols were approved by the Institutional Animal Care and Use Committee, IACUC at Vanderbilt University. Mice were anesthetized by intraperitoneal injection of a 25 mg/ml Avertin solution (5 mg Avertin per 10 g body weight, T48402, Sigma-Aldrich) containing 3 mg/10ml Heparin (H9399, Sigma-Aldrich). The heart was rapidly excised and placed into ice-cold Ca^{2+}-free Hepes-buffered Tyrode solution (NT). The aorta was cannulated and the heart was perfused retrograde with Ca^{2+}-free NT solution at room temperature for 10 min to stop contractions. The NT solution contained (in mM): Na^+ 140, K^+ 4.5, Mg^{2+} 0.5., Cl^- 150, $H_2PO_4^-$ 0.4, HCO_3^- 10, Hepes 10. Calcium was added when specified. The perfusion was switched to NT solution containing 10 μM Ca^{2+}, 178 U/ml collagenase (CLS2, Worthington Biochemical) and 0.64 U/ml protease (P5147, Sigma-Aldrich) for 8 to 10 minutes at 37 ºC. Ventricles and septum were cut away, coarsely minced, and placed into Ca^{2+} -free Tyrode solution containing 0.5 % BSA at room temperature. Myocytes were dispersed by gentle agitation and Ca^{2+} concentration was gradually increased within 30 min from 0 mM to 0.5 mM to obtain calcium tolerant cardiac myocytes. Cells were stored in the BSA solution until used. All experiments were performed within the first three hours after isolation.

Measurement of x-rhod-1 calcium transients

We measured absorption spectra of AC3-I and AC3-C cells and found intense autofluorescence peaks in the wavelength range of 350 to 380 nm, likely originating from the AC3-I – EGFP construct. Therefore, the ratiometric dye fura-2 was not suitable for

this study. We considered other ratiometric dyes and found that the fluorescence of the red-shifted version of fura-2, fura-red, was contaminated by the AC3-I – EGFP protein as well [178]. The ratiometric-emission dye indo-1 was compatible with EGFP, but showed a poor signal-to-noise ratio (S/N) due to the wavelength separation of the fluorescence intensity [110, 111]. We decided to use the single wavelength dye X-Rhod-1 for this study (4 μM, X14210, Molecular Probes-Invitrogen) which displayed a good separation of both excitation and emission wavelength from that of the AC3-I – EGFP protein and a very bright fluorescence resulting in a good S/N ratio [179]. For every cell, AC3-I or AC3-C expression was confirmed by green fluorescence after the acquisition of the Ca^{2+} transient. The dye was purchased in 50 μg aliquots. For each experiment 25 μg dye in 20 μl DMSO (276855, Sigma-Aldrich) was added to 5 ml of cell suspension.

Cells were kept in the staining solution for 5 min at room temperature and then centrifuged at 27 g for 10 min. The supernatant was removed and the cells re-suspended in NT solution containing 1.0 mM $CaCl_2$.The bath solution was kept at 37 ºC and contained NT solution with 1.0 mM $CaCl_2$, supplemented with 10 μg/ml insulin, 5.5 μg/ml transferring and 6.7 ng/ml sodium selenite (100X medium supplement, 41400, Gibco-Invitrogen).

The medium supplement had previously been shown to benefit mouse myocyte cultures by promoting glucose uptake and monovalent cation and phosphate transport and allowed prolonged high-speed stimulation in the serum free bath solution. Myocytes were stimulated by two parallel platinum wires connected to a field stimulator (701B, Aurora Scientific, Inc.) at six different rates of 0.2; 1; 2; 4; 8 and 10 Hz.

Table 1. Number n of cells (animals) used in the study that involved 6 genotypes and 6 different stimulation frequencies. For each cell, only one fluorescence measurement was taken to minimize phototoxic effects. About half of the cells in each group were isolated from male, the other half from female animals.

F Hz	*AC3-I*	*AC3-C*	*WT*	*AC3-I xPLN*	*AC3-C xPLN*	*PLN*	*Σ*
0.2	24(4)	12(2)	23(3)	9(2)	13(3)	20(2)	101
1	9(2)	8(2)	20(3)	8(2)	9(3)	16(2)	70
2	7(2)	9(2)	20(4)	9(2)	12(3)	13(3)	70
4	10(4)	12(2)	18(3)	8(2)	14(3)	12(3)	74
8	22(5)	11(2)	27(4)	8(2)	17(4)	15(3)	100
10	9(3)	14(2)	22(4)	9(2)	13(4)	13(3)	80
Σ	81	66	130	51	78	89	495

Cells were stimulated for at least 60 contractions until they reached steady state. Multiple exposures were avoided in order to minimize phototoxic effects. This was accomplished by replacing the entire bath solution with cells after each exposure. The data presented in this study was taken from 495 cells. The number of cells and the number of animals are shown for each frequency and genotype in Table 1.

Microscope configuration

Fluorescence measurements were carried out using an inverted microscope (Axiovert 200, Carl Zeiss, Germany) equipped with a 63X, 1.4 NA oil immersion lens (Plan Apochromat, Carl Zeiss, Germany). The dye was excited by a monochromator (Optoscan, Cairn Research Ltd, UK) at a wavelength of 560 ± 15 nm. The fluorescence emission was directed through a 595 nm dichroic mirror (XF2029, Omega Optical Inc.), a 645 ± 37 nm emission filter (XF3081, Omega) and a 1 mm diameter optical fiber to a photomultiplier module (H6780, Hamamatsu).

The signals were amplified by a high-bandwidth, custom built amplifier and digitized at a sampling rate of 20 KHz by an A/D converter board (PCI-6071E, National Instruments) using a PC. EGFP expression was confirmed by visual control of the green fluorescence using a standard EGFP filter set (XF104-2, Omega).

Data analysis and statistics

Data were processed using Matlab (R14, The MathWorks, Inc.). Background and autofluorescence were subtracted from the Ca^{2+} transients and the time course of the normalized x-rhod-1 fluorescence emission was used as a measure of the time course of intracellular $[Ca^{2+}]_i$ concentration.

Although single wavelength dye calibration is described in the literature, its reliability and reproducibility is highly questionable. The total fluorescence amplitude measured at a single wavelength depends on many parameters which are difficult to control over long periods of time involving hundreds of experiments (e.g. dye distribution, excitation intensity, extinction coefficient, optical path length and detector sensitivity).

Therefore, frequency-dependent changes in the time course of the Ca^{2+} transients were analyzed using normalized fluorescence transients. Ca^{2+} transients were fit to mathematical models for the purpose of calculating time derivatives. Calcium release was best fit by a modified model of RyR activation which was previously published [121]: $[Ca^{2+}]_i(t)=[P(t)/(1-P(t))]^n$, where t is time, and P(t) is the time-dependence of the Ca^{2+} release described by $P(t) = 0.5\cdot(1-e^{-t/\tau})^m$.

The parameters τ, n and m were used as fit parameters. Calcium uptake was best fit by a

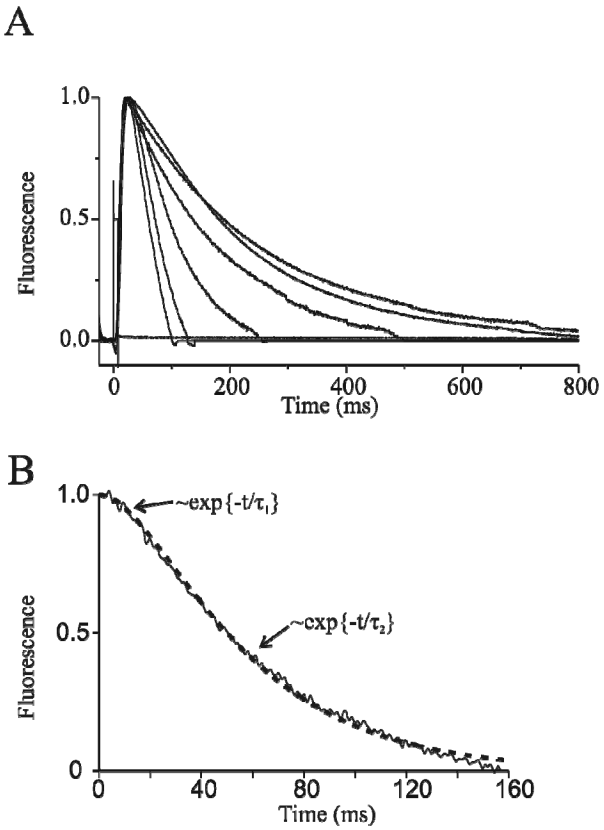

Figure 21. Analysis of x-rhod-1 Ca^{2+} transients. A, average X-Rhod-1 fluorescence transients from WT myocytes at frequencies of 0.2, 1 ,2 ,4 ,8 and 10 Hz showing the frequency-dependent shortening of the transients. B, representative dual exponential fit (dotted line) to the Ca^{2+} uptake (solid line) for a cell paced at 8 Hz.

sum of two exponential functions, $[Ca^{2+}]_i = Ae^{-t/\tau 1} + Be^{-t/\tau 2}$, where A, B, τ_1 and τ_2 were used as fit parameters. For statistical comparison 2-tailed t-tests or ANOVA with correction for multiple comparisons were used. Unless otherwise noted, data is expressed as mean ± standard error. Significance level was set at $p < 0.05$.

5.4 Results

Chronic CaMKII inhibition and PLN ablation did not prevent the frequency-dependent shortening of the time constant of the SR Ca^{2+} uptake

Cytosolic Ca^{2+} transients were measured in field stimulated cells paced from 0.2 to 10 Hz. Shortening of the transients occurred with increasing pacing frequencies as shown in Figure 21A for WT cardiac myocytes. Two time constants, τ_1 and τ_2, were used to fit to the tail of each transient as described in the methods section. A representative fit for a cell paced at 8 Hz is shown in Figure 21B. One time constant was consistently smaller than the other contributing less than 1 % to the total transient 50 ms after the peak of the transient. The value of the larger time constant, however, was consistently on the order of the duration of the transient and was therefore used to quantify the fluorescence decay.

The frequency dependence of the second time constant is shown in Figure 22A for AC3-I, AC3-C and WT cells. With the increase in pacing frequency from 0.2 Hz to 10 Hz, significant shortening of the Ca^{2+} time constant occurred in the AC3-I (170 ± 28 ms at 0.2 Hz vs. 18.96 ± 0.69 ms at 10 Hz), AC3-C (222 ± 23 ms at 0.2 Hz vs. 18.25 ± 0.34 ms at 10 Hz) and in the WT myocytes (174 ± 15 ms at 0.2 Hz vs. 18.78 ± 0.37 ms at 10 Hz) and is shown in Figure 22A and C. The mean values of the time constant were

consistently smaller in the AC3-I compared to the AC3-C or WT myocytes, but the differences were not significant for most frequencies.

PLN deficiency reduced the time constant of the Ca^{2+} uptake at all frequencies due to the higher Ca^{2+} pump activity, but our data still show a frequency-dependent shortening, as

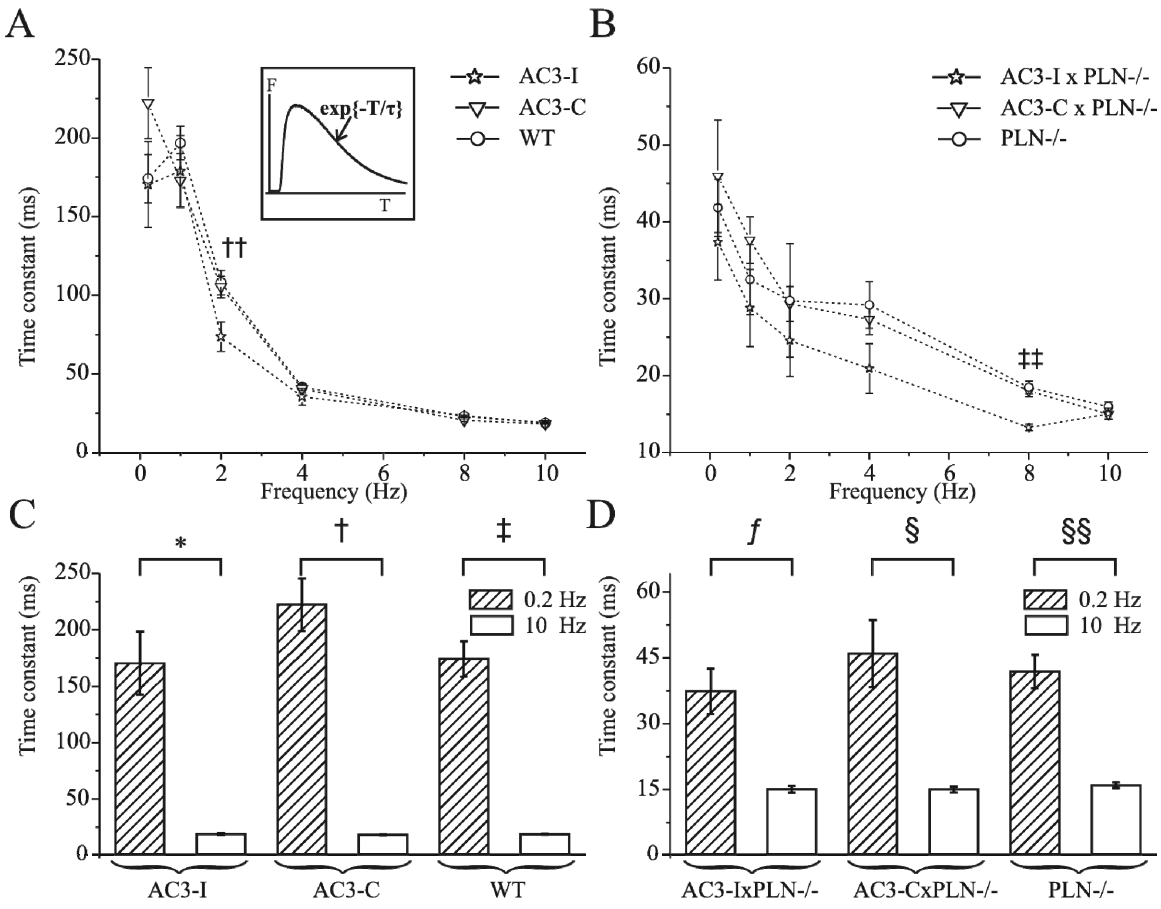

Figure 22. Frequency-dependent decrease of the time constant of the Ca^{2+} uptake after exponential fit. A, time constant for AC3-I, AC3-C and WT myocytes as a function of pacing frequency. ††: $p<0.05$. B, Ca^{2+} uptake time constant for AC3-I x PLN-/-, AC3-C x PLN-/- and PLN-/- myocytes. ‡‡: $p<0.005$. C,D, statistical comparison between 0.2 Hz and 10Hz. *,†,‡,*f*,§,§§: $p<0.001$.

indicated by Figure 22B and D. In the absence of PLN, significant shortening of the time constant occurred with increasing pacing frequencies in AC3-I x PLN-/- (37.3 ± 5.2 ms at 0.2 Hz vs. 15.05 ± 0.75 ms at 10 Hz), AC3-C x PLN-/- (45.9 ± 7.7 ms at 0.2 Hz vs. 14.99 ± 0.66 ms at 10 Hz), and in PLN-/- (41.8 ± 3.8 ms at 0.2 Hz vs. 15.99 ± 0.67 ms at 10 Hz) myocytes. Similar as in the presence of PLN, mean values of the Ca^{2+} uptake time constant were slightly shorter in the AC3-I x PLN-/- cells, but the difference was not significant for most frequencies.

Chronic CaMKII inhibition and PLN ablation did not prevent the frequency-dependent shortening of the Ca^{2+} transient

As a second criterion for the frequency-dependent shortening of the Ca^{2+} transients, we measured the fluorescence decay time from 90 % to 20 % of the maximum.
With an increase in pacing frequency, Ca^{2+} transients shortened (Figure 21A). Similar to the time constant, the duration of calcium uptake decreased significantly with increasing pacing frequency in the AC3-I cells (269 ± 41 ms at 0.2 Hz vs. 45.3 ± 1.6 ms at 10 Hz), AC3-C (351 ± 31 ms at 0.2Hz vs. 43.5 ± 1.2 ms), and in the WT (281 ± 21 ms at 0.2Hz vs. 46.5 ± 1.1 ms at 10Hz) myocytes as shown in Figure 23A and C. Mean values of the Ca^{2+} uptake duration were slightly smaller in the AC3-I than in the AC3-C or WT cells, but the difference was not significant at most frequencies.

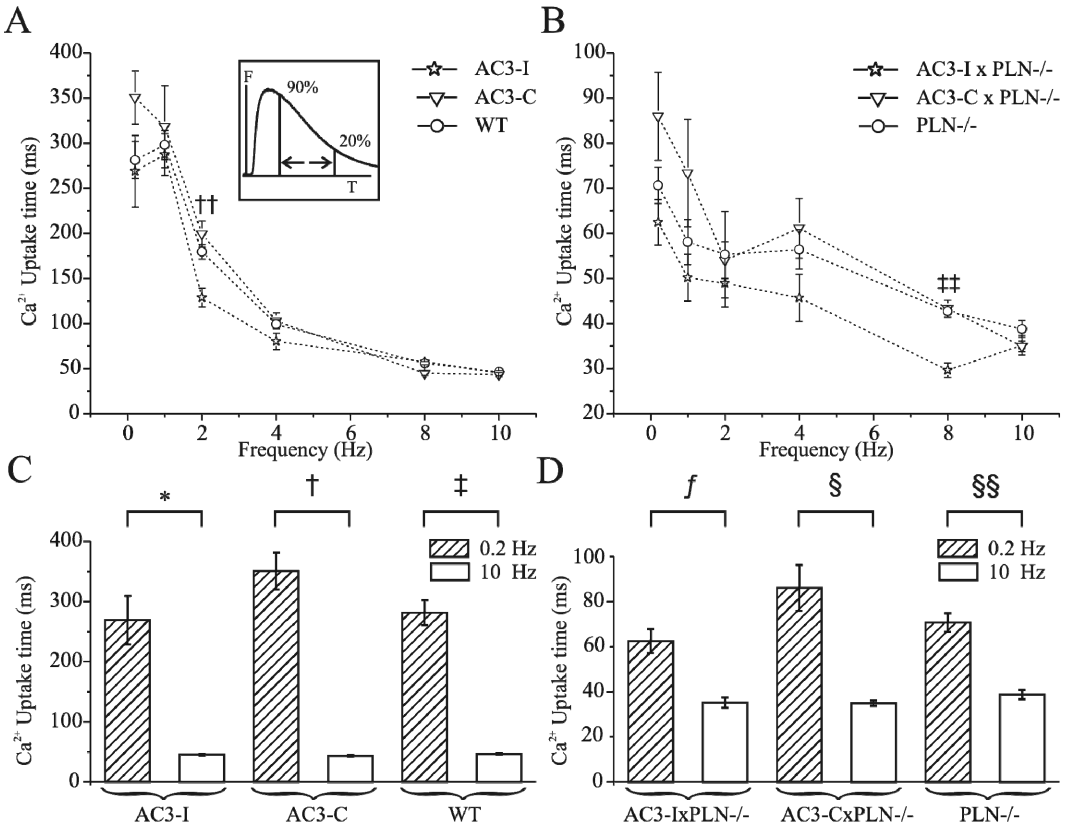

Figure 23. Frequency-dependent shortening of the SR Ca^{2+} uptake duration as measured by the fluorescence decay duration from 90 % to 20 % of maximum. A, duration of Ca^{2+} uptake for AC3-I, AC3-C and WT myocytes. ††: $p<0.005$. B, duration of the Ca^{2+} uptake for AC3-I x PLN-/-, AC3-C x PLN-/- and PLN-/- myocytes. ‡‡: $p < 0.001$. C,D, statistical analysis for 0.2 Hz and 10 Hz. *,†,‡,*f*,§,§§:$p<0.001$

PLN ablation generally increased the rate of SR Ca^{2+} uptake leading to a shorter decay phase during the transient at all frequencies and for all mouse models as indicated by Figure 23B. However, consistent with the measurement of the Ca^{2+} uptake time constant, phospholamban ablation did not abolish the frequency-dependent shortening of the transient as presented in Figure 23B and D because the duration of Ca^{2+} uptake was

significantly decreased at higher pacing frequencies in the AC3-I x PLN-/- (62.5 ± 5.4 ms at 0.2 Hz vs. 35.2 ± 5.3 ms at 10 Hz), AC3-C x PLN-/- (86 ± 10 ms at 0.2 Hz vs. 34.9 ± 1.2 ms at 10 Hz) and in the PLN-/- (70.7 ± 4.1 ms at 0.2 Hz vs. 38.8 ± 2.0 ms at 10 Hz) myocytes.

Mean values of Ca^{2+} uptake duration were consistently smaller in the AC3-I x PLN-/- compared to the AC3-C x PLN-/- cells, but the difference was not significant for most frequencies.

Chronic CaMKII inhibition and PLN deficiency did not prevent the frequency-dependent increase in the Ca^{2+} uptake rate

The maximum Ca^{2+} uptake rate (Vmax) was defined as the maximum time-derivative of the falling phase of the Ca^{2+} transient and increased approximately linear with pacing frequency in AC3-I, AC3-C and WT myocytes as shown in Figure 24A.

With an increase in pacing frequency, Vmax (in 100 ms^{-1}) increased significantly in the AC3-I (0.648 ± 0.082 at 0.2 Hz vs. 1.964 ± 0.081 at 10 Hz, $p<0.001$), AC3-C (0.325 ± 0.024 at 0.2 Hz vs. 2.025 ± 0.039 at 10 Hz, $p<0.001$) and in the WT (0.436 ± 0.020 at 0.2 Hz vs. 1.974 ± 0.041 at 10 Hz, $p<0.001$) cardiac myocytes as presented in Figure 24A and C. Maximum Ca^{2+} uptake rates were higher in cells expressing the CaMKII inhibitor, and the differences were significant at 0.2, 2, and 4 Hz. In the absence of PLN, Ca^{2+} uptake rates were higher, and the frequency dependence was reduced, but interestingly, the frequency-dependent increase in Vmax was still significant over the full range of frequencies. Vmax (in 100 ms^{-1}) increased with increasing pacing frequencies in the AC3-I x PLN-/- (1.70 ± 0.11 at 0.2 Hz vs. 2.50 ± 0.13 at 10 Hz), AC3-C x PLN-/- (1.134 ± 0.097 at 0.2 Hz vs. 2.608 ± 0.096 at 10 Hz) and in the PLN-/- (1.435 ± 0.043 at 0.2 Hz-

vs. 2.35 ± 0.11 at 10 Hz) cardiac myocytes as presented in Figure 24D. Similar to Figure 24A, Ca^{2+} release was significantly faster at several pacing frequencies, i.e. 0.2, 1, and 8 Hz, in the AC3-I x PLN-/- cells compared to the control cells, AC3-C x PLN-/- and PLN-/-.

To show that the frequency dependence of Vmax was reduced by phospholamban ablation, we fitted the Vmax-frequency relationship to linear functions, and calculated the slopes of the Vmax-frequency relationships as shown in Figure 24E and F. In PLN deficient cells the slopes of the Vmax-frequency relationships were all positive and smaller than in cells in which PLN was present. The frequency dependence of Vmax was reduced in the AC3-I vs. AC3-I x PLN-/- cells (1.500 ± 0.058 vs. 1.00 ± 0.12), in the AC3-C vs. AC3-C x PLN-/- cells (1.766 ± 0.042 vs. 1.32 ± 0.12), and in the WT vs. PLN-/- cells (1.599 ± 0.040 vs. 0.863 ± 0.078).

Combined chronic CaMKII inhibition and PLN ablation prevented early activation of Ca^{2+} uptake at increasing pacing frequencies.

We determined the time to maximum SR Ca^{2+} pump activation by measuring the time from the peak fluorescence to the time at which Vmax was reached. When the pacing frequency was increased, the Ca^{2+} pump activated earlier resulting in a shorter time-to-Vmax as shown in Figure 25A.

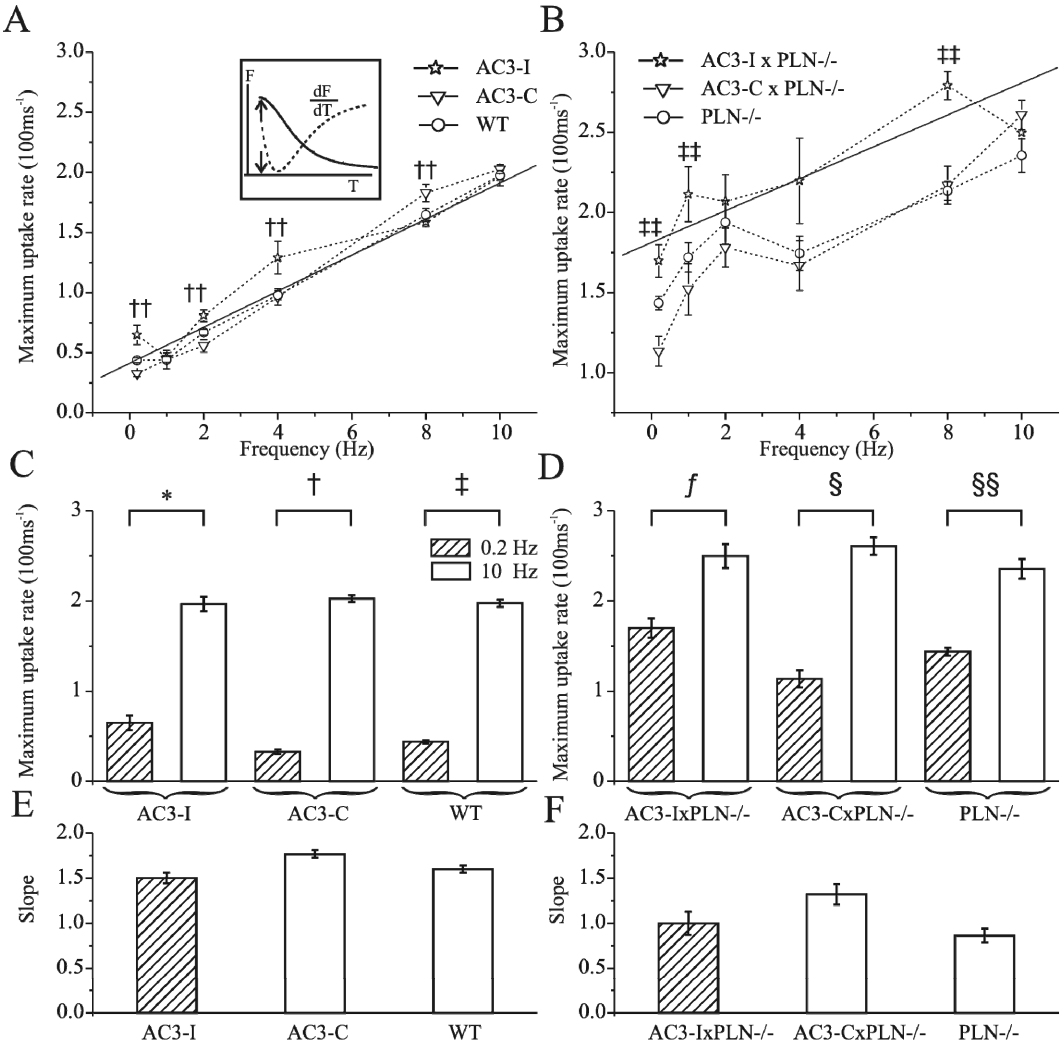

Figure 24. Frequency-dependent increase of the maximum SR Ca^{2+} uptake rate as measured by the maximum time derivative of the tail of the transient. A, maximum Ca^{2+} uptake rate for AC3-I, AC3-C and WT myocytes and linear fit of the AC3-I data (line). ††: $p<0.05$. B, maximum Ca^{2+} uptake rate for AC3-I x PLN-/-, AC3-C x PLN-/- and PLN-/- myocytes and linear fit of the AC3-I x PLN-/- data (line). ‡‡: $p<0.01$. C,D statistical comparison between 0.2Hz and 10Hz. *,†,‡,*f*,§,§§:$p<0.001$. E,F slopes of the linear functions fitted to the frequency dependence as demonstrated in A,B.

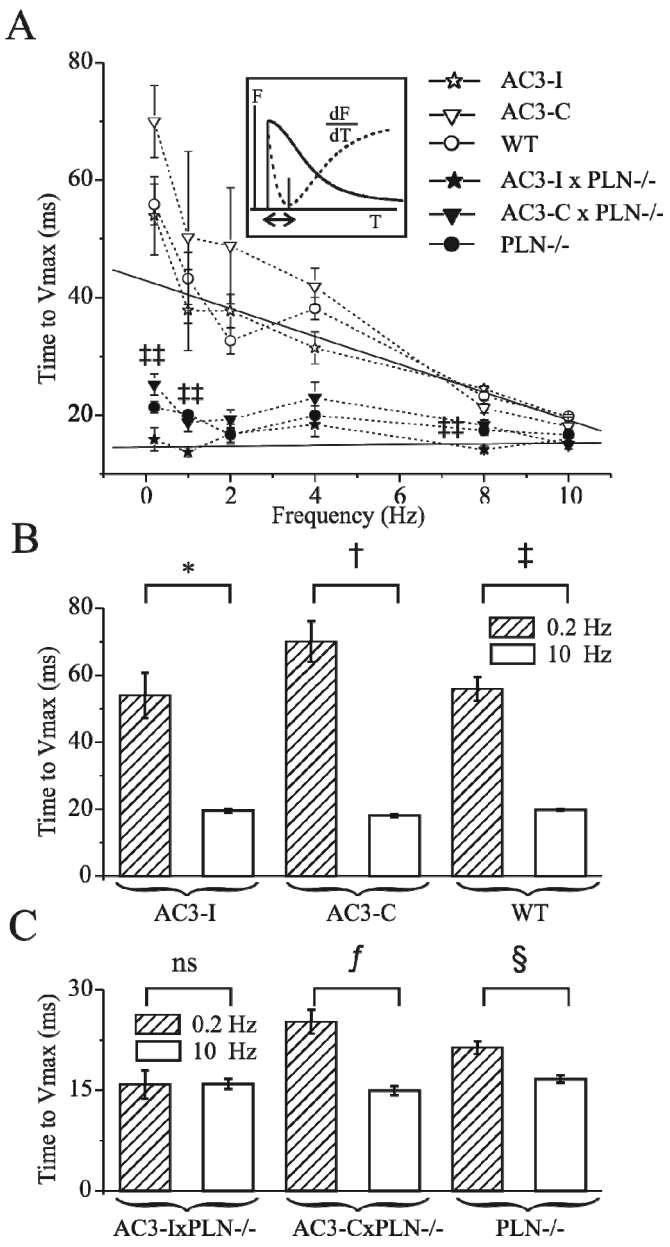

Figure 25. Frequency-dependent shift of Vmax from the time of peak release. A, time to Vmax for AC3-I, AC3-C and WT myocytes (open symbols) and for AC3-I x PLN-/-, AC3-C x PLN-/- and PLN-/- myocytes (filled symbols). Linear fits to the data of the AC3-I data (top line) and the AC3-I x PLN-/- data (bottom line). ‡‡: $p<0.05$. B,C Statistical comparison between 0.2 Hz and 10 Hz. *,†,‡,*f*,§:$p < 0.005$.

Time-to-Vmax shortened significantly in the AC3-I (53.9 ± 6.8 ms at 0.2 Hz vs. 19.54 ± 0.51 ms at 10 Hz), AC3-C (70.0 ± 6.1 ms at 0.2 Hz vs. 18.09 ± 0.47 ms) and in the WT (55.8 ± 3.6 ms at 0.2 Hz vs. 19.80 ± 0.26 ms at 10 Hz) myocytes.

There was no significant difference in the frequency dependence of the time-to-Vmax between AC3-I, AC3-C and WT myocytes.

PLN gene deletion dramatically reduced the frequency dependence of the time-to-maximum Ca^{2+} pump activation, but did not abolish it in the AC3-C x PLN-/- and in the PLN-/- myocytes as these cells showed a significant earlier activation during the transient at 10 Hz compared to 0.2 Hz as shown in Figure 25C.

Time-to-Vmax decreased significantly in the AC3-C x PLN-/- (25.2 ± 1.8ms at 0.2Hz vs. 14.95 ± 0.70 ms at 10 Hz) and in the PLN-/- (21.35 ± 0.97 ms at 0.2 Hz vs. 16.67 ± 0.57 ms at 10 Hz) myocytes. The combination of CaMKII inhibition and PLN deficiency in the AC3-I x PLN-/- cells completely abolished the frequency dependence of the time-to-Vmax as evidenced by the mean values of this parameter at the smallest and highest frequencies (15.9 ± 2.1 ms at 0.2 Hz vs. 15.94 ± 0.77 ms at 10 Hz) and by the slope of the linear fit to the time to Vmax – frequency relationship drawn in Figure 25A, which was 0.07 ± 0.11 ms/Hz in the AC3-I x PLN-/- myocytes. At all frequencies, time-to-Vmax was slightly shorter in AC3-I x PLN-/- than in the AC3-C x PLN-/- or PLN-/- cells, although the difference was significant only at 0.2, 1 and 8 Hz.

Chronic CaMKII inhibition increased the duration of the Ca^{2+} release in cardiac myocytes lacking PLN.

We investigated the influence of pacing frequency on the time course of the intracellular calcium release by measuring the time-to-maximum from 10 % to 90 % of the peak

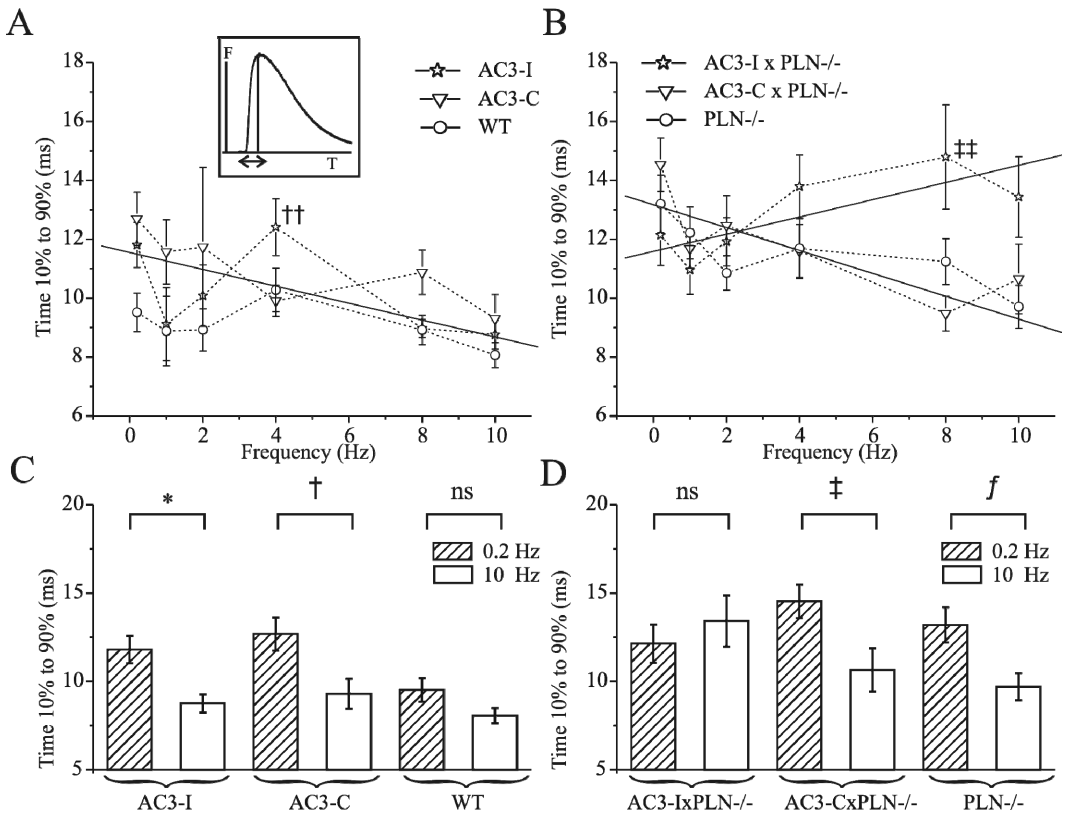

Figure 26. Frequency-dependent acceleration of RyR2 activation as measure by the time from 10 % to 90 % of peak release. A, RyR2 activation time for AC3-I, AC3-C and WT myocytes. ††: $p<0.05$. B, RyR2 activation time for AC3-I x PLN-/-, AC3-C x PLN-/- and PLN-/- myocytes. ‡‡: $p < 0.001$. C,D statistical analysis for 0.2Hz and 10Hz. *,†,‡,*f*:$p < 0.05$.

fluorescence. Although the frequency dependence of the SR Ca^{2+} release was smaller than 0.5ms/Hz, the differences between 0.2 and 10 Hz were still significant in some cases. Figure 26A shows that time-to-maximum Ca^{2+} release was slightly smaller at higher pacing frequencies in the AC3-I (11.80 ± 0.78 ms at 0.2 Hz vs. 8.76 ± 0.52 ms at 10 Hz) and in the AC3-C (12.68 ± 0.95 ms at 0.2 Hz vs. 9.31 ± 0.84 ms at 10 Hz) cells. In the WT myocytes the mean value of the time-to-maximum release was also reduced at

the maximum frequency (9.52 ± 0.67 ms at 0.2 Hz vs. 8.07 ± 0.43 ms at 10 Hz), but the difference was not significant, showing that CaMKII may not significantly influence the Ca^{2+} release dynamics in these cells. Consistently, there was no significant difference across all frequencies in the time-to-maximum between AC3-I, AC3-C and WT myocytes. In the absence of PLN, calcium release was faster at higher frequencies in the AC3-C x PLN-/- (14.53 ± 0.95 ms at 0.2 Hz vs. 10.6 ± 1.2 ms at 10 Hz, $p < 0.05$) and in the PLN-/- myocytes (13.20 ± 1.00 ms at 0.2 Hz vs. 9.70 ± 0.76 ms at 10 Hz, $p < 0.05$). However, in the myocytes with combined chronic CaMKII inhibition and PLN deficiency, Ca^{2+} release was slowed, i.e. in the AC3-I x PLN-/- cells, time-to-maximum was 12.1 ± 1.1 ms at 0.2 Hz and 13.4 ± 1.5 ms at 10 Hz, but the difference was not significant.

The tendency of AC3-I in the PLN-/- cells to slow Ca^{2+} release at higher frequencies was further emphasized by the positive slope of the linear fit to the time-to-maximum – frequency relationship in the AC3-I x PLN-/- myocytes (0.29 ± 0.14 ms/Hz), while the slope was negative in the AC3-C x PLN-/- and the PLN-/- myocytes (-0.39 ± 0.09 ms/Hz and -0.20 ± 0.09 ms/Hz, respectively).

Chronic CaMKII inhibition slowed Ca^{2+} release in cardiac myocytes lacking PLN

We measured the maximum time derivative of the rising phase of the Ca^{2+} transient as a second criterion to characterize the frequency dependence of the time course of the Ca^{2+} release and the results are shown in Figure 27. The maximum Ca^{2+} release rate (in 100 ms^{-1}) slightly increased when the pacing rate was raised from 0.2Hz to 10 Hz in the AC3-I (10.47 ± 0.64 at 0.2Hz vs. 13.27 ± 0.73 at 10Hz) and AC3-C (9.71 ± 0.98 at 0.2Hz vs.

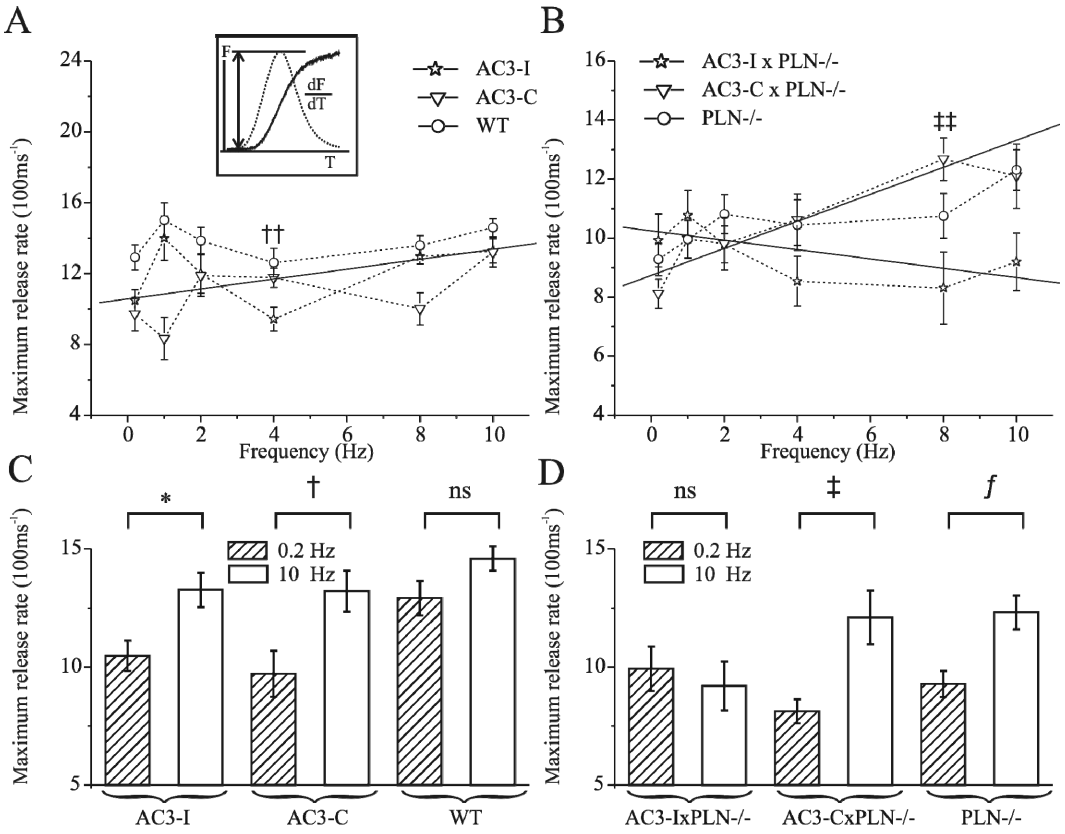

Figure 27. Frequency-dependent increase of the maximum Ca^{2+} release rate. A, maximum release rate for AC3-I, AC3-C and WT myocytes. Linear fit to the AC3-I data. ††: $p < 0.005$. B, maximum release rate for AC3-I x PLN-/-, AC3-C x PLN-/- and PLN-/- myocytes. Linear fit to the AC3-I x PLN-/- data (line, positive slope) and AC3-C x PLN-/- data (line, negative slope). ‡‡: $p < 0.005$ C, D Statistical comparison between 0.2Hz and 10Hz. *,†,‡,*f*,§:$p < 0.005$.

13.21 ± 0.87) cells (Figure 27A). It was also increased in the WT cardiac myocytes (12.91 ± 0.73 at 0.2Hz vs. 14.60 ± 0.52 at 10Hz), but the difference was not significant ($p = 0.07$). There was no significant difference in the maximum Ca^{2+} release rate between AC3-I, AC3-C and WT myocytes across all frequencies. In the phospholamban deficient

cardiac myocytes, however, the maximum Ca^{2+} release rate showed the tendency to increase with pacing frequency in the AC3-C x PLN-/- (8.12 ± 0.51 at 0.2 Hz vs. 12.1 ± 1.1 at 10 Hz) and in the PLN-/- (9.28 ± 0.56 at 0.2 Hz vs. 12.31 ± 0.72 at 10 Hz) myocytes, and decrease in the AC3-I x PLN-/- myocytes (9.92 ± 0.94 at 0.2 Hz vs. 9.2 ± 1.0 at 10 Hz) although the latter difference was not significant (Figure 27B and D). Therefore, the combination of chronic CaMKII inhibition and PLN deficiency significantly reduced the frequency dependence of the Ca^{2+} release. Consistently, a linear fit to the maximum Ca^{2+} release rate – frequency relationship revealed a slightly negative slope for the AC3-I x PLN-/- of -1.6 ± 1.1 s^{-1}/Hz and a clearly positive slope for the AC3-C x PLN-/- and PLN-/- myocytes of 4.6 ± 0.9 s^{-1}/Hz and 2.3 ± 0.7 s^{-1}/Hz, respectively. This result was consistent with the time-to-maximum measurement, suggesting that Ca^{2+} release was slowed in the AC3-I x PLN-/- myocytes with increasing pacing frequency.

5.5 Discussion

Ca^{2+}/Calmodulin dependent protein kinase II has been implicated to play a role in the frequency-dependent shortening of the Ca^{2+} transient in mouse, rat and ferret ventricular myocytes [123, 125, 156] leading to the frequency-dependent acceleration of relaxation. FDAR was suggested to originate from the frequency-dependent phosphorylation of phospholamban and therefore to rely on both CaMKII and phospholamban. Most published experiments were performed under non physiological conditions, i.e. low temperatures and low pacing rates and often used pharmacological inhibitors e.g. KN-93 or KN-63 which are known for their unspecific side effects. The distinctive nature of the physiological pacing rate (on the order of 600-700 bpm in the mouse heart) is appreciated by our measurements of the Ca^{2+} uptake presented in Figure

22 to Figure 25. Although the mean values of the time constant, duration of the Ca^{2+} uptake, maximum uptake rate and early activation of the Ca^{2+} uptake varied considerably in the low frequency range among the various cell types, they clearly converged at the physiological pacing rate of 10 Hz. In fact, considering the results at the maximum pacing frequency of 10Hz alone, neither of the quantification methods describing the Ca^{2+} uptake experiments showed a significant difference between the expression of the inhibitory peptide AC3-I or the control peptide AC3-C despite the prominent and well documented differences in baseline PLN phosphorylation [162, 180].

Chronic CaMKII inhibition and phospholamban ablation do not eliminate the frequency-dependent shortening of the Ca^{2+} transient.

The equivalence of characterizing the shortening of the Ca^{2+} transient by either fitting the data to an exponential decay with a characteristic time constant or by calculating the duration of the fluorescence decay is supported by the consistency of the results presented in Figure 22 and Figure 23. These figures clearly show that chronic CaMKII inhibition did not change the frequency-dependent acceleration of the Ca^{2+} uptake. This observation is consistent with earlier reports that showed that calmodulin blockade by W7 in isolated rat myocytes or more specific CaMKII inhibition by KN-93 and KN-62 or even collective PKA, PKC, PKG and CaMKII inhibition by K252-a did not affect the frequency dependence of muscle relaxation and Ca^{2+} uptake in single cells [181, 182]. However, our findings appear to contradict those of Bassani [156] *et al.* and Li *et al*. [125] who reported that rate-dependent acceleration of $[Ca^{2+}]_i$ transient duration in rat cardiac myocytes was mediated by CaMKII by comparing steady-state with post-rest twitches. The discrepancies might be related to the different experimental protocols.

Comparing the rate of relaxation during steady-state twitches with that of post-rest twitches following periods of rest may not be equivalent to examining the steady-state properties at a number of different frequencies as in our study. We tested the hypothesis that phospholamban is a major determinant of the frequency dependence of the Ca^{2+} uptake by using PLN deficient cells. We found that PLN ablation did not inhibit the frequency adaptation of the Ca^{2+} uptake, although significantly hastening the decay of $[Ca^{2+}]_i$ as expected based on the inhibitory action of PLN on SERCA2a. Nevertheless, PLN deficiency caused a 70 % reduction in the dynamic range of the time constant at all frequencies. Therefore, phospholamban is a major contributor to the frequency dependence of the Ca^{2+} uptake but not the only regulatory mechanism. This result is consistent with other studies in isolated myocytes and muscle preparations from phospholamban knockout mice [52, 123] showing significant slowing of the Ca^{2+} and force transients with decreasing frequencies and after rest. However, the increased Ca^{2+} uptake rate in the absence of phospholamban seems to contradict the study from Bluhm *et al*. [36] who reported complete loss of FDAR and a negative force-frequency relationship in isolated mouse papillary muscles after phospholamban ablation. However, the small frequency interval of 2 to 6 Hz in their PLN null preparations might have hampered the observation of a prominent frequency adaptation. It has been argued that the frequency-dependent shortening of the Ca^{2+} transient in PLN-/- myocytes may result from CaMKII phosphorylation of the SR Ca^{2+} pump because KN-93 prevented the shortening of the Ca^{2+} uptake time constant at higher frequencies in PLN null myocytes [52, 123]. Our results demonstrate that in PLN deficient myocytes the ability to shorten

SR Ca^{2+} transients is clearly preserved during chronic CaMKII inhibition (Figure 22B and Figure 23B).

Chronic CaMKII inhibition and phospholamban ablation do not prevent the frequency-dependent increase in the maximum rate of Ca^{2+} uptake

The maximum Ca^{2+} uptake rate increased approximately linear with pacing frequency in the AC3-I, AC3-C and WT cells as presented in Figure 24. PLN ablation increased the Ca^{2+} uptake rate at all frequencies although reducing the dynamic range of uptake rates by about 40 % as evident by comparing Figure 24A and Figure 24B. However, the increase in Ca^{2+} uptake rate was still 1.47 ± 0.08 fold in the phospholamban deficient cardiac myocytes that expressed the CaMKII inhibitor AC3-I ($P<0.001$) when the pacing frequency was raised from 0.2 to 10 Hz. We suggest therefore, that shortening of the Ca^{2+} transient may occur at increasing pacing frequencies through a frequency-dependent increase in SERCA2a activity that does not require phospholamban or CaMKII activity.

Chronic CaMKII inhibition and phospholamban ablation prevents early activation of Ca^{2+} uptake at increasing pacing frequencies.

When the pacing is increased the maximum activity of SERCA2a was reached earlier during the time course of the Ca^{2+} transient in the AC3-I, AC3-C and WT cardiac myocytes, as evident in the time from peak $[Ca^{2+}]_i$ to Vmax (insert in Figure 25A). There was no difference in the activation times between AC3-I, AC3-C and WT myocytes in the presence of phospholamban. In PLN null myocytes, however, the frequency dependence of maximum SERCA2a activation was still present but only significantly reduced in the AC3-C x PLN-/- and the PLN-/- myocytes, although the activation time at

the largest frequency was still significantly shorter in these cells when compared to the AC3-I, AC3-C and WT myocytes. Chronic CaMKII inhibition by cytosolic AC3-I expression in combination with PLN ablation abolished the frequency dependence of the SERCA2a activation in AC3-I x PLN-/- cells as shown in Figure 25C and indicated by the slope of the frequency dependence, which was negligible in the AC3-I x PLN-/- cells and negative in all other cell types. This result indicates that the time at which the maximum Ca^{2+} uptake rate occurs seems to be dependent on both phospholamban and CaMKII.

Increase in pacing frequency slows SR Ca^{2+} release in phospholamban deficient cardiac myocytes with chronic CaMKII inhibition.

Because CaMKII activity is known to influence the open probability the SR Ca^{2+} release channel [183], we investigated the effect of chronic CaMKII inhibition on the time course of the rising phase of the intracellular Ca^{2+} transient. Although phospholamban does not directly interact with RyR2, interruption of the SERCA2a - phospholamban interaction increases SR Ca^{2+} uptake and SR Ca^{2+} load [21, 22, 52, 55]. Therefore, phospholamban null mice may serve as a model of increased SR Ca^{2+} load. Importantly, expression of RyR2 was not affected by phospholamban gene deletion [56, 57] or chronic CaMKII inhibition [180]. When the pacing frequency was increased, SR Ca^{2+} release was accelerated in AC3-I, AC3-C and WT myocytes as shown in Figure 26A and Figure 27A, although the difference was not significant for the WT cells (Figure 26C and Figure 27C). Furthermore, the tendency to hasten Ca^{2+} release at higher frequencies was indicated by the slopes of the linear fit to the frequency dependence, showing a shorter time-to-maximum (Figure 26A) and a higher maximum rate of the Ca^{2+} release with

increasing pacing frequencies. In the presence of PLN there was no apparent difference in the frequency dependence of the time course of the Ca^{2+} release between AC3-I, AC3-C and WT cells. However, combined phospholamban deletion and chronic CaMKII inhibition (AC3-I x PLN-/-) resulted in a slowing of the Ca^{2+} release at higher frequencies as shown in B and Figure 27B, while phospholamban deletion alone (AC3-C x PLN-/- and PLN-/-) still displayed an accelerated Ca^{2+} release at higher pacing frequencies, as presented in Figure 26D and Figure 27D. The slopes of the linear fits to the SR Ca^{2+} release time (rate) – frequency relationships shown in Figure 26B (Figure 27B) were consistently positive (negative) in the AC3-I x PLN-/- myocytes and negative (positive) in the AC3-C x PLN-/- and PLN-/- control myocytes. Therefore, we suggest that when SR Ca^{2+} load is high, chronic CaMKII inhibition slows Ca^{2+} release at higher pacing rates. This finding is consistent with a significant reduction in RyR2 phosphorylation at the known CaMKII site (Ser 2815) reported in the AC3-I myocytes [180] which in turn had been associated with a decreased open probability of the isolated channel [159, 167, 168] and a decreased amplitude and rate of SR Ca^{2+} release in intact cardiac myocytes [125, 169, 170].

A potential role for CaMKII in regulating calcium release at high SR Ca^{2+} load

Genetic CaMKII inhibition did not seem to affect the frequency dependence of the SR Ca^{2+} uptake as measured by the time constant, the duration and the rate of fluorescence decay at physiological frequencies and temperatures. CaMKII inhibition also did not affect the slight increase in the rate of Ca^{2+} release with pacing frequency in the presence of PLN. When SR Ca^{2+} load was increased artificially by PLN ablation, CaMKII

inhibition reduced the rate of Ca^{2+} release. Therefore, we hypothesize that CaMKII activity may have a regulatory function on the RyR2 by increasing Ca^{2+} release when the SR Ca^{2+} load is high, hereby reducing the risk of Ca^{2+} overload.

Acknowledgments

This work was supported in part by DARPA, AFOSR, NIH, the Whitaker Foundation, and the Vanderbilt Institute for Integrative Biosystems Research and Education (VIIBRE).

Note

This Chapter will be submitted for publication with the following list of authors:

Andreas A. Werdich[1]; Eduardo A. Lima[1], Mark E. Anderson[2] and Franz J. Baudenbacher[1]

[1] Department of Biomedical Engineering, Vanderbilt University, Nashville, TN, USA

[2] Departments of Medicine and Physiology, Carver College of Medicine, University of Iowa, Iowa City, IA

CHAPTER VI

A MICROFLUIDIC DEVICE TO CONFINE A SINGLE CARDIAC MYOCYTE IN A SUB-NANOLITER VOLUME ON PLANAR MICROELECTRODES FOR EXTRACELLULAR POTENTIAL RECORDINGS

6.1 Abstract

A hybrid chip is described which combines a microfluidic network fabricated in a silicone elastomer (PDMS) with planar microelectrodes. It was used to measure extracellular potentials from single adult murine cardiac myocytes in a restricted extracellular space. The recorded variations in the extracellular potentials were caused by transmembrane currents associated with spontaneously initiated intracellular calcium waves. Single cells were trapped inside the 100 pl microchamber by pressure gradients and maintained for several hours by continuous perfusion. In addition, the localized delivery of drugs to a portion of the cell was demonstrated. The impedance of the electrodes was reduced by a factor of 10 to 20 after the electrodeposition of platinum black. Biopotentials recorded from single cells with platinum black electrodes showed a three-fold decrease in the noise, resulting in a maximum signal-to-noise ratio of 15:1. Characteristic variations in the frequency and shape of the extracellular potential peaks were observed among different cells which are most likely due to differences in the sarcoplasmic reticulum Ca^{2+} load. Our device architecture permits the integration of electrochemical and optical sensors for multi-parameter recordings.

6.2 Introduction

Extracellular potentials from small cells are generally measured using saline-filled glass micropipettes [184] which are loosely held to the cell membrane mechanically or by suction. The movement of the cell during the measurement and the risk of destroying it by rupturing the thin membrane make this technique laborious and time consuming. In addition, simultaneous recordings from multiple separate sites with defined interelectrode spacing on the same cell are not practical. Voltage sensitive dyes [185, 186] have been employed to overcome these problems, but phototoxicity and photobleaching make them unsuitable for long-term recordings. In contrast, extracellular microelectrodes offer a non-invasive alternative for the long-term study of excitable cells from cardiac and neuronal tissue. Biosensors based on monolayers of embryonic cardiac myocytes cultured on microelectrode arrays [187, 188] and transistor arrays [189-191] have become a useful tool in physiology [192] and pharmacology, [193] and have already been deployed as portable, non-specific toxin detectors [83, 194].

A single-cell fluorescence assay based on a microfluidic channel structure fabricated in poly(dimethylsiloxane) (PDMS) was recently reported by A.R. Wheeler et al. [95], who demonstrated the delivery of nanoliter volumes of analytes to a single Jurkat T cell confined in a 500-picoliter microchamber.

As pointed out by G.T. Kovacs, [82] measurements of extracellular potentials using planar microelectrodes require the size of each recording electrode to be comparable to the size of the cell. If an electrode is not entirely covered by a cell, a recordable signal cannot be obtained from that electrode because of a voltage division across the areas exposed to the conducting solution. It is therefore common practice to grow cells on the

electrodes in a confluent monolayer. In particular for cardiac experiments, the requirement to culture cells on the electrodes generally limits the cell types suitable for extracellular recordings to those which can proliferate in culture, e.g. embryonic cells or cells derived from tumor cell lines, such as the cardiac HL-1 cell line [195]. Klauke *et al [93]* recently described an array of microelectrodes designed to stimulate single adult rabbit ventricular myocytes in 100- picoliter large microscopic chambers on a chip, but their design did not incorporate microfluidics. Single cells had to be selected individually from an external cell suspension and manually pipetted into the small, oil-covered compartments on the chip. Moreover, with the lack of continuous perfusion, normal homeostasis could not be sustained for a long period of time, leading eventually to unpredictable and irreversible pathologic changes. In general, the difficulty of positioning and keeping single cells at a well defined location close to the recording electrode may be one important reason why planar microelectrodes have not yet been used to measure extracellular potentials from isolated, non-attached excitable cells.

To overcome all these limitations, we have developed a hybrid microfluidic device, the Nanophysiometer, which confines a single cardiac myocyte to a 100 picoliter volume on a set of planar microelectrodes.

As one possible application, we measured extracellular potentials from isolated murine cardiac myocytes associated with the propagation of intracellular calcium waves.

In cardiac cells, excitation-contraction coupling is mediated by a small influx of Ca^{2+} through the voltage-gated Ca^{2+} channels in the external cell membrane. The small increase in intracellular Ca^{2+} subsequently leads to the activation of intracellular Ca^{2+}-receptors (ryanodine and IP3), which trigger a massive release of Ca^{2+} from the

sarcoplasmic reticulum (SR). The calcium-induced calcium release (CICR) mechanism greatly amplifies the amount of calcium ions which enters the cell via the sarcolemma during the activation of contraction and can also feed back on sarcolemmal ion currents. [196, 197] Localized spontaneous elevations in intracellular calcium concentration, known as calcium sparks, are usually observed in quiescent cells, occur at low rates (1-3 s^{-1}), [198] and lead to both the initiation and the propagation of slow (50-100 μm/s) [198] intracellular calcium waves. Their frequencies and amplitudes depend on the SR Ca^{2+} load [199] which itself varies with the extracellular Ca^{2+} concentration [198, 200]. Previous studies have convincingly shown that spontaneous release of Ca^{2+} ions in cardiac myocytes activates a transient depolarizing inward current which constitutes a potential arrhythmogenic process in the heart [200-203].

For the investigation of the fundamental cellular mechanisms of spontaneous activity it is essential that experiments are carried out on isolated cells rather than tissues or cell cultures to eliminate spurious interactions with other cells. We believe that our Nanophysiometer could be a valuable tool in investigating the electrical activity of non-attached isolated primary cardiac cells in a controlled extracellular space.

6.3 Device concept and fabrication

A schematic drawing and a microscope image of the Nanophysiometer are shown in Figure 28 and Figure 29, respectively. The device is composed of a PDMS microchannel network auto adhered to a set of microelectrodes on a glass slide, which were fabricated by thin film deposition of platinum.

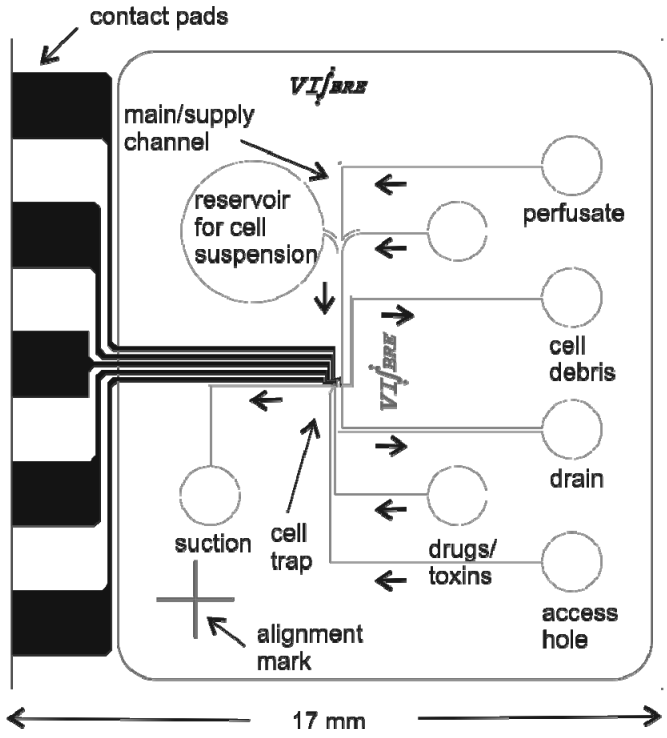

Figure 28. Schematic overview of the microfluidic channels and microelectrodes. The cell trap is located in the center of the device at the confluence of the vertical fluidics channels and the horizontal electrode traces. The cell suspension is pipetted into the 40 µl reservoir on the upper left side of the chip, from where single cells are drawn into the microchamber by pressure gradients. Arrows indicate the directions of the pressure gradients applied by using external syringes during the experiment.

The microchannels were realized in PDMS (RTV 615, GE Silicones) by replica molding [101] using a rigid mold (master) on a silicon wafer. The master was fabricated by spinning a 30-µm thick layer of photoresist (SU-8 2050, Microchem) on a 3" diameter silicon wafer and by exposing it to UV light through a metal mask using a contact mask aligner. The photoresist was processed according to the manufacturer's datasheet. An optional 30 minutes hard bake at 200 °C on a hot plate was performed to increase the durability of the resist. Each master containing four relief structures was placed in a plastic culture dish and covered by a 5 mm layer of the PDMS/curing agent mixture at a mixing ratio of 10/1. After curing of the elastomer for five hours at 60 °C in a convection oven, the devices were cut out and mechanically separated from the master. Access holes

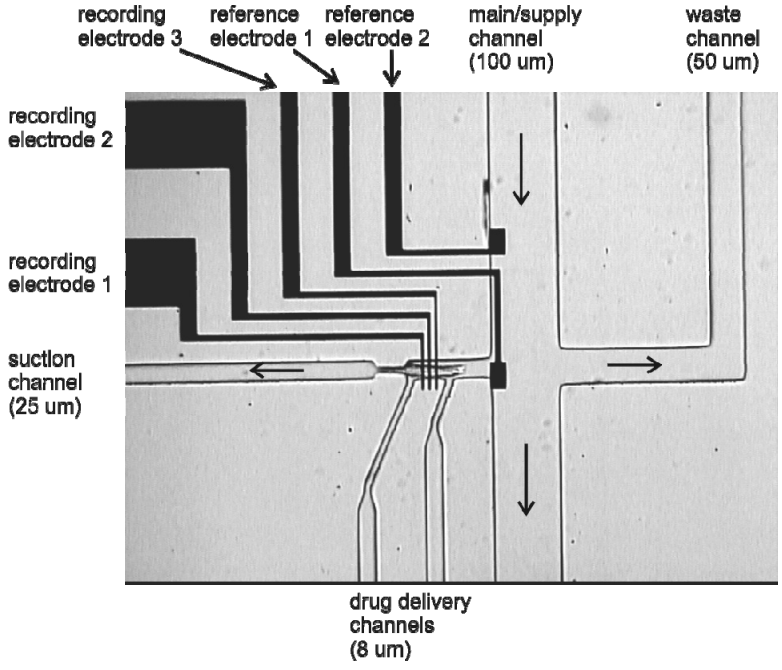

Figure 29. Bright-field microscope image of the cell trap for the electrode configuration shown in Figure 28. An isolated cardiac myocyte is captured in a 125 µm long and 25 µm wide microchamber in the chip. With a channel height of 30 µm, the cell trap has a volume of about 100 pl. Arrows indicate the directions of the applied pressure gradients.

to the channels were then punched by using a sharp stainless steel pipe. On average, it took eight hours to fabricate a set of four microfluidics chips, which were in general all functional. More technical details about the microfabrication process can be obtained from the work of G. Whitesides [98] and S.R.Quake [104].

The PDMS structure was manually aligned relative to the electrodes by using an inverted microscope and sealed on the glass substrate by autoadhesion. As shown in Figure 2, only the tips of the electrodes were exposed to the conducting Tyrode's solution inside the microchamber.

We used stainless steel capillaries inserted into the access holes to connect the microfluidics channels via standard microtubing (0.5 mm inner diameter, Cole Parmer) to 1 ml syringes. For efficient cell manipulation we controlled the syringes coupled to the suction and waste channels by hand. The syringes linked to the two 8 μm wide drug-delivery channels were mounted in computer-controlled syringe pumps (PHD 22/2000, Harvard Apparatus), which allowed a minimum flow rate of 40 pl/s.

Microelectrode fabrication

The microelectrodes were fabricated by means of an ion etch process. Titanium and platinum were first deposited on a 17 mm square and 1-mm thick glass substrate by electron beam evaporation. First, a 10-nm thick titanium layer acting as adhesion layer was deposited, followed by a 90-nm thick platinum layer. Then, a mask was patterned on the platinum films by standard photolithography in 1-μm thick photoresist (AZ5214-E, Clariant Corp.). In the following ion etch [204] process, the metal was removed in all areas which were not protected by the resist. Then, the photoresist was stripped off the

electrodes in an ultrasonic remover bath (AZ400-T, Clariant Corp.) at a temperature of 70 °C. Finally, the surface was thoroughly cleaned with acetone. The yield of fabricating thin film electrodes was about 80% after process optimization.

The microelectrodes were electroplated with platinum black to reduce their impedance. Prior to the electrodeposition, the substrates were thoroughly cleaned in an ultrasonic acetone bath, soaked for 5 minutes in hexane and then rinsed several times with acetone. Platinum black was deposited with the microfluidic channels aligned on the electrodes to limit the area of deposition and to deliver the electrolyte. Therefore, only the tips of the electrodes were exposed to the platinizing solution. The deposition process was monitored via an inverted microscope.

We used a voltage-controlled current source (circuit diagram not shown) interfaced with a PC to control the deposition current. The channel was filled with a 2.5% chloroplatinic/0.05% lead acetate solution (3140, diluted, YSI Inc.). Generally, we applied a 0.7 μA DC current to the small recording electrodes (125 μm^2 area, Figure 29) and a 2.0 μA DC current to the large reference electrode (500 μm^2 area) in order to obtain approximately the same current density for each electrode. The current was switched off as soon as a widening of the edges of the electrode was observed under the microscope. The deposition times were usually between 10 and 20s. We used a stylus surface profiler (Alphastep 200, Tencor Instruments) to measure the thickness of the deposit. We also measured the impedance of the microelectrodes before and after the deposition of platinum black with a dynamic signal analyzer (3562A, Hewlett-Packard).

Amplifier design

Extracellular potentials were amplified by a custom-designed low-noise differential amplifier built from off-the-shelf components. A simplified schematic is shown in Figure 30. More detailed diagrams of all circuits described herein can be obtained from the authors. The device consisted of an instrumentation amplifier, an integrator, a gain stage, and a low-pass filter. Instead of using a high-pass RC filter network, which would cause a significant decrease of the input impedance and the common mode rejection ratio, we used an integrator to implement AC coupling. Its inverted output was connected to the reference pin of the instrumentation amplifier to attenuate constant and very low frequency components of the input signal. With this technique, the microelectrodes were directly coupled to the inputs of the instrumentation amplifier, which had an input impedance of 1.014 kΩ. The time constant of the integrator was chosen to give a high-

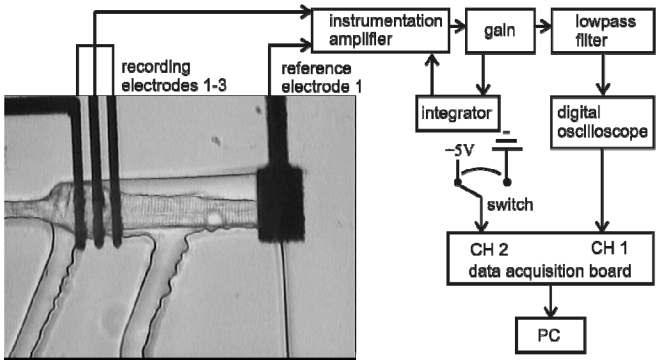

Figure 30. Setup of the measurement electrodes and the readout electronics for the extracellular recordings. The amplifier was connected to the three recording electrodes connected in parallel and to the large reference electrode 1. The push-button switch was linked to a second recording channel and used to mark visually observed contractions of the cell.

pass cut-off frequency of 0.08 Hz to reduce low frequency background noise. The signal was then further amplified by a second stage resulting in a total gain of 20,000, and subsequently low-pass filtered with a selectable cut-off frequency ranging from 15 to 100Hz. The noise of the amplifier (inputs shorted) referred to the input was 14.9 nV $Hz^{-1/2}$. After connecting the microelectrodes to the inputs of the amplifier, the noise increased about 5 fold, which is comparable with previously described amplifiers for extracellular recordings [189, 193, 205].

Device assembly

When the PDMS microfluidic device was sealed on the glass substrate, sufficient insulation was provided by the elastomer to prevent shorting of the interconnecting traces, and therefore no further passivation was required. To improve the seal between the elastomer and the electrodes, a mechanical clamp (Figure 31) was used to press the PDMS block against the substrate and fix the assembly to a heated microscope stage. The temperature of the device was controlled by flowing water from a heat exchanger through a tube integrated within the aluminum base plate as shown in the schematic in Figure 31B.

6.4 Experimental Procedures

Single cardiac myocytes inside the cell trap were monitored with an inverted fluorescence microscope (Axiovert 200, Zeiss, Germany) equipped with a CCD camera. Images were captured by a digital videodisc (DVD) recorder and digitized by an image capture board (Bandit II CV, Edmund Optics) linked to a standard PC.

A

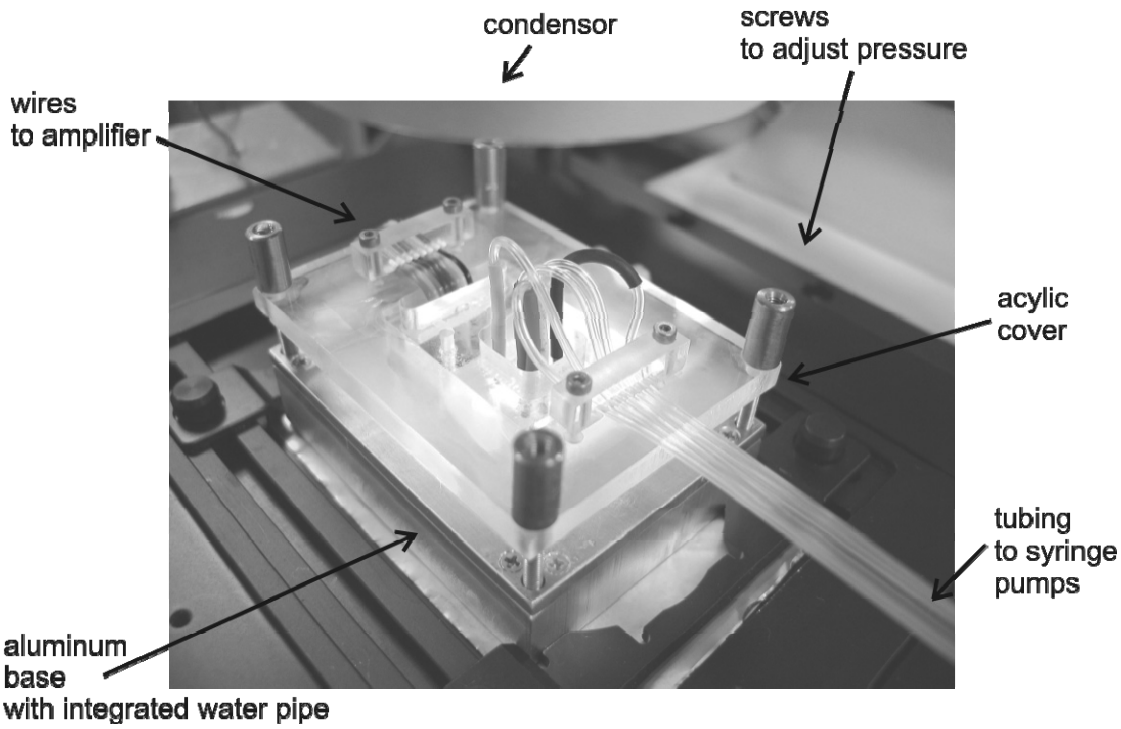

B

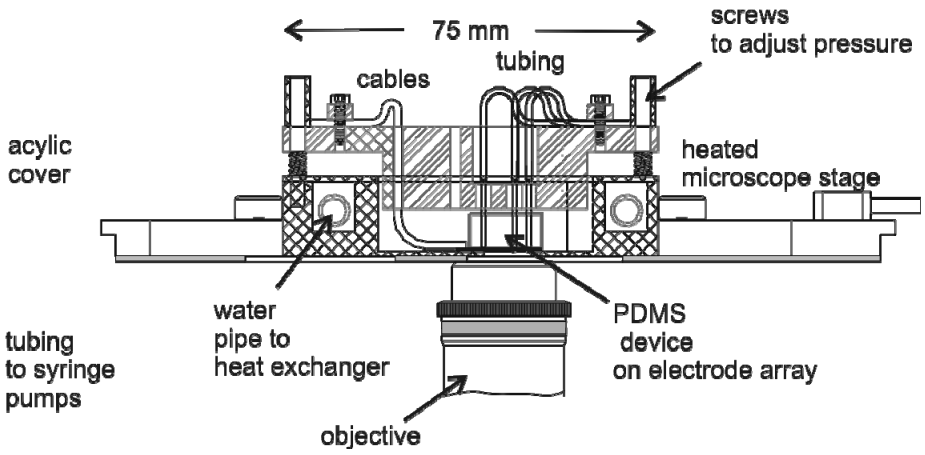

Figure 31. (A) Sectional drawing of the clamp on the stage of an inverted microscope. Temperature control of the device was provided by the heated microscope stage and an integrated water tube that could be connected to an external circulating heat exchanger.
(B) Photograph of the clamp mechanism that ensures a reliable seal between the PDMS micro channels and the electrodes. The transparent lid permitted the observation of the cell in transmitted light.

Myocyte isolation

Single ventricular myocytes were isolated from 2 to 5 months old mice according to the method described in detail by Anderson et al [206]. Briefly, animals were paralyzed by a pentobarbital (50 mg/kg) overdose and hearts were rapidly excised and placed in ice-cold nominally Ca^{2+}-free HEPES-buffered saline solution. The aorta was cannulated and the heart was perfused in a retrograde fashion with a Ca^{2+}-free solution for 5 minutes at 37 °C. To release single cells from the tissue, a 15-minute perfusion with a collagenase-containing solution was carried out, followed by a 5-minute perfusion with a 0.2 mM Ca^{2+} solution. The ventricle and septum were cut away, coarsely minced, and placed in a beaker containing a low-Ca^{2+} solution with 1% bovine serum albumin at 37 °C. Myocytes were dispersed by gentle agitation and maintained in Tyrode's solution, which contained (in mM) NaCl 137, glucose 10, HEPES 10, KCl 5.4, $CaCl_2$ 2.5, $MgCl_2$ 1.0, NaH_2PO_4 0.3. Experiments were usually done within the first three hours after the isolation.

Single-cell manipulation and trapping

The cell suspension was pipetted into a 4 mm diameter hole on the chip, which formed a 60 µl volume cell reservoir (Figure 28). The bottom of the reservoir was linked to the 100 µm wide main channel, which was connected to the microchamber (cell trap) in the center of the device. A pressure gradient was manually applied to pull single cells from the reservoir into the main channel. A single cell was trapped in the microchamber perpendicular to the main channel by a second pressure differential, as indicated by arrows in Figure 29. The directions of all pressure gradients are specified in Figure 28.

The cell trap consisted of a 125 μm long and 25 μm wide side channel with a 5 μm wide restriction at the end.

Assuming that 80 % or more of the cells were alive after the isolation, a single cell could reliably be trapped in the microchamber within seconds. However, approximately 30% of the trapped cells changed cell morphology and rounded up within a few seconds after the trapping, indicating a severe mechanical damage. The other fraction of cells showed no changes in morphology and could be maintained in the cell trap for one hour or longer. The success rate for trapping large single cells decreased with the condition of the cells in bulk cell suspension. Experiments were stopped if less than 30% of the cells were viable, which was usually the case 5 hours or more after the isolation from the tissue.

Single cardiac myocytes captured in the cell trap are shown in Figure 29 and Figure 30. Cell debris was sometimes caught in the trap but could be removed by reversing the pressure gradient in the suction channel. We expect that the capture rate of viable cells would be higher if round-shaped cell types were used.

Impedance measurements

The impedance of the microelectrodes was measured with the PDMS device aligned on them, as shown in Figure 30. The cell trap was filled with Tyrode's solution and the electrodes were connected to an auxiliary circuit. It consisted of a high input impedance unity-gain amplifier to measure the voltage across a pair of microelectrodes and a current-to-voltage converter to detect the current. The circuit was designed with carefully chosen components to minimize loading effects and its outputs were connected to the signal analyzer. The frequency of a sine wave was swept logarithmically over the range

of 0.05 to 50 Hz, which resembled the bandwidth used in the biological experiments. The magnitude and the phase of the impedance were computed by the signal analyzer based on the current and voltage measurements.

Recording of extracellular potentials

Large single adult cardiac myocytes were individually trapped inside the microchamber. The 30 μm height and the rectangular shape of the micro channel left a gap between the cell and the suction channel, which allowed a continuous perfusion with Tyrode's solution during the experiment. This can be inferred from Figure 32, which shows a single cell partly exposed to a fluorescein solution (F6377, Sigma-Aldrich Corp.).

Prior to the extracellular potential recordings, each cell was perfused with Tyrode's solution for several minutes to ensure its integrity and to allow it to recover from the possible mechanical stress experienced during the trapping procedure.

The electrode configuration and the setup for the recording of extracellular potentials are shown in Figure 30. Potentials were measured differentially between the large reference electrode 1 and the three small recording electrodes 1-3 connected in parallel. The reference electrode 1 was situated in the main channel, while the recording electrodes were located inside the cell trap. The other reference electrode 2, shown in Figure 29, was not used for the extracellular recordings described herein. The amplified signals were visualized by a digital oscilloscope and digitized by an analog-to-digital converter board (PCI 6071E, National Instruments).

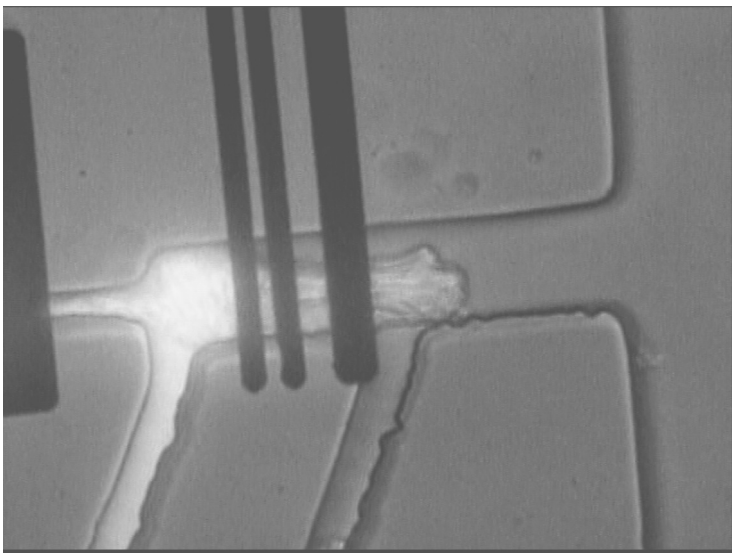

Figure 32. Fluorescence-microscope image of a single cardiac myocyte partially exposed to a fluorescein solution. The cell did not block the suction channel, so that perfusion could be sustained during the experiments.

We used a push-button switch to identify the visually observed contractions in the potential recordings where the signal-to-noise ratio was low.

The switch generated rectangular pulses (shown in Figure 35 a and b) which were recorded simultaneously with the potentials.

We have used two different electrode designs, shown in Figure 29 and Figure 30 and in Figure 32. The configuration depicted in Figure 30 was used for all extracellular recordings. The other electrode arrangement, shown in Figure 32, was designed for

combined electrochemical and optical experiments, but its performance has not yet been evaluated.

6.5 Results

An important feature of our microfluidics design is the ability to deliver drugs locally to a single cell. To demonstrate this, we trapped a large single cardiac myocyte inside the microchamber and perfused it locally with a fluorescein solution. The microscope image in Figure 32 shows a portion of the cell exposed to the solution. The dye was absorbed by the cell resulting in bright fluorescence of the entire intracellular space.

To characterize the performance of our microelectrodes, we took scanning–electron microscope (SEM) images of the metal surfaces, determined the thickness of the

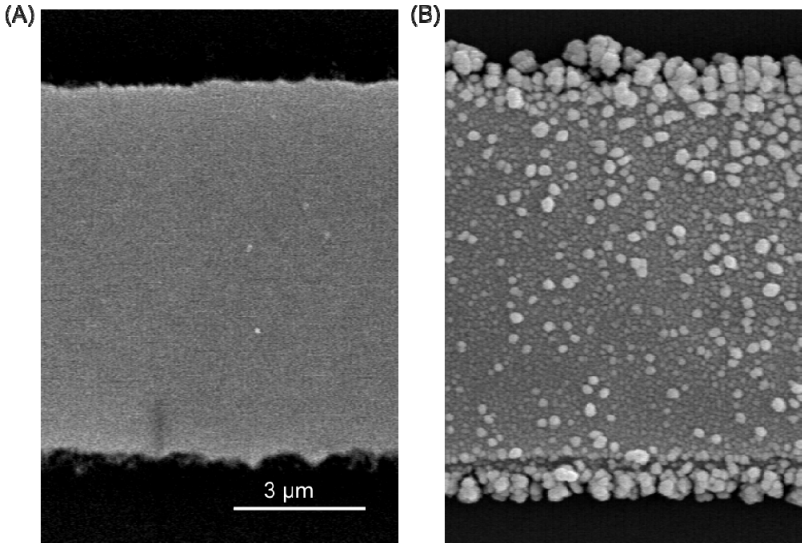

Figure 33. SEM images of a platinum electrode surface before (A) and after (B) the electrodeposition of platinum black.

platinum black deposition, and measured their associated impedance. The electrodeposition of platinum black resulted in a rough surface, thereby increasing its effective area. SEM images of a platinum microelectrode before and after the deposition process are shown in Figure 33 (A) and (B), respectively. The average thickness of the platinum black layer was 0.6 μm and increased with longer plating time. We restricted the deposition time to 10-20 seconds to avoid tall crystalline spikes that reduced the height of the trap and resulted in cell damage.

We measured the impedances of gold and platinum microelectrodes in a frequency range of 0.05 Hz to 50 Hz, before and after the electrodeposition of platinum black. The graph in Figure 34 clearly shows that the impedances of both platinized electrodes were about 10 to 20 times lower than those of the bare metal electrodes. Furthermore, all electrodes exhibited a decrease in impedance with increasing frequency, which is a characteristic behavior for an electrode-electrolyte interface. We have modeled the frequency dependence of the electrode impedance by a series combination of a resistance R and a polarization capacitance C, the value of each is frequency-dependent, according to the Warburg concept. [207-210] It states that the resistance and reactance of a metal-electrolyte interface are approximately equal and that the capacitance varies with the frequency f as f^{α}, where α is a constant ranging for most metal electrode/electrolyte interfaces from 0.2 to 0.7 [184].The fits of the curves in Figure 8 yielded a capacitance per unit area of 7540 $f^{-0.47}$μF cm^{-2} (f is the frequency in Hz) and an impedance times unit area of 29.86 $f^{-0.53}$Ωθcm^2 for the platinum black-coated platinum electrode. For the platinum black-coated gold electrode, the linear fit yielded a capacitance per unit area of

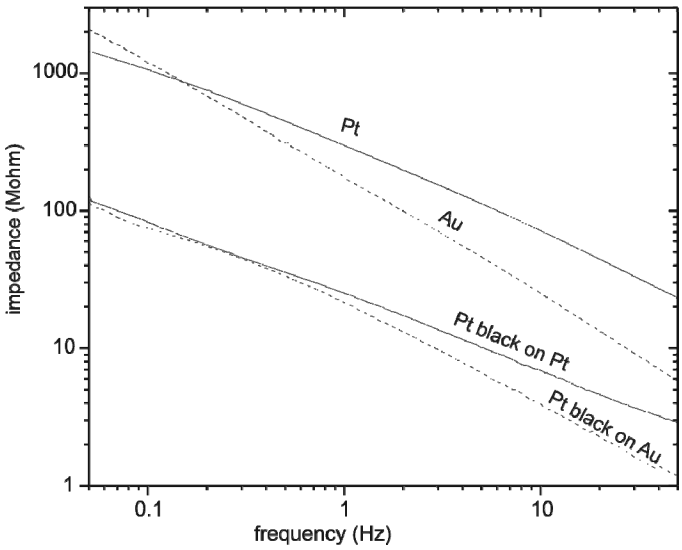

Figure 34. Impedance measurements of platinum and gold electrodes before and after electrodeposition of platinum black in the frequency range used for the recording of extracellular potentials.

6240 $f^{0.26}$ μF cm^{-2} and an impedance times unit area of 36.10 $f^{0.74}$ Ωθcm^2. The standard error of the fit was in both cases smaller than 0.5%.

The estimated values of the capacitance and the impedance of our electrodes were consistent with those reported in the literature [184]. Even though the platinum black-on-gold electrodes showed smaller impedance in the higher frequency range, we used platinum black-on-platinum electrodes in our experiments. The reason was that the gold electrodes showed a considerable degradation of the platinum black layer after a single use, while the platinum electrodes could be reused for at least five experiments. This may be due to poor adhesion properties of platinum on gold surfaces.

Figure 34 shows a series of 20-s long extracts from recordings of four different experiments, corresponding to distinct cells. The peaks were correlated with the

spontaneous contraction waves and were expected to occur in quiescent cardiac myocytes under our experimental conditions. The occurrence of contraction waves was indicated in the first two measurements by the rectangular pulses below the potential traces.

The calcium-activated inward current which accompanies the propagating calcium wave is carried by Na^+ ions entering the cell via the Ca^{2+}-activated Na^+/Ca^{2+} exchanger. [211-213] There is also a calcium-activated outward current, carried by chloride ions, which contributes significantly to the early repolarization during the regular action potential [214-217].

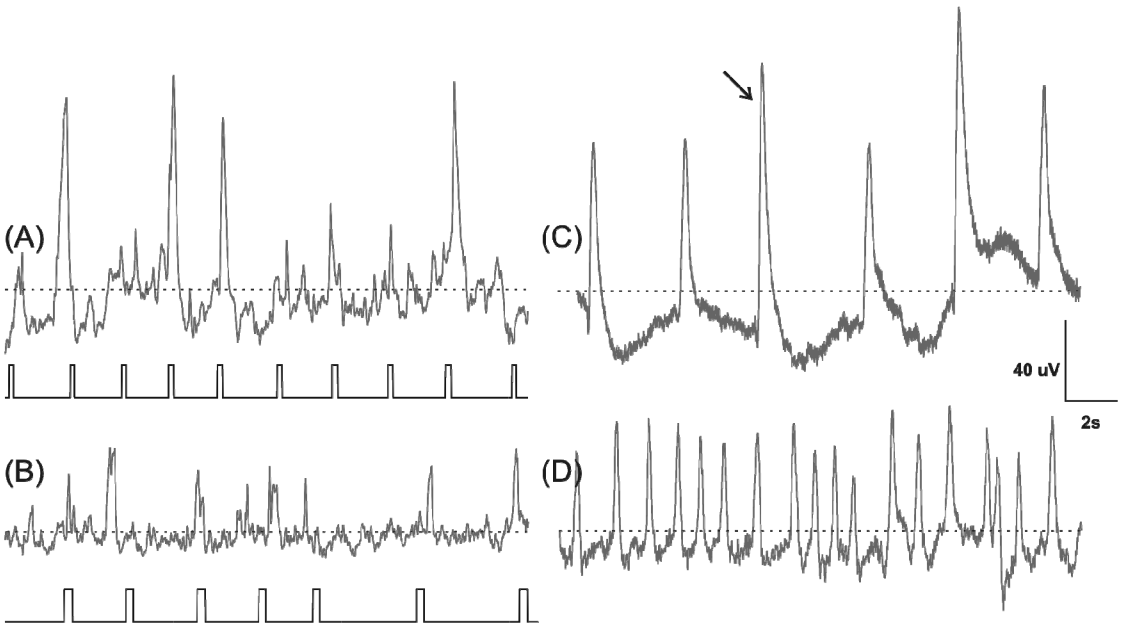

Figure 35. Four 20-s long extracts from typical extracellular potential recordings. All measurements were carried out with the same electrode configuration shown in Figure 29 andFigure 30. Traces (A) and (B) were recorded using bright metal platinum electrodes and a bandwidth of 15 Hz, while traces (C) and (D) were recorded by using platinum black-coated platinum electrodes with a bandwidth of 30 Hz. Visually observed contractions were marked in the traces (A) and (B) to correlate the contraction waves with the extracellular potential recordings when the signal-to-noise ratios were low. The Arrow in (C) points to the peak shown in Figure 36.

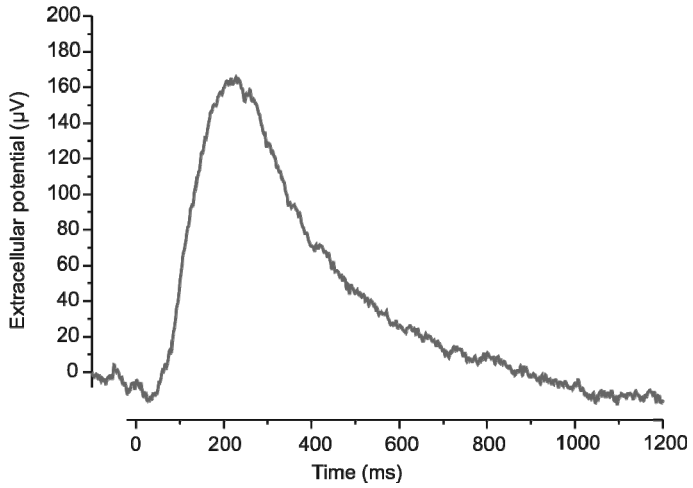

Figure 36. Time course of an extracellular potential peak caused by a spontaneous intracellular calcium wave. The data was taken from the third peak of the recording shown in Figure 35 (C).

These transmembrane currents produced variations in the extracellular potentials that were detected by the microelectrodes. However, extracellular potential recordings with comparable signal-to-noise ratios to those shown in Figure 35 (C) and (D) could be obtained only from cells that met two criteria. First, they had to be at least 20 µm in diameter to cover 80 % or more of the recording electrode surface. Second, they had to be in focus with the bottom of the cell trap and thus close to the recording electrodes. Usually, less than 50 % of the trapped cells met those requirements. An even smaller cell trap would probably improve the success rate, although it could obstruct large cells. Measurements (A) and (B) were recorded using bare platinum electrodes and a bandwidth of 15 Hz, while measurements (C) and (D) were recorded using platinum black electrodes and a bandwidth of 30 Hz. Traces (C) and (D) showed a three times

higher signal-to-noise ratio (for a two times larger bandwidth) than traces (A) and (B), which could be attributed to the platinum black deposition.

Repeatedly, we observed considerable variations in frequency and peak width for different cells taken from the same preparation. These differences are particularly noticeable by comparing traces (C) and (D), and are most likely due to either variations in SR Ca^{2+} load or properties of the SR release mechanism, as reported by other investigators based on fluorescence experiments [114, 198, 200] or numerical models [218, 219]. Contraction waves occurred approximately 17 times per minute in the cell represented by trace (C), with an average peak width (FWHM) of 230 ± 50ms. Spontaneous activity was significantly increased in the cell represented by trace (D), with almost one contraction wave per second. This cell displayed a peak width (FWHM) of 142 ± 8ms, indicating a higher propagation velocity or altered channel kinetics. The observed differences among the four experiments are in agreement with results reported by Cheng et al. [198], who described variations of more than 50 % in spark frequency and wave propagation velocity. The time course of a single extracellular potential peak is shown in Figure 36. The qualitative comparison of its shape with data from fluorescence experiments using the calcium dye fluo-3 [198, 220] suggests a correlation of the intracellular Ca^{2+} wave and the Ca^{2+}-mediated extracellular currents.

To understand the differences in wave occurrence and propagation, and to elucidate the coupling of intracellular calcium release and extracellular currents, combined fluorescence and electrical measurement are required.

6.6 Outlook

Our device architecture permits trapping and maintaining of single cells in a restricted extracellular space. Although we have used the integrated microelectrodes to measure extracellular potentials from cardiac myocytes, the use of the Nanophysiometer is not limited to this application. Other cell types, such as skeletal muscle or nerve cells, could be expected to perform similarly in the microfluidic environment. Depending on their size and shape, the dimensions of the microchamber would have to be adapted. The microfluidic design provides a small extracellular volume and in general assures small distances from the cell to the measurement electrodes. This not only permits electrical recordings with an adequate signal-to-noise ratio, but also significantly reduces diffusion-limited response times of electrochemical sensors. Furthermore, the restricted extracellular space allows rapid control of the chemical environment while the cell is kept alive by perfusion and fixed at a stable position close to the recording electrodes by the microfluidic cell trap. With the integration of electrical, electrochemical and optical sensors, the Nanophysiometer provides a basis for the future development of single cell biosensors and automated single cell assays.

Acknowledgements

We would like to thank André G. Kléber for fruitful discussions and Jinying Yang for the isolation of cardiac myocytes. This work was supported in part by the Defense Advanced Research Projects Agency under ONR contract N66001-01-C-8064, and Vanderbilt University.

Note

This Chapter has been published in Lab Chip, Vol. 4, pp. 357-362, May 2004, with the following list of authors: Andreas A. Werdich[1], Eduardo A. Lima[1], Borislav Ivanov[1], Igor Ges[1], John P. Wikswo[1], Mark E. Anderson[2], and Franz J. Baudenbacher[1]

[1] Department of Biomedical Engineering, Vanderbilt University, Nashville, TN, USA

[2] Departments of Medicine and Physiology, Carver College of Medicine, University of Iowa, Iowa City, IA

CHAPTER VII

SUMMARY AND FUTURE WORK

7.1 Summary

The dissertation describes the development and application of the Nanophysiometer, a microfluidic network combined with a thin film microelectrode array, to study force – excitation coupling in single cardiac myocytes. The microfluidic device was used for simultaneous recordings of multiple physiological variables from single non-attached adult cardiac myocytes in a chemically controlled microenvironment. The Nanophysiometer was fabricated in a silicone elastomer and imaged using an inverted microscope, a high speed CCD camera and an optical fiber array coupled to photomultipliers for high bandwidth fluorescence recordings. Using microfluidics, the localized delivery of a fluorescent dye to a membrane patch of a cardiac myocyte was demonstrated. The Nanophysiometer automatically aligned and stabilized single cardiac myocytes on the microscope during long term sarcomere contraction measurements, thereby reducing motion artifacts. Intracellular calcium transients and sarcomere contraction measurements were combined to test the hypothesis that phospholamban (PLN) ablation in mice increases the cardiac myofilament response to cytosolic calcium concentration. It was demonstrated that sarcomere acceleration may be used as an index of contractility when length dependent passive resistance and velocity dependent viscous damping are considered. The results show that sarcomere acceleration during contraction was increased 9.1 ± 2.1 fold and indicate that the slightly, 1.65 ± 0.30 fold elevated

amplitude of the SR Ca^{2+} release may not be the only cause of the increased contractility in the PLN deficient cells. A previously published proteomic analysis of PLN deficient mouse hearts and our results indicate that significant changes in myofilament protein expression and phosphorylation may have contributed significantly to the increased force development in these hearts.

Further more, genetic phospholamban ablation significantly reduced the dependence of the SR Ca^{2+} uptake on the stimulation frequency, but did not abolish it. Even the combination of genetic deletion of PLN and chronic inhibition of the Ca^{2+}/Calmodulin dependent protein kinase II (CaMKII) did not prevent the frequency dependence of the SR Ca^{2+} uptake. Our results suggest that a mechanism of frequency adaptation must exist in the mammalian ventricle that does not require phospholamban or CaMKII. However, chronic CaMKII inhibition significantly slowed Ca^{2+} release at physiological frequencies in the absence of PLN indicating a role of CaMKII in the regulation of Ca^{2+} release at high SR Ca^{2+} load.

When the techniques described here are combined, the Nanophysiometer will be capable of simultaneous measurements of extracellular potentials, intracellular and extracellular ion and metabolite concentrations (Ca^{2+}, pH, O_2, glucose, lactate) and sarcomere length in a chemically controlled microfluidic environment.

7.2 Future work

Precise chemical control of the extracellular environment using on-chip valves and peristaltic pumps

Single cardiac myocytes were confined and stabilized in the microfluidic cell trap of the Nanophysiometer for optical recordings. The success rate for trapping cells was 50-70 % even when the cell isolation yielded 80 % or more viable cells. Pressure gradients in the microfluidic device were established manually via attached syringes. The lack of precise pressure control due to large dead off-chip volumes lead to sudden

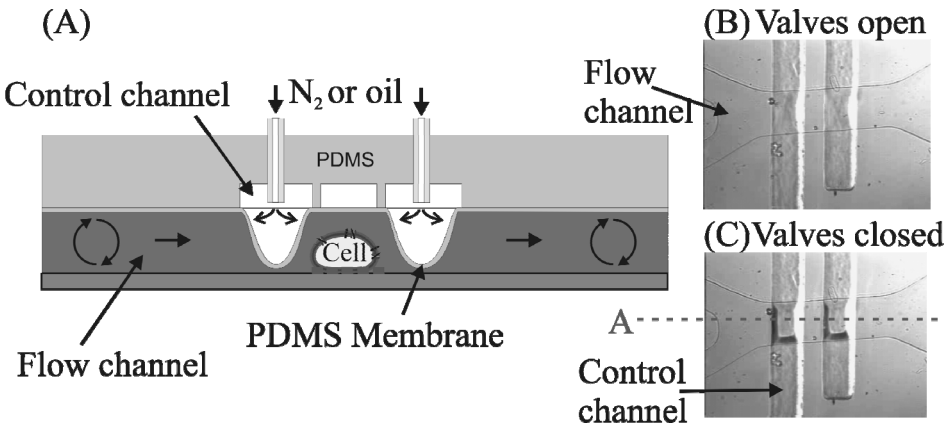

Figure 37. Principle of operation of on-chip valves fabricated in crossed-channel architecture. (A) Cross section of a flow channel with two valves when viewed after a cut along the dotted line (lower microscope image). The membrane between the upper pressurized control channel and the lower flow channel is very thin (~30 μm) and is deflected downward after the application of pressure. (B) Bottom-view microscope image of the device with two open valves. (C) Bottom-view of the microfluidic device with two closed valves.

changes in pressure during the measurement or myocyte trapping causing mechanical damage of the sarcolemma and leading to hyper contracture and cell death.

In the future, the success rate could be significantly increased by optimizing the on-chip active valves and peristaltic pumps in the Nanophysiometer. Valves are fabricated by multilayer soft lithography as described by Unger *et al.* [79].

The principle of operation of two on-chip valves is shown in Figure 37. A two layer PDMS device is fabricated by bonding the pneumatic/hydraulic control layer and a perpendicular flow channel together so that the two channels are separated by a thin PDMS membrane. The control channel can be pressurized with Nitrogen (or preferably oil) causing deflection of the membrane and pinching of the flow channel below. Because the active element is the roof of the channel itself, simple on-off valves as the ones shown in Figure 37 have truly zero dead volume. A peristaltic pump may be realized by

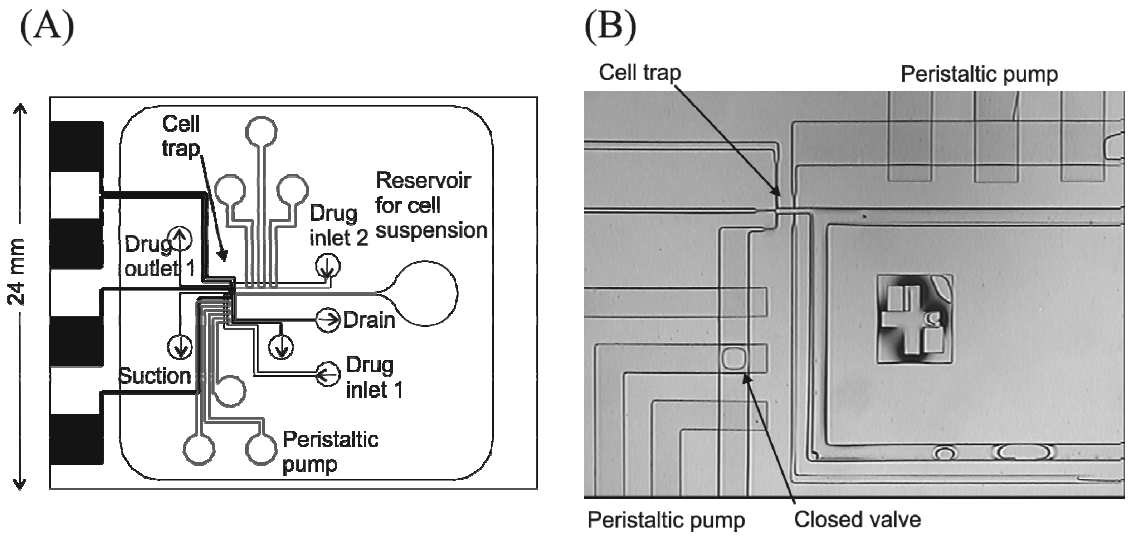

Figure 38. (A) Schematic of a prototype Nanophysiometer with peristaltic pumps along the two vertical perfusion channels, drug inlet 1 and drug inlet 2, and microelectrodes. (B) Microscope image of the multilayer Nanophysiometer without microelectrodes for better presentation (courtesy Yuxin Liu).

arranging three valves in series along a single channel with a dead volume about equal to volume of one valve, (i.e. on the order of ~ 25 pl) [79]. A Nanophysiometer design with two peristaltic pumps for rapid chemical control of the extracellular environment is shown in Figure 38. It is important to note that the ability for a valve to close at a given pressures strongly depends on the aspect ratio of the lower flow channel, i.e. the ratio of channel width to its height. This flow channel aspect ratio must be equal or larger than 10 for a valve to close at reasonable pressures, < 30 psi (207 kPa). Therefore, the higher the roof of a flow channel, the wider it must be in order to be closed by a membrane valve. Because the flow channels in the Nanophysiometer are 40 - 50 µm high to allow cardiac myocytes to pass through, they would have to be designed extremely wide in order close. To avoid mm-size microfluidic structures, the flow channels can be fabricated using a two layer photolithographic process leading to shallower areas where the fluidic lines cross the control channels.

Direct force – $[Ca^{2+}]_i$ relationship measurement in isolated heart muscle preparations and single cardiac myocytes

For a more detailed understanding of myocyte excitation contraction coupling and dynamics it would be beneficial to measure forces directly under a varying loading conditions [71]. Direct force measurements in intact cardiac myocytes are extremely difficult and require the attachment of the fragile sarcolemma membrane to a force transducing device. Optical recordings of intracellular calcium concentration and sarcomere shortening in phospholamban deficient cardiac myocytes revealed an increased sensitivity of the myofilaments to cytosolic [Ca^{2+}]. We presented a novel method that allows evaluating relative changes in the active force of shortening in

unattached myocytes by analyzing relative changes in maximum acceleration under consideration of passive elastic and viscous forces that resist shortening. Our measurement of unloaded myocyte shortening needs further validation in a well characterizes system that allows a direct assessment of contraction force indicative of the underlying inotropic and lusitropic state of the myocardium. Being able to measure forces dynamically and apply variable loading conditions would allow us to explore the length-tension relation ship in great detail and would provide insight into the mechanical feedback through stretch activated $[Ca^{2+}]_i$ ion channels [69, 221].

Sarcomere acceleration and force frequency relationships in isolated cardiac myocytes with chronic CaMKII inhibition.

Chronic CaMKII inhibition did not influence the time course of calcium uptake at physiological frequencies and temperatures, even in the absence of phospholamban. At first glance the data presented in Chapter V seem to suggest that CaMKII is not involved in the frequency-dependent acceleration of relaxation (FDAR). However, sarcomere shortening (or better, sarcomere contraction force) as a function of pacing frequency in CaMKII deficient cardiac myocytes might reveal a potential role of CaMKII in the frequency-dependent regulation of contraction and relaxation through direct interaction with other contraction modulating proteins. The calcium sensitivity of the myofilaments is known to depend on temperature, pH, $[PO_4]_i$ and $[Mg^{2+}]_i$ [41, 42], as well as on the phosphorylation of the myofilament proteins troponin-I (TnI) and myosin binding protein-C (MyBP-C) [222]. Phosphorylation of TnI decreases the calcium sensitivity of the myofilaments suggesting that phosphorylated TnI promotes relaxation [59, 222-225], while calcium-mediated phosphorylation of MyBP-C increases maximum force at a given

$[Ca^{2+}]_i$ [64]. In fact, analysis of force – $[Ca^{2+}]_i$ relationships in isolated mouse papillary muscle bundles shows that increasing stimulation frequency increased force production per unit change of calcium concentration (positive force-frequency relationship) and decreased the frequency-dependent calcium sensitivity of the myofilaments during relaxation [226]. Therefore, the measurement of myofilament protein phosphorylation, sarcomere shortening (or better, sarcomere contraction force) as a function of pacing frequency in CaMKII deficient cardiac myocytes might reveal a possible role of CaMKII in the frequency-dependent regulation of contraction and relaxation interacting with other contraction regulating proteins.

Implications of high diastolic Ca^{2+} concentration and origin of arrhythmias in VLCAD deficient mice

The results presented in Appendix B show that VLCAD deficiency in mice increased SR Ca^{2+} calcium load and fractional Ca^{2+} release, diastolic calcium concentration and the rate of sarcomere shortening. On the other hand, the most striking observation in the intact VLCAD deficient mouse heart was inducible ventricular tachycardia by physiological stress such as fasting, cold or exercise [227]. The data shown in this chapter are an attempt to characterize the physiological and pathological changes associated with a metabolic defect in fatty acid beta oxidation on the single cell level, but the role of these changes in the genesis of arrhythmias was not investigated.

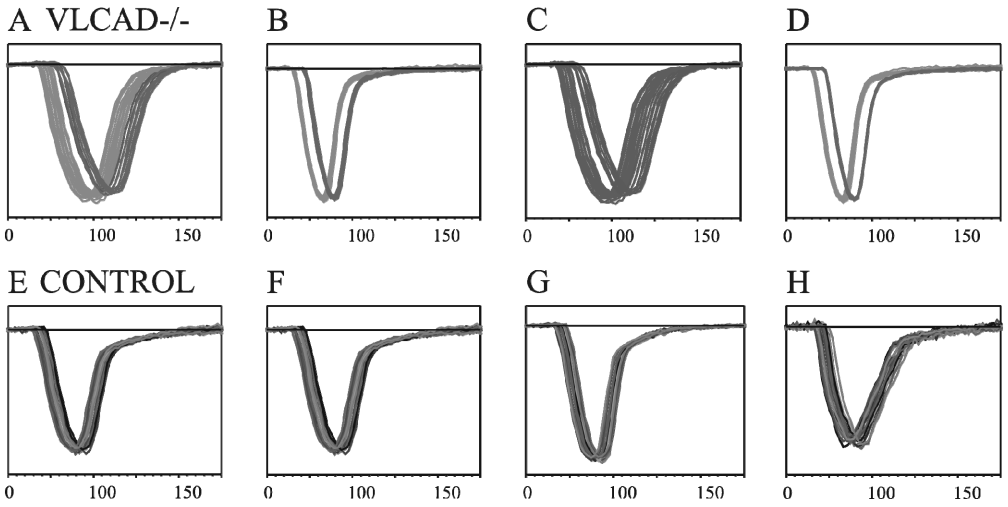

Figure 39 Beat-to-beat variations of normalized sarcomere transients in four VLCAD-/- (A-D) and four WT CONTROL (E-H) cardiac myocytes. Time is measured in ms from the onset of the stimulus.

The increased diastolic Ca^{2+} concentration could trigger delayed afterdepolarizations resulting from the depolarizing inward current of the sarcolemmal Na^{+}/Ca^{2+} exchanger [228-230]. Future experiments on VLCAD deficiency need to address the molecular mechanism of arrhythmia on the organ, tissue and single cell level. Figure 39 shows a set of sarcomere contractions recorded from four VLCAD-/- (A-D) and four WT control (E-H) myocytes. For each cell, 25 consecutive sarcomere contractions were recorded and superposed with the stimulus occurring at time zero. The data show that a noticeable delay between the sarcomere length minima occurred in the VLCAD deficient cells (in about 30 % of the analyzed cells), which was never observed in the WT control cells. However, more contraction data must be collected and if possible complemented by whole heart LV pressure and simultaneous calcium or action potential recordings to decide if these delays in single cell sarcomere contractions are statistically significant and whether they may lead to arrhythmias in the VLCAD deficient heart.

APPENDIX A

THIN-FILM IRO_X PH MICROELECTRODE FOR MICROFLUIDIC-BASED MICROSYSTEMS

A.1 Abstract

Microsensors are valuable tools to monitor cell metabolism in cell culture volumes. The present research describes the fabrication and characterization of on-chip thin-film iridium oxide pH microsensors with dimensions of 20×20 μm^2 and 20×40 μm^2 suitable to be incorporated into nl volumes. IrO_x thin films were formed on platinum microelectrodes by electrochemical deposition in galvanostatic mode. Anodically grown iridium oxide films showed a near super-Nernstian response with a slope of -77.6 ± 2 mV/pH at 22 ^oC, and linear responses within the pH range of 4-11. Freshly deposited electrodes showed response times as low as 6 s. Long-term studies showed a baseline drift of 2-3 mV/month, which could easily be compensated by calibration. This work demonstrated for the first time the use of planar IrO_x pH microelectrodes to measure the acidification rate of CHO and fibroblast cells in an on chip cell culture volume of 25 nl with microfluidic control.

A.2 Introduction

We are witnessing the introduction of bioinstrumentation that combines microfabrication, microfluidics, and micromechanics to create self-contained Bio-Micro-Electro-Mechanical Systems (BioMEMS), which serve as a complete biological laboratory-on-a-chip [231-240]. Devices to monitor physiological parameters and cellular activity of living cells *in vitro* generally employ fluorescent dyes, calorimetric probes,

radioactive labels, or electrochemical/electrical sensors. Sensors located in the extracellular space do not require invasive manipulation or cause toxic effects, and therefore allow for long term recordings. The sensing of extracellular pH has been used to detect perturbations in metabolic activity as a result of receptor activation, drug and toxin effects, or enzyme inhibition [241, 242]. Biosensors based on extracellular pH measurement have been demonstrated, and a Microphysiometer system (Cytosensor Microphysiometer - Molecular Devices, Inc.) is commercially available to assess metabolism in microliter cell culture volumes with temporal resolutions on the order of minutes [243-245].

The Cytosensor uses a Light Addressable Potentiometric Sensor to determine acidification rates, and has been used for a number of cellular studies ranging from measuring metabolic activity during pharmacological and toxicological interventions to cell signal transduction [242, 246]. Typically, 3×10^5 cells are cultured between two membranes in a 4-μl volume equipped with the sensor and a perfusion system. The resolutions of the instrument for pH and acidification rate measurements are 0.001 pH and 0.001 pH min^{-1}, respectively.

Ion-sensitive field effect transistors (ISFET) have also been used to measure acidification rates of living cells cultured on gate electrode surface areas ranging from 400 μm^2 up to 6000 μm^2 [247, 248]. Furthermore, ISFET's have been incorporated in 10 μl chambers filled with approximately 2×10^5 cells. The measured acidification rate for RT112 and LS174T tumor cells are in the range of 0.065-0.08 pH min^{-1} [249].

The scaling down of this approach requires the development of a miniature pH sensor for nl cell culture volumes in a microfluidic-controlled environment. Additionally, if the device is compatible with optical techniques, it will enable better understanding of

complex cellular processes. In contrast to use of a multitude of agent-specific analytical methods, sensors that respond to effects on cell homeostasis would provide a broader and more effective method to detect and identify environmental toxins. This concept will have numerous applications in medical research, as it would improve the efficiency of drug discovery, drug development, pharmaceutical screening, and environmental monitoring [250].

Micro pH electrodes with sensing areas typically below 500 μm^2 are needed to measure pH inside microfluidic devices. As described in the literature [232-239, 251], one of the most promising materials for thin-layer pH electrodes is IrO_x film. The main advantages of IrO_x in comparison with other pH-sensitive oxides include a wide pH response range, fast response time, high pH sensitivity, low potential drift, and low sensitivity to redox pair interference [252]. An additional technological advantage is the ability to form IrO_x layers by means of different chemical and physical methods, which can match application-specific requirements in chemistry, biology and medicine. These attributes make IrO_x one of the best choices as sensitive material for pH electrodes.

Different techniques have been used to produce iridium oxide pH electrodes, such as reactive sputtering using iridium targets in an oxygen plasma [253-255], thermal oxidation of Ir wire [256, 257], high-temperature carbonate-melt oxidation of Ir wire [237, 258], thermal decomposition of an iridium salt [259], electrochemical oxidation of Ir electrodes during potential cycling [233, 234, 239, 251, 260], and anodic iridium oxide film (AIROF) electrodeposition in galvanostatic mode [232, 238, 252, 261-263]. While other methods require complex procedures such as high-temperature treatment, electrochemical activation, or expensive iridium targets, the electrochemical methods

have found a wide range of practical applications because of their relative simplicity and their manufacturability in large-scale applications. Furthermore, these methods allows for selective deposition on planar microelectrodes.

Conventional IrO_x pH electrodes are formed by thermal or electrochemical oxidation of Ir wire with diameters as small as 20 μm. Because the integration of wire electrodes into microfluidic devices is very difficult or practically impossible, the only feasible alternative is planar thin-film electrodes. Few applications of thin-film IrO_x pH electrodes—with active surface areas of 1×1 mm^2, 0.1×1 mm^2 and 0.2×0.05 mm^2—have been found in the literature [239, 252, 264]. The scope of our research was to develop technologies for the fabrication of thin-film planar IrO_x electrodes with active sensing areas below 500 μm^2, to incorporate the sensors into an on-chip miniature cell culture volume, and to evaluate their performance in acidification rate measurements to monitor cell physiology.

A.3 Methods

Materials and reagents

Hydrogen peroxide (30% solution in water), iridium tetrachloride, oxalic acid dihydrate, 5% Nafion solution, and anhydrous potassium carbonate supplied by Aldrich, Inc. were used. Universal pH buffers (for pH 2, 4, 6, 7, 8, and 10) were obtained from VWR Scientific. Titanium (99.95%, rod diam. 2mm), and platinum (99.95%, rod diam. 2mm) were purchased from Goodfellow Corp., and fused quartz (rod diam. 24mm), from Technical Glass Product. RPMI 1640 buffer was supplied by Molecular Devices Corp. Mouse fibroblast cells (A9 L HD2 S.C. 18) and Chinese hamster ovary (CHO) cells (M 3

WT4) were supplied by ATCC (CRL-10255 and CRL-1981, respectively). The cell media and additives were all supplied by BioWhittaker. All chemicals were used as received. Double-distilled (DI) water was used for the preparation of all solutions.

Electrode fabrication

The electrode structures were formed on glass microscope slides (76 mm x 25 mm x 1mm, Fisher Scientific), which were initially cleaned in accordance to a standard cleaning procedure [237]. The electrodes consisted of two layers: a Ti adhesive layer (10 nm) and a Pt working layer (100 nm). Thin-film electrodes were formed by e-beam vacuum evaporation of Ti and Pt from carbon crucible liners (Kurt J. Lesker, Inc.). The total gas pressure and substrate temperature were maintained at $5x10^{-6}$ torr and 273 K, respectively, during the film deposition. The deposition rate was 0.5 nm/sec for Ti films and 1.0 nm/sec for Pt films. The deposition rate and the thickness of the films were controlled by a quartz crystal microbalance (Maxtek, Ink.). The Ti and Pt films were deposited in a single process without breaking vacuum. After deposition, each substrate was cut into individual 1×1 in^2 chips for thin-film microelectrode fabrication. For electrode insulation we used thin films of silicon oxide. The 150 nm SiO_x films were deposited by e-beam evaporation using fused quartz targets at a residual pressure of 2 x 10^{-5} torr (the rate of deposition was 0.1-0.2 nm/s). The microelectrode configuration was created by patterning platinum films using standard photolithography with 1 μm-thick photoresist (AZ5214-E, Clariant Corp.). The metal was removed using an ion etch process in all areas that were not protected by the resist. The photoresist was stripped from the electrodes in an ultrasonic remover bath (AZ400-T, Clariant Corp.) at 70 °C.

Finally, the surface was thoroughly cleaned with acetone and distilled water. The windows in the silicon oxide films were formed by a standard lift-off photolithographic process. Microelectrodes with working areas of $20 \times 40\ \mu m^2$, $20 \times 20\ \mu m^2$ and $5 \times 10\ \mu m^2$ were fabricated using the processes described above. A microscope image and a schematic cross section of the micro electrodes are shown in Figure 40A and B, respectively.

A

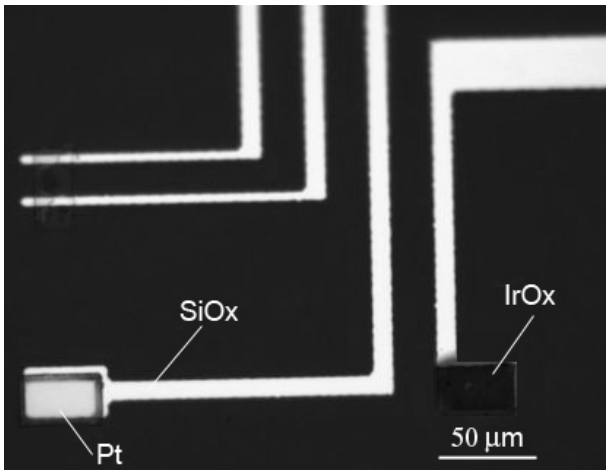

B

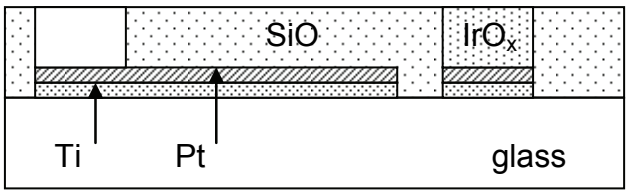

Figure 40 (A) Bright-field microscope image of Pt microelectrodes covered with a 150-nm thick SiO_2 layer. One of the two rectangular openings is exposing the bare Pt surface, while the other is coated with a electrochemically deposited IrO_x thin film for pH sensing. (B) Schematic cross section of the Ti/Pt microelectrodes with SiO_2 layer for electrical insulation, and IrO_x coating of the pH microelectrode.

IrOx electrochemical deposition

IrO_x films were selectively electrodeposited onto the microfabricated Pt electrodes through small windows in the SiO_x insulation layer. The deposition solution was prepared based on the method described by Yamanaka [238, 263] and Marzouk [232, 252]. In our protocol, a 75-mg portion of iridium tetrachloride was dissolved in 50 ml of DI water, and the solution was magnetically stirred for 15 min. A 0.5 ml aliquot of aqueous 30% hydrogen peroxide was added, and the resulting solution was stirred for another 10 minutes. A 250-mg portion of oxalic acid dihydrate was added, and the solution was stirred again for 10 min. Small amounts of anhydrous potassium carbonate were gradually added to the stirred solution to adjust its pH to 10.5. The solution was contained and stored at room temperature for 2 days to allow for stabilization. The color of the solution changed from yellow to light-violet, indicating it could be used for a successful deposition. After stabilization, the solution was stored in a dark bottle at 4^oC in a refrigerator until use [232]. We used deposition solution for up to two months after its preparation.

All electrochemical experiments were performed with a CHI model 660A potentiostat/galvanostat (CH Instruments) in a three-electrode cell. In beaker experiments, potentials were measured relative to an Ag/AgCl (CHI 111, CH Instruments) reference electrode. The counter electrode was a Pt wire, 1mm diam., (CHI 115, CH Instruments). The IrO_x electrode potential was monitored in open circuit potential (OCP) mode. A DRIREF-450 (WPI) Ag/AgCl reference electrode, 450 μm diam., was used for pH measurement inside microchannels.

Both modes – galvanostatic and cyclic potential cycling – were used for the deposition of iridium oxide films. A constant current density of 1-1.5 mA/cm^2 applied for 500 s proved to be the optimal condition for the formation of a dark blue IrOx film in galvanostatic mode. Light-blue iridium oxide films were created by cycling 100 times between 0.0 V and 0.55 V at 75 mV/s in the potential cycling mode. The thickness of the anodic IrO_x films ranged from 0.05 to 0.1 μm, depending on the deposition method and process parameters. We used a stylus surface profiler (Alphastep 200, Tencor Instruments) to measure the thickness of the films after electrodeposition. Immediately after deposition, the pH sensitive IrO_x films were rinsed with distilled water and dried under a stream of nitrogen. Then, for comparison purposes, some of the iridium oxide microelectrodes were coated with proton-exchanging Nafion resin by momentarily dipping them into a 5% Nafion solution and subsequently air-drying them at 80^oC [232, 252]. The pH microelectrodes were ready for use after they were soaked in a universal buffer of pH 7.0 for two days, a practice which proved to be necessary in order to reduce potential drifts [232, 252]. When not in use, the microelectrodes were stored in universal buffer solution (pH 7.0) at room temperature in a dark place.

Microfluidic device fabrication

The microchannels in our microfluidic devices were fabricated by replica molding using a patterned photoresist on a silicon wafer as the master, and poly(dimethylsiloxane) (PDMS) as the biocompatible polymer (Sylgard 184, Dow Corning, Midland, MI). The master was fabricated by spinning a 20 μm layer of photoresist (SU-8 2050, Microchem) on a 3 in.-diameter silicon wafer, followed by a UV light exposure through a metal mask

using a contact mask aligner. The photoresist was processed according to the manufacturer's recommendation on the datasheet. An optional 30- minute hard bake at 200 °C was performed on a hot plate to increase the durability of the resist. The master was placed in a plastic culture dish and covered by a 5 mm layer of the PDMS/curing agent mixture at a ratio of 10:1 by weight. After curing the elastomer in the moulding dish for five hours at 60 °C in an oven, the devices were cut out and mechanically separated from the master. The feature sizes of the microfluidic networks ranged from 20-1000 μm. Access holes to the channels were punched with a sharpened stainless steel pipe. Each microfluidic device was manually aligned relative to the pH electrode by using an inverted microscope, and sealed onto the electrode/glass substrate by autoadhesion. We used glass capillaries inserted into the access holes to connect the microfluidic channels via standard microtubing (0.5 mm inner diam., Cole Parmer) to 1 ml syringes. The microsyringe pump controller "Micro 4" (WPI, Sarasota, FL) was used to control the flow of solution in the microfluidic device with flow rates ranging from 10 nl/min to 10,000 nl/sec.

A.4 Results and discussion

Properties of electrochemical IrOx films

The key characteristics of thin-film IrO_x electrochemical pH electrodes are sensitivity, response time, stability, and reproducibility. We studied these properties of our films and demonstrated the possibility of using them in microfluidic devices. We deposited IrO_x films by galvanostatic and potential cycling methods. However, our

results show that films deposited by the galvanostatic method had superior properties and therefore we will not further discuss IrO_x films formed by the potential cycling method. We incorporated miniature pH sensors in microfluidic devices with the following active electrode areas: $5 \times 10\ \mu m^2$, $20 \times 20\ \mu m^2$ and $20 \times 40\ \mu m^2$. We observed a decrease in stability and reproducibility for iridium oxide films with areas of 5 x 10 μm^2. We attribute this behavior to non-uniform film deposition, an issue which can be addressed by optimizing the electrode design and the deposition conditions. However, experiments on a small number of cells in a microfluidic device do not require electrode dimensions comparable to the cell size. We therefore chose to optimize and characterize the properties of the larger ($20 \times 20\ \mu m^2$ and $20 \times 40\ \mu m^2$) electrodes.

The analytical characteristics of IrO_x pH microelectrodes were tested before their application in microfluidics devices. The response of our IrO_x electrodes to exposure to a series of universal buffer solutions in the pH range between 4 and 10 is presented in Figure 41A. Figure 41B demonstrates a linear super-Nernstian response resulting in a sensitivity of -77.6 ± 2 mV/pH. This value agrees with results obtained in the literature for the electrochemical deposition of IrO_x on macroelectrodes [232, 252, 260]. We further developed the fabrication process, allowing for the selective deposition of IrO_x films on microelectrodes. In addition, our pH electrode sensitivity was superior compared to that of electrodes formed by other methods, like reactive sputtering [253-255] and thermal decomposition of $IrCl_3 \cdot H_2O$ [259], which typically have lower sensitivities in the range of 55 - 70 mV/pH.

As stated in [236, 265], the response of anhydrous IrO_2 films to pH changes with a slope of approximately 59 mV/pH (Nernstian response) can be explained using the following redox reaction

A

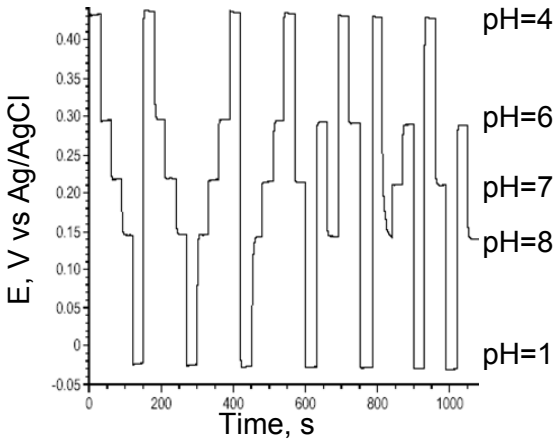

B

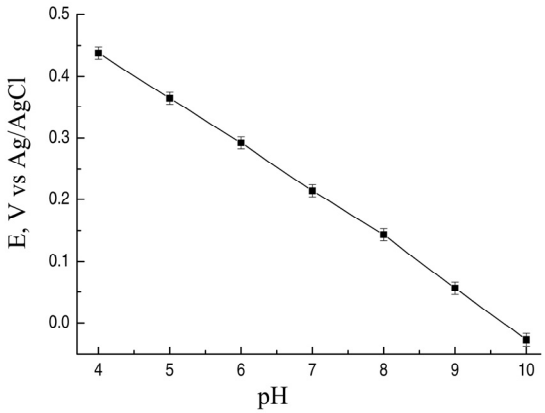

Figure 41. Calibration of microelectrodes for pH measurements. (A) Open circuit potential of a IrO_x pH electrode during periodic cycling of 5 different standard pH calibration solutions with 30 s measurement intervals.
(B) Average potentiometric response of a IrO_x pH electrode in the pH range of 4 to 10 at a temperature of 22^{o}C, The error bars represent the standard deviation for all measurement points corresponding to a particular pH.

$IrO_2 + H^+ + e^- \leftrightarrow IrO \cdot OH$

or

$2IrO_2 + 2H^+ + 2e^- \leftrightarrow Ir_2O_3 + 2H_2O$.

Hydrated iridium oxide exhibits super-Nernstian responses explained by the mechanism of one transferred electrons per 1.5 H^+ ion, resulting in a slope of approximately 90 mV/pH [236, 266]:

$2[IrO_2(OH)_2 \cdot 2H_2O]^{2-} + 3H^+ + 2e^- \leftrightarrow [Ir_2O_3(OH)_3 \cdot 3H_2O]^{3-} + 3H_2O$

Our films had near-super-Nernstian response, which suggests the prevalence of a hydrated form of iridium oxides [236, 264].

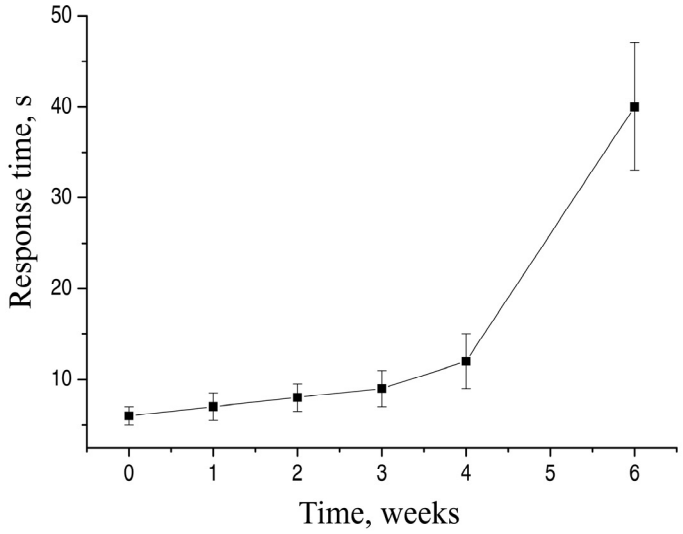

Figure 42. Response time of the IrO_x microelectrode as a function of storage time.

The sensitivity of the pH electrodes remained practically constant during 5-6 weeks storage time in pH 7 buffer solution, as previously described. Dry storage of IrO_x electrodes led to noticeable sensitivity decrease of typically 20-30%. Soaking these electrodes for 1 h in buffer solution restored their sensitivity to the original value.

We observed a substantial influence of the age of the deposition solution on the sensitivity of the IrO_x pH electrodes. Iridium oxide films deposited from fresh solution showed the maximum sensitivity of -77 mV/pH. We observed practically no change from process to process (± 1-2 mV/pH) up to a shelf life of 1 month for the deposition solution. The films deposited from solutions older than 1 month showed a 10-15 % decrease in sensitivity, and a spread in sensitivity reproducibility of ±5 mV/pH.

The potential drift during pH measurements is another important characteristic of IrO_x electrodes. We used standard buffer solutions in the pH range of 4-10 to calibrate the deposited IrO_x films. We recorded the OCP of the IrO_x electrode relative to the Ag/AgCl reference at room temperature.

In order to quantify potential drifting we placed the IrO_x electrodes and the reference electrode in 50-ml beakers with different buffer solutions according to the following procedure. The potential measurement corresponding to each pH buffer was conducted for 30 s, which proved to be long enough to reach steady state in the potential response for fresh electrodes. Then, the potential measurement was paused while the pH buffer solution was replaced by a different one.

These kinds of measurements were usually conducted within 2 hours, with a total of 200 alternations among buffer solutions. Figure 41a shows typical kinetics of electrical potential for iridium oxide pH electrodes ($20 \times 20\ \mu m^2$) exposed to different buffer

solutions. Usually, the potential drift was ± 2-3 mV for each buffer solution. This phenomenon is identified in the literature as "hysteresis of the sensor response." The drift is typically ± 2 mV for IrO_x-coated Ti wires [252]. Fast response times are crucial for biological experiments in microfluidic devices. Therefore, we quantified response times of the IrO_x pH microelectrodes and their long-term behavior. As usually described in the literature, the response time of pH electrodes is defined as the time required to reach 90 % of the equilibrium value [267, 268]. The typical response time of our pH microelectrodes was 6 s within one week of deposition. A 50% increase in the response time was observed for the first 3 weeks of aging, as well as a two-fold increase of the standard deviation, as shown in Figure 42. After four weeks of aging, we observed a 100% increase in the response time relative to the freshly deposited IrO_x pH electrodes. These data are in close agreement with the response times reported in the literature, which range from 5 to 15 s for 1 mm IrO_x-coated wire pH electrodes [232, 252]. This response-time range is suitable for many biological applications including pH measurement. Aging of more than four weeks caused substantial increase in the response time of the pH electrodes — over 40 s on average — which is obviously unacceptable in many cases. This study demonstrated that our electrochemically deposited IrO_x electrodes can be used within a month of their formation, provided that the characteristic times of processes intended to be measured are longer than the pH electrode response time. Several publications describe the use of Nafion layers to minimize the interfering effects associated with anion redox species and for protection of the sensor surface from aggressive solutions [252, 254]. We conducted analogous studies to investigate the protection of IrO_x films by dip coating with Nafion. However, we found that Nafion

deposition caused substantial increases in response time, which reached 150–200 s for dip-coated Nafion layers post baked between 60-100 ºC.

We also investigated the compatibility of bare IrO_x sensing electrodes and cell culture media using different buffer solutions (Dulbecco Modified Phosphate Buffered Saline (DPBS), with and without Hepes) used for cell growth, and found no degradation in the sensing properties. Therefore, we used IrO_x without Nafion coating in all subsequent experiments.

In summary, our results showed that IrO_x films formed by using the galvanostatic method have near-super-Nernstian response: -77.6 ± 2 mV/pH in the 4-10 pH range. We measured potential drifts of 2-3 mV and response times ranging from 6 to 12 seconds for up to one month of storage. IrO_x thin-film pH-sensing microelectrodes with such characteristics were integrated into our microfluidic devices, as described in the following paragraphs.

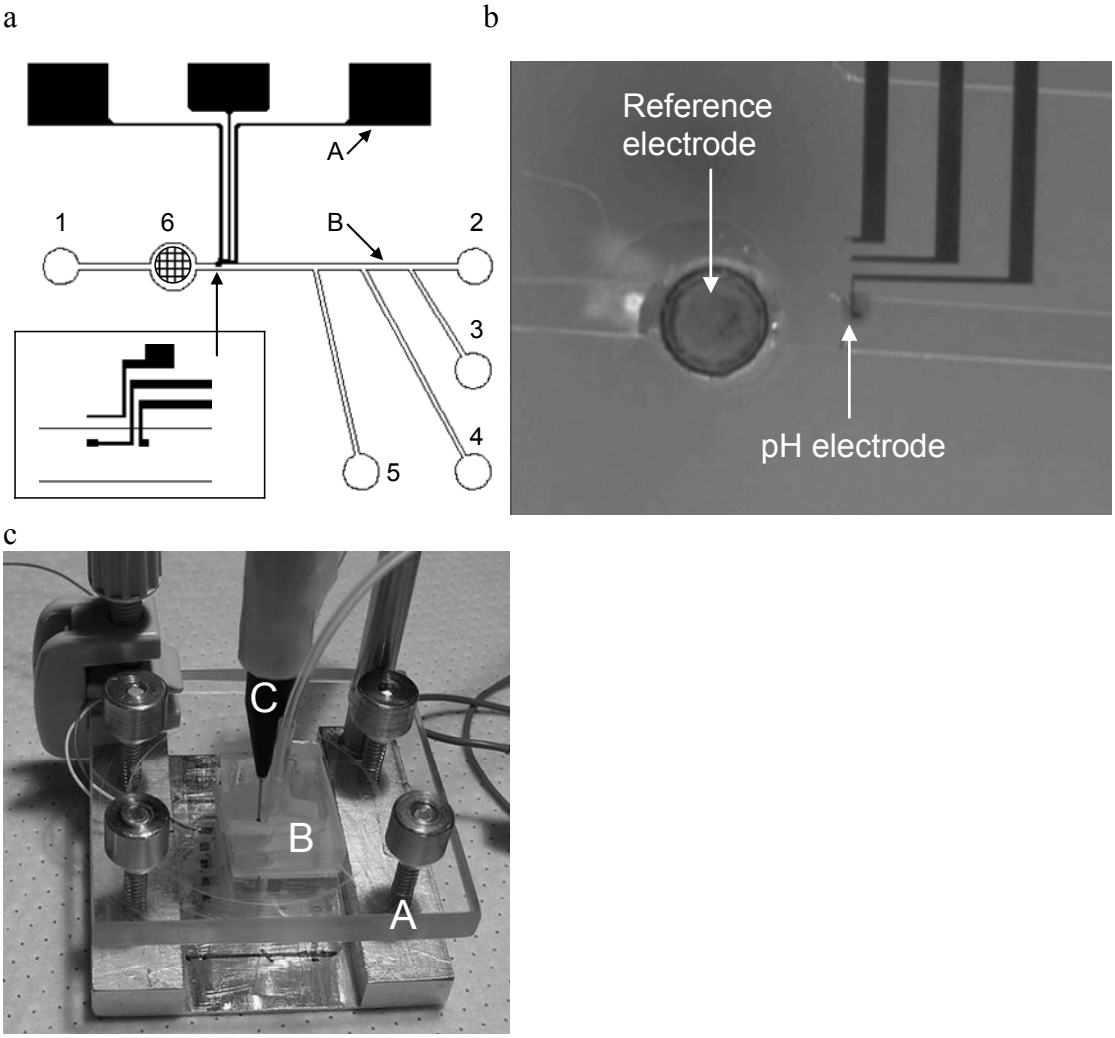

Figure 43. (a) Schematics of a microfluidic device for investigating the properties of our pH microelectrodes (A) in microfluidic channels (B). 1 – waste channel; 2, 3, 4, and 5 – input channels for DI water, pH 6, 7, 8 buffer solution, respectively; 6 – Ag/AgCl reference electrode; The inset shows a detailed view of the pH microelectrode in the sensing channel. (b) Optical image of the sensing channel with pH microelectrode and Ag/AgCl reference electrode. (c) Picture of the clamp mechanism (A), which ensures a reliable seal between the PDMS block containing the microchannels (B), Ag/AgCl reference electrode (C) and the glass substrate with thin film microelectrodes.

A schematic drawing and a microscope image of our microfluidic device with multiple input ports are shown in Figure 43a and b, respectively. The device was comprised of a PDMS microchannel network auto adhered to a glass slide patterned with an array of platinum microelectrodes, one of which was coated with IrO_x for pH sensing. Additionally, we used a clamp to provide mechanical stability and to achieve a good seal between the elastomer and the substrate (Figure 43c). This assembly was mounted on a microscope stage for observation. The microchannels were designed to direct buffer

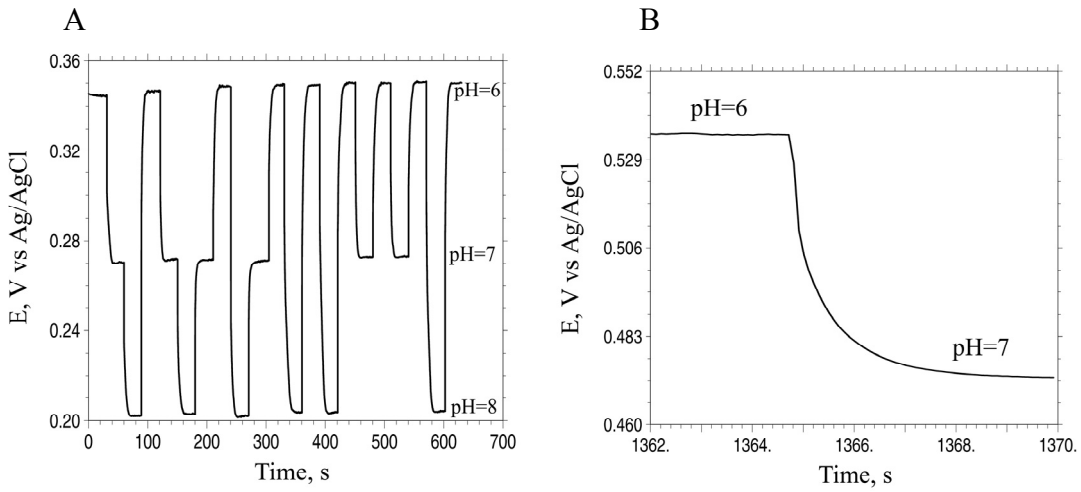

Figure 44 (A) Open circuit potential of IrO_x pH microelectrode inside the microfluidic sensing channel during exposure to different standard pH calibration solutions in 30 s measurement intervals. (B) Potential transient after a step-like change of the calibration solution by one pH unit.

solution across the IrO_x pH electrode ($20 \times 20\ \mu m^2$) and the reference electrode (450 μm diam.) located in the sensing channel. The calibration of pH electrodes in the microfluidic channel was done in the biologically relevant pH range of 6-8, as these electrodes were intended to be used for the acidification-rate measurements of various living cells. Input

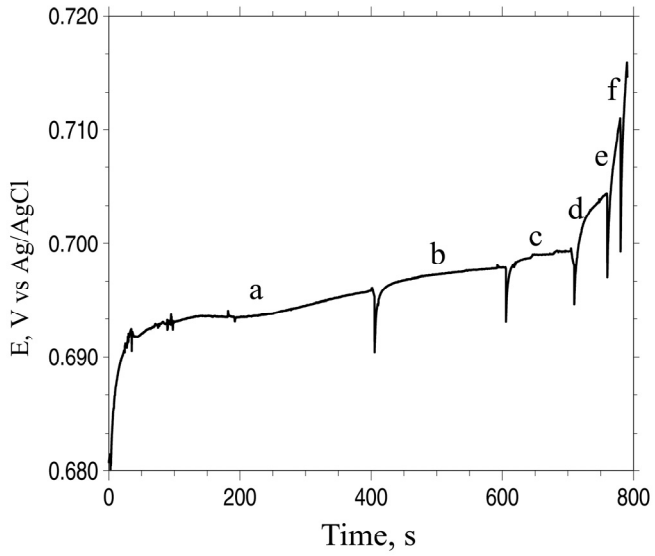

Figure 45. Open circuit potential of the IrO_x pH microelectrode for different flow rates of solution in the microfluidic channel. *a* corresponds to a flow rate of 250 nl/s, *b* 500 nl/s, *c* 1000 nl/s, *d* 2500 nl/s, *e* 5000 nl/s, and *f* 10 000 nl/s.

channels 3, 4, and 5 were designated for the delivery of buffer solutions with pH 8, 7, and 6, respectively. Input channel 2 was used for DI water delivery to flush the working area. Calibration of the IrO_x pH electrodes was conducted by repeating the following steps: (i) filling the sensing channel with buffer solution of known pH; (ii) measuring the resulting OCP between the reference and the IrOx electrodes. The calibration process for pH electrodes consisted of more than 100 changes of buffer solutions. Data from an

exemplary calibration of IrO_x pH microelectrodes in our microfluidic device are shown in Figure 44. Each individual measurement was performed for 30 s. We determined the maximum deviation from the average potential for each individual pH level to be 2 mV over the course of the 1-hour calibration. The sensitivity of these electrodes was in the range of 70-78 mV/pH. A fast response is an important requirement for IrO_x pH electrodes in microfluidic applications. Figure 45 shows the typical response of an IrO_x pH microelectrode to a change of 1 pH unit in the sensing channel. The response time extracted from the data was 5 s. In summary, measurements taken with our IrO_x pH microelectrodes in microfluidic channels were virtually the same as those from macroscopic experiments in beakers, with respect to sensitivity, potential drift, and response time.

Next, we investigated the performance of the IrO_x sensing electrodes in our microfluidic devices under flow conditions ranging from 10-10,000 nl/s. We observed that flow rates < 200 nl/s did not result in a considerable potential increase. The behavior of the OCP at six different flow rates above 200 nl/s is depicted in Figure 45. We used the same volume of buffer solution for each segment, therefore the measurement interval decreased with increasing flow rate. The spikes depicted in the graph were caused by the adjustments between flow rates. We noticed a constant potential increase of 0.6 mV/min for the first three flow rates, which ranged from 250 to 1000 nl/s (marked *a*, *b* and *c* in the graph). The potential increase reached 6 mV/min for 2500 nl/s, 30 mV/min for 5000 nl/s and became irreproducible for flow rates above 10,000 nl/s. However, for flow rates between 200 and 1000 nl/s, the potential increase was quite reproducible, a behavior which allowed pH measurements to be conducted at these flow rates. The reason for this

potential increase is not well understood, however Marzouk *et al.* reported similar changes in the electrode characteristics at increased flow rates for IrO_x-coated Ti wire in a flow-injection-analysis device [232]. We did not investigate this effect further because

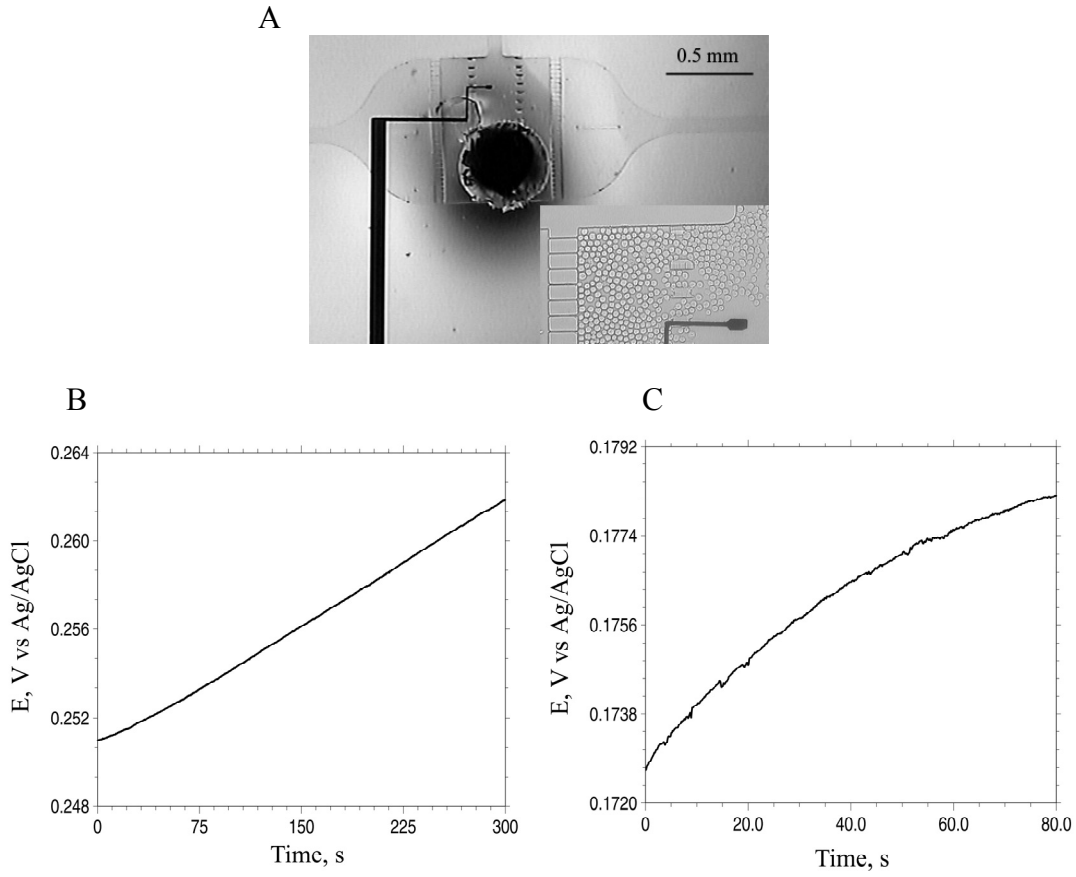

Figure 46. Test of the thin film pH microelectrode in a microfluidic device (a) Optical image of the pH sensing, reference electrode and a 25 nl cell culture volume filled with fibroblast cells for acidification measurements. The inset shows a close view of the sensing volume, the pH microelectrode and the filter structure used to trap cells. (b) Time course of the Open circuit potential of the IrO_x pH microelectrode during an acidification rate measurement for A9 L HD2 fibroblast cells.
(c) Acidification rate measurement of M3 WT4 CHO cells.

flow rates > 200 nl/s are unrealistic for cell culture experiments in lab-on-a-chip devices with nl culture volumes.

Incorporation of IrOx microsensors into nl cell culture volumes

The metabolic activity and the physiological state of a living cell can be characterized by the rate at which the cell produces acidic byproducts. In order to record metabolic changes of a small number (1-1000) of cells in multiple wells in a parallel approach for high throughput drug screening applications, it is necessary to scale down the sensor size and provide fluidic access to the cell culture volume for perfusion and drug delivery. We used an optically-transparent PDMS polymer in combination with our miniature pH sensing electrodes to fabricate microfluidic-based microsystems to achieve this goal. The optical transparency would allow for parallel fluorescence measurements for a multi parameter assessment of cell physiology.

Such a device, as shown in Figure 46A, can be mass-produced, each unit consisting of a glass substrate with thin-film IrO_x pH microsensors and a PDMS microfluidic network containing a 25 nl cell culture volume connected to perfusion and cell-seeding channels. A magnified image, showing live fibroblasts and the thin-layer IrO_x pH electrode, is presented in the inset of Figure 46A. All cells were grown in T-flasks to 85% confluency. Medium was removed; cells were washed with DPBS (Dulbecco Modified Phosphate Buffered Saline) and detached by a trypsin treatment. Detached cells were suspended in growing medium. Immediately before starting pH measurements, the cell medium was replaced with modified RPMI 1640 with low buffering power (1 mM PBS). The cells were then seeded into our PDMS Nanobioreactor, which had the following dimensions:

1000 μm wide, 1000 μm long, 25 μm high, and a total volume of 25 nl. Cells were loaded by applying a vacuum to either perfusion channel, thereby pulling the cells from the seeding channel into the Nanobioreactor chamber.

The cells were confined by two 3-μm filters located at the entrance of the left and right channels. We successfully trapped most of the administered fibroblast and CHO cells, which have diameters of about 11-18 μm and 10-12 μm, respectively.

After seeding 10-25% of the surface area with cells, we stopped the media flow by releasing the vacuum, and we started to record the OCP between the IrO_x and the Ag/AgCl reference electrode. The results are presented in Figure 46B and C for fibroblast and CHO cells, respectively. The potential changes are directly proportional to pH variations inside the Nanobioreactor chamber and can be expressed in pH units if divided by the electrode sensitivity of -70 mV/pH. We observed a near-linear signal increase, which corresponded to an acidification rate of 0.03 pH min^{-1} for fibroblast cells, presented on Figure 46B. After a deviation from linearity was observed we stopped measurements because the pH was beyond the physiologically relevant range. After the experiment the sensitivity of our pH electrodes was re-measured and we found no degradation. However, there could be a sensitivity change in long term experiments when the electrodes are exposed to small organic molecules and proteins produced by the cells [269]. Similar measurements were conducted using CHO cells as shown in Figure 46C. Based on these data we calculated an acidification rate of 0.06 pH min^{-1} for the linear region of the graph. The larger acidification rate for the CHO cells was expected since they are metabolically more active than fibroblast cells. Comparable acidification rates are reported in the literature [241, 245].

A.5 Conclusions

We developed planar pH microelectrodes with dimensions smaller than 500 μm^2 on transparent glass slides using selective electrochemical deposition of IrO_x onto lithographically-defined Pt thin-film electrodes. The IrO_x pH microelectrode was incorporated as a transducer into a microfluidic-based PDMS device with a 25 nl cell culture volume. The characteristics of our IrO_x pH electrodes were highly reproducible: sensitivities of -77.6 ± 2 mV/pH, potential drifts of 2-3 mV/month (static solution), and response times of 5-15 s within one month of deposition. The properties of our pH electrodes did not change when incorporated into microfluidic devices. We demonstrated for the first time the use of IrO_x microelectrodes for acidification rate measurements in nl on-chip cell culture volumes for CHO cells and fibroblast cells. The average acidification rates were 0.03 pH min^{-1} and 0.06 pH min^{-1} for fibroblast and CHO cells, respectively, and are in agreement with previously published data. Our results demonstrate the feasibility to scale down pH electrodes and cell culture volumes to measure acidification rates in volumes less than 1 nl.

Acknowledgments

We especially thank John Wikswo and Ales Prokop for helpful discussions, Eugene Kozlov for culturing CHO and fibroblast cells and Ron Reiserer for technical assistance. This work was supported in part by DARPA under ONR contract N66001-01-C-8064, and the Vanderbilt Institute for Integrative Biosystem Research and Education (VIIBRE).

Note

This manuscript has been published in Biosensors and Bioelectronics, Vol. 21, pp. 248-256, November 2004, with the following list of authors:

Igor A. Ges, Borislav l. Ivanov, David K. Schaffer, Eduardo A. Lima, Andreas A. Werdich, Franz J. Baudenbacher

Department of Biomedical Engineering, Vanderbilt University, Nashville, TN, USA

APPENDIX B

FATTY ACID β-OXIDATION DEFECTS, BIDIRECTIONAL VENTRICULAR TACHYCARDIA, AND RYANODINE RECEPTOR DYSFUNCTION IN VLCAD NULL MICE

B.1 Abstract

Familial catecholaminergic polymorphic ventricular tachycardia is characterized by polymorphic ventricular tachycardia, bidirectional ventricular tachycardia (BVT), and a high risk of sudden cardiac death. Recently, mutations involving the cardiac ryanodine receptor (RyR) and calsequestrin have been identified in patients with these arrhythmias. Patients with mutations in the mitochondrial very-long-chain Acyl-CoA dehydrogenase (VLCAD) enzyme are also at risk for sudden cardiac death. Here we identify a novel mechanism of fatty acid and catecholamine-dependent BVT due to cardiac RyR dysregulation in mice lacking VLCAD (VLCAD-/-). These mice exhibit: VT with the typical bidirectional morphology with isoproterenol infusion, increased levels of cardiac ryanodine receptor 2, increased [^{3}H] ryanodine binding in heart microsomes, and enhanced intracellular calcium release at the cardiomyocyte level. Both the amplitude and rate of intracellular SR Ca^{2+} release was increased in single cardiac myocytes isolated from VLCAD-/- mice, while the L-type Ca^{2+} current (I_{Ca}) was not changed. Diastolic cytosolic calcium as measured by indo-1 fluorescence was higher in VLCAD-/- cells suggesting an increase in the time-independent cytosolic and mitochondrial Ca^{2+} concentration. This defect in calcium homeostasis was not seen in VLCAD wild type controls. We conclude that mitochondrial VLCAD deficiency represents a novel

mechanism of ryanodine receptor channelopathy leading to abnormal intracellular calcium handling and arrhythmias in mice and perhaps also in VLCAD deficient humans.

Key Words: | genetics - inborn errors| VLCAD| Ryanodine Receptor| Mitochondria| Calcium| Catecholaminergic and bidirectional ventricular tachycardia.

B.2 Introduction

Children with mitochondrial very-long-chain acyl-CoA dehydrogenase deficiency (VLCAD) are usually diagnosed at presentation in the clinic by episodes of metabolic crisis and death. Deficiencies in these mitochondrial fatty acid oxidation (FAO) enzymes have been implicated in cardiomyopathy, arrhythmias, and sudden unexpected death, as well as in a variety of other illnesses [270]. Phenotypes of FAO deficiency in humans include non-ketotic hypoglycemia, heart and liver lipidosis, encephalopathy, skeletal myopathy and sudden death. VLCAD deficiency (the focus of this report) causes ventricular tachycardia (VT) in almost 50% of the presenting cases [271-275]. Most of the cases of sudden death occur in the first year of life. The molecular mechanisms of arrhythmias associated with these defects have yet to be delineated. Survival into adulthood is possible, but long-term follow-up of patients who survive both the infancy and childhood periods has not been carried out. Thus, it remains unknown whether older patients with these defects contribute to a subset of cases with familial or catecholaminergic ventricular tachycardia.

While VLCAD is a mitochondrial protein encoded by a nuclear gene [276], ryanodine receptors are intracellular Ca^{2+} release channels, mainly clustered in the root structures of the sarcoplasmic reticulum of striated muscles. The RyRs are characterized by their large size and four-fold symmetry [277]. Three distinct isoforms encoded on different

chromosomes share about 2/3 sequence homology [278]. The RyRs are hetero-oligomers consisting of four RyR protomers and four FK 506 (tacrolimus) binding proteins (FKBP) [279]. The RyRs have a mass of 2.3megaD, (the protomers are about 0.56megaD) while FKBP is approximately 12kD [279, 280]. RyRs are now known to be widely distributed in tissues. In skeletal muscle, RyR1 is morphologically identical to the foot-structures spanning the gap between the terminal cisternae of SR and the sarcolemma/ transverse tubules (T-tubule) [281]. Similar morphological structures have been identified and characterized in cardiac muscle fractions for RyR2 [282]. The third isoform, RyR3 is widely expressed in a variety of tissues but in minuscule amounts. The functional characteristics of RyR1, RyR2 and RyR3 have been studied in isolated SR membrane fractions as well as in purified receptors. Mutations in the cardiac ryanodine receptor (RyR2) gene are known to cause both catecholaminergic polymorphic ventricular tachycardia (CPVT) - also termed familial polymorphic ventricular tachycardia (FPVT), or bidirectional VT [283-286] and arrhythmogenic right ventricular dysplasia (ARVD2) [287, 288]. These mutations cause abnormalities in the regulation of channel activity. A "gain-of-function" or increased Ca^{2+} leak from the sarcoplasmic reticulum (SR) has been proposed [289]. In this paper, we use our mouse model of VLCAD deficiency [227], to show a novel role for mitochondrial fatty acid β-oxidation defects in disturbances of calcium homeostasis in heart. The working hypothesis of our study was to test whether mitochondrial VLCAD deficiency leads to functional changes in the cardiac ryanodine receptor at the subcellular level, with enhanced intracellular Ca^{2+} release from the sarcoplasmic reticulum (SR) that is reminiscent of human cases with defective RyR2

channels. Here, we also discuss the possible role for FAO defects in the clinical manifestations of affected patients with these inherited arrhythmogenic diseases.

B.3 Materials and Methods

VLCAD deficient mice

All animals in this study were cared for according to the Institutional Animal Care and Use Committee (IACUC) at Vanderbilt University. Mice were generated and genotyped as previously described [227, 290]. Upon sacrifice or at autopsy, whole heart ventricles and skeletal muscle (slow- and fast-twitch) were harvested for total protein. Immunoelectron microscopy was performed in heart tissue from two month old VLCAD +/+ and VLCAD -/- mice.

Preparation and characterization of subcellular fractions from different organs

Hearts and other organs are harvested from euthanized animals in conformity with the IACUC animal care codes. Subcellular fractionation was performed by the method of Chamberlain and Fleischer [291]. The resulting subcellular fractions or pellets were resuspended in a small volume of resuspension buffer, flash-frozen in liquid nitrogen and stored at -80ºC.

[^{3}H] Ryanodine Binding Assay.

[^{3}H] ryanodine binding was determined at 60 nM ryanodine as described previously [278]. Summarizing the process briefly, cardiac microsomes (50 µg) were incubated in 50µl of buffer containing 10mM K-HEPES, pH 7.4, 1M KCl, 25µM CaCl2, and 60nM [3H]ryanodine (~15,000 cpm/pmole, obtained from Amersham) for 1 h at room

temperature. Nonspecific binding was measured in the presence of 20μM cold ryanodine (Sigma). Free ligand was separated from the bound by sedimenting the microsomes in a Beckman TL-100.1 rotor at 95,000 revolutions / min for 15 min at 4ºC. The supernatant was removed by aspiration, the pellets rinsed twice and resuspended in 200 μl water, and the radioactivity was measured in 5 ml of Cytoscint (ICN, Cleveland, OH) in a Beckman LS 5000TD scintillation counter.

Calcium loading assays using antipyrylazo III

Calcium loading assays were performed in a diode array spectrophotometer. Ca^{2+} loading assay medium consisted of 100 mM potassium phosphate buffer, pH 7, 1 mM of $MgCl_2$, 0.2mM antipyrylazo III, and 50 μg of protein. Na_2ATP (1 mM) was added, and the reaction was initiated by addition of 50 μM $CaCl_2$ (antipyrylazo III is used as the metallochromic indicator). Measurement of the difference in absorbance between 710 and 790 nm was done at 37 ºC. Ruthenium red (10 μM) was added to selected samples 70 seconds after the reaction has been initiated to block Ca^{2+} leak from the SR. A general formula was used to calculate the rate of Ca^{2+} loading as previously published [292].

Preparation of ventricular myocytes

VLCAD knockout and wild-type control mice were anesthetized by intraperitoneal injection of Avertin solution (5mg Avertin per 10 g body weight, T48402, Sigma-Aldrich) containing Heparin (3 mg/10ml, H9399, Sigma-Aldrich). The heart was rapidly excised and placed into ice-cold Ca^{2+}-free Hepes-buffered normal Tyrode (NT) solution. The aorta was cannulated and the heart was perfused with Ca^{2+}-free NT solution at room

temperature for 10 min to stop contractions. The NT solution contained (in mM): Na^+ 140, K^+ 4.5, Mg^{2+} 0.5., Cl^- 150, $H_2PO_4^-$ 0.4, HCO_3^- 10, Hepes 10, glucose 10. The perfusion was switched to NT solution containing 10μM Ca^{2+}, collagenase (178 U/ml, CLS2, Worthington Biochemical) and protease (0.64 U/ml, P5147, Sigma-Aldrich) for 12 min at 37 ºC. Tissue from the atria and aorta was discarded. The remaining ventricular tissue was coarsely minced and placed into NT solution containing bovine serum albumin (10 mg/ml, A9647, Sigma-Aldrich). Myocytes were dissociated by gentle agitation. Ca^{2+} concentration in the working solution was increased from 0.1 mM to 0.5 mM. For the glucose-free experiments, glucose was replaced by palmitic acid (10 μM, P0500, Sigma-Aldrich) in all solutions. Cells were stored in 0.5 mM Ca^{2+} Tyrode solution until used, usually within 3 hours after isolation.

Measurement of indo-1 calcium transients

Dissociated cardiomyocytes were loaded with 20 μM of an acetoxymethyl ester form of the Ca^{2+}-sensitive fluorescence dye indo-1 (I1203, Molecular Probes-Invitrogen). Cells were kept in this solution for 15 min at room temperature and then centrifuged at 27 g for 10min. The supernatant was removed and the cells were re-suspended in glucose free Tyrode solution containing 1.0 mM Ca^{2+}. Experiments were started approximately 30 min after washing to allow complete de-esterification of the fluorescent dye. To minimize phototoxic effects on Ca^{2+} transients, only 100 ul of stained cells were pipetted into the bath solution which was completely replaced after each exposure to the excitation light. The bath contained glucose free Tyrode solution with 1.0 mM Ca^{2+} at 37ºC, supplemented with an insulin/transferrin/selenium mixture (100X medium supplement,

41400, consisting of 10 µg/ml insulin, 5.5 µg /ml transferrin, 6.7 ng/ml sodium selenite, Gibco-Invitrogen) to improve the performance of the isolated cells at the high stimulation frequencies [293]. Myocytes were field stimulated at the physiological rate of 600 beats per minute via two parallel platinum wires. Fluorescence measurements were carried out using an inverted microscope (Axiovert 200, Carl Zeiss, Germany) equipped with a 63X, 1.4 NA oil immersion lens (Plan Apochromat, Carl Zeiss, Germany). The excitation light was emitted by a monochromator (Optoscan, Cairn Research Ltd, UK) at a wavelength of 365 ± 15 nm and reflected by a 390 nm dichroic mirror (390DRLP, Omega Optical). The fluorescence emission was split into two components by a second dichroic mirror (450DCLP, Omega Optical). The transmitted light was passed through a 495 ± 10 nm (495DF20, Omega Optical), and the reflected component was passed through a 405 ± 21 nm bandpass filter (405DF43, Omega Optical). The light from each wavelength was collected by 1 mm diameter optical fibers mounted directly behind the emission filters imaging a ~16 µm diameter spot on the cell. The light from each fiber was collected by photomultiplier modules (H6780, Hamamatsu) and amplified by a custom-built low-noise DC coupled amplifier. The signals were digitized at a sampling rate of 20 KHz by an A/D converter board (PCI-6071E, National Instruments) in a conventional PC.

Fluorescence calibration

Intracellular Ca^{2+} measurements were converted to free $[Ca^{2+}]_i$ according to the equation [110]: $[Ca^{2+}]_i = K_d \beta [R-Rmin]/(Rmax-R)]$, using an in vivo dissociation constant of the dye of 844nM [146]. The β value, the ratio of the free to the bound indo-1 fluorescence was measured at 485nm. Rmin and Rmax were determined *in vivo* as previously

described [146]. Indo-1 loaded cells were exposed to 10 mM caffeine twice to empty the SR stores and subsequently superfused with Ca^{2+}-free Tyrode solution. The bath solution was then replaced with a Ca^{2+} buffer solution containing 5 mM EGTA and 10 μM of the nonfluorescent ionophore Br-A23187 (B7272, Sigma-Aldrich). Measurements were taken after the fluorescence reached stable values at both wavelengths. For Rmax determination, the metabolic inhibitor cyanide p-(trifluoromethoxy)-phenylhydrazone (3μM, C2920, Sigma-Aldrich) was added to the solution to avoid spontaneous contractions during the increase of the extracellular Ca^{2+} concentration. Cells were perfused for 15 min with EGTA-free solution containing 15 mM Ca^{2+} before Rmax was measured. The Ca^{2+} ionophore was present throughout the entire experiment.

Sarcomere contraction measurement

Sarcomere contraction was measured in single cells using a commercial contractility measurement system (Ionoptix) consisting of a 240 frames-per-second CCD camera (MYO100, Ionoptix) connected to a side port of the microscope, a frame grabber PC card (FRGRAB, Ionoptix) and an analog/digital converter (DSI200, Ionoptix) to record the stimulus. Data were acquired using the Ion Wizard software. Cells were field-stimulated at 240 beats per minute to obtain 60 data points for each contraction at the maximum acquisition rate of 240 frames per second. Although faster stimulation rates are more physiological and desirable, the limiting camera frame rate reduced the number of data points per contraction at higher frequencies.

Electrophysiology

L-type Ca^{2+} current (I_{Ca}) was recorded in whole-cell mode voltage clamp configuration according to previously published methods [294]. Briefly, pipettes (2-3 MΩ) contained (in mM): Cs^{+} 120, Ca^{2+} 3, Cl^{-} 126, MgATP 1, NaGTP 1, phosphocreatine 5, HEPES 10, EGTA 10 [295]. The pH was adjusted to 7.2 with CsOH. The bath solution contained NT solution as described above with 10 μM palmitic acid and 1.8 mM Ca^{2+}. Holding potential was -90 mV. I_{Ca} was measured during 500 ms test pulses at potentials from -40mV to +40mV following a 50 ms pulse at -50 mV to inactivate the Na^{+} current [158, 169].

Data analysis and statistics

Data were expressed as means ± SEM. Statistical analysis was performed by Student's t-test between VLCAD-/- and VLCAD+/+ myocytes. Data were analyzed with Matlab (R14, The MathWorks, Inc.). Ca^{2+} release and uptake, as well as sarcomere contraction and relaxation were fit to empirical mathematical functions for the purpose of calculating release and contraction rates by numerical differentiation. Ca^{2+} release was best fit by a modified model of RyR activation previously published [121]:

$[Ca^{2+}]_i(t)=[Ca^{2+}]^{max}\cdot(P(t)/1-P(t))^n$, where t is time, $[Ca^{2+}]^{max}$ is the peak Ca^{2+} release, and P(t) the time-dependence of the Ca^{2+} release described by $P(t)=(1-e^{-t/\tau})m$. The parameters τ, n and m were used as fit parameters. Ca^{2+} uptake was best fit by a sum of two exponential function $[Ca^{2+}]_i=Ae^{-t/\tau1}+Be^{-t/\tau2}$ where A, B, τ1 and τ2 were used as fit parameters. Sarcomere contraction and relaxation were fitted by the same functions after replacing the Ca^{2+} concentration by the sarcomere length in each equation.

Data were expressed as means ± SEM. Statistical analysis was performed by Student's t-test between VLCAD-/- and VLCAD+/+ myocytes.

B.4 Results

Polymorphic ventricular tachycardia and bidirectional VT in VLCAD deficient mice

VLCAD +/+ and VLCAD-/- mice were used for this report. These mice, although viable, demonstrated easily inducible VT in the absence of physiological stress [290]. Ventricular tachycardia in the VLCAD deficient mice was consistently polymorphic. VT with the typical bidirectional morphology with isoproterenol infusion is shown in Figure 47 and is characteristic of patients with catecholaminergic ventricular tachycardia. Using programmed ventricular stimulation, ventricular tachycardia could be induced in 6/12 (50 %) of VLCAD deficient mice compared with 2/16 (12 %) wild-type mice. Inducibility of ventricular tachycardia was increased in the VLCAD-/- mice to 10/12 (83 %) when isoproterenol was used, while isoproterenol did not increase arrhythmia inducibility in wild type mice.

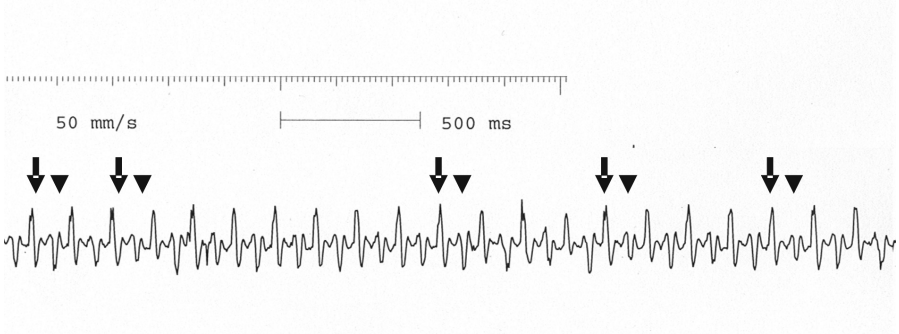

Figure 47. Surface electrocardiogram (lead I) during VT in a VLCAD-/- mouse. ECG recording of bidirectional VT in a VLCAD-/- mouse. Arrows indicate positive QRS complexes and arrowheads indicate negative QRS complexes. The alternating QRS axis in lead I is typical of bidirectional VT.

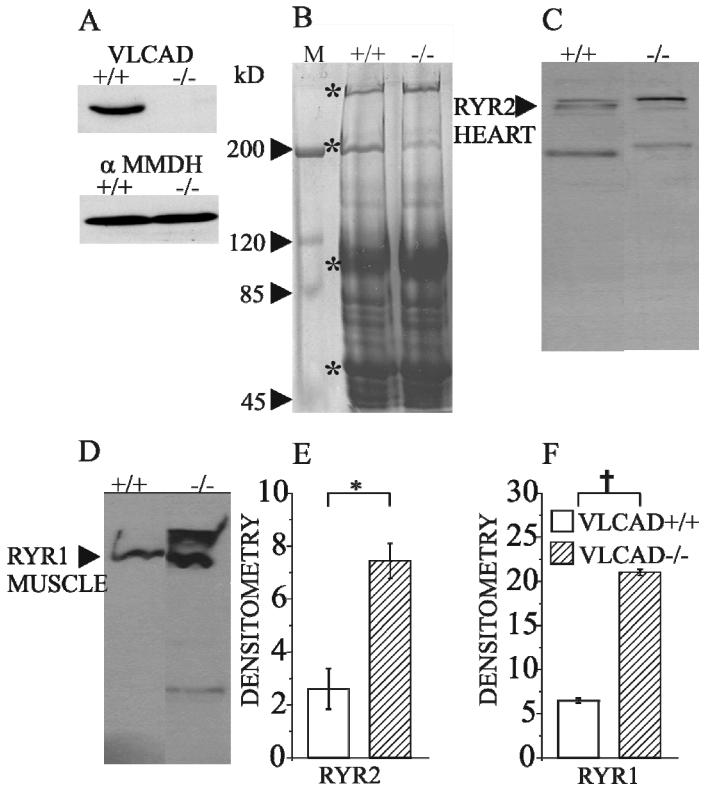

Figure 48. Western blots for cardiac and skeletal muscle RyR isoforms. (A) Western blot from whole heart for VLCAD, in wild type (+/+, VLCAD+/+) and homozygous deleted (-/-, VLCAD-/-), control lane, α-MMDH, Mitochondrial Malate Dehydrogenase. (B) SDS-PAGE for subcellular fractions as observed with Coomassie Blue. Lane 1 M = Marker, lane +/+ = heart microsomes from the VLCAD+/+ mice, lane -/- = microsomes from the VLCAD-/- mice. Asterisks denote typical characteristics of microsomal fractions from top to bottom (RyRs, myosin, Ca^{2+} pump, and calsequestrin) as previously described [1]. Protein expression by Western blot analyses for the RyRs at two months of age in wild-type (+/+, VLCAD+/+) and homozygote deleted (-/-, VLCAD-/-). 45 μg of total protein was loaded per lane. (C) RyR2 expression in heart microsomes. (D) RyR1 expression in skeletal muscle microsomes. The faster mobility bands below the RyRs in C and D have been previously referred to as proteolytic cleavage products of the RyRs. (E and F) corresponding densitometry for protein levels of RyR2 and RyR1 respectively. All data are in mean ± SE from three experiments (* $p<0.01$, † $p<.0002$, VLCAD+/+ vs. VLCAD-/-).

Increased expression of ryanodine receptor 2 isoform in mouse hearts with fatty acid β-oxidation deficiency

Bidirectional VT is linked to excessive RyR activity [289]. We tested whether the RyRs were differently expressed in the VLCAD deficient mouse.

Western blot analyses using isoform specific antibodies showed a 3.0 ± 0.8 fold increase in RyR2 expression in VLCAD-/- mice compared with VLCAD +/+ hearts ($p<0.01$, Figure 48B). We subsequently performed western blot analyses in skeletal muscle and brain tissue homogenates to assess the expressions of RyR1 and RyR3. We found that in VLCAD-/- mice RyR1 levels were increased 3.3 ± 0.1 fold in skeletal muscle, ($p<0.0002$, Figure 48C), and RyR 3 levels were increased 2.4 ± 0.8 fold in brain homogenates (data not shown). Densitometry to quantify RyR1 and RyR2 expression is shown in Figure 48E and F, respectively. Overexpression of RyR2 was confirmed in cardiomyocytes from VLCAD-/- hearts by immunoelectron microscopy (Figure 49A VLCAD+/+, B VLCAD-/-, C Negative control). We also quantified immunogold particles in the vicinity of the Z-line. The number of gold particles in the vicinity of the z-line was 10 ± 4 particles for the VLCAD+/+ and 19 ± 4 particles for the VLCAD -/- mice ($p<0.03$, Figure 49D). Given a previous report of RyR localization in the mitochondria [296], we also quantified gold particles present in the mitochondrial cristae of VLCAD+/+ and VLCAD-/- mice. The number of gold particles in the mitochondrial cristae was 4 ± 2 particles for the VLCAD+/+ mitochondria and 9 ± 3 for the VLCAD-/- mitochondria ($p<0.003$, Figure 49D).

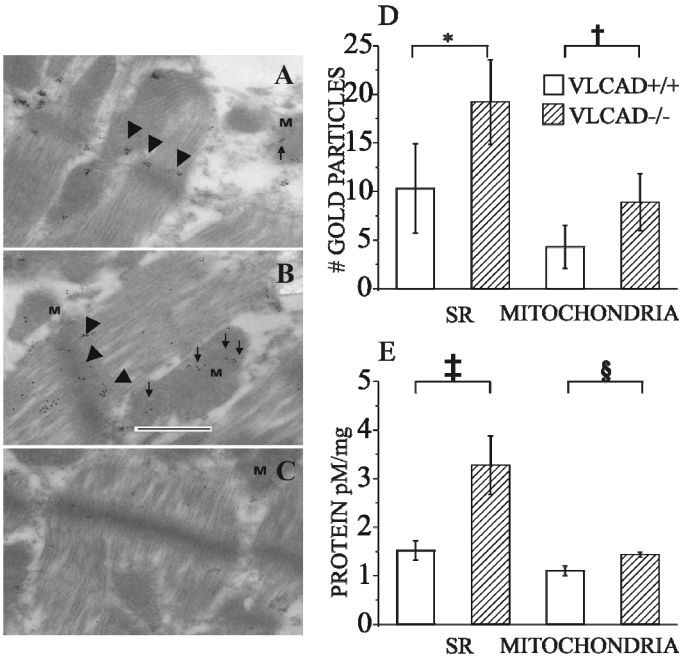

Figure 49. Representative immunogold staining of RyR2 in mouse heart and 3[H]ryanodine binding assays. A to D are related to RyR 2 specific antibody labeling of the myocardial sarcomeric units around the Z-line (arrow-heads) and the mitochondria (M ~ arrows). (A). VLCAD +/+, (B). VLCAD-/-, and (C). Negative control lacking antibody in the VLCAD -/- mice. One should note the distribution of the gold particles, which appear to be less organized in the VLCAD-/- mice. The Particles are spread over the longitudinal tubules. These gold particles in the VLCAD -/- mice are also less organized over the mitochondria. (D). Quantitative assessment of gold particles in the vicinity of the z-line and over the mitochondria, *p< 0.03, comparing SR = Sarcoplasmic reticulum, † p<0.008 comparing mitochondria, VLCAD+/+ vs. VLCAD-/- . (E) [3H] ryanodine binding assays. Ryanodine binding assays with RyR enriched microsomes and mitochondrial fractions from the VLCAD+/+ and VLCAD-/- mice. Binding assay results from four independent experiments in the microsomes and three independent experiments in the mitochondria are plotted as Mean ± SE, ‡ p<0.001 comparing SR = Sarcoplasmic reticulum, § p<0.004 comparing mitochondria, VLCAD +/+ vs. VLCAD-/-.

We subsequently performed [^{3}H] ryanodine binding assays with purified microsomal and mitochondrial fractions from the VLCAD+/+ and VLCAD-/- mice.

Ryanodine binding was 1.7 ± 0.3 pmol / mg protein in the VLCAD+/+ microsomes and 3.5 ± 0.2 in the VLCAD-/- microsomes ($p<0.001$, Figure 49E). Ryanodine binding assays in mitochondrial fractions were 1.16 ± 0.05 pmol / mg protein for the VLCAD+/+ mitochondria and 1.43 ± 0.05 for the VLCAD-/- mitochondria ($p<0.04$). We performed Ca^{2+} loading assays with heart microsomes to assess the sarcoplasmic reticulum Ca^{2+} content, using antipyrylazo III (APIII). We found no difference in Ca^{2+} loading in heart microsomes between the VLCAD+/+ and VLCAD-/- mice. Loading rates were 29 ± 2 in the VLCAD-/- microsomes, compared with 34 ± 6 nmol/ min/ mg protein for the VLCAD+/+ control microsomes ($p<0.2$, VLCAD+/+ vs. VLCAD-/-), suggesting that the sarcoplasmic reticulum Ca^{2+} uptake capacity was not impaired in VLCAD-/- hearts.

Enhanced SR Ca^{2+} release in VLCAD deficient Cardiomyocytes

Given the hypothesis that arrhythmias due to RyR2 mutations are caused by enhanced Ca^{2+} release from the SR [284, 297], we subsequently measured Ca^{2+} transients in dissociated cardiomyocytes from the VLCAD +/+ and VLCAD-/- mouse, to test whether the observed RyR2 overexpression in VLCAD deficiency was associated with changes in intracellular Ca^{2+}.

We initially measured SR Ca^{2+} release by fluorescent imaging in the presence of either glucose or fatty acid substrates, using the Ca^{2+}-sensitive dye x-rhod-1 (4μM, X14210, Molecular Probes-Invitrogen).

Our initial analyses using glucose in the recording solution showed no difference in the normalized fluorescent Ca^{2+} signals between the VLCAD +/+ and VLCAD-/- cardiomyocytes (Figure 50A and B, VLCAD+/+ and -/-, GL = Glucose).

Because VLCAD deficiency is mainly a defect in fat metabolism and not of glucose metabolism, we investigated the effect of palmitate (C16-fatty acids) on the intracellular Ca^{2+} transient of the VLCAD+/+ and VLCAD-/- cardiomyocytes. We found that substitution of glucose by 10μM palmitic acid did not alter the SR Ca^{2+} release in the

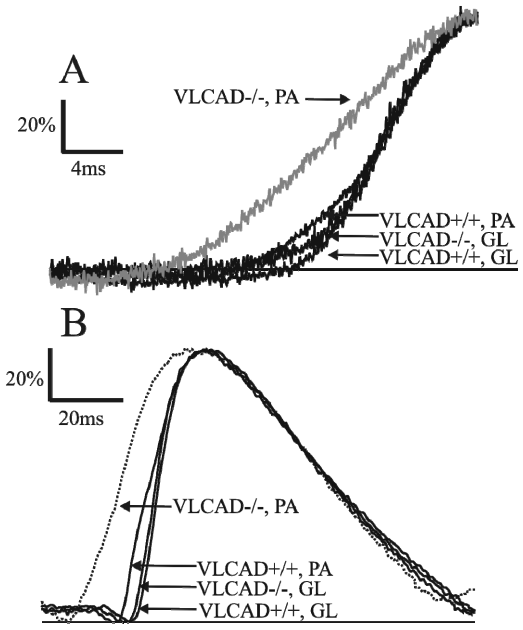

Figure 50. Palmitate enhances SR Ca^{2+} release in VLCAD-/- cardiomyocytes. Normalized fluorescence intensities using the cytosolic Ca2+ indicator x-rhod-1 in VLCAD+/+ and VLCAD-/- cardiomyocytes. There are changes in the time course of intracellular Ca2+ release when glucose is replaced with palmitic acid. (A). Mean x-rhod-1 fluorescence upstrokes measured in the presence of 10mM glucose (GL) or 10μM palmitic acid (PA). (B) The averaged and normalized Ca^{2+} transient in VLCAD+/+ and VLCAD-/- cardiomyocytes with glucose and palmitic acid using x-rhod-1 fluorescence. We used 10mM glucose (GL) in the bath solution from VLCAD+/+ (n=19) and VLCAD-/- (n=9) cells. We used 10μM palmitic acid (PA) for VLCAD+/+ cells (n=17) and VLCAD-/- (n=16). Cells were field-stimulated at 10Hz and data were digitally low-pass filtered at 600Hz.

VLCAD+/+ cardiomyocytes (Figure 50A and B, VLCAD+/+, PA = Palmitate), but significantly altered the Ca^{2+} transient of VLCAD-/- cardiomyocytes (Figure 50A and B)

Increased Ca^{2+} release and systolic $[Ca^{2+}]_i$ in VLCAD deficient cardiomyocytes with palmitate

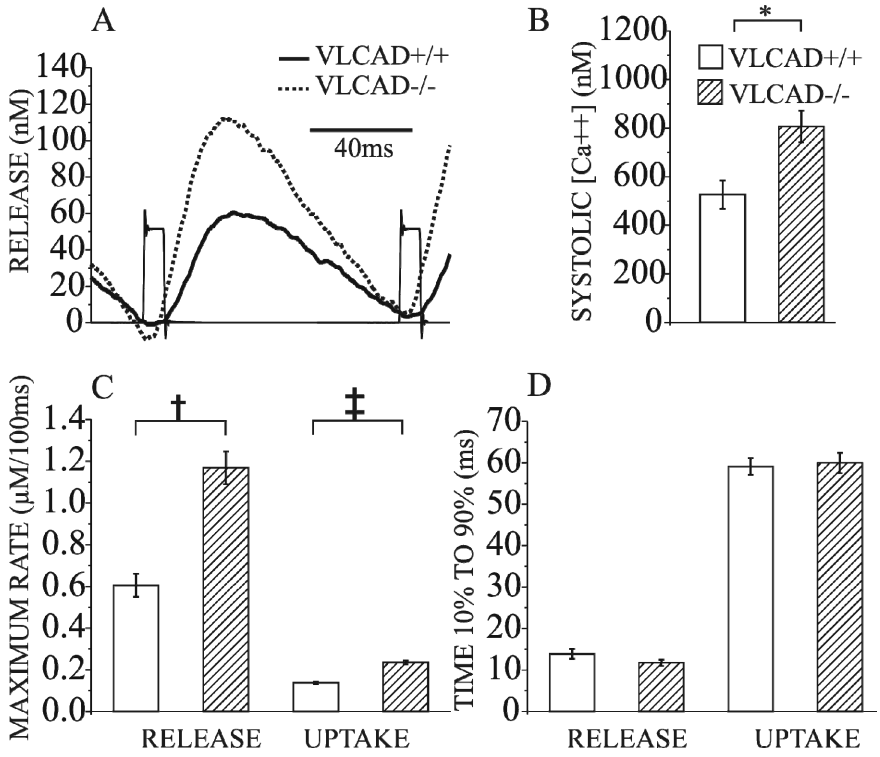

Figure 51. VLCAD deficiency is associated with increased release of Ca^{2+} from intracellular stores. (A) Averaged intracellular indo-1 Ca^{2+} transients from VLCAD-/- (n=20) cells and VLCAD+/+ (n=18) cells field stimulated at 600 beats per minute. (B) Systolic intracellular Ca^{2+} was significantly increased in VLCAD-/- cardiomyocytes (n=20) compared with control (n=18), *p=0.003, VLCAD+/+ vs. VLCAD-/-. (C) Maximum intracellular Ca^{2+} release rates were significantly increased in VLCAD-/- cells (n=20) compared to control (n=18), † $p<0.001$, VLCAD+/+ vs. VLCAD-/-. We also found an increase in SR uptake rate ‡ $p<0.05$, VLCAD+/+ vs. VLCAD-/-. (D) Both the duration of the Ca^{2+} release and the Ca^{2+} uptake were unaffected by VLCAD knockout in the same cells.

We proceeded to measure intracellular Ca^{2+} release and uptake with the ratiometric dye indo-1 (see Method section) in order to more precisely quantify the intracellular Ca^{2+} concentration ($[Ca^{2+}]_i$). We found a 1.9 ± 0.3 fold increase of pacing stimulated SR Ca^{2+} release in the VLCAD-/- cells compared to the control. The absolute Ca^{2+} release was 110 ± 18nM in VLCAD-/- and 59.6 ± 7.6nM in VLCAD+/+ myocytes (Fig. 5A). Similarly, systolic intracellular Ca^{2+} levels were also elevated in the VLCAD-/- mice. It was 806 ± 65 nM in the VLCAD-/- mice and 526 ± 58 nM in VLCAD+/+ controls (Fig. 5B). As a result, diastolic $[Ca^{2+}]_i$, as calculated from the difference of the peak $[Ca^{2+}]_i$ and the Ca^{2+} release for each cell, was also increased 1.5 ± 0.20 fold in the VLCAD-/- cardiomyocytes. We also determined the maximum Ca^{2+} release rate as defined by the maximum time-derivative of Ca^{2+} release, expressed in units of nM per 100ms. We found a 1.9 ± 0.2 fold increase in the maximum Ca^{2+} release rate from VLCAD-/- cardiomyocytes compared to the VLCAD+/+ control, with a maximum Ca^{2+} release rate of 1170 ± 80 nM in the VLCAD-/- cells and 605 ± 56 nM in VLCAD+/+ cells per 100 ms (Fig. 5C). In both groups, SR Ca^{2+} uptake rates were about five times slower than the release rates, with absolute amounts of 235 ± 10 nM and 138 ± 5nM per 100 ms in the VLCAD-/- and VLCAD+/+ control, respectively (Fig. 5C). Thus, the maximum Ca^{2+} uptake rates were increased 1.7 ± 0.1 fold in the VLCAD deficient cardiomyocytes, which was to be expected due to the increased Peak Ca^{2+} release in these cells. In contrast, the durations of the SR Ca^{2+} uptake and release as measured by the times from 10 % to 90 % of the rise and the fall of the transients, respectively, were unchanged (Figure 51D).

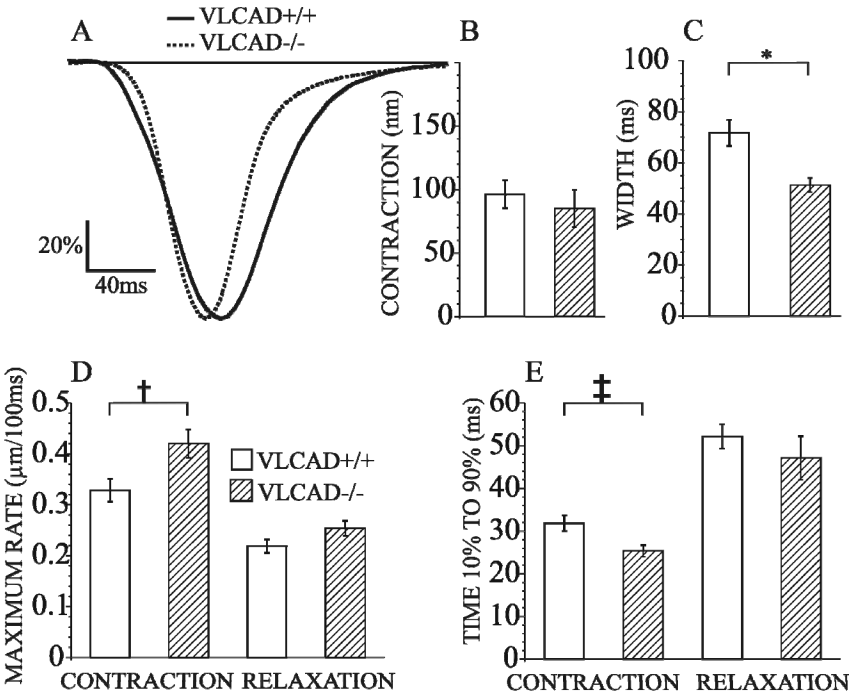

Figure 52. VLCAD deficiency leads to changes in the time course of the sarcomere contraction. (A) Representative normalized sarcomere contractions in VLCAD-/- cells (n=15) and VLCAD+/+ cells (n=16). (B) Maximum amplitude of sarcomere contraction was found unchanged in VLCAD-/- cells (n=15) compared with VLCAD+/+ cells (n=16). (C) Width of contracion (D) Maximum rate of sarcomere contraction was significantly higher in VLCAD-/- cardiomyocytes, * p=0.016, VLCAD+/+ vs. VLCAD-/-. Sarcomere relaxation was found not affected in the VLCAD-/- cells.

We subsequently tested whether the defect in Ca^{2+} homeostasis at the cellular level led to changes in cardiomyocyte contractility in the VLCAD deficient mouse. We found that the time course of sarcomere contraction was hastened in the VLCAD deficient cardiomyocytes (Figure 52A), although there was no significant difference in the sarcomere contraction amplitude, which was 85 ± 15 nm in the VLCAD-/- cells, and 96 ±

11 nm in the VLCAD+/+ cells (Figure 52B), despite the increase in peak $[Ca^{2+}]_i$ (Figure 51A and B). Diastolic sarcomere length was 1.75 ± 0.01 μm in the VLCAD-/- cells and 1.74 ± 0.07 in the VLCAD+/+ cells. The width of the sarcomere length transient was defined as the time from 50 % of sarcomere contraction to 50 % of sarcomere relaxation. It was 70 ± 5 in the VLCAD+/+ and 51 ± 3 in the VLCAD-/- cells (Figure 52C). Maximum contraction velocity was defined by the maximum time-derivative of the contraction amplitude and was expressed in units of μm per 100 ms. The maximum contraction velocities were 0.42 ± 0.03 μm in the VLCAD-/-, and 0.33 ± 0.02 μm per 100 ms in VLCAD+/+ cells (Figure 52D). Time from 10 % to 90 % of the maximum sarcomere contraction was shorter in the VLCAD-/- cells. Contraction times were 25 ± 1 ms in the VLCAD-/- cells and 32 ± 2 ms in the VLCAD+/+ cells (Figure 52E). Sarcomere relaxation was not changed in the VLCAD +/+ and VLCAD-/- cells (Figure 52D and E). We found no differences in the maximum sarcomere relaxation velocities (Figure 52D) and the times from 90 % to 10 % of sarcomere relaxation (Figure 52E) between the VLCAD+/+ and VLCAD-/- cardiomyocytes.

Altered Ca^{2+} release in VLCAD deficient cardiac myocytes is not due to changes in I_{Ca}

We subsequently tested whether the increase in SR Ca^{2+} release was due to changes in I_{Ca} in the presence of palmitate. The slow and the fast time constants of the inactivation at 0mV were unchanged, with 92 ± 6 ms and 12 ± 4 ms in the VLCAD-/- and 92 ± 5 ms and 12 ± 3ms in the VLCAD+/+ cells, respectively

Figure **53**A). We measured the current-voltage relationship of mean peak I_{Ca} and found no difference in the in the VLCAD-/- and the VLCAD+/+ cells (Figure 53B).

These data suggest that the observed changes in intracellular Ca^{2+} release in VLCAD-/- cells in the presence of palmitate are not due to the amount of Ca^{2+} entering the cell through sarcolemmal L-type Ca^{2+} channels.

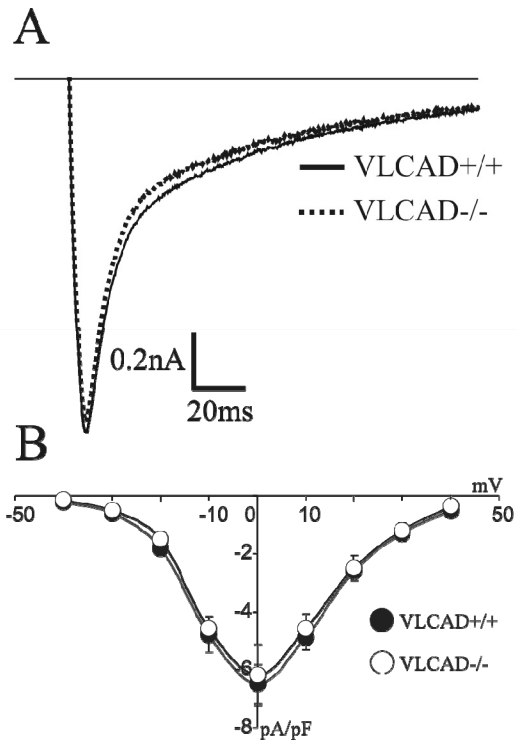

Figure 53 VLCAD deficiency does not lead to changes ICa. (A) Current-voltage relationships of mean peak ICa recorded in VLCAD-/- (n=7) and VLCAD+/+ (n=5) cardiomyocytes. (B) Representative ICa traces in VLCAD-/- (n=7) and VLCAD+/+ (n=5) cells.

Inactivation of the VLCAD gene in mice leads to alterations in other calcium related proteins in heart

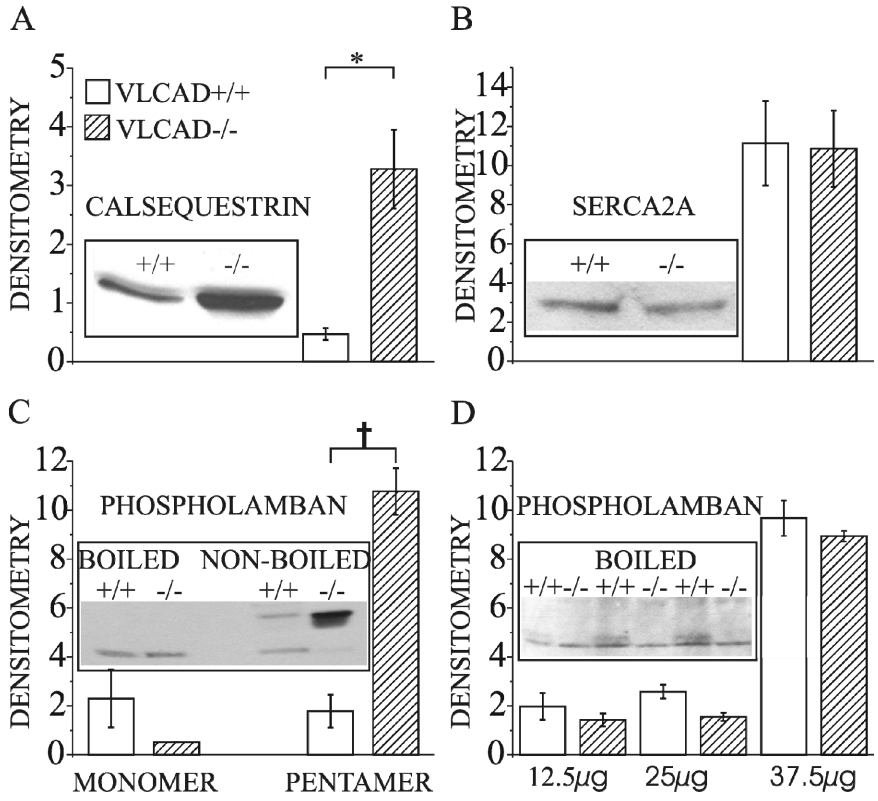

Figure 54. Western blot analysis of SR proteins involved in CICR. Western blots are for A) calsequestrin, B) SERCA, C) Monomeric and pentameric phospholamban, D) Monomeric phospholamban at different protein concentrations. Densitometry for protein levels is given with each representative blot, and it is calculated from three independent experiments, (*p< 0.01, † p<0.001, VLCAD+/+ vs. VLCAD-/-)

Although changes in calcium homeostasis in the mouse heart appear to be mainly a defect in SR Ca^{2+} release, we also tested whether VLCAD inactivation led to alterations in other calcium related proteins. We found that in addition to increased RyR expression (Figure 48), western blot analyses showed a modest increase in calsequestrin levels (Figure 54A),

which suggests an increase in absolute SR Ca^{2+} content. Protein levels of sarcoplasmic reticulum Ca^{2+} adenosine triphosphatase (SERCA) were not changed (Figure 54B). Similarly, there were no significant changes in the protein levels of the monomeric form of phospholamban (boiled products, Figure 54C and D), although the pentameric form of phospholamban (PLN) was increased 6.0 ± 0.9 fold in the VLCAD-/- cells (non-boiled Figure 54C, VLCAD-/-) compared with control (non-boiled Figure 54C, VLCAD+/+).

B.5 Discussion

VLCAD deficiency and Cardiac EC coupling

The present data show for the first time that there might be a link between genetic defects in mitochondrial fatty acid oxidation and calcium disorders in the heart. Our results show that VLCAD deficiency leads to significant changes in the intracellular calcium release (Figure 51) and sarcomere contraction (Figure 52). In VLCAD-/- cells, Ca^{2+} release was significantly higher and faster. This may have lead to the increased contraction velocity observed in these cells (Figure 52), although the amplitude of contraction was the same in both groups. VLCAD ablation did not alter the amplitude of the trigger calcium current, I_{Ca}, nor did it change the time course of I_{Ca} inactivation. Taken together, our data suggest that VLCAD deficiency increases the gain of the cardiac EC coupling.

VLCAD and SR protein expression

We found significant RyR2 overexpression in whole heart tissues as evidenced by isoform specific Western blot analysis (Figure 48) and immunoelectron microscopy

(Figure 49), the latter revealing increased ryanodine receptor localization in the mitochondria of the VLCAD deficient cardiomyocytes. These changes in ion channel expression may be part of compensatory molecular events that occur in the absence of the VLCAD gene. Similarly, calsequestrin was overexpressed in VLCAD-/- myocytes indicating an increased amount of Ca^{2+} stored in the SR of the VLCAD-/- cells. Taken together, VLCAD deficiency likely increases intracellular Ca^{2+} release by increasing Ca^{2+} stores and the number of Ca^{2+} release channels. Consequently, the ratio of the pentameric to the monomeric form of PLN was increased in the VLCAD-/- cells indicating a higher level of PLN phosphorylation. This may be a compensatory response to VLCAD ablation aimed to increase SR Ca^{2+} pump activity in the setting of an increased $[Ca^{2+}]_i$ release and possibly higher diastolic intracellular calcium concentration, but without an increase in SERCA2a expression (Figure 51 and Figure 54).

VLCAD and energy metabolism

We have previously shown that VLCAD deficient mice have a number of biochemical changes, suggestive of complex alterations in lipid metabolism and lipid transport that are present in the heart at birth, while ultra structural abnormalities develop postnatal [227]. It is therefore conceivable that several of these biochemical changes directly relate to the disease phenotype. Mitochondria in the VLCAD-/- heart muscle are larger, more variable in size and morphology, and fill a substantially larger portion of the sarcoplasmic volume. Although the slow mitochondrial Ca^{2+} fluxes might not contribute to EC coupling on a beat-to-beat basis, small graduate changes in mitochondrial calcium concentration ($[Ca^{2+}]_m$) may influence mitochondrial energy production and cytosolic

calcium concentration. Mitochondria can accumulate massive amounts of Ca^{2+}, as much as 100nmol Ca^{2+} per mg mitochondrial protein (corresponding to 10 mmol per liter cytosol, assuming 40 mg mitochondrial protein per g wet weight), although under physiological conditions, $[Ca^{2+}]_m$ is likely to be much smaller [298]. $[Ca^{2+}]_m$ increase can occur when energy demands are relatively high, i.e. when contractile activation and Ca^{2+} pumping are consuming ATP at high rates, or when cellular energy production is low. The rise in $[Ca^{2+}]_m$ provides a negative feedback on mitochondrial ATP production and eventually compromises the mitochondria [299]. Our results show that despite the larger size and the larger amount of mitochondria, total ATP production was not increased in the VLCAD-/- hearts. Therefore, mitochondrial metabolism was in fact depressed. The increased diastolic indo-1 fluorescence (Figure 51) would support the hypothesis that more Ca^{2+} is stored in the mitochondria of the VLCAD-/- cells than in the mitochondria of the VLCAD+/+ control cells, thereby increasing the time-independent fluorescence signal. A larger mitochondrial Ca^{2+} load would also suggest that an increased Ca^{2+} release into the cytosol via Na/Ca exchange when $[Na^+]_i$ is high [300]. The increased number of RyR2 that we found in the mitochondria may support this hypothesis (Figure 49). However, further experiments are needed to decide whether the increase in diastolic indo-1 fluorescence (Figure 51) was in fact due to an increase in free $[Ca^{2+}]_i$ or possibly caused by significant Ca^{2+} accumulation in the mitochondria. This, in turn, would point to a more important role of $[Ca^{2+}]_m$ in the hearts of the VLCAD deficient mice.

VLCAD and substrate dependence of $[Ca^{2+}]_i$

At a molecular level, palmitate cannot be readily metabolized in the absence of VLCAD, and fatty acids likely accumulate in the VLCAD-/- cells. While RyR2 and calsequestrin overexpression may have caused the larger Ca^{2+} transient amplitude in the VLCAD-/- cells, the observed changes in the time course of the normalized Ca^{2+} transient in these cells seemed to be substrate dependent as they did not occur when the recording solution contained glucose instead of palmitate (Figure 50). Our study was focused on the effects of VLCAD deficiency on proteins which are involved in EC coupling and we addressed possible mechanisms in single cardiac myocytes that could lead to the arrhythmia observed in the VLCAD-/- mice. Most of our experiments were performed under the same energy substrate conditions. However, Figure 50 warrants further investigation whether the accumulation of toxic metabolites lead to the observed changes in intracellular calcium signaling and sarcomere contraction.

Clinical relevance of this study

Pediatric patients with VLCAD deficiency often present with acute episodes of arrhythmias and death without prior evidence of myocardial dysfunction. We have created a knock out mouse model of VLCAD deficiency in which polymorphic VT and bidirectional VT were much more likely to be induced by programmed stimulation (50 %) or by isoproterenol infusion (83 %) than in the wild-type control. The features of these arrhythmias observed in the VLCAD-/- mice mimic the electrophysiological consequences of mutations in the cardiac ryanodine receptor in humans. Using dissociated ventricular cardiac myocytes from VLCAD-/- mice, we have demonstrated

that the genetic defect in the fatty acid metabolism resulted in a compensatory increase in the intracellular calcium transients leading to changes in sarcomere contractility. Our results indicate that intracellular calcium dynamics was altered in VLCAD-/- cells with fatty acid substrates and may therefore also point to the molecular basis for lipidosis induced arrhythmias in other cases of fatty acid oxidation deficiency. Long-term follow-up of patients with VLCAD deficiency has been limited by the fact that most of the cases present in childhood with sudden death and cardiac dysfunction. However, patients may survive into adulthood with rare reported complaints of skeletal myopathy, encephalopathy, and normal structural heart. In this present work we provide first evidence in mice that abnormal fat metabolism caused by genetic deletion of the VLCAD gene is associated with increased intracellular calcium release, increased diastolic calcium concentration and increased sarcomere contractility in single cells which could lead to delayed afterdepolarizations in the heart, a known cause of ventricular tachycardia. Further studies are necessary to determine whether the changes identified in isolated cardiomyocytes and ventricular tissue in fact contribute to the disease phenotype that causes sudden death mice and in humans.

Acknowledgements

This work was supported in part by a Grant in Aid from the American Heart Association-South East Affiliate and by the Vanderbilt Institute for Integrative Biosystems Research and Education (VIIBRE).

Note

This Chapter will be submitted for publication with the following list of authors: Andreas A. Werdich, PhD[1]; Loice H. Jeyakumar, MD[3]; Prince J. Kannankeril, MD, MSCI[2], Igor Dzhura, PhD[1]; Sidney Fleischer, PhD[4]; Alison LeGrone,MS[2]; Dejan Milatovic, PhD[2]; Michael Aschner, PhD[2]; James Atkinson, MD[5]; Arnold W. Strauss, MD[2]; Mark Anderson, MD, PhD[6]; Franz Baudenbacher, PhD[1]; Vernat J. Exil, MD[2]

[1]Department of Biomedical Engineering, Vanderbilt University, Nashville, TN.

[2]Department of Pediatrics, Vanderbilt University School of Medicine, Nashville, TN.

[3]Division of Gastroenterology, Vanderbilt University Medical Center, Nashville, TN.

[4]Department of Biological Sciences, Vanderbilt University, Nashville, TN.

[5]Department of Pathology, Vanderbilt University School of Medicine, Nashville, TN.

[6]Departments of Medicine and Physiology, Carver College of Medicine, University of Iowa, Iowa City, IA

REFERENCES

[1] L. H. Jeyakumar, L. A. Gleaves, B. D. Ridley, P. Chang, J. Atkinson, J. V. Barnett and S. Fleischer (2002) The skeletal muscle ryanodine receptor isoform 1 is found at the intercalated discs in human and mouse hearts. J Muscle Res Cell Motil **23**, 285-292.

[2] D. M. Lloyd-Jones, E. P. Leip, M. G. Larson, R. B. D'Agostino, A. Beiser, P. W. Wilson, P. A. Wolf and D. Levy (2006) Prediction of lifetime risk for cardiovascular disease by risk factor burden at 50 years of age. Circulation **113**, 791-798.

[3] D. M. Lloyd-Jones, T. J. Wang, E. P. Leip, M. G. Larson, D. Levy, R. S. Vasan, R. B. D'Agostino, J. M. Massaro, A. Beiser, P. A. Wolf and E. J. Benjamin (2004) Lifetime risk for development of atrial fibrillation: the Framingham Heart Study. Circulation **110**, 1042-1046.

[4] F. Ahmad, J. G. Seidman and C. E. Seidman (2005) The genetic basis for cardiac remodeling. Annu Rev Genomics Hum Genet **6**, 185-216.

[5] J. A. Hill (2003) Electrical remodeling in cardiac hypertrophy. Trends in Cardiovascular Medicine **13**, 316-322.

[6] J. A. Birkeland, O. M. Sejersted, T. Taraldsen and I. Sjaastad (2005) EC-coupling in normal and failing hearts. Scand Cardiovasc J **39**, 13-23.

[7] C. W. Balke and S. R. Shorofsky (1998) Alterations in calcium handling in cardiac hypertrophy and heart failure. Cardiovasc Res **37**, 290-299.

[8] S. R. Houser, V. Piacentino, III and J. Weisser (2000) Abnormalities of calcium cycling in the hypertrophied and failing heart. J Mol Cell Cardiol **32**, 1595-1607.

[9] A. G. Kleber and Y. Rudy (2004) Basic mechanisms of cardiac impulse propagation and associated arrhythmias. Physiological Reviews **84**, 431-488.

[10] A. M. Gordon, M. Regnier and E. Homsher (2001) Skeletal and cardiac muscle contractile activation: tropomyosin "rocks and rolls". News Physiol Sci **16**, 49-55.

[11] J. G. Pinto and A. Boe (1991) A method to characterize the passive elasticity in contracting muscle bundles. J Biomech Eng **113**, 72-78.

[12] J. G. Pinto and P. J. Patitucci (1980) Visco-elasticity of passive cardiac muscle. J Biomech Eng **102**, 57-61.

[13] A. J. Brady, S. T. Tan and N. V. Ricchiuti (1981) Perturbation measurements of papillary muscle elasticity. Am J Physiol **241**, H155-H173.

[14] J. G. Pinto and R. Win (1977) Non-uniform strain distribution in papillary muscles. Am J Physiol **233**, H410-H416.

[15] J. K. Gwathmey, L. Copelas, R. MacKinnon, F. J. Schoen, M. D. Feldman, W. Grossman and J. P. Morgan (1987) Abnormal intracellular calcium handling in myocardium from patients with end-stage heart failure. Circ Res **61**, 70-76.

[16] V. Piacentino, III, C. R. Weber, X. Chen, J. Weisser-Thomas, K. B. Margulies, D. M. Bers and S. R. Houser (2003) Cellular basis of abnormal calcium transients of failing human ventricular myocytes. Circ Res **92**, 651-658.

[17] J. P. Morgan, R. E. Erny, P. D. Allen, W. Grossman and J. K. Gwathmey (1990) Abnormal intracellular calcium handling, a major cause of systolic and diastolic dysfunction in ventricular myocardium from patients with heart failure. Circulation **81**, III21-III32.

[18] J. K. Gwathmey, L. A. Bentivegna, B. J. Ransil, W. Grossman and J. P. Morgan (1993) Relationship of abnormal intracellular calcium mobilisation to myocyte hypertrophy in human ventricular myocardium. Cardiovasc Res **27**, 199-203.

[19] del Monte F., S. E. Harding, U. Schmidt, T. Matsui, Z. B. Kang, G. W. Dec, J. K. Gwathmey, A. Rosenzweig and R. J. Hajjar (1999) Restoration of contractile function in isolated cardiomyocytes from failing human hearts by gene transfer of SERCA2a. Circulation **100**, 2308-2311.

[20] M. F. del, C. M. Johnson, A. C. Stepanek, A. A. Doye and J. K. Gwathmey (2002) Defects in calcium control. J Card Fail **8**, S421-S431.

[21] H. K. B. Simmerman and L. R. Jones (1998) Phospholamban: Protein structure, mechanism of action, and role in cardiac function. Physiological Reviews **78**, 921-947.

[22] D. H. MacLennan and E. G. Kranias (2003) Phospholamban: a crucial regulator of cardiac contractility. Nat Rev Mol Cell Biol **4**, 566-577.

[23] K. L. Koss and E. G. Kranias (1996) Phospholamban: A prominent regulator of myocardial contractility. Circ Res **79**, 1059-1063.

[24] W. S. Luo, I. L. Grupp, J. Harrer, S. Ponniah, G. Grupp, J. J. Duffy, T. Doetschman and E. G. Kranias (1994) Targeted Ablation of the Phospholamban Gene Is Associated with Markedly Enhanced Myocardial-Contractility and Loss of Beta-Agonist Stimulation. Circ Res **75**, 401-409.

[25] U. Schmidt, R. J. Hajjar, C. S. Kim, D. Lebeche, A. A. Doye and J. K. Gwathmey (1999) Human heart failure: cAMP stimulation of SR Ca(2+)-ATPase activity and phosphorylation level of phospholamban. Am J Physiol **277**, H474-H480.

[26] R. H. Schwinger, G. Munch, B. Bolck, P. Karczewski, E. G. Krause and E. Erdmann (1999) Reduced Ca(2+)-sensitivity of SERCA 2a in failing human myocardium due to reduced serin-16 phospholamban phosphorylation. J Mol Cell Cardiol **31**, 479-491.

[27] M. F. del, E. Williams, D. Lebeche, U. Schmidt, A. Rosenzweig, J. K. Gwathmey, E. D. Lewandowski and R. J. Hajjar (2001) Improvement in survival and cardiac metabolism after gene transfer of sarcoplasmic reticulum Ca(2+)-ATPase in a rat model of heart failure. Circulation **104**, 1424-1429.

[28] W. Luo, B. M. Wolska, I. L. Grupp, J. M. Harrer, K. Haghighi, D. G. Ferguson, J. P. Slack, G. Grupp, T. Doetschman, R. J. Solaro and E. G. Kranias (1996) Phospholamban gene dosage effects in the mammalian heart. Circ Res **78**, 839-847.

[29] S. E. Harding, S. M. Jones, P. O'Gara, M. F. del, G. Vescovo and P. A. Poole-Wilson (1992) Isolated ventricular myocytes from failing and non-failing human heart; the relation of age and clinical status of patients to isoproterenol response. J Mol Cell Cardiol **24**, 549-564.

[30] C. H. Davies, K. Davia, J. G. Bennett, J. R. Pepper, P. A. Poole-Wilson and S. E. Harding (1995) Reduced contraction and altered frequency response of isolated ventricular myocytes from patients with heart failure. Circulation **92**, 2540-2549.

[31] J. W. M. Bassani, W. L. Yuan and D. M. Bers (1995) Fractional Sr Ca Release Is Regulated by Trigger Ca and Sr Ca Content in Cardiac Myocytes. American Journal of Physiology-Cell Physiology **37**, C1313-C1319.

[32] B. Pieske, L. S. Maier, D. M. Bers and G. Hasenfuss (1999) Ca2+ handling and sarcoplasmic reticulum Ca2+ content in isolated failing and nonfailing human myocardium. Circ Res **85**, 38-46.

[33] C. A. Valverde, C. Mundina-Weilenmann, M. Said, P. Ferrero, L. Vittone, M. Salas, J. Palomeque, M. V. Petroff and A. Mattiazzi (2005) Frequency-dependent acceleration of relaxation in mammalian heart: a property not relying on phospholamban and SERCA2a phosphorylation. J Physiol **562**, 801-813.

[34] V. J. A. Schouten (1990) Interval Dependence of Force and Twitch Duration in Rat-Heart Explained by Ca-2+ Pump Inactivation in Sarcoplasmic-Reticulum. Journal of Physiology-London **431**, 427-444.

[35] D. Hagemann, M. Kuschel, T. Kuramochi, W. Z. Zhu, H. P. Cheng and R. P. Xiao (2000) Frequency-encoding Thr(17) phospholamban phosphorylation is independent of Ser(16) phosphorylation in cardiac myocytes. Journal of Biological Chemistry **275**, 22532-22536.

[36] W. F. Bluhm, E. G. Kranias, W. H. Dillmann and M. Meyer (2000) Phospholamban: a major determinant of the cardiac force-frequency relationship. Am J Physiol Heart Circ Physiol **278**, H249-H255.

[37] W. Zhao, Y. Uehara, G. X. Chu, Q. J. Song, J. Qian, K. Young and E. G. Kranias (2004) Threonine-17 phosphorylation of phospholamban: a key determinant of frequency-dependent increase of cardiac contractility. Journal of Molecular and Cellular Cardiology **37**, 607-612.

[38] G. Yellen (1998) The moving parts of voltage-gated ion channels. Q Rev Biophys **31**, 239-295.

[39] A. G. Kleber and V. Fast (1997) Molecular and cellular aspects of re-entrant arrhythmias. Basic Research in Cardiology **92**, 111-119.

[40] D. M. Bers and T. Guo (2005) Calcium signaling in cardiac ventricular myocytes. Ann N Y Acad Sci **1047**, 86-98.

[41] D. M. Bers (2002) Cardiac excitation-contraction coupling. Nature **415**, 198-205.

[42] D. M. Bers (2001) Excitation-Contraction Coupling and Cardiac Contractile Force.

[43] M. S. Nieminen and V. P. Harjola (2005) Definition and epidemiology of acute heart failure syndromes. Am J Cardiol **96**, 5G-10G.

[44] S. Minamisawa, Y. Sato and M. C. Cho (2004) Calcium cycling proteins in heart failure, cardiomyopathy and arrhythmias. Exp Mol Med **36**, 193-203.

[45] K. R. Chien, J. Ross, Jr. and M. Hoshijima (2003) Calcium and heart failure: the cycle game. Nat Med **9**, 508-509.

[46] J. W. M. Bassani, R. A. Bassani and D. M. Bers (1994) Relaxation in Rabbit and Rat Cardiac-Cells - Species-Dependent Differences in Cellular Mechanisms. Journal of Physiology-London **476**, 279-293.

[47] A. D. Wegener, H. K. Simmerman, J. P. Lindemann and L. R. Jones (1989) Phospholamban phosphorylation in intact ventricles. Phosphorylation of serine 16 and threonine 17 in response to beta-adrenergic stimulation. J Biol Chem **264**, 11468-11474.

[48] S. Bartel, D. Vetter, W. P. Schlegel, G. Wallukat, E. G. Krause and P. Karczewski (2000) Phosphorylation of phospholamban at threonine-17 in the absence and presence of beta-adrenergic stimulation in neonatal rat cardiomyocytes. Journal of Molecular and Cellular Cardiology **32**, 2173-2185.

[49] K. S. Ginsburg and D. M. Bers (2004) Modulation of excitation-contraction coupling by isoproterenol in cardiomyocytes with controlled SR Ca2+ load and Ca2+ current trigger. J Physiol **556**, 463-480.

[50] X. H. Wehrens and A. R. Marks (2004) Molecular determinants of altered contractility in heart failure. Ann Med **36 Suppl 1**, 70-80.

[51] S. Chakraborti, T. Chakraborti and G. Shaw (2000) beta-adrenergic mechanisms in cardiac diseases - A perspective. Cellular Signalling **12**, 499-513.

[52] L. Li, G. X. Chu, E. G. Kranias and D. M. Bers (1998) Cardiac myocyte calcium transport in phospholamban knockout mouse: relaxation and endogenous CaMKII effects. American Journal of Physiology-Heart and Circulatory Physiology **43**, H1335-H1347.

[53] T. G. Hampton, E. G. Kranias and J. P. Morgan (1996) Simultaneous measurement of intracellular calcium and ventricular function in the phospholamban-deficient mouse heart. Biochemical and Biophysical Research Communications **226**, 836-841.

[54] B. M. Wolska, M. O. Stojanovic, W. Luo, E. G. Kranias and R. J. Solaro (1996) Effect of ablation of phospholamban on dynamics of cardiac myocyte contraction and intracellular Ca2+. Am J Physiol **271**, C391-C397.

[55] L. F. Santana, E. G. Kranias and W. J. Lederer (1997) Calcium sparks and excitation-contraction coupling in phospholamban-deficient mouse ventricular myocytes. J Physiol **503 (Pt 1)**, 21-29.

[56] G. X. Chu, J. P. Kerr, B. Mitton, G. F. Egnaczyk, J. A. Vazquez, M. L. Shen, G. W. Kilby, T. I. Stevenson, J. E. Maggio, J. Vockley, S. T. Rapundalo and E. G. Kranias (2004) Proteomic analysis of hyperdynamic mouse hearts with enhanced sarcoplasmic reticulum calcium cycling. Faseb Journal **18**.

[57] G. Chu, D. G. Ferguson, I. Edes, E. Kiss, Y. Sato and E. G. Kranias (1998) Phospholamban ablation and compensatory responses in the mammalian heart. Ann N Y Acad Sci **853**, 49-62.

[58] R. L. Moss, M. Razumova and D. P. Fitzsimons (2004) Myosin crossbridge activation of cardiac thin filaments: implications for myocardial function in health and disease. Circ Res **94**, 1290-1300.

[59] R. J. Solaro and H. M. Rarick (1998) Troponin and tropomyosin: proteins that switch on and tune in the activity of cardiac myofilaments. Circ Res **83**, 471-480.

[60] J. J. Rice and P. P. de Tombe (2004) Approaches to modeling crossbridges and calcium-dependent activation in cardiac muscle. Prog Biophys Mol Biol **85**, 179-195.

[61] S. Palmer and J. C. Kentish (1998) Roles of Ca2+ and crossbridge kinetics in determining the maximum rates of Ca2+ activation and relaxation in rat and guinea pig skinned trabeculae. Circ Res **83**, 179-186.

[62] J. K. Gwathmey and R. J. Hajjar (1990) Relation between steady-state force and intracellular [Ca2+] in intact human myocardium. Index of myofibrillar responsiveness to Ca2+. Circulation **82**, 1266-1278.

[63] P. H. Backx, W. D. Gao, M. D. zan-Backx and E. Marban (1995) The relationship between contractile force and intracellular [Ca2+] in intact rat cardiac trabeculae. J Gen Physiol **105**, 1-19.

[64] G. McClellan, I. Kulikovskaya and S. Winegrad (2001) Changes in cardiac contractility related to calcium-mediated changes in phosphorylation of myosin-binding protein C. Biophys J **81**, 1083-1092.

[65] A. M. Gordon and G. H. Pollack (1980) Effects of calcium on the sarcomere length-tension relation in rat cardiac muscle. Implications for the Frank-Starling mechanism. Circ Res **47**, 610-619.

[66] A. J. Brady, S. T. Tan and N. V. Ricchiuti (1979) Contractile force measured in unskinned isolated adult rat heart fibres. Nature **282**, 728-729.

[67] R. E. Palmer, A. J. Brady and K. P. Roos (1996) Mechanical measurements from isolated cardiac myocytes using a pipette attachment system. Am J Physiol **270**, C697-C704.

[68] S. Nishimura, S. Yasuda, M. Katoh, K. P. Yamada, H. Yamashita, Y. Saeki, K. Sunagawa, R. Nagai, T. Hisada and S. Sugiura (2004) Single cell mechanics of rat cardiomyocytes under isometric, unloaded, and physiologically loaded conditions. Am J Physiol Heart Circ Physiol **287**, H196-H202.

[69] S. Yasuda, S. Sugiura, H. Yamashita, S. Nishimura, Y. Saeki, S. Momomura, K. Katoh, R. Nagai and H. Sugi (2003) Unloaded shortening increases peak of Ca2+ transients but accelerates their decay in rat single cardiac myocytes. Am J Physiol Heart Circ Physiol **285**, H470-H475.

[70] S. I. Yasuda, S. Sugiura, N. Kobayakawa, H. Fujita, H. Yamashita, K. Katoh, Y. Saeki, H. Kaneko, Y. Suda, R. Nagai and H. Sugi (2001) A novel method to study contraction characteristics of a single cardiac myocyte using carbon fibers. American Journal of Physiology-Heart and Circulatory Physiology **281**, H1442-H1446.

[71] A. J. Brady (1991) Mechanical properties of isolated cardiac myocytes. Physiol Rev **71**, 413-428.

[72] M. S. Kellermayer, C. Bustamante and H. L. Granzier (2003) Mechanics and structure of titin oligomers explored with atomic force microscopy. Biochim Biophys Acta **1604**, 105-114.

[73] C. Bouchiat, M. D. Wang, J. Allemand, T. Strick, S. M. Block and V. Croquette (1999) Estimating the persistence length of a worm-like chain molecule from force-extension measurements. Biophys J **76**, 409-413.

[74] C. E. Ganote and R. S. Vander Heide (1987) Cytoskeletal lesions in anoxic myocardial injury. A conventional and high-voltage electron-microscopic and immunofluorescence study. Am J Pathol **129**, 327-344.

[75] C. Steenbergen, M. L. Hill and R. B. Jennings (1987) Cytoskeletal damage during myocardial ischemia: changes in vinculin immunofluorescence staining during total in vitro ischemia in canine heart. Circ Res **60**, 478-486.

[76] S. E. Harding, G. Vescovo, M. Kirby, S. M. Jones, J. Gurden and P. A. Poole-Wilson (1988) Contractile responses of isolated adult rat and rabbit cardiac myocytes to isoproterenol and calcium. J Mol Cell Cardiol **20**, 635-647.

[77] E. Niggli and W. J. Lederer (1991) Restoring forces in cardiac myocytes. Insight from relaxations induced by photolysis of caged ATP. Biophys J **59**, 1123-1135.

[78] S. K. Sia and G. M. Whitesides (2003) Microfluidic devices fabricated in poly(dimethylsiloxane) for biological studies. Electrophoresis **24**, 3563-3576.

[79] M. A. Unger, H. P. Chou, T. Thorsen, A. Scherer and S. R. Quake (2000) Monolithic microfabricated valves and pumps by multilayer soft lithography. Science **288**, 113-116.

[80] B. D. DeBusschere and G. T. Kovacs (2001) Portable cell-based biosensor system using integrated CMOS cell-cartridges. Biosens Bioelectron **16**, 543-556.

[81] K. H. Gilchrist, V. N. Barker, L. E. Fletcher, B. D. DeBusschere, P. Ghanouni, L. Giovangrandi and G. T. Kovacs (2001) General purpose, field-portable cell-based biosensor platform. Biosens Bioelectron **16**, 557-564.

[82] G. T. A. Kovacs (2003) Electronic sensors with living cellular components. Proceedings of the Ieee **91**, 915-929.

[83] J. J. Pancrazio, P. P. Bey, D. S. Cuttino, J. K. Kusel, D. A. Borkholder, K. M. Shaffer, G. T. A. Kovacs and D. A. Stenger (1998) Portable cell-based biosensor system for toxin detection. Sensors and Actuators B-Chemical **53**, 179-185.

[84] G. Xu, X. Ye, L. Qin, Y. Xu, Y. Li, R. Li and P. Wang (2005) Cell-based biosensors based on light-addressable potentiometric sensors for single cell monitoring. Biosens Bioelectron **20**, 1757-1763.

[85] P. J. Lee, P. J. Hung, V. M. Rao and L. P. Lee (2005) Nanoliter scale microbioreactor array for quantitative cell biology. Biotechnol Bioeng.

[86] R. Pantoja, J. M. Nagarah, D. M. Starace, N. A. Melosh, R. Blunck, F. Bezanilla and J. R. Heath (2004) Silicon chip-based patch-clamp electrodes integrated with PDMS microfluidics. Biosens Bioelectron **20**, 509-517.

[87] C. H. Hsu, C. Chen and A. Folch (2004) "Microcanals" for micropipette access to single cells in microfluidic environments. Lab Chip **4**, 420-424.

[88] K. G. Klemic, J. F. Klemic, M. A. Reed and F. J. Sigworth (2002) Micromolded PDMS planar electrode allows patch clamp electrical recordings from cells. Biosens Bioelectron **17**, 597-604.

[89] C. Ionescu-Zanetti, R. M. Shaw, J. Seo, Y. N. Jan, L. Y. Jan and L. P. Lee (2005) Mammalian electrophysiology on a microfluidic platform. Proc Natl Acad Sci U S A **102**, 9112-9117.

[90] J. Seo, C. Ionescu-Zanetti, J. Diamond, R. Lal and L. P. Lee (2004) Integrated multiple patch-clamp array chip via lateral cell trapping junctions. Applied Physics Letters **84**, 1973-1975.

[91] B. Yao, G. Luo, L. Wang, Y. Gao, G. Lei, K. Ren, L. Chen, Y. Wang, Y. Hu and Y. Qiu (2005) A microfluidic device using a green organic light emitting diode as an integrated excitation source. Lab Chip **5**, 1041-1047.

[92] O. Hofmann, X. Wang, J. C. Demello, D. D. Bradley and A. J. Demello (2005) Towards microalbuminuria determination on a disposable diagnostic microchip with integrated fluorescence detection based on thin-film organic light emitting diodes. Lab Chip **5**, 863-868.

[93] N. Klauke, G. L. Smith and J. Cooper (2003) Stimulation of single isolated adult ventricular myocytes within a low volume using a planar microelectrode array. Biophysical Journal **85**, 1766-1774.

[94] N. Klauke, G. L. Smith and J. M. Cooper (2005) Stimulation of isolated ventricular myocytes within an open architecture microarray. IEEE Trans Biomed Eng **52**, 531-538.

[95] A. R. Wheeler, W. R. Throndset, R. J. Whelan, A. M. Leach, R. N. Zare, Y. H. Liao, K. Farrell, I. D. Manger and A. Daridon (2003) Microfluidic device for single-cell analysis. Analytical Chemistry **75**, 3581-3586.

[96] X. J. Li and P. C. H. Li (2005) Microfluidic selection and retention of a single cardiac myocyte, on-chip dye loading, cell contraction by chemical stimulation, and quantitative fluorescent analysis of intracellular calcium. Analytical Chemistry **77**, 4315-4322.

[97] T. C. Merkel, V. I. Bondar, K. Nagai, B. D. Freeman and I. Pinnau (2000) Gas sorption, diffusion, and permeation in poly(dimethylsiloxane). Journal of Polymer Science Part B-Polymer Physics **38**, 415-434.

[98] D. C. Duffy, J. C. McDonald, O. J. A. Schueller and G. M. Whitesides (1998) Rapid prototyping of microfluidic systems in poly(dimethylsiloxane). Analytical Chemistry **70**, 4974-4984.

[99] J. C. McDonald and G. M. Whitesides (2002) Poly(dimethylsiloxane) as a material for fabricating microfluidic devices. Acc Chem Res **35**, 491-499.

[100] G. M. Whitesides, E. Ostuni, S. Takayama, X. Y. Jiang and D. E. Ingber (2001) Soft lithography in biology and biochemistry. Annual Review of Biomedical Engineering **3**, 335-373.

[101] Y. N. Xia and G. M. Whitesides (1998) Soft lithography. Annual Review of Materials Science **28**, 153-184.

[102] A. Y. Fu, H. P. Chou, C. Spence, F. H. Arnold and S. R. Quake (2002) An integrated microfabricated cell sorter. Analytical Chemistry **74**, 2451-2457.

[103] J. W. Hong and S. R. Quake (2003) Integrated nanoliter systems. Nature Biotechnology **21**, 1179-1183.

[104] S. R. Quake and A. Scherer (2000) From micro- to nanofabrication with soft materials. Science **290**, 1536-1540.

[105] T. Thorsen, R. W. Roberts, F. H. Arnold and S. R. Quake (2001) Dynamic pattern formation in a vesicle-generating microfluidic device. Physical Review Letters **86**, 4163-4166.

[106] G. M. Walker, H. C. Zeringue and D. J. Beebe (2004) Microenvironment design considerations for cellular scale studies. Lab Chip **4**, 91-97.

[107] L. Tung and J. R. Borderies (1992) Analysis of Electric-Field Stimulation of Single Cardiac- Muscle-Cells. Biophysical Journal **63**, 371-386.

[108] V. Sharma, S. N. Lu and L. Tung (2002) Decomposition of field-induced transmembrane potential responses of single cardiac cells. Ieee Transactions on Biomedical Engineering **49**, 1031-1037.

[109] V. Sharma and L. Tung (2002) Spatial heterogeneity of transmembrane potential responses of single guinea-pig cardiac cells during electric field stimulation. Journal of Physiology-London **542**, 477-492.

[110] G. Grynkiewicz, M. Poenie and R. Y. Tsien (1985) A New Generation of Ca-2+ Indicators with Greatly Improved Fluorescence Properties. Journal of Biological Chemistry **260**, 3440-3450.

[111] K. R. Sipido and G. Callewaert (1995) How to Measure Intracellular [Ca2+] in Single Cardiac-Cells with Fura-2 Or Indo-1. Cardiovascular Research **29**, 717-726.

[112] L. H. Pojoga and R. H. Hilderman (2003) A theoretical and experimental approach to the use of single wavelength calcium indicators. J Theor Biol **221**, 543-557.

[113] M. Maravall, Z. F. Mainen, B. L. Sabatini and K. Svoboda (2000) Estimating intracellular calcium concentrations and buffering without wavelength ratioing. Biophys J **78**, 2655-2667.

[114] S. Guatimosim, K. Dilly, L. F. Santana, M. S. Jafri, E. A. Sobie and W. J. Lederer (2002) Local Ca2+ signaling and EC coupling in heart: Ca2+ sparks and the regulation of The [Ca2+](i) transient. Journal of Molecular and Cellular Cardiology **34**, 941-950.

[115] L. F. Santana, H. Cheng, A. M. Gomez, M. B. Cannell and W. J. Lederer (1996) Relation between the sarcolemmal Ca2+ current and Ca2+ sparks and local control theories for cardiac excitation-contraction coupling. Circ Res **78**, 166-171.

[116] M. Dura, I. Zahradnik and A. Zahradnikova (2003) Kinetics of cardiac RyR channel gating studied at high temporal resolution. Physiol Res **52**, 571-578.

[117] J. N. Weiss (1997) The Hill equation revisited: uses and misuses. Faseb Journal **11**, 835-841.

[118] A. Zahradnikova and I. Zahradnik (1996) A minimal gating model for the cardiac calcium release channel. Biophysical Journal **71**, 2996-3012.

[119] R. Hinch, J. L. Greenstein, A. J. Tanskanen, L. Xu and R. L. Winslow (2004) A simplified local control model of calcium-induced calcium release in cardiac ventricular myocytes. Biophysical Journal **87**, 3723-3736.

[120] L. Xu, A. Tripathy, D. A. Pasek and G. Meissner (1998) Potential for pharmacology of ryanodine receptor calcium release channels. Cardiac Sarcoplasmic Reticulum Function and Regulation of Contractility **853**, 130-148.

[121] A. Zahradnikova, I. Zahradnik, I. Gyorke and S. Gyorke (1999) Rapid activation of the cardiac ryanodine receptor by submillisecond calcium stimuli. Journal of General Physiology **114**, 787-798.

[122] M. D. Stern, L. S. Song, H. P. Cheng, J. S. K. Sham, H. T. Yang, K. R. Boheler and E. Rios (1999) Local control models of cardiac excitation-contraction coupling - A possible role for allosteric interactions between ryanodine receptors. Journal of General Physiology **113**, 469-489.

[123] J. DeSantiago, L. S. Maier and D. M. Bers (2002) Frequency-dependent acceleration of relaxation in the heart depends on CaMKII, but not phospholamban. Journal of Molecular and Cellular Cardiology **34**, 975-984.

[124] M. Endoh (2004) Force-frequency relationship in intact mammalian ventricular myocardium: physiological and pathophysiological relevance. European Journal of Pharmacology **500**, 73-86.

[125] L. Li, H. Satoh, K. S. Ginsburg and D. M. Bers (1997) The effect of Ca2+-calmodulin-dependent protein kinase II on cardiac excitation-contraction coupling in ferret ventricular myocytes. Journal of Physiology-London **501**, 17-31.

[126] A. S. Armand and L. J. De Windt (2004) Calcium cycling in heart failure: how the fast became too furious. Cardiovascular Research **62**, 439-441.

[127] E. G. Kranias (1985) Regulation of Ca2+ transport by cyclic 3',5'-AMP-dependent and calcium-calmodulin-dependent phosphorylation of cardiac sarcoplasmic reticulum. Biochim Biophys Acta **844**, 193-199.

[128] M. Tada, M. Inui, M. Yamada, M. Kadoma, T. Kuzuya, H. Abe and S. Kakiuchi (1983) Effects of phospholamban phosphorylation catalyzed by adenosine 3':5'-monophosphate- and calmodulin-dependent protein kinases on calcium transport ATPase of cardiac sarcoplasmic reticulum. J Mol Cell Cardiol **15**, 335-346.

[129] L. Li, J. DeSantiago, G. X. Chu, E. G. Kranias and D. M. Bers (2000) Phosphorylation of phospholamban and troponin I in beta-adrenergic-induced acceleration of cardiac relaxation. American Journal of Physiology-Heart and Circulatory Physiology **278**, H769-H779.

[130] B. D. Hoit, V. J. Kadambi, D. A. Tramuta, N. Ball, E. G. Kranias and R. A. Walsh (2000) Influence of sarcoplasmic reticulum calcium loading on mechanical and relaxation restitution. Am J Physiol Heart Circ Physiol **278**, H958-H963.

[131] S. Minamisawa, M. Hoshijima, G. Chu, C. A. Ward, K. Frank, Y. Gu, M. E. Martone, Y. Wang, J. Ross, Jr., E. G. Kranias, W. R. Giles and K. R. Chien (1999) Chronic phospholamban-sarcoplasmic reticulum calcium ATPase interaction is the critical calcium cycling defect in dilated cardiomyopathy. Cell **99**, 313-322.

[132] del Monte F. and R. J. Hajjar (2003) Targeting calcium cycling proteins in heart failure through gene transfer. J Physiol **546**, 49-61.

[133] Y. Sato, H. Kiriazis, A. Yatani, A. G. Schmidt, H. Hahn, D. G. Ferguson, H. Sako, S. Mitarai, R. Honda, L. Mesnard-Rouiller, K. F. Frank, B. Beyermann, G. Wu, K. Fujimori, G. W. Dorn and E. G. Kranias (2001) Rescue of contractile parameters and myocyte hypertrophy in calsequestrin overexpressing myocardium by phospholamban ablation. J Biol Chem **276**, 9392-9399.

[134] M. Hoshijima, Y. Ikeda, Y. Iwanaga, S. Minamisawa, M. O. Date, Y. Gu, M. Iwatate, M. Li, L. Wang, J. M. Wilson, Y. Wang, J. Ross, Jr. and K. R. Chien (2002) Chronic suppression of heart-failure progression by a pseudophosphorylated mutant of phospholamban via in vivo cardiac rAAV gene delivery. Nat Med **8**, 864-871.

[135] Y. Iwanaga, M. Hoshijima, Y. Gu, M. Iwatate, T. Dieterle, Y. Ikeda, M. O. Date, J. Chrast, M. Matsuzaki, K. L. Peterson, K. R. Chien and J. Ross (2004) Chronic phospholamban inhibition prevents progressive cardiac dysfunction and pathological remodeling after infarction in rats. Journal of Clinical Investigation **113**, 727-736.

[136] Q. Song, A. G. Schmidt, H. S. Hahn, A. N. Carr, B. Frank, L. Pater, M. Gerst, K. Young, B. D. Hoit, B. K. McConnell, K. Haghighi, C. E. Seidman, J. G. Seidman, G. W. Dorn and E. G. Kranias (2003) Rescue of cardiomyocyte dysfunction by phospholamban ablation does not prevent ventricular failure in genetic hypertrophy. J Clin Invest **111**, 859-867.

[137] A. M. Janczewski, M. Zahid, B. H. Lemster, C. S. Frye, G. Gibson, Y. Higuchi, E. G. Kranias, A. M. Feldman and C. F. McTiernan (2004) Phospholamban gene ablation improves calcium transients but not cardiac function in a heart failure model. Cardiovasc Res **62**, 468-480.

[138] K. Haghighi, F. Kolokathis, L. Pater, R. A. Lynch, M. Asahi, A. O. Gramolini, G. C. Fan, D. Tsiapras, H. S. Hahn, S. Adamopoulos, S. B. Liggett, G. W. Dorn, D. H. MacLennan, D. T. Kremastinos and E. G. Kranias (2003) Human phospholamban null results in lethal dilated cardiomyopathy revealing a critical difference between mouse and human. J Clin Invest **111**, 869-876.

[139] Y. Pan, T. Kislinger, A. O. Gramolini, E. Zvaritch, E. G. Kranias, D. H. MacLennan and A. Emili (2004) Identification of biochemical adaptations in hyper- or hypocontractile hearts from phospholamban mutant mice by expression proteomics. Proc Natl Acad Sci U S A **101**, 2241-2246.

[140] N. Frey, T. A. McKinsey and E. N. Olson (2000) Decoding calcium signals involved in cardiac growth and function. Nature Medicine **6**, 1221-1227.

[141] M. C. Olsson, J. R. Patel, D. P. Fitzsimons, J. W. Walker and R. L. Moss (2004) Basal myosin light chain phosphorylation is a determinant of Ca2+ sensitivity of force and activation dependence of the kinetics of myocardial force development. Am J Physiol Heart Circ Physiol **287**, H2712-H2718.

[142] van der Velden, Z. Papp, R. Zaremba, N. M. Boontje, J. W. de Jong, V. J. Owen, P. B. Burton, P. Goldmann, K. Jaquet and G. J. Stienen (2003) Increased Ca2+-sensitivity of the contractile apparatus in end-stage human heart failure results from altered phosphorylation of contractile proteins. Cardiovasc Res **57**, 37-47.

[143] W. Luo, B. M. Wolska, I. L. Grupp, J. M. Harrer, K. Haghighi, D. G. Ferguson, J. P. Slack, G. Grupp, T. Doetschman, R. J. Solaro and E. G. Kranias (1996) Phospholamban gene dosage effects in the mammalian heart. Circ Res **78**, 839-847.

[144] A. Werdich, E. Lima, B. Ivanov, I. Ges, M. E. Anderson, J. P. Wikswo and F. J. Baudenbacher (2004) A microfluidic device to confine a single cardiac myocyte in a sub-nanoliter volume on planar microelectrodes for extracellular potential recordings. Lab on A Chip.

[145] I. A. Ges, B. L. Ivanov, D. K. Schaffer, E. A. Lima, A. A. Werdich and F. J. Baudenbacher (2004) Thin-film IrOx pH microelectrode for microfluidic-based microsystems. Biosens Bioelectron **In Press, Corrected Proof**.

[146] J. W. M. Bassani, R. A. Bassani and D. M. Bers (1995) Calibration of Indo-1 and Resting Intracellular [Ca](I) in Intact Rabbit Cardiac Myocytes. Biophysical Journal **68**, 1453-1460.

[147] H. Ishida, H. Seguchi, N. Sakata, F. Ohusuzu, N. Aosaki, H. Nakamura and H. Okino (1991) Effects of fura-2 and indo-1 on [Ca++]i in spontaneously beating cultured heart cells. Tokai J Exp Clin Med **16**, 3-9.

[148] H. A. Spurgeon, W. H. duBell, M. D. Stern, S. J. Sollott, B. D. Ziman, H. S. Silverman, M. C. Capogrossi, A. Talo and E. G. Lakatta (1992) Cytosolic calcium and myofilaments in single rat cardiac myocytes achieve a dynamic equilibrium during twitch relaxation. J Physiol **447**, 83-102.

[149] W. D. Gao, N. G. Perez, C. E. Seidman, J. G. Seidman and E. Marban (1999) Altered cardiac excitation-contraction coupling in mutant mice with familial hypertrophic cardiomyopathy. J Clin Invest **103**, 661-666.

[150] W. D. Gao, N. G. Perez and E. Marban (1998) Calcium cycling and contractile activation in intact mouse cardiac muscle. J Physiol **507 (Pt 1)**, 175-184.

[151] B. D. Stuyvers, A. D. McCulloch, J. Guo, H. J. Duff and H. E. ter Keurs (2002) Effect of stimulation rate, sarcomere length and Ca(2+) on force generation by mouse cardiac muscle. J Physiol **544**, 817-830.

[152] H. L. Granzier and S. Labeit (2004) The giant protein titin: a major player in myocardial mechanics, signaling, and disease. Circ Res **94**, 284-295.

[153] M. Helmes, C. C. Lim, R. Liao, A. Bharti, L. Cui and D. B. Sawyer (2003) Titin determines the Frank-Starling relation in early diastole. J Gen Physiol **121**, 97-110.

[154] J. P. Konhilas, T. C. Irving and P. P. de Tombe (2002) Frank-Starling law of the heart and the cellular mechanisms of length-dependent activation. Pflugers Arch **445**, 305-310.

[155] L. S. Maier, D. M. Bers and B. Pieske (2000) Differences in Ca2+-handling and sarcoplasmic reticulum Ca2+-content in isolated rat and rabbit myocardium. Journal of Molecular and Cellular Cardiology **32**, 2249-2258.

[156] R. A. Bassani, A. Mattiazzi and D. M. Bers (1995) CaMKII is responsible for activity-dependent acceleration of relaxation in rat ventricular myocytes. Am J Physiol **268**, H703-H712.

[157] L. M. Bilezikjian, E. G. Kranias, J. D. Potter and A. Schwartz (1981) Studies on phosphorylation of canine cardiac sarcoplasmic reticulum by calmodulin-dependent protein kinase. Circ Res **49**, 1356-1362.

[158] I. Dzhura, Y. J. Wu, R. J. Colbran, J. R. Balser and M. E. Anderson (2000) Calmodulin kinase determines calcium-dependent facilitation of L-type calcium channels. Nature Cell Biology **2**, 173-177.

[159] X. H. T. Wehrens, S. E. Lehnart, S. R. Reiken and A. R. Marks (2004) Ca2+/Calmodulin-Dependent Protein Kinase II Phosphorylation Regulates the Cardiac Ryanodine Receptor. Circ Res **94**, e61-e70.

[160] De Koninck P. and H. Schulman (1998) Sensitivity of CaM kinase II to the frequency of Ca2+ oscillations. Science **279**, 227-230.

[161] Y. Ji, B. L. Li, T. D. Reed, J. N. Lorenz, M. A. Kaetzel and J. R. Dedman (2003) Targeted inhibition of Ca2+/calmodulin-dependent protein kinase II in cardiac longitudinal sarcoplasmic reticulum results in decreased phospholamban phosphorylation at threonine 17. Journal of Biological Chemistry **278**, 25063-25071.

[162] R. Zhang, M. S. C. Khoo, Y. J. Wu, Y. B. Yang, C. E. Grueter, G. M. Ni, E. E. Price, W. Thiel, S. Guatimosim, L. S. Song, E. C. Madu, A. N. Shah, T. A. Vishnivetskaya, J. B. Atkinson, V. V. Gurevich, G. Salama, W. J. Lederer, R. J. Colbran and M. E. Anderson (2005) Calmodulin kinase II inhibition protects against structural heart disease. Nature Medicine **11**, 409-417.

[163] T. Toyofuku, K. K. Curotto, N. Narayanan and D. H. MacLennan (1994) Identification of Ser38 as the site in cardiac sarcoplasmic reticulum Ca(2+)-ATPase that is phosphorylated by Ca2+/calmodulin-dependent protein kinase. J Biol Chem **269**, 26492-26496.

[164] A. Xu and N. Narayanan (1999) Ca2+/calmodulin-dependent phosphorylation of the Ca2+-ATPase, uncoupled from phospholamban, stimulates Ca2+-pumping in native cardiac sarcoplasmic reticulum. Biochem Biophys Res Commun **258**, 66-72.

[165] A. Odermatt, K. Kurzydlowski and D. H. MacLennan (1996) The vmax of the Ca2+-ATPase of cardiac sarcoplasmic reticulum (SERCA2a) is not altered by

Ca2+/calmodulin-dependent phosphorylation or by interaction with phospholamban. J Biol Chem **271**, 14206-14213.

[166] L. G. Reddy, L. R. Jones, R. C. Pace and D. L. Stokes (1996) Purified, reconstituted cardiac Ca2+-ATPase is regulated by phospholamban but not by direct phosphorylation with Ca2+/calmodulin-dependent protein kinase. J Biol Chem **271**, 14964-14970.

[167] D. R. Witcher, R. J. Kovacs, H. Schulman, D. C. Cefali and L. R. Jones (1991) Unique Phosphorylation Site on the Cardiac Ryanodine Receptor Regulates Calcium-Channel Activity. Journal of Biological Chemistry **266**, 11144-11152.

[168] J. Hain, H. Onoue, M. Mayrleitner, S. Fleischer and H. Schindler (1995) Phosphorylation Modulates the Function of the Calcium-Release Channel of Sarcoplasmic-Reticulum from Cardiac-Muscle. Journal of Biological Chemistry **270**, 2074-2081.

[169] L. S. Maier, T. Zhang, L. Chen, J. DeSantiago, J. H. Brown and D. M. Bers (2003) Transgenic CaMKII delta(C) overexpression uniquely alters cardiac myocyte Ca2+ handling - Reduced SR Ca2+ load and activated SR Ca2+ release. Circ Res **92**, 904-911.

[170] S. Currie, C. M. Loughrey, M. A. Craig and G. L. Smith (2004) Calcium/calmodulin-dependent protein kinase II delta associates with the ryanodine receptor complex and regulates channel function in rabbit heart. Biochemical Journal **377**, 357-366.

[171] J. X. Wang and P. M. Best (1992) Inactivation of the Sarcoplasmic-Reticulum Calcium-Channel by Protein-Kinase. Nature **359**, 739-741.

[172] A. J. Lokuta, T. B. Rogers, W. J. Lederer and H. H. Valdivia (1995) Modulation of Cardiac Ryanodine Receptors of Swine and Rabbit by A Phosphorylation-Dephosphorylation Mechanism. Journal of Physiology-London **487**, 609-622.

[173] S. Rezazadeh, T. W. Claydon and D. Fedida (2005) KN-93, a Calcium/Calmodulin-Dependent Protein Kinase II Inhibitor, is a Direct Extracellular Blocker of Voltage-Gated Potassium Channels. J Pharmacol Exp Ther.

[174] M. E. Anderson, A. P. Braun, Y. Wu, T. Lu, Y. Wu, H. Schulman and R. J. Sung (1998) KN-93, an inhibitor of multifunctional Ca++/calmodulin-dependent protein kinase, decreases early afterdepolarizations in rabbit heart. J Pharmacol Exp Ther **287**, 996-1006.

[175] A. P. Braun and H. Schulman (1995) A non-selective cation current activated via the multifunctional Ca(2+)-calmodulin-dependent protein kinase in human epithelial cells. J Physiol **488 (Pt 1)**, 37-55.

[176] A. P. Braun and H. Schulman (1995) A non-selective cation current activated via the multifunctional Ca(2+)-calmodulin-dependent protein kinase in human epithelial cells. J Physiol **488 (Pt 1)**, 37-55.

[177] E. Kiss, I. Edes, Y. Sato, W. Luo, S. B. Liggett and E. G. Kranias (1997) beta-Adrenergic regulation of cAMP and protein phosphorylation in phospholamban-knockout mouse hearts. Am J Physiol **272**, H785-H790.

[178] S. Bolsover, O. Ibrahim, N. O'luanaigh, H. Williams and S. Cockcroft (2001) Use of fluorescent Ca2+ dyes with green fluorescent protein and its variants: problems and solutions. Biochem J **356**, 345-352.

[179] S. Bolsover, O. Ibrahim, N. O'luanaigh, H. Williams and S. Cockcroft (2001) Use of fluorescent Ca2+ dyes with green fluorescent protein and its variants: problems and solutions. Biochem J **356**, 345-352.

[180] Y. Wu, A. Shintani, C. Grueter, R. Zhang, Y. Hou, J. Yang, E. G. Kranias, R. J. Colbran and M. E. Anderson (2006) Suppression of dynamic Ca(2+) transient responses to pacing in ventricular myocytes from mice with genetic calmodulin kinase II inhibition. J Mol Cell Cardiol.

[181] Z. Kassiri, R. Myers, R. Kaprielian, H. S. Banijamali and P. H. Backx (2000) Rate-dependent changes of twitch force duration in rat cardiac trabeculae: a property of the contractile system. J Physiol **524 Pt 1**, 221-231.

[182] J. E. Frampton and C. H. Orchard (1992) The effect of a calmodulin inhibitor on intracellular [Ca2+] and contraction in isolated rat ventricular myocytes. J Physiol **453**, 385-400.

[183] M. E. Anderson (2005) Calmodulin kinase signaling in heart: an intriguing candidate target for therapy of myocardial dysfunction and arrhythmias. Pharmacology & Therapeutics **106**, 39-55.

[184] L. A. Geddes (1972) Electrodes and the measurement of bioelectric events. .

[185] L. B. Cohen, B. M. Salzberg and A. Grinvald (1978) Optical Methods for Monitoring Neuron Activity. Annual Review of Neuroscience **1**, 171-182.

[186] I. Johnson (1998) Fluorescent probes for living cells. Histochemical Journal **30**, 123-140.

[187] M. C. T. Denyer, M. Riehle, S. T. Britland and A. Offenhauser (1998) Preliminary study on the suitability of a pharmacological bio- assay based on cardiac myocytes cultured over microfabricated microelectrode arrays. Medical & Biological Engineering & Computing **36**, 638-644.

[188] P. Connolly, P. Clark, A. S. G. Curtis, J. A. T. Dow and C. D. W. Wilkinson (1990) An Extracellular Microelectrode Array for Monitoring Electrogenic Cells in Culture. Biosensors & Bioelectronics **5**, 223-234.

[189] C. Sprossler, M. Denyer, S. Britland, W. Knoll and A. Offenhausser (1999) Electrical recordings from rat cardiac muscle cells using field-effect transistors. Physical Review e **60**, 2171-2176.

[190] S. Ingebrandt, C. K. Yeung, M. Krause and A. Offenhausser (2001) Cardiomyocyte-transistor-hybrids for sensor application. Biosensors & Bioelectronics **16**, 565-570.

[191] H. Ecken, S. Ingebrandt, M. Krause, D. Richter, M. Hara and A. Offenhausser (2003) 64-Channel extended gate electrode arrays for extracellular signal recording. Electrochimica Acta **48**, 3355-3362.

[192] D. Israel, W. H. Barry, D. J. Edell and R. G. Mark (1984) An Array of Microelectrodes to Stimulate and Record from Cardiac-Cells in Culture. American Journal of Physiology **247**, H669-H674.

[193] K. H. Gilchrist, L. Giovangrandi and G. T. A. Kovacs (2001) Analysis of Microelectrode-Recorded Signals from a Cardiac Cell Line as a Tool for Pharmaceutical Screening.
390-393.

[194] K. H. Gilchrist, V. N. Barker, L. E. Fletcher, B. D. DeBusschere, P. Ghanouni, L. Giovangrandi and G. T. A. Kovacs (2001) General purpose, field-portable cell-based biosensor platform. Biosens Bioelectron **16**, 557-564.

[195] W. C. Claycomb, N. A. Lanson, B. S. Stallworth, D. B. Egeland, J. B. Delcarpio, A. Bahinski and N. J. Izzo (1998) HL-1 cells: A cardiac muscle cell line that contracts and retains phenotypic characteristics of the adult cardiomyocyte. Proceedings of the National Academy of Sciences of the United States of America **95**, 2979-2984.

[196] D. R. Bers and E. Perez-Reyes (1999) Ca channels in cardiac myocytes: structure and function in Ca influx and intracellular Ca release. Cardiovascular Research **42**, 339-360.

[197] L. F. Santana, H. Cheng, A. M. Gomez, M. B. Cannell and W. J. Lederer (1996) Relation between the sarcolemmal Ca2+ current and Ca2+ sparks and local control theories for cardiac excitation-contraction coupling. Circulation Research **78**, 166-171.

[198] H. Cheng, M. R. Lederer, W. J. Lederer and M. B. Cannell (1996) Calcium sparks and [Ca2+](i) waves in cardiac myocytes. American Journal of Physiology-Cell Physiology **39**, C148-C159.

[199] B. D. Stuyvers, P. A. Boyden and H. E. D. J. ter Keurs (2000) Calcium waves - Physiological relevance in cardiac function. Circulation Research **86**, 1016-1018.

[200] T. Kaneko, H. Tanaka, M. Oyamada, S. Kawata and T. Takamatsu (2000) Three distinct types of Ca2+ waves in Langendorff-perfused rat heart revealed by real-time confocal microscopy. Circ Res **86**, 1093-1099.

[201] R. S. Kass, W. J. Lederer, R. W. Tsien and R. Weingart (1978) Role of Calcium-Ions in Transient Inward Currents and After Contractions Induced by Strophanthidin in Cardiac Purkinje-Fibers. Journal of Physiology-London **281**, 187-208.

[202] W. J. Lederer and R. W. Tsien (1976) Transient Inward Current Underlying Arrhythmogenic Effects of Cardiotonic Steroids in Purkinje-Fibers. Journal of Physiology-London **263**, 73-100.

[203] D. Fedida, D. Noble, A. C. Rankin and A. J. Spindler (1987) The Arrhythmogenic Transient Inward Current Iti and Related Contraction in Isolated Guinea-Pig Ventricular Myocytes. Journal of Physiology-London **392**, 523-542.

[204] J. P. Chang and J. W. Coburn (2003) Plasma–surface interactions. Journal of Vacuum Science & Technology A-Vacuum Surfaces and Films **21**, S145-S151.

[205] J. J. Pancrazio, P. P. Bey, A. Loloee, S. R. Manne, H. C. Chao, L. L. Howard, W. M. Gosney, D. A. Borkholder, G. T. A. Kovacs, P. Manos, D. S. Cuttino and D. A. Stenger (1998) Description and demonstration of a CMOS amplifier-based-system with measurement and stimulation capability for bioelectrical signal transduction. Biosensors & Bioelectronics **13**, 971-979.

[206] M. E. Anderson, A. P. Braun, H. Schulman and B. A. Premack (1994) Multifunctional Ca2+/Calmodulin-Dependent Protein-Kinase Mediates Ca2+-Induced Enhancement of the L-Type Ca2+ Current in Rabbit Ventricular Myocytes. Circulation Research **75**, 854-861.

[207] V. S. Muralidharan (1997) Warburg impedance - Basics revisited. Anti-Corrosion Methods and Materials **44**, 26-&.

[208] H. Fricke (1932) The theory of electrolyte polarization. Philosophical Magazine **14**, 310-318.

[209] E. Warburg (1899) Über das Verhalten sogenannter unpolarisierter Elektroden gegen Wechselstrom. Annalen der Physik **67**, 493-499.

[210] S. R. Taylor and E. Gileadi (1995) Physical Interpretation of the Warburg Impedance. Corrosion **51**, 664-671.

[211] D. M. Bers and C. R. Weber (2002) Na/Ca exchange function in intact ventricular myocytes. Cellular and Molecular Physiology of Sodium-Calcium Exchange **976**, 500-512.

[212] A. A. Armoundas, I. A. Hobai, G. F. Tomaselli, R. L. Winslow and B. O'Rourke (2003) Role of sodium-calcium exchanger in modulating the action potential of ventricular myocytes from normal and failing hearts. Circ Res **93**, 46-53.

[213] J. Weisser-Thomas, V. Piacentino, J. P. Gaughan, K. Margulies and S. R. Houser (2003) Calcium entry via Na/Ca exchange during the action potential directly contributes to contraction of failing human ventricular myocytes. Cardiovascular Research **57**, 974-985.

[214] A. C. Zygmunt (1994) Intracellular Calcium Activates A Chloride Current in Canine Ventricular Myocytes. American Journal of Physiology-Heart and Circulatory Physiology **36**, H1984-H1995.

[215] S. Kawano, Y. Hirayama and M. Hiraoka (1995) Activation Mechanism of Ca2+-Sensitive Transient Outward Current in Rabbit Ventricular Myocytes. Journal of Physiology-London **486**, 593-604.

[216] M. Hiraoka and S. Kawano (1989) Calcium-Sensitive and Insensitive Transient Outward Current in Rabbit Ventricular Myocytes. Journal of Physiology-London **410**, 187-212.

[217] A. C. Zygmunt and W. R. Gibbons (1991) Calcium-Activated Chloride Current in Rabbit Ventricular Myocytes. Circulation Research **68**, 424-437.

[218] P. H. Backx, P. P. Detombe, J. H. K. Vandeen, B. J. M. Mulder and H. E. D. J. Terkeurs (1989) A Model of Propagating Calcium-Induced Calcium Release Mediated by Calcium Diffusion. Journal of General Physiology **93**, 963-977.

[219] A. Glukhovsky, D. R. Adam, G. Amitzur and S. Sideman (1998) Mechanism of Ca++ release from the sarcoplasmic reticulum: A computer model. Annals of Biomedical Engineering **26**, 213-229.

[220] J. Engel, A. J. Sowerby, S. A. E. Finch, M. Fechner and A. Stier (1995) Temperature-Dependence of Ca2+ Wave Properties in Cardiomyocytes - Implications for the Mechanism of Autocatalytic Ca2+ Release in Wave-Propagation. Biophysical Journal **68**, 40-45.

[221] A. Kamkin, I. Kiseleva, K. D. Wagner, J. Bohm, H. Theres, J. Gunther and H. Scholz (2003) Characterization of stretch-activated ion currents in isolated atrial myocytes from human hearts. Pflugers Arch **446**, 339-346.

[222] R. J. Solaro, A. J. Moir and S. V. Perry (1976) Phosphorylation of troponin I and the inotropic effect of adrenaline in the perfused rabbit heart. Nature **262**, 615-617.

[223] A. J. Moir, R. J. Solaro and S. V. Perry (1980) The site of phosphorylation of troponin I in the perfused rabbit heart. The effect of adrenaline. Biochem J **185**, 505-513.

[224] H. M. Rarick, H. P. Tang, X. D. Guo, A. F. Martin and R. J. Solaro (1999) Interactions at the NH2-terminal interface of cardiac troponin I modulate myofilament activation. J Mol Cell Cardiol **31**, 363-375.

[225] H. M. Rarick, X. H. Tu, R. J. Solaro and A. F. Martin (1997) The C terminus of cardiac troponin I is essential for full inhibitory activity and Ca2+ sensitivity of rat myofibrils. J Biol Chem **272**, 26887-26892.

[226] C. W. Tong, R. D. Gaffin, D. C. Zawieja and M. Muthuchamy (2004) Roles of phosphorylation of myosin binding protein-C and troponin I in mouse cardiac muscle twitch dynamics. J Physiol **558**, 927-941.

[227] V. J. Exil, R. L. Roberts, H. Sims, J. E. McLaughlin, R. A. Malkin, C. D. Gardner, G. Ni, J. N. Rottman and A. W. Strauss (2003) Very-long-chain acyl-coenzyme a dehydrogenase deficiency in mice. Circ Res **93**, 448-455.

[228] S. M. Pogwizd, M. Qi, W. Yuan, A. M. Samarel and D. M. Bers (1999) Upregulation of Na(+)/Ca(2+) exchanger expression and function in an arrhythmogenic rabbit model of heart failure. Circ Res **85**, 1009-1019.

[229] D. M. Bers and C. R. Weber (2002) Na/Ca exchange function in intact ventricular myocytes. Cellular and Molecular Physiology of Sodium-Calcium Exchange **976**, 500-512.

[230] D. M. Bers, W. J. Lederer and J. R. Berlin (1990) Intracellular Ca-Transients in Rat Cardiac Myocytes - Role of Na-Ca Exchange in Excitation-Contraction Coupling. American Journal of Physiology **258**, C944-C954.

[231] A. C. R. Grayson, R. S. Shawgo, A. M. Johnson, N. T. Flynn, Y. W. Li, M. J. Cima and R. Langer (2004) A BioMEMS review: MEMS technology for physiologically integrated devices. Proceedings of the Ieee **92**, 6-21.

[232] S. A. M. Marzouk (2003) Improved electrodeposited iridium oxide pH sensor fabricated on etched titanium substrates. Analytical Chemistry **75**, 1258-1266.

[233] R. D. Meyer, S. F. Cogan, T. H. Nguyen and R. D. Rauh (2001) Electrodeposited iridium oxide for neural stimulation and recording electrodes. Ieee Transactions on Rehabilitation Engineering **9**, 2-11.

[234] W. Olthuis, M. A. M. Robben, P. Bergveld, M. Bos and W. E. Vanderlinden (1990) Ph Sensor Properties of Electrochemically Grown Iridium Oxide. Sensors and Actuators B-Chemical **2**, 247-256.

[235] M. F. Smiechowski and V. F. Lvovich (2003) Iridium oxide sensors for acidity and basicity detection in industrial lubricants. Sensors and Actuators B-Chemical **96**, 261-267.

[236] P. Vanhoudt, Z. Lewandowski and B. Little (1992) Iridium Oxide Ph Microelectrode. Biotechnology and Bioengineering **40**, 601-608.

[237] M. Wang, S. Yao and M. Madou (2002) A long-term stable iridium oxide pH electrode. Sensors and Actuators B-Chemical **81**, 313-315.

[238] K. Yamanaka (1991) The Electrochemical-Behavior of Anodically Electrodeposited Iridium Oxide-Films and the Reliability of Transmittance Variable Cells. Japanese Journal of Applied Physics Part 1-Regular Papers Short Notes & Review Papers **30**, 1285-1289.

[239] H. S. Yang, S. K. Kang, C. A. Choi, H. Kim, D. H. Shin, Y. S. Kim and Y. T. Kim (2004) An iridium oxide reference electrode for use in microfabricated biosensors and biochips. Lab on A Chip **4**, 42-46.

[240] D. L. Polla, A. G. Erdman, W. P. Robbins, D. T. Markus, J. az-Diaz, R. Rizq, Y. Nam, H. T. Brickner, A. Wang and P. Krulevitch (2000) Microdevices in medicine. Annual Review of Biomedical Engineering **2**, 551-576.

[241] S. E. Eklund, D. Taylor, E. Kozlov, A. Prokop and D. E. Cliffel (2004) A microphysiometer for simultaneous measurement of changes in extracellular glucose, lactate, oxygen, and acidification rate. Anal Chem **76**, 519-527.

[242] H. M. Mcconnell, J. C. Owicki, J. W. Parce, D. L. Miller, G. T. Baxter, H. G. Wada and S. Pitchford (1992) The Cytosensor Microphysiometer - Biological Applications of Silicon Technology. Science **257**, 1906-1912.

[243] F. Hafner (2000) Cytosensor((R)) Microphysiometer: technology and recent applications. Biosensors & Bioelectronics **15**, 149-158.

[244] D. Smart and M. D. Wood (2000) Cytosensor techniques for examining signal transduction of neurohormones. Biochemistry and Cell Biology-Biochimie et Biologie Cellulaire **78**, 281-288.

[245] B. Stein, M. George, H. E. Gaub, J. C. Behrends and W. J. Parak (2003) Spatially resolved monitoring of cellular metabolic activity with a semiconductor-based biosensor. Biosensors & Bioelectronics **18**, 31-41.

[246] J. C. Owicki, L. J. Bousse, D. G. Hafeman, G. L. Kirk, J. D. Olson, H. G. Wada and J. W. Parce (1994) The Light-Addressable Potentiometric Sensor - Principles and Biological Applications. Annual Review of Biophysics and Biomolecular Structure **23**, 87-113.

[247] M. Lehmann, W. Baumann, M. Brischwein, H. J. Gahle, I. Freund, R. Ehret, S. Drechsler, H. Palzer, M. Kleintges, U. Sieben and B. Wolf (2001) Simultaneous measurement of cellular respiration and acidification with a single CMOS ISFET. Biosensors & Bioelectronics **16**, 195-203.

[248] M. Lehmann, W. Baumann, M. Brischwein, R. Ehret, M. Kraus, A. Schwinde, M. Bitzenhofer, I. Freund and B. Wolf (2000) Non-invasive measurement of cell membrane associated proton gradients by ion-sensitive field effect transistor arrays for microphysiological and bioelectronical applications. Biosensors & Bioelectronics **15**, 117-124.

[249] W. H. Baumann, M. Lehmann, A. Schwinde, R. Ehret, M. Brischwein and B. Wolf (1999) Microelectronic sensor system for microphysiological application on living cells. Sensors and Actuators B-Chemical **55**, 77-89.

[250] T. Vilkner, D. Janasek and A. Manz (2004) Micro total analysis systems. Recent developments. Analytical Chemistry **76**, 3373-3385.

[251] J. E. Baur and T. W. Spaine (1998) Electrochemical deposition of iridium(IV) oxide from alkaline solutions of iridium(III) oxide. Journal of Electroanalytical Chemistry **443**, 208-216.

[252] S. A. M. Marzouk, S. Ufer, R. P. Buck, T. A. Johnson, L. A. Dunlap and W. E. Cascio (1998) Electrodeposited iridium oxide pH electrode for measurement of extracellular myocardial acidosis during acute ischemia. Analytical Chemistry **70**, 5054-5061.

[253] J. Hendrikse, W. Olthuis and P. Bergveld (1998) A method of reducing oxygen induced drift in iridium oxide pH sensors. Sensors and Actuators B-Chemical **53**, 97-103.

[254] P. J. Kinlen, J. E. Heider and D. E. Hubbard (1994) A Solid-State Ph Sensor-Based on A Nafion-Coated Iridium Oxide Indicator Electrode and A Polymer-Based Silver-Chloride Reference Electrode. Sensors and Actuators B-Chemical **22**, 13-25.

[255] J. D. Klein, S. L. Clauson and S. F. Cogan (1989) Morphology and Charge Capacity of Sputtered Iridium Oxide-Films. Journal of Vacuum Science & Technology A-Vacuum Surfaces and Films **7**, 3043-3047.

[256] K. Kinoshita and M. J. Madou (1984) Electrochemical Measurements on Pt, Ir, and Ti Oxides As Ph Probes. Journal of the Electrochemical Society **131**, 1089-1094.

[257] Y. Sato (1989) Electrochromism in Thermally Oxidized Iridium Oxide-Films in Liclo4 Propylene Carbonate. Japanese Journal of Applied Physics Part 1-Regular Papers Short Notes & Review Papers **28**, 1290-1291.

[258] S. Yao, M. Wang and M. Madou (2001) A pH electrode based on melt-oxidized iridium oxide. Journal of the Electrochemical Society **148**, H29-H36.

[259] S. Ardizzone, A. Carugati and S. Trasatti (1981) Properties of Thermally Prepared Iridium Dioxide Electrodes. Journal of Electroanalytical Chemistry **126**, 287-292.

[260] H. Suzuki, T. Hirakawa, S. Sasaki and I. Karube (2000) An integrated module for sensing pO(2), pCO(2), and pH. Analytica Chimica Acta **405**, 57-65.

[261] S. C. Mailley, M. Hyland, P. Mailley, J. M. McLaughlin and E. T. McAdams (2002) Electrochemical and structural characterizations of electrodeposited iridium oxide thin-film electrodes applied to neuro stimulating electrical signal. Materials Science & Engineering C-Biomimetic and Supramolecular Systems **21**, 167-175.

[262] M. A. Petit and V. Plichon (1998) Anodic electrodeposition of iridium oxide films. Journal of Electroanalytical Chemistry **444**, 247-252.

[263] K. Yamanaka (1989) Anodically Electrodeposited Iridium Oxide-Films (Aeirof) from Alkaline-Solutions for Electrochromic Display Devices. Japanese Journal of Applied Physics Part 1-Regular Papers Short Notes & Review Papers **28**, 632-637.

[264] K. Pasztor, A. Sekiguchi, N. Shimo, N. Kitamura and H. Masuhara (1993) Iridium Oxide-Based Microelectrochemical Transistors for Ph Sensing. Sensors and Actuators B-Chemical **12**, 225-230.

[265] A. N. Bezbaruah and T. C. Zhang (2002) Fabrication of anodically electrodeposited iridium oxide film pH microelectrodes for microenvironmental studies. Analytical Chemistry **74**, 5726-5733.

[266] L. D. Burke, J. K. Mulcahy and D. P. Whelan (1984) Preparation of An Oxidized Iridium Electrode and the Variation of Its Potential with Ph. Journal of Electroanalytical Chemistry **163**, 117-128.

[267] H. R. Clark, T. A. Barbari and G. Rao (1999) Modeling the response time of an in vivo glucose affinity sensor. Biotechnology Progress **15**, 259-266.

[268] N. Izu, W. Shin and N. Murayama (2002) Numerical analysis of response time for resistive oxygen gas sensors. Sensors and Actuators B-Chemical **87**, 99-104.

[269] N. Wisniewski and M. Reichert (2000) Methods for reducing biosensor membrane biofouling. Colloids and Surfaces B-Biointerfaces **18**, 197-219.

[270] D. C. Wallace (1999) Mitochondrial diseases in man and mouse. Science **283**, 1482-1488.

[271] A. W. Strauss, C. K. Powell, D. E. Hale, M. M. Anderson, A. Ahuja, J. C. Brackett and H. F. Sims (1995) Molecular basis of human mitochondrial very-long-chain acyl-CoA dehydrogenase deficiency causing cardiomyopathy and sudden death in childhood. Proc Natl Acad Sci U S A **92**, 10496-10500.

[272] J. Vockley (1994) The changing face of disorders of fatty acid oxidation. Mayo Clin Proc **69**, 249-257.

[273] B. S. Andresen, S. Olpin, B. J. Poorthuis, H. R. Scholte, C. Vianey-Saban, R. Wanders, L. Ijlst, A. Morris, M. Pourfarzam, K. Bartlett, E. R. Baumgartner, J. B. deKlerk, L. D. Schroeder, T. J. Corydon, H. Lund, V. Winter, P. Bross, L. Bolund and N. Gregersen (1999) Clear correlation of genotype with disease phenotype in very-long-chain acyl-CoA dehydrogenase deficiency. Am J Hum Genet **64**, 479-494.

[274] D. P. Kelly and A. W. Strauss (1994) Inherited cardiomyopathies. N Engl J Med **330**, 913-919.

[275] A. Mathur, H. F. Sims, D. Gopalakrishnan, B. Gibson, P. Rinaldo, J. Vockley, G. Hug and A. W. Strauss (1999) Molecular heterogeneity in very-long-chain acyl-CoA dehydrogenase deficiency causing pediatric cardiomyopathy and sudden death. Circulation **99**, 1337-1343.

[276] B. S. Andresen, P. Bross, C. Vianey-Saban, P. Divry, M. T. Zabot, C. R. Roe, M. A. Nada, A. Byskov, T. A. Kruse, S. Neve, K. Kristiansen, I. Knudsen, M. J. Corydon and N. Gregersen (1996) Cloning and characterization of human very-long-chain acyl-CoA dehydrogenase cDNA, chromosomal assignment of the gene and identification in four patients of nine different mutations within the VLCAD gene. Hum Mol Genet **5**, 461-472.

[277] S. Fleischer and M. Inui (1989) Biochemistry and biophysics of excitation-contraction coupling. Annu Rev Biophys Biophys Chem **18**, 333-364.

[278] Y. Ogawa (1994) Role of ryanodine receptors. Crit Rev Biochem Mol Biol **29**, 229-274.

[279] T. Jayaraman, A. M. Brillantes, A. P. Timerman, S. Fleischer, H. Erdjument-Bromage, P. Tempst and A. R. Marks (1992) FK506 binding protein associated with the calcium release channel (ryanodine receptor). J Biol Chem **267**, 9474-9477.

[280] A. P. Timerman, T. Jayaraman, G. Wiederrecht, H. Onoue, A. R. Marks and S. Fleischer (1994) The ryanodine receptor from canine heart sarcoplasmic reticulum is associated with a novel FK-506 binding protein. Biochem Biophys Res Commun **198**, 701-706.

[281] A. Saito, S. Seiler, A. Chu and S. Fleischer (1984) Preparation and morphology of sarcoplasmic reticulum terminal cisternae from rabbit skeletal muscle. J Cell Biol **99**, 875-885.

[282] M. Inui, S. Wang, A. Saito and S. Fleischer (1988) Junctional and longitudinal sarcoplasmic reticulum of heart muscle. Methods Enzymol **157**, 100-106.

[283] H. Swan, K. Piippo, M. Viitasalo, P. Heikkila, T. Paavonen, K. Kainulainen, J. Kere, P. Keto, K. Kontula and L. Toivonen (1999) Arrhythmic disorder mapped to chromosome 1q42-q43 causes malignant polymorphic ventricular tachycardia in structurally normal hearts. J Am Coll Cardiol **34**, 2035-2042.

[284] S. G. Priori, C. Napolitano, N. Tiso, M. Memmi, G. Vignati, R. Bloise, V. Sorrentino and G. A. Danieli (2001) Mutations in the cardiac ryanodine receptor gene (hRyR2) underlie catecholaminergic polymorphic ventricular tachycardia. Circulation **103**, 196-200.

[285] H. Lahat, M. Eldar, E. Levy-Nissenbaum, T. Bahan, E. Friedman, A. Khoury, A. Lorber, D. L. Kastner, B. Goldman and E. Pras (2001) Autosomal recessive catecholamine- or exercise-induced polymorphic ventricular tachycardia: clinical features and assignment of the disease gene to chromosome 1p13-21. Circulation **103**, 2822-2827.

[286] P. J. Laitinen, K. M. Brown, K. Piippo, H. Swan, J. M. Devaney, B. Brahmbhatt, E. A. Donarum, M. Marino, N. Tiso, M. Viitasalo, L. Toivonen, D. A. Stephan and K. Kontula (2001) Mutations of the cardiac ryanodine receptor (RyR2) gene in familial polymorphic ventricular tachycardia. Circulation **103**, 485-490.

[287] A. Rampazzo, A. Nava, P. Erne, M. Eberhard, E. Vian, P. Slomp, N. Tiso, G. Thiene and G. A. Danieli (1995) A new locus for arrhythmogenic right ventricular cardiomyopathy (ARVD2) maps to chromosome 1q42-q43. Hum Mol Genet **4**, 2151-2154.

[288] N. Tiso, D. A. Stephan, A. Nava, A. Bagattin, J. M. Devaney, F. Stanchi, G. Larderet, B. Brahmbhatt, K. Brown, B. Bauce, M. Muriago, C. Basso, G. Thiene, G. A. Danieli and A. Rampazzo (2001) Identification of mutations in the cardiac ryanodine receptor gene in families affected with arrhythmogenic right ventricular cardiomyopathy type 2 (ARVD2). Hum Mol Genet **10**, 189-194.

[289] A. R. Marks, S. Priori, M. Memmi, K. Kontula and P. J. Laitinen (2002) Involvement of the cardiac ryanodine receptor/calcium release channel in catecholaminergic polymorphic ventricular tachycardia. J Cell Physiol **190**, 1-6.

[290] V. J. Exil, C. D. Gardner, J. N. Rottman, H. Sims, B. Bartelds, Z. Khuchua, R. Sindhal, G. Ni and A. W. Strauss (2005) Abnormal Mitochondrial Bioenergetics and Heart Rate Dysfunction in Mice Lacking Very-Long-Chain Acyl-CoA Dehydrogenase. Am J Physiol Heart Circ Physiol.

[291] B. K. Chamberlain and S. Fleischer (1988) Isolation of canine cardiac sarcoplasmic reticulum. Methods Enzymol **157**, 91-99.

[292] A. P. Timerman, E. Ogunbumni, E. Freund, G. Wiederrecht, A. R. Marks and S. Fleischer (1993) The calcium release channel of sarcoplasmic reticulum is modulated by FK-506-binding protein. Dissociation and reconstitution of FKBP-12 to the calcium release channel of skeletal muscle sarcoplasmic reticulum. J Biol Chem **268**, 22992-22999.

[293] G. R. Sambrano, I. Fraser, H. Han, Y. Ni, T. O'Connell, Z. Yan and J. T. Stull (2002) Navigating the signalling network in mouse cardiac myocytes. Nature **420**, 712-714.

[294] O. P. Hamill, A. Marty, E. Neher, B. Sakmann and F. J. Sigworth (1981) Improved patch-clamp techniques for high-resolution current recording from cells and cell-free membrane patches. Pflugers Arch **391**, 85-100.

[295] M. E. Anderson, A. P. Braun, H. Schulman and B. A. Premack (1994) Multifunctional Ca2+/calmodulin-dependent protein kinase mediates Ca(2+)-induced enhancement of the L-type Ca2+ current in rabbit ventricular myocytes. Circ Res **75**, 854-861.

[296] G. Beutner, V. K. Sharma, D. R. Giovannucci, D. I. Yule and S. S. Sheu (2001) Identification of a ryanodine receptor in rat heart mitochondria. J Biol Chem **276**, 21482-21488.

[297] A. R. Marks (2001) Ryanodine receptors/calcium release channels in heart failure and sudden cardiac death. J Mol Cell Cardiol **33**, 615-624.

[298] E. Carafoli (1987) Intracellular calcium homeostasis. Annu Rev Biochem **56**, 395-433.

[299] R. Brandes and D. M. Bers (1997) Intracellular Ca2+ increases the mitochondrial NADH concentration during elevated work in intact cardiac muscle. Circ Res **80**, 82-87.

[300] E. J. Griffiths, M. D. Stern and H. S. Silverman (1997) Measurement of mitochondrial calcium in single living cardiomyocytes by selective removal of cytosolic indo 1. Am J Physiol **273**, C37-C44.